



TECHNISCHE
UNIVERSITÄT
WIEN

VIENNA
UNIVERSITY OF
TECHNOLOGY

DISSERTATION

Computer Graphics in Historical and Modern Sky Observations

ausgeführt zum Zwecke der Erlangung des akademischen Grades
eines Doktors der technischen Wissenschaften

unter der Leitung von

Univ.-Prof. Dr. Werner Purgathofer
E 186 Institut für Computergraphik und Algorithmen

unter Mitwirkung von
Univ.-Ass. Dipl.-Ing. Dr. Alexander Wilkie

eingereicht an der Technischen Universität Wien
Fakultät für Informatik

von

Dipl.-Ing. Georg Zotti, Bakk.rer.nat.
Matrikelnummer 9126124
Ghelengasse 13a, A-1130 Wien

Wien, am 29. Oktober 2007

Kurzfassung

Diese Arbeit behandelt drei Aspekte von Himmelsbeobachtungen in Kombination mit dem Bereich Computergraphik. Thematisch überstreicht die Arbeit mehrere Jahrtausende und umfaßt Fragen aus Bereichen wie Archäologie, Astronomie, Kulturerbe, digitaler Bildverarbeitung und Computergraphik.

Der erste Teil umfaßt interdisziplinäre Arbeit aus den Bereichen Archäo-Astronomie, Visualisierung und virtueller Rekonstruktion. Ein neuartiges Diagramm bietet eine intuitive Visualisierung zur Untersuchung archäologischer Vermessungspläne auf Hinweise astronomisch motivierter Orientierungen (etwa gegen Sonnenauf- und Untergänge zu den Sonnenwenden, oder zu Auf- und Untergangspunkten gewisser Sterne). Diese Visualisierung wurde zur Untersuchung gut datierbarer jungsteinzeitlicher Kreisgrabenanlagen in Niederösterreich entwickelt, und tatsächlich bietet die Anwendung des Diagramms klare Hinweise auf derart astronomisch motivierte Ausrichtung von Toren in einigen dieser Anlagen, was zusammen mit einer dazugehörigen astronomischen Erklärung der stellaren Ausrichtung die Aufstellung einer Hypothese über einen Aspekt der praktischen Astronomie der Vorzeit ermöglichte.

Virtuelle Rekonstruktionen stellen eine immer stärker genutzte Möglichkeit dar, Erkenntnisse aus der Archäologie einem breiten Publikum zu vermitteln. Die praktische, publikumsgerechte Aufbereitung der archäo-astronomischen Ergebnisse durch Kombination virtueller Rekonstruktion mit der jeder digitalen Projektion überlegenen Himmelssimulation in einem modernen Planetarium ist daher Thema des folgenden Kapitels.

Der zweite Teil der Arbeit behandelt ein konkretes historisches Beobachtungsinstrument und seine Rekonstruktion mit Methoden der Computergraphik. Lange nach der Steinzeit, im Mittelalter, war das Astrolabium das astronomische Beobachtungs- und Recheninstrument schlechthin, und sein Bau wurde auch in zeitgenössischer Literatur meist mit umfangreichen Tabellen der Größen der Konstruktionselemente beschrieben. Heute finden sich derartige Instrumente meist unzureichend erklärt in historischen Sammlungen und Ausstellungen. Die Vermittlung der verschiedenen Funktionen ist ohne praktische Demonstration schwierig. Hier bieten sich Methoden der prozeduralen Modellierung für dieses Paradebeispiel mathematisch-geometrisch konstruierter Instrumente geradezu an. Dabei wird nicht das gesamte Modell statisch mit primitiven Zeichenoperatoren (Strecke, Kreisbogen) beschrieben, sondern die Konstruktionsanleitung der verschiedenen Diagramme und -teile wird in Prozeduren umgesetzt, die dann zur Erzeugung eines konkreten Instruments mit unterschiedlichen Parametern ausgeführt werden. Auch die Umsetzung der zweidimensionalen Diagramme in virtuelle 3D-Modelle ist recht einfach, und man kann sogar aus den Diagrammen mit einem Lasergravierer hölzerne Instrumente zur praktischen Demonstration der Funktionsweise herstellen.

Der dritte und längste Teil behandelt Methoden der Himmelssimulation, -darstellung und -erfassung aus dem eigentlichen Bereich der Computergraphik. In dieser Disziplin wurden in den letzten zwei Jahrzehnten große Fortschritte bei der Darstellung des Himmels und atmosphärischer Effekte erzielt, die in einer ausführlichen Literaturübersicht präsentiert werden, in der auch Querbezüge zur Literatur aus dem Gebiet der Atmosphärenphysik nicht zu kurz kommen.

Die Ansprüche von physikalisch basiertem Rendering beinhalten auch ein realitätsnahes Modell der Himmelshelligkeit. Helligkeitsmessungen am klaren Himmel zeigen, daß das derzeit meistverwendete analytische Himmelsmodell [PREETHAM *et al.* 1999] nur mit Einschränkungen einsetzbar ist.

Himmelsmodelle ließen sich bisher in 2 große Gruppen einteilen: numerische Simulation der Streuungsprozesse in der Erdatmosphäre und schnelle analytische Modelle. In jüngerer Zeit werden zur Verbesserung des realistischen Eindrucks auch Fischaugen-Photos des gesamten Himmels mit Digitalkameras erstellt und zu Bildern mit erweitertem Dynamikumfang (*High Dynamic Range*, HDR) kombiniert. Diese können durch photometrische Punktmessungen auf absolute Helligkeitswerte kalibriert werden, und derartige Aufnahmen bieten auch Anwendungen außerhalb der eigentlichen Computergraphik. Langzeitbelichtungen gestatten auch die Untersuchung und Quantifizierung der nächtlichen Himmelshelligkeit und Lichtverschmutzung durch künstliche Beleuchtung. Ein derartiges System wurde vom Autor entwickelt. Ergebnisse unseres Systems werden hier dargestellt, die notwendigen Arbeitsschritte werden in einem Anhang beschrieben.

Die Arbeit schließt mit einigen Ideen für zukünftige Arbeiten.

Abstract

This work describes work done in three areas of research where sky observations meet computer graphics. The whole topic covers several millennia of human history and posed combined challenges from fields including archaeology, astronomy, cultural heritage, digital image processing and computer graphics.

The first part presents interdisciplinary work done in the fields of archaeo-astronomy, visualisation and virtual reconstruction. A novel diagram has been developed which provides an intuitive, easy visualisation to investigate archaeological survey maps for evidence of astronomically motivated orientation of buildings. This visualisation was developed and first applied to a certain class of neolithic circular structures in Lower Austria in order to investigate the idea of solar orientation of access doorways. This diagram and its intuitive interpretation allowed the author to set up a new hypothesis about practical astronomical activities in the middle neolithic period in central Europe.

How virtual reconstructions of these buildings characteristic for a short time during the neolithic epoch can be combined with the excellent sky simulation of a modern planetarium to communicate these results to a broader audience is described thereafter.

The second part of this work describes a certain class of historical scientific instruments for sky observations and its reconstruction with methods of computer graphics. Long after the stone age, in the Middle Ages, the astrolabe was the most celebrated instrument for celestial observations and has been explained in contemporary literature, usually with the help of precomputed tables for a certain size or kind of instrument. Today, historical exhibitions frequently present one of these instruments, but its various applications are hard to explain to the general audience without hands-on demonstration. For this challenge from the cultural heritage domain, an approach using the idea of procedural modelling is presented. Here, a computer graphics model is not statically drawn but specified by parametrised plotting functions, which can then be repeatedly executed with different parameters to create the final model. This approach is demonstrated to provide a very flexible solution which can immediately be applied to specific needs just by tweaking a few parameters, instead of having to repetitively draw the whole model manually. From the two-dimensional procedural model, 3D models can be easily created, and even the production of wooden instruments on a Laser engraver/plotter is demonstrated.

The third and longest part deals with methods of sky simulation and rendering in the domain of computer graphics. In this discipline, modelling of skylight and atmospheric effects has developed tremendously over the last two decades, which is covered by an extensive survey of literature from the computer graphics and also atmosphere physics domains.

The requirements of physically correct or at least plausible rendering include realistic values for sky brightness. Measurements performed with a luminance meter on a clear sky

in order to verify the currently most widely used analytic skylight model [PREETHAM *et al.* 1999] shows however its limited applicability.

There are two classical groups of clear-sky models: numerical simulations of scattering in the atmosphere, and fast analytical models. Recently, another method for more realistic looking skylight models has been developed: digital images taken with a fisheye lens are combined into high dynamic range images which can be used for scene illumination and as sky background. These images can be calibrated by photometric measurements of absolute luminance values. Long-time exposures allow to apply this system to quantitative investigations of sky brightness, sky colours, and also nocturnal light pollution by artificial illumination. Results and other applications of the system are described, and the pipeline for creating such images is described in the appendix.

This work closes with some notes of future directions of research.

Preface

This work is an expression of the combined interdisciplinary interests of the author. One of the oldest sciences, astronomy, provided the motivation for the research in several fields of a modern science, computer graphics, presented in this work.

The sky has interested and fascinated people all over the world since the beginning of humankind. Some of the oldest indications of consideration of the daily and annual movements of the sun and the sky can be found in the orientation of burials from the Neolithic period [SCHLOSSER and CIERNY 1996, p.72ff]. Our allegedly primitive ancestors tended to let their dead look towards sunrise or sunset, which is a good indication of some sort of nature religion and thoughts about an afterlife. Even older bone fragments with regular scratch symbols can be interpreted as aid to the counting of days with the help of the moon 30000 years ago [KRUPP 1994, p.158ff]. Also, ice-age cave paintings have been interpreted to show constellations, some of which we today are still using; however, this interpretation is not universally accepted [SCHLOSSER and CIERNY 1996, p.69].

In late 2003, the author was invited to investigate the presumed astronomical orientation of neolithic circular ditch systems (*Kreisgrabenanlagen*) of Lower Austria. The first part of this dissertation provides an introduction into the aspects of archeo-astronomy necessary to understand the research results later presented and describes how a novel diagram developed for this investigation provides a combined visualisation of an archaeological survey map, the horizon profile at that location and a map of the sky at that time. The diagram provided the key for the proposal of a new hypothesis concerning the sky observations which may have been performed by the people of that time and the orientation of gateways in these neolithic buildings (Chapter 1). For a proper presentation towards a broader audience, virtual reconstructions of the buildings can be combined with a sky simulated either in software or with the still unsurpassed sky simulation of a planetarium (Chapter 2).

In late antiquity, an astronomical instrument was invented in the Near East that combined several earlier instruments in a most elegant fashion. The astrolabe is seen as the apex of medieval astronomical instruments and has been in use for the observation of celestial bodies and related computations for centuries, first in the region of early Islam, and after about the year 1000 also in Europe. The strictly geometrical construction was frequently combined with rich decoration, expressing both the wealth of the respective client and the virtuosity of the respective instrument maker. Today, computer graphics is frequently used in the cultural heritage sector to provide virtual reconstructions of old buildings and machinery, and the astrolabe provides an excellent playground for an attempt in *procedural modelling*, where, instead of painstakingly drawing each line manually, the *idea* of the construction is encoded in parametrised plotting functions which are then called multiple times with different parameters. This allows to produce a wide variety of instruments of different sizes, not only in print, but also in wood, by driving a laser engraver/cutter, opening the possibility

to provide affordable durable instruments usable for hands-on group demonstrations, for example in a science museum (Chapter 3).

Finally, the simulation of the sky itself and atmospheric effects have a history of several decades in physics and also computer graphics. Chapter 4 is an extensive survey of existing clear-sky models that have been proposed in the computer graphics literature, enriched with papers on related topics like rendering of refraction effects in the atmosphere, and with many papers of the atmosphere physics domain, where several of the effects that are only recently being dealt with by the computer graphics community have already been discussed, some of them decades ago.

The two classical possibilities to represent the sky in computer graphics are a brute-force numeric simulation of the physical processes of radiation distribution in the Earth's atmosphere, or the use of a fast parametric model which may be built from a fit against measurements or simulation. The currently most widely used parametric skylight model is investigated in more detail in an attempt to *validate* it with measurements taken with a luminance meter. It turned out that its purported wide applicability is not as wide, and that for very clear skies an approach with numerical simulation is still the better solution.

More recently, direct digital photographic captures of the sky have been presented, where typically several digital images have to be combined into a *High Dynamic Range* (HDR) image to capture the extremely wide dynamic range found in daylight scenes in nature. HDR images are intended to record all scene luminance values observable in nature. Aside from their uses in image-based lighting for computer graphics, a calibrated HDR processing system can also be used to study sky brightness and colour, and also the adverse effect of our civilisation on the upper half of our outdoor environment: light pollution by nocturnal illumination, which depraves many city inhabitants of the beauty and magnificence of a clear, dark, starry night sky. Some results of such a system are presented in chapter 6, and the pipeline for capturing and processing HDR images of the sky dome is presented in appendix A.

Acknowledgments

I would like to thank Prof. Werner Purgathofer for providing the excellent work infrastructure at the Institute of Computer Graphics and Algorithms.

Prof. Maria G. Firneis from the Institute of Astronomy of Vienna University provided valuable input especially to the topics on historical aspects of astronomy covered in this work.

Data of the neolithic *Kreisgrabenanlagen* and local horizons (chapter 1) have been provided by Wolfgang Neubauer. Thanks go to Michael Gervautz and Heimo Kramer from Imagination Computer Services, Vienna, responsible for the virtual reconstruction of KGAs in chapters 1 and 2, and for the interesting discussion during development of the flipped star map. I further thank Eva Lenneis and Andreas Lippert for discussing a few archaeological aspects.

The work described in chapter 2 would not have been possible without the technical support of the staff of the Zeiss Planetarium Vienna, most notably Harry Halas. I owe its former director, Prof. Hermann Mucke, many thanks for exciting my astronomical interest with countless lectures on the basics of astronomy and astronomical phenomenology which I enjoyed from the time when I attended primary school.

Thanks go to the Institute for Forming and Laser Technology of the Vienna University of Technology, esp. Ferdinand Bammer for his support with the laser engraver used in chapter 3.

Comments and helpful references on uses of the HDR capturing system for studies of light pollution have been provided by Günther Wuchterl of Tautenburg Observatory and Kuffner Observatory, Vienna, and Thomas Posch and Franz Kerschbaum from the Institute of Astronomy of Vienna University.

Thomas Kment and Michael Rauter helped collecting some of the material in chapter 4. The remote control application used in chapter 6 was implemented by Franz Daubner.

I thank my colleagues at the institute, first and foremost Alexander Wilkie, who has been a close friend for years and invited me into his group, giving me the chance to fulfill this work. Ralf Habel created an animation of the opening sky dome, snapshots of which are shown in Figures 1.2 and 1.5. The 3D astrolabe model in Fig. 3.11 was created by Andrea Weidlich. Former institute member Robert Tobler, now at VRVis Research Center, Vienna, kindly provided further comments. I may also thank our beloved Meister Eduard Gröller for comments on the visualisation in chapter 1, and his spiritual guidance in general.

Finally, I thank my parents for their perpetual support and encouragement.

This work was supported by the Austrian Science Fund (FWF) under contract number P17558 and the *Hochschuljubiläumsstiftung der Stadt Wien* by project number H-1085/2004.

Vienna, October 2007

Georg Zotti

Contents

1	Visualisation of Astronomical Orientations	1
1.1	Introduction	1
1.2	Celestial Positions	3
1.2.1	Sun	6
1.2.2	Moon	7
1.2.3	Stars	7
1.3	Mapping the Sky Dome	8
1.3.1	Radial Geographic Maps	8
1.3.2	All-Sky Map	10
1.3.3	Star Path Map	10
1.3.4	Flipped Star Path Map	12
1.3.5	Improving the Diagram	15
1.4	Discoveries	19
1.5	User Reactions	21
1.6	Conclusion and Future Work	21
2	Virtual Reconstructions in a Planetarium	23
2.1	Introduction	23
2.2	Related Work	24
2.3	The Planetarium for Simulations in Archaeo-Astronomy	26
2.4	Our Work	27
2.5	Discussion and Future Work	31
3	Procedural Modelling of Astrolabes	33
3.1	Introduction	33
3.2	Related Work	36
3.2.1	Procedural Modelling	36
3.2.2	Astrolabes	36
3.3	Description of the Astrolabe	37
3.4	Implementation of the Astrolabe Construction	38
3.4.1	The star map, or <i>rete</i>	39
3.4.2	The horizon plates, or <i>tympan</i> s	42
3.4.3	The case, or <i>mater</i>	47
3.4.4	The back, or <i>dorsum</i>	47
3.4.5	Universal Astrolabes	49
3.4.6	Persian Astrolabes	49

3.5	Applications of the Model	49
3.5.1	Production: Cardboard and Laser Woodcutting	50
3.5.2	3D Modelling	52
3.6	Discussion	52
4	Modelling Skylight with Computer Graphics	55
4.1	Spectral Power Distribution of Sunlight	56
4.2	The Atmosphere	56
4.3	Light and the Atmosphere	57
4.3.1	Scattering, Absorption and Extinction	57
4.3.2	Refraction	62
4.4	Rendering of the Sky Dome and Physically-Based Skylight Models	64
4.4.1	Special Topics of Atmospheric Effects	68
4.5	Analytic Skylight Models	78
4.5.1	Polarisation	83
4.6	Photographic Methods for Skylight Capturing and Modelling	83
5	Critical Review of the Preetham Skylight Model	85
5.1	Introduction	85
5.2	Related Work	86
5.3	Preetham's Model	86
5.3.1	Coordinate System	86
5.3.2	Turbidity	87
5.3.3	A problem with zenith luminance Y_z	87
5.3.4	Sky luminance Y	87
5.4	CIE Standard Sky	90
5.5	Measurements	91
5.6	Comparison	91
5.7	Conclusion and Future Work	92
5.8	Figures and Tables	92
6	Skylight Measurements with a Digital Camera	119
6.1	Introduction	119
6.2	Related Work	121
6.3	Creation of HDR Images with PFSTools	122
6.4	Results and Applications	123
6.4.1	Measurements of Sky Luminance and Colours	123
6.4.2	Measurements of Nocturnal Light Pollution with HDR Images	129
6.4.3	Estimation of Sunshine Hours	136
6.4.4	Application of HDR Imaging in Archaeo-Astronomy	137
6.5	Discussion	137
7	Conclusions and Directions for Future Work	139

A Skydome Capture System Based on PFStools	143
A.1 Skydome Capture System	143
A.2 Decoding RAW Images from Consumer Cameras	144
A.3 Creation of HDR Sky Images with PFStools	144
A.3.1 Finding Sensor Response	144
A.3.2 Creating Ordinary HDR Images	147
A.3.3 Correction of Lens Effects	147
A.3.4 Camera Colour Calibration	149
A.3.5 Absolute Calibration	149
A.3.6 HDR Skylight Script	151
A.3.7 Masking Empty Pixels	151
A.3.8 Tone Mapping	153
A.3.9 Zenith Brightness Evaluation	153

List of Figures

1.1	Archaeological map of the <i>Kreisgrabenanlage</i> Steinabrunn in Lower Austria .	3
1.2	Sky dome spanning over an archaeological site in a 3D scene	6
1.3	Typical all-sky map	9
1.4	Map of diurnal arcs (daily paths) on the sky	11
1.5	Opening and unfolding the sky dome.	13
1.6	The flipped sky	13
1.7	Combination of flipped sky, horizon and archaeological map	14
1.8	Histogram view with flipped sky map	16
1.9	Flipped sky with nonlinear altitude mapping	17
1.10	Flipped sky map with diurnal arcs of the Sun	18
1.11	Virtual reconstruction of a view in KGA Steinabrunn	20
2.1	Virtual reconstruction of the Steinabrunn site.	24
2.2	Horizon Panorama for the center of the Steinabrunn site.	26
2.3	Horizon Panorama for a location near the south-east gate.	26
2.4	Sunrise over a hill, comparing desktop software and the Planetarium view.	28
2.5	“Archaeo-Astrophotography” of the Milky Way	29
2.6	Pleiades in the morning twilight	30
3.1	Front of a Planispheric Astrolabe	34
3.2	<i>Rete</i> : Stereographic construction	39
3.3	<i>Rete</i> : Effect of precession	41
3.4	<i>Tympan</i> : Stereographic construction of altitude circles	42
3.5	<i>Tympans</i> : Examples for latitudes 13° and 62°	44
3.6	<i>Tympan</i> : Construction of azimuths	45
3.7	<i>Tympan</i> : Construction of <i>houses</i> after REGIOMONTANUS	46
3.8	<i>Dorsum</i> : Typical late-16th century instrument	48
3.9	Universal astrolabes	49
3.10	Persian back	50
3.11	Various applications for the procedural modelling	51
3.12	The <i>rete</i> in a 3D modelling program	53
4.1	Solar Spectrum	56
4.2	Scattering phase functions for unpolarised light.	60
4.3	Refractive near-horizon phenomena.	63
4.4	KANEDA <i>et al.</i> [1991] sky model.	65
4.5	DOBASHI <i>et al.</i> [1994b, 1997] sky segmentation.	66

4.6	NISHITA <i>et al.</i> [1996a] sky model.	67
4.7	Airlight	69
4.8	Geometry for aerial perspective.	70
4.9	Interactive atmospheric scattering [DOBASHI <i>et al.</i> 2002].	71
4.10	Twilight phenomena	73
4.11	Comparison of daylit and moonlit landscapes	76
4.12	Earth from outer space: NISHITA <i>et al.</i> [1993] <i>vs.</i> Photos	77
4.13	Earth simulation from outer space [NISHITA <i>et al.</i> 1993]	78
4.14	Angles and directions on the sky dome used in the analytical models.	79
4.15	Comparison of analytic skylight models.	81
4.16	PREETHAM <i>et al.</i> [1999] sky model.	82
4.17	Real time atmospheric scattering [HOFFMAN and PREETHAM 2002]	82
5.1	Preetham zenith luminance as function of solar zenith angle and turbidity	88
6.1	Zenith luminance and colour measured on 2006 July 5	126
6.2	Zenith luminance and colour measured on 2007 August 7	126
6.3	Dark Sky Conditions	128
6.4	Sky during Total Solar Eclipse	128
6.5	Lake Bled during the day and at night	129
6.6	Examples of bad lighting	129
6.7	Limiting Magnitude <i>vs.</i> Sky Luminance	131
6.8	Sky Quality Plots	132
6.9	Sky Quality Plots	134
6.10	Sky Quality Plots	135
6.11	Estimation of Sunshine Hours	136
A.1	Camera response curves	145
A.2	dcraw2hdrgen	146
A.3	pfsnormalize: Setting maximum luminance to 1.	148
A.4	pfsflatfield: Pixel-wise division of image data.	148
A.5	Removing colour shift caused by a filter	149
A.6	Patched version of pfsindcraw	150
A.7	mkSky: Capture series to HDR conversion Script	152
A.8	pfscircle: Masking Image Corners	152

List of Tables

1.1	Extinction angles for a few stars	5
3.1	Symbols for the Signs of the Zodiac	40
4.1	US Standard Atmosphere Temperature Gradients.	57
5.1	Absolute sky luminance in the Preetham model for various Solar zenith angles	89
5.2	The CIE 2003 Standard General Sky models	90
5.3	Comparison of very clear sky luminance distribution, $\theta_s = 50^\circ$	93
5.4	Comparison of very clear sky luminance distribution, $\theta_s = 72^\circ$	94
5.5	Comparison of slightly hazy sky luminance distribution, $\theta_s = 50^\circ$	95
5.6	Comparison of clear sky luminance distribution, $\theta_s = 80^\circ$	96
5.7	Comparison of extremely clear sky luminance distribution, $\theta_s = 60^\circ$	97
5.8	Relative sky luminance distributions of the 16 CIE 2003 Standard General Sky models, for various solar zenith distances θ_s	98
5.9	Absolute sky luminance distributions based on the CIE 2003 Standard General Sky models, for various solar zenith distances θ_s	102
5.10	Relative sky luminance distributions of the Preetham model, for various solar zenith distances θ_s and turbidities.	106
5.11	Absolute sky luminance distributions of the Preetham model, for various solar zenith distances θ_s and turbidities.	112
6.1	Sky captures of 2006 July 5.	124
6.2	Sky captures of 2007 August 7.	125
6.3	Visibility of the Milky Way depending on average Polluted Sky Luminance	132
6.4	Zenith Sky Luminance values after CINZANO [1997]	132

Chapter 1

A Sky Dome Visualisation for Identification of Astronomical Orientations

These the seven names they bear:
Alcyone and Merope, Celæno,
Taygeta, and Sterope, Electra,
And queenly Maia, small alike and faint,
But by the will of Jove illustrious all
At morn and evening, since he makes them mark
Summer and winter, harvesting and seed time.

— ARATOS OF SOLI, *Phenomena* [OLCOTT 2004, p.419]

It has long been known that ancient temples were frequently oriented along the cardinal directions or to certain points along the horizon where the Sun or the Moon rises or sets on special days of the year. In the last decades, archaeologists have found evidence of even older building structures buried in the soil, with doorways that also appear to have distinct orientations.

This chapter presents a novel diagram combining archaeological maps with a folded-apart, flattened view of the whole sky, showing the local horizon and the daily paths of the Sun, Moon and brighter stars. By use of this diagram, interesting groupings of astronomical orientation directions, *e.g.*, to certain sunrise and sunset points could be identified, which were evidently used to mark certain days of the year. Orientations towards rising and setting points of a few significant stars very likely indicated the beginning of the agricultural year in the middle neolithic period. This chapter extends papers for IEEE InfoVis 2005 [ZOTTI and GRÖLLER 2005] and Palgrave Journal on Information Visualisation [ZOTTI 2006].

1.1 Introduction

A large body of evidence shows the connection of ancient cultures to annually repeating celestial events. In many old cultures, temple axes were typically aligned either along cardinal directions (*e.g.*, the Pyramids in Egypt are the most popular and best studied example) or towards solstitial risings and settings of the Sun, *e.g.*, Persepolis [SCHLOSSER and CIERNY 1996]. Another frequently cited example is Stonehenge and many other megalithic sites,

which were presumably overinterpreted by various authors, most notably THOM [1967] and [1978], but are largely accepted as sun- and moon-oriented buildings [KRUPP 1994]. Also medieval churches were frequently oriented towards the rising point of the Sun on the day of the church's patron [FIRNEIS 1984], and Muslim mosques (at least their interior) must be geographically oriented towards Mecca.

Apparently the orientation of buildings has a much older tradition. Since the 1960s, systematic aerial photography, later combined with geomagnetic prospection with highly sensitive caesium magnetometers and, where possible, successive excavations, discovered a certain class of neolithic circular enclosures: *Kreisgrabenanlagen* (KGA). They typically consisted of 1–3 nearly circular wooden palisade walls, surrounded by 1–3 ditches, which were V-shaped and up to 6m deep and 12m wide. The circular ditches were broken by “earth bridges”, which allowed people to enter the *enclosure* through gaps (“doors”) in the palisades. The overall diameter of these *Kreisgrabenanlagen* is approximately 40–180m. The best archaeological survey results, short of the slow and very costly direct excavation, come from measuring the minute deviations of the Earth's natural magnetic field caused by the different qualities of soil which today fill the ditches: a set of very sensitive magnetometers is mounted on a hand-moved cart, and the cart is moved over the soil in parallel lines, providing a “subsurface scan” of the terrain. According to ^{14}C dating of excavated bone material, all KGAs have been erected in the very short time span between 4800 and 4500 B.C. [STADLER 1995] These structures have been found over a large part of central Europe, from Hungary to northern Germany [DAIM and NEUBAUER 2005], with a concentration of over 40 such structures known in Lower Austria (e.g., Figure 1.1). In contrast to the megalithic buildings on the British islands and in Brittany there usually are no visible traces of the ditches or palisades left in the surface profile.

Since the 1980s, as the number of known KGAs steadily increased, a number of theories about their use have been discussed and rejected, spanning from cattle paddocks to fortifications. Most of the theories had to be rejected as inconsistent with archaeological evidence. The current interpretation is their use as a place for special gatherings, cultic worship, or initiations. But, in parallel to the much younger megalithic constructions of Great Britain and Brittany [HAWKINS 1973; THOM 1967; THOM and THOM 1978], also some astronomical alignments have been proposed, most notably by BECKER [1996], who found that *Kreisgrabenanlagen* of Bavaria had doors and access bridges aligned to rising or setting points of the Sun at the solstices.

During the preparation of the first large public exhibition on *Kreisgrabenanlagen* in 2005, the theory of astronomical connections has also been investigated by the author [ZOTTI to appear, 2005b; KASTOWSKI *et al.* 2005; ZOTTI 2008]. This chapter describes what had to be taken into account for these orientation studies. Not only possible Sun-related directions have been studied, but also Moon- and star-related directions. A key element on the way to an interesting discovery has been a diagram combining the archaeological map with a celestial map, which allows the immediate identification of possible alignments.

The rest of the chapter is as follows: first, important terms from astronomical visual phenomenology are defined, and necessary astronomical computations are pointed out. Next, some examples of radial mappings in geographical maps are given. Then, a methodology is developed which shows how to apply various diagrams to questions related to astronomical orientations. *Kreisgrabenanlagen* are used as primary example, but the same idea can be and has been applied [ZOTTI 2005a] to other buildings or geological structures for which an ori-



Figure 1.1: Archaeological map of the *Kreisgrabenanlage* (KGA) Steinabrunn in Lower Austria [EDER-HINTERLEITNER *et al.* 1999]. The wide brown rings indicate the circular ditches which are connected by narrower radial ditches along 4 access bridges. In the central area, traces of 3 concentric palisade walls are marked in a lighter shade of brown. Small brown dots indicate singular postholes, the green area marks a central pit. A multitude of similar KGA traces has been found in the last decades, and among the many theories which have been put forward concerning their use, the idea that the orientation of the doorways has an astronomical significance has gained importance in the past years.

ented maps exist. Then a combined result from a multitude of KGAs is shown, which allows the postulation of an archaeo-astronomical hypothesis, which is described shortly.

1.2 Celestial Positions

To compute the position of a celestial object, we need

- the *geographical position* (λ, φ) of the observer, where the geographical longitude λ is positive for longitudes east of Greenwich and latitude φ is positive on the northern hemisphere,
- the object's *celestial coordinates* (α, δ) on the imaginary infinite celestial sphere, with the longitudinal coordinate α named *right ascension* and counted in hours instead of degrees, eastward from the *First Point of Aries* Υ . This point marks the one intersection of the celestial equator with the Sun's annual path, the *ecliptic*, where the Sun crosses the celestial equator northward, this event defining the beginning of astronomical spring in the northern hemisphere. The latitudinal coordinate δ is called *declination* and is positive for objects north of the celestial equator.
- the *time* of observation. Here we have to take care not to use just zone time (maybe even further denaturalised by daylight saving time), but *local mean solar time*. From time and

date, we compute *sidereal time* θ , *i.e.*, the time that passed since the last culmination (meridian transit) of Υ . Then, the object's *hour angle* H describes the (sidereal) time past its last culmination and is $H = \theta - \alpha$.

From this data, we can compute an object's *azimuth* A , *i.e.*, its horizontal direction, counted from north (0°) eastward in this work. Following a different, equally valid convention, Azimuth can also be counted from south westward, which will be labelled A_s here. The second coordinate in this horizontal system is *altitude* a . The computation of positions can be found in general astronomical literature [*e.g.*, MEEUS 1998, p.93], from which we take

$$\tan A_s = \frac{\sin H}{\cos H \sin \varphi - \tan \delta \cos \varphi} \quad (1.1)$$

$$A = A_s + 180^\circ \quad (1.2)$$

$$\sin a = \sin \varphi \sin \delta + \cos \varphi \cos \delta \cos H \quad (1.3)$$

On any day of the year, stars rise and set approximately 4 minutes earlier than on the day before. Stars which surround the celestial pole of the observer's hemisphere do not set, are visible in every clear night and are called *circumpolar*. Others are only visible during certain parts of the year, the Sun being too close to them to be observable at other times. The last time such a star is visible at dusk is called its *heliacal setting*, where the star becomes visible slightly above the horizon in the darkening twilight, only to set moments later or vanish in the horizon haze. After typically a few weeks of invisibility due to its proximity to the Sun, the star emerges in the morning on the day of its *heliacal rising*: in the morning twilight, the star appears shortly over the horizon haze, only to become too washed out a few moments later by the increasing brightness of the emerging daylight. On each successive day, the star will be visible about four minutes earlier. It has long been known that heliacal risings of selected stars have been used by various peoples all over the world to mark specific days of the year [KRUPP 1994], the best known example being the Egyptian use of the heliacal rising of the sky's brightest star, Sirius, as "herald" of the Nile flood.

While the exact day in each year also depends on atmospheric conditions, the average day can be computed at least approximately, and Schoch's empirical method [MUCKE 1993] is still widely used. An observation run in 1993 confirmed object visibility at least very close to the computed dates, although some corrections seem necessary [PACHNER 1994]. Other methods have been presented by MEEUS [1997, ch.46] and SCHAEFER [1985, 1987].

The rising and setting azimuths A_\uparrow , A_\downarrow on a location's horizon depend on its geographical latitude φ , the star's declination δ and the local horizon's altitude, and can be given for the mathematical horizon [MEEUS 1998], using the *hour angles* H_\uparrow , H_\downarrow at the time of rising and setting. If we disregard refraction, we set $h = 0$ in equation (1.3), so that

$$\cos H_{\uparrow,\downarrow} = -\tan \varphi \tan \delta \quad (1.4)$$

$$H_\uparrow < 0, \quad H_\downarrow > 0 \quad (1.5)$$

$$A_{s,\uparrow} = \arctan \frac{\sin H_\uparrow}{\cos H_\uparrow \sin \varphi - \tan \delta \cos \varphi} \quad (1.6)$$

$$A_{s,\downarrow} = \arctan \frac{\sin H_\downarrow}{\cos H_\downarrow \sin \varphi - \tan \delta \cos \varphi} \quad (1.7)$$

The arctan function has to be evaluated in the correct quadrant, so *e.g.* `atan2()` should be used where available. These azimuth values are angles counted from the south point on

Table 1.1: Extinction angles a_E for a few stars [MÜLLER 1970, p.130].

Name	Constellation	mag	a_E
Arcturus	Bootes	-0.1	0°
Vega	Lyra	0.0	0°
Capella	Auriga	0.1	0°
Procyon	Canis Minor	0.4	0.3°
Altair	Aquila	0.8	0.7°
Antares	Scorpius	0.9	0.9°
Pollux	Gemini	1.2	1.2°
Deneb	Cygnus	1.3	1.3°

the horizon, and may be converted to those counted from north again using equation (1.2). Note again that these results are the azimuths on the mathematical horizon. On the northern hemisphere, any elevation on the horizon will shift both rising and setting points southward.

In addition, for the investigation of rising and setting alignments along the horizon, two phenomena caused by the Earth's atmosphere have to be taken into consideration:

refraction, causing a slight increase of the apparent altitude for all celestial objects, most pronounced close to the horizon. Refraction also causes the Sun and Moon to appear vertically compressed when they are near the horizon, because their respective lower limbs will be raised more than their upper limbs, and raise both these objects by about 1/2 degree on the horizon, thus causing also a slight northward shift in both rising and setting points. The shift is more pronounced in high latitudes and for objects far from the celestial equator, because here the diurnal paths intersect the horizon in a more oblique angle. The refraction correction R , in arcminutes, to be added to the geometrically computed altitude, amounts to

$$R ['] = 0.0019279 + \frac{1.02}{\tan(a + \frac{10.3}{a+5.11})} \cdot \frac{P}{1010} \cdot \frac{283}{273 + T} \quad (1.8)$$

for yellow light, where P is pressure given in *mbar* and T temperature on the Celsius scale [MEEUS 1998, p.106].

This shift also applies to stars, but only the very brightest stars are visible in so low altitudes where the effect would be notable with the naked eye, because of the

extinction, which reduces all objects' luminosities, usually making dimmer stars invisible near the horizon. A star's brightness is given on the logarithmic *magnitude* scale, the brightest stars having slightly negative numbers. The dimmest stars observable without optical aid under best conditions are about *mag* 6.5, but only close to the zenith. In low altitudes, esp. close to the horizon, the atmosphere absorbs much of the starlight. Only the brightest stars are visible on the horizon under best conditions, and most stars are not visible below a certain altitude, their respective *extinction angle* a_E . Table 1.1 shows a few extinction angles for best conditions. Depending on humidity and dust, a_E can be larger.

For the Sun and the Moon, one more aspect could have played a role: whether an alignment intended to point towards the point of first (respectively last) visibility (*i.e.*, upper limb), disk center or full visibility (lower limb).

1.2.1 Sun

Mirroring the Earth's motion around it, the Sun annually describes a great circle on the celestial sphere, which due to the Earth's tilted axis intersects the celestial equator on the *First Points of Aries* Υ and *Libra* Ω . The moments the Sun is at these points define the beginnings of astronomical spring and autumn, respectively, in the northern hemisphere. The Sun can reach northern and southern declinations equal to the Earth's axis tilt from orbit normal, which is currently about $\varepsilon = 23.5^\circ$, but slowly and slightly varies over millennia. Reflecting this, the annual points of sunrise and sunset span a wide arc along the eastern and western horizons. Near the solstices ("standstills"), the Sun rises or sets on almost the same positions for several days. The full range of positions the Sun can reach on the sky dome during a year can be seen in Figure 1.2.

It is known from older cultures [KRUPP 1994] that some peoples defined the seasons not as beginning and ending at solstices and equinoxes, but centered the seasons around these dates; this practice leads to terms like "midsummer", which is still used for summer solstice. Traces of this tradition survive in today's All Saints' Day/Halloween and Candlemas as alternative start and end dates of Winter, and May Day as alternative start of Summer. In total, the Sun provides eight calendarical *key dates* with five characteristic declinations, which lead to ten characteristic azimuths (rising/setting at equinoxes, solstices and the intermediate dates).

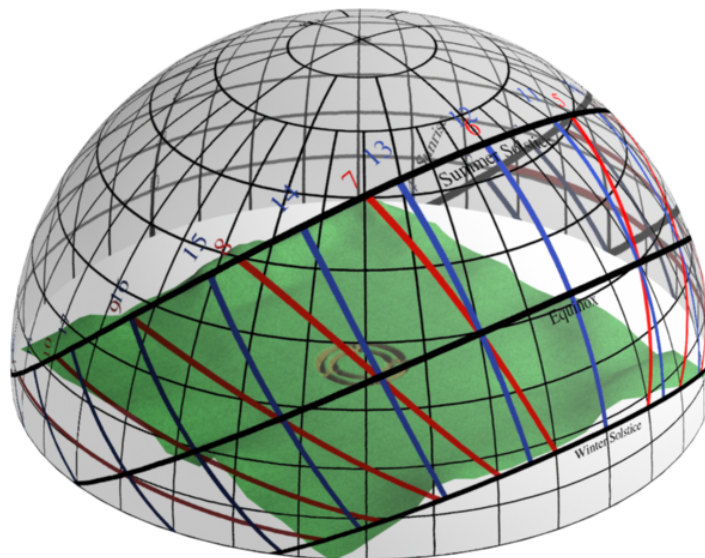


Figure 1.2: The sky dome spanning over an archaeological site in a 3D scene, viewed from south-west. The image shows the horizontal coordinate system and the Sun's annual sky coverage. A virtual walkthrough of the archaeological site will show possible alignments.

1.2.2 Moon

Similar to the Sun, the Moon can reach a wide area of declinations. Due to its orbit being tilted about $i = 5^\circ$ from Earth's orbit, its extreme north and south declinations vary even wider, with outer extremes ("major standstills", $\delta = \varepsilon + i$) and inner extremes ("minor standstills", $\delta = \varepsilon - i$) [THOM and THOM 1978]. Due to orbital motions, these extreme standstills occur in intervals of about 18.6 years [MEEUS 1998, p.367]. Buildings that would be classified as "lunar oriented" would be expected to be oriented, or show some other sight lines, towards one of these standstill directions.

THOM and THOM [1978] found interesting alignments in the orientation of stone circles in Great Britain and Brittany with Moon-related azimuths, and PAVÚK and KARLOVSKÝ [2004] investigated lunar orientations in KGAs of Slovakia. However, our results from the Austrian KGAs currently do not show significant correlation with lunar risings or settings, so further discussion will be omitted here.

1.2.3 Stars

Although called *fixed stars*, over the course of centuries and millennia, stars do change their position on the celestial sphere mostly due to

precession, a motion of Earth's axis counteracting the tug of the Moon and the Sun on the Earth's equatorial bulge, which both attempt to erect Earth's rotational axis. Acting like a spinning top, Earth evades this erection by moving its axis sideways. This results in a motion where the Earth's axis over about 25800 years traces a double cone with the tip in the Earth's center. Reflecting this motion, the stars seem to move parallel to the ecliptic (the red line in figure 1.3), slowly changing their coordinates on the celestial sphere. For this reason, the star we now know as Pole Star will be far from the pole in just a few centuries, rendering it unusable for navigational purposes. We must note that the neolithic sky was shifted by about 90° from today's sky.

On the other hand, the stars'

proper motion in space is hardly noticeable even after several thousand years, due to their enormous distance from the Solar system, with only a handful of bright exceptions.

MEEUS [1998, Ch.21] describes algorithms to correct stellar catalog positions given for one epoch to another.

The Effect of Precession on Rising and Setting Positions on the Mathematical Horizon

If a structure's age cannot be narrowed down to be within at most a few hundred years, searching for alignments with stars is useless, because almost every azimuth will be covered by some bright star rising or setting there at some point in time. In such cases, only solar and lunar alignments can be investigated.

Precession approximately moves a star's ecliptical longitude λ by about one degree in 72 years, or $\Delta\lambda \approx 300/72 = 4.167^\circ$ in 300 years, parallel to the ecliptic. On the celestial equator, the shift in declination $\Delta\delta$ is greatest if the star is on the ecliptic, *i.e.*, near the points Υ or Ω , and follows from a spherical triangle as

$$\sin \Delta\delta = \sin \Delta\lambda \sin \varepsilon \quad (1.9)$$

A star on the celestial equator at Υ or Ω will thus shift by $\Delta\delta \approx 1.7^\circ$ in the 300 year period in question, and elsewhere on the sphere the amount is smaller.

To compute the shift in rising and setting azimuth we can use equations (1.4)–(1.7). In the latitude of $\varphi = 48.5^\circ$, during the 300 year period, the maximum azimuth shift of a star on the celestial equator amounts to about 2.6° , meaning that working with an average date within the interesting period the values should not be much more than $\pm 1.3^\circ$ off. Note, however, that a shift of higher declinations may cause a stronger shift along the horizon, and may even change a star's circumpolar attribute!

Fortunately, the epoch where *Kreisgrabenanlagen* were in use is known and is even short enough to use a single mean date for all sites without too large errors. Many lines inside the KGAs cannot meaningfully be given to sub-degree accuracy, because the exact positions of, e.g., post tops above the surface is lost and can only be estimated from post hole positions.

1.3 Mapping the Sky Dome

For archaeo-astronomical research, a method has to be found to combine archaeological data, e.g., an excavation map, with astronomical data, i.e., positional data of celestial objects. Research typically concentrates on alignments of artificial structures towards rising and setting points of the Sun, Moon and selected bright stars.

Earlier studies frequently just pointed out orientations towards these directions on a map, assuming a flat horizon, because surveyed horizon data was rarely available in archaeological studies, and data of rising and setting points for zero altitude (i.e., along the mathematical horizon) are easy to compute (see section 1.2.3). The resulting plots typically resemble *starplots* [SPENCE 2001, p.50] of the number of orientations *vs.* direction (azimuth). For example, SCHLOSSER and CIERNY [1996, pp.72ff] describe the change of orientation of burials in different stone-age cultures, where one group buried their dead in east-west orientation, another in north-south orientation, while both oriented male and female burials in opposite directions. From such diagrams it is possible to see clear trends of burial orientations along the cardinal directions. However, in these diagrams and similar ones showing axes of megalithic buildings [e.g., MÜLLER 1970, p.114], a reader cannot follow the authors' arguments in favour or against possible stellar alignments, because even if they are outlined in such a diagram, it is not clear whether they point to the rising respectively setting point on the mathematical horizon or take into account the local horizon. Horizon profiles nowadays can be acquired from a Geographical Information System (GIS) including a Digital Elevation Model (DEM), so a diagram combining the archaeological structure, sky dome and horizon could be created.

1.3.1 Radial Geographic Maps

There exist a few examples of artistic geographical maps that combine local landscape with its respective horizon. A famous 1530 woodcut by Niklas Meldemann shows the first siege of Vienna by the Turks (1529). The map is centered on St. Stephen's Cathedral in the city centre and shows the city buildings, the besiegers' tents and surrounding landscape almost as if seen from above through a fish-eye lens. Whichever way the map is turned, its upper part will show a panoramic view of the landscape in front of the viewer, who is thought to

Star map, Lat 48.5

Corrected for Refraction, not Extinction

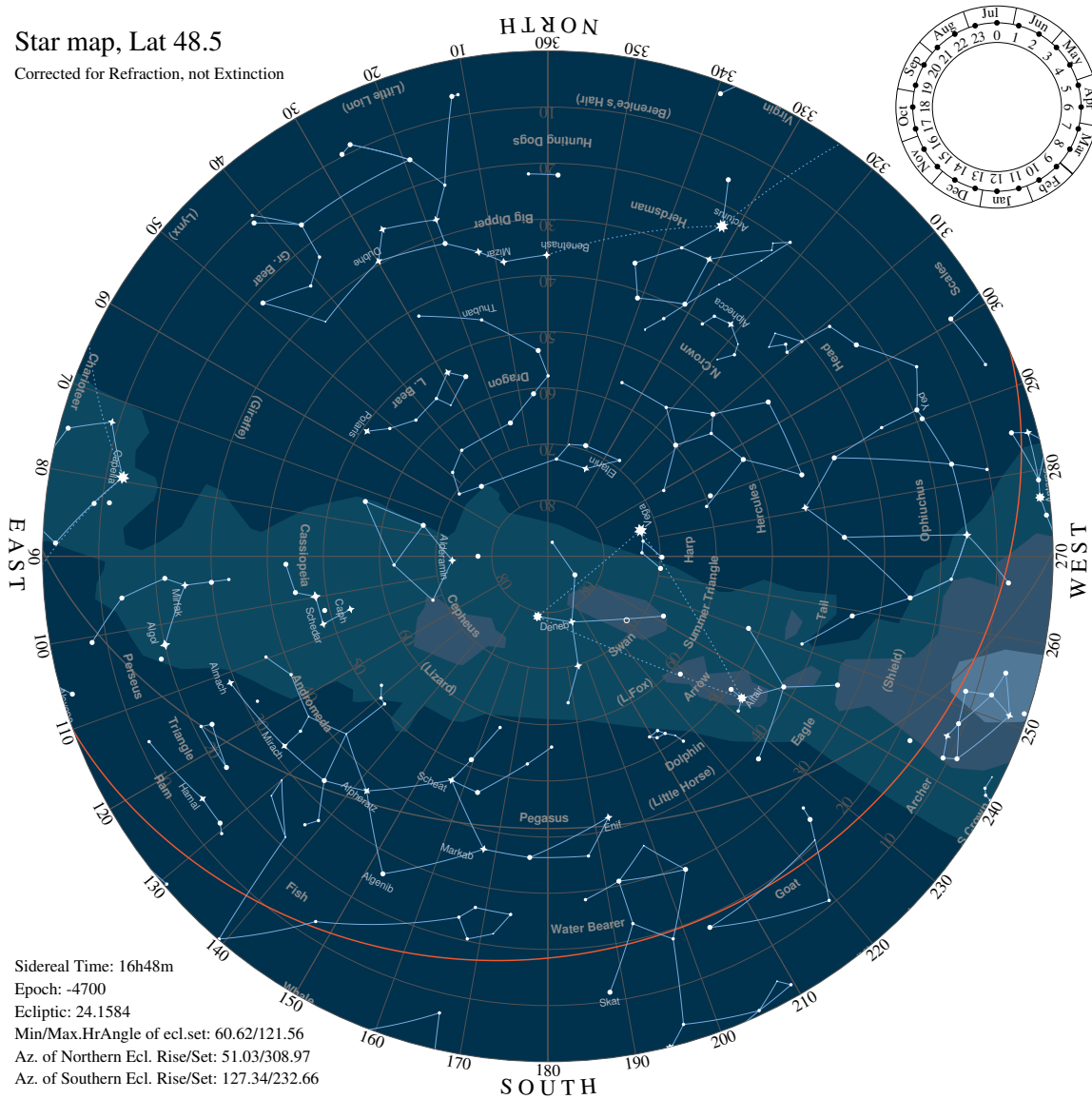


Figure 1.3: Typical all-sky map. When looking up from the Earth, cardinal directions appear mirrored compared to a geographical map. The red arc is part of the annual solar path, the *ecliptic*. The circle at upper right aligns mean solar time and calendar date to show when this map is applicable each day. The setting is for a situation in the year 4701 B.C. (the astronomical year -4700), described later in the text (Section 1.4).

be situated above the city center. However, it shows the façade, not the roof of St. Stephen's Cathedral. The map is on display at the Wien Museum in Vienna.¹

Much more recently, a radial panorama map has been published by the tourist board of the skiing resort of Obertauern (Austria) only several years ago. Again the center shows the central area, with ski slopes and lift systems radiating towards the map's borders, which show a panorama view of the surrounding mountains. Recent editions however have returned to the traditional panorama map layout with the valley near the bottom and the panorama of the surrounding mountains near the top of the map, which seems more appropriate also for simple online presentation.

1.3.2 All-Sky Map

A common way to show an all-sky star map, often found in introductory books on astronomy and sometimes found in newspaper columns, consists of a fisheye-like round star map of radius r_0 either in stereographic projection or with linearly mapped zenith distance (Figure 1.3). In the linear mapping, a point with azimuth A (counted from North towards the East) and altitude $a > 0$ on the hemisphere is mapped to a point with radius $r = r_0 \frac{90^\circ - a}{90^\circ}$ and polar angle $\theta = A$, counted counterclockwise from top. For the stereographic mapping (not shown here), $r = r_0 \frac{\cos a}{1 + \sin a}$. The zenith in the center shows stars immediately overhead at a certain time, whereas the stars close to the outer border are low on the horizon. A grid helps to visually estimate azimuth and altitude of any object.

This mapping nicely shows an instantaneous view of the sky, but is almost totally useless for investigations of points on the horizon where the Sun or stars rise or set.

1.3.3 Star Path Map

Our interest while investigating possible astronomical alignments at first does not involve an instantaneous view, but a representation of all possible positions a star can reach for a certain geographical location. This leads to a map showing the *diurnal arcs* (daily paths) of the stars (Figure 1.4). In this figure, we exchanged east and west to provide a mapping which represents a view from "outside", or "above", the local sky dome, so east and west are oriented like on an ordinary geographical map, and $\theta = A$, but counted clockwise from top. This map allows us to read the rising and setting points of celestial objects on the outer border, and also the altitudes and combined azimuths an object can reach. Of course, the star trails must be computed taking refraction into account (eq. 1.8), so all rising and setting points will show a slight northward bend near the horizon.

In this map it can also be seen which stars pass close to the zenith (center of the map). Such stars may also have played a significant role in the culture's mythology and star lore.

Such a mapping can be combined with fisheye photographs of the full sky dome so that nearby trees, houses *etc.* will be seen in the photographs. This combined image can be used to estimate hours of sunlight for any given place, which can be of interest for architects or real-estate agents, or planners of solar power plants, or even movie directors planning to shoot outdoor scenes ([Sunprognosis], and see Section 6.4.3).

¹ Unfortunately, the license fees for the reproduction in this work are prohibitive.

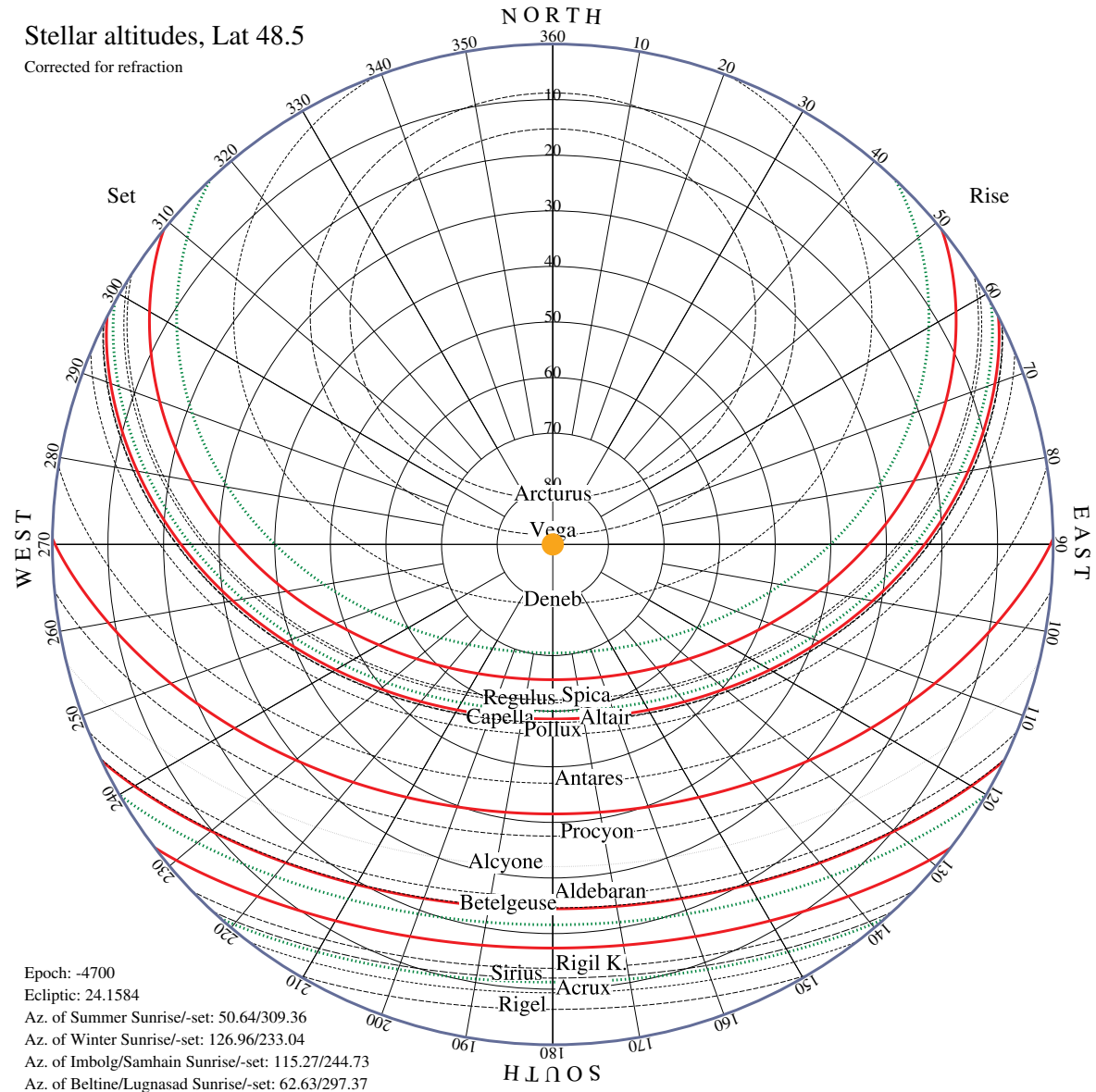


Figure 1.4: Map showing diurnal arcs (daily paths) of brighter stars on the sky, together with the Sun's diurnal arcs on the 8 solar key dates of the year (red) and extreme (standstill) arcs of the Moon (green). The viewer is looking downward from the outside of the apparent sky dome, so the cardinal directions are aligned like on an ordinary geographical map. The stellar arcs change over centuries due to precession and (much less) stellar proper motion. Rising and setting directions can be read off at the horizon line (blue). Like in figure 1.3, the map is centered around the zenith (orange dot).

Application for a 3D Scene

The map of figure 1.4 is perfectly usable as texture on a large (infinite, if possible) hemisphere for a virtual reconstruction inside a 3D modeling or VR application (Figure 1.2). During a virtual walkthrough of the scene inside the sky dome, astronomical alignments can be identified. However, 3D reconstructions of archaeological sites including their surrounding landscapes require lots of effort, so a simpler way had to be found.

1.3.4 Flipped Star Path Map

The map of figure 1.4 is a valuable tool in itself, however, superposing maps from archaeological sites (Figure 1.1) with it is difficult due to cluttering.

Our aim was to find a mapping in which the orientation lines (ditches, palisade gaps) can be combined with points on the horizon which in nature lie outside of the structure. To achieve this, we must leave the traditional mapping of the hemisphere to the circle with the zenith in the center. Instead, we flip the mapping by opening the sky dome at the zenith and “folding” the sky outward (Figure 1.5). This creates a map with an opening in the center, where we leave room for other data, and the whole sky flattened outward, with the point of the zenith mapped to the outermost circle (Figure 1.6). So, with the symbols defined in section 1.3.2, polar angle $\theta = A$, counted clockwise from north like on a geographical map, but $r = r_0 + sa$, where r_0 is the radius of the inner area and s some arbitrary scaling factor. The stars’ diurnal arcs appear largely unnatural at first but are still readable. Rising and setting points can be read again on the horizon, which is now the inner circle.

The red arcs in Figures 1.4 and 1.6 represent the Sun’s paths at the abovementioned key dates, *i.e.*, dates of solstices (northern-/ southernmost), equinoxes (east to west) and dates lying between these dates. Dashed green lines represent the standstill lines of the Moon. Star paths are marked in black arcs with various dot patterns according to the brightness of the respective star. The maps show star paths of the year 4701 B.C. (the astronomical year -4700).

This mapping now provides an inner area which we used for two distinct purposes: Investigations of singular KGAs and an interpretation of a histogram of all identified directions.

Identification of Alignments

When the center of the map, which is the observer’s position, is moved through the archaeological map, plausible alignments can be located. For a preliminary study, the diagram was simply printed on an overhead transparency and used with hardcopy prints of maps of the archaeological artifacts.

For more thorough investigations concerning phenomena on the horizon (rising, setting), a local horizon should and can be added, slightly shifting all rising and setting events southward (on the northern hemisphere). We used horizon data extracted from Geographical Information System (GIS) data. Not all radial lines in KGAs intersect in a common center, so loading the KGA map and flipped star map into separate layers of a graphical editor allowed shifting of the KGA map and thus selecting the exact observer position, which was usually still close to the center (Figure 1.7). Directions not radiating from a common center have

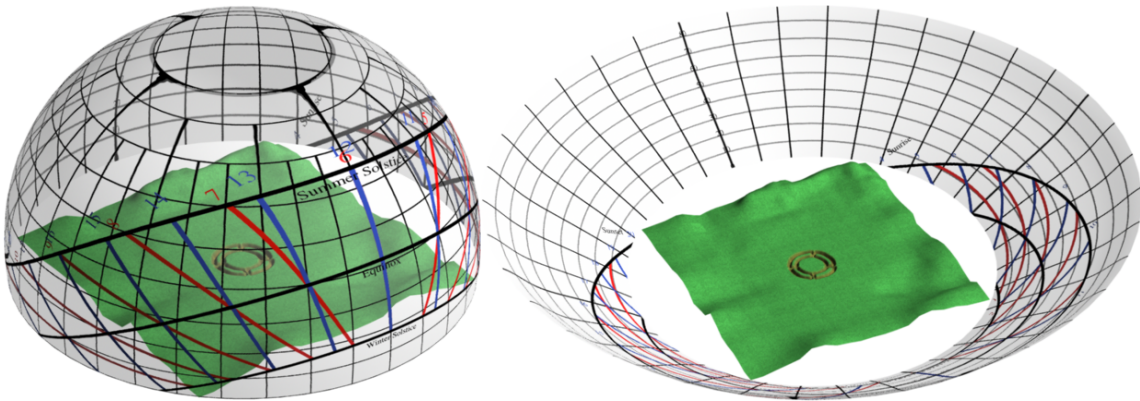


Figure 1.5: Opening and unfolding the sky dome.

Stellar altitudes, Lat 48.5

Corrected for refraction

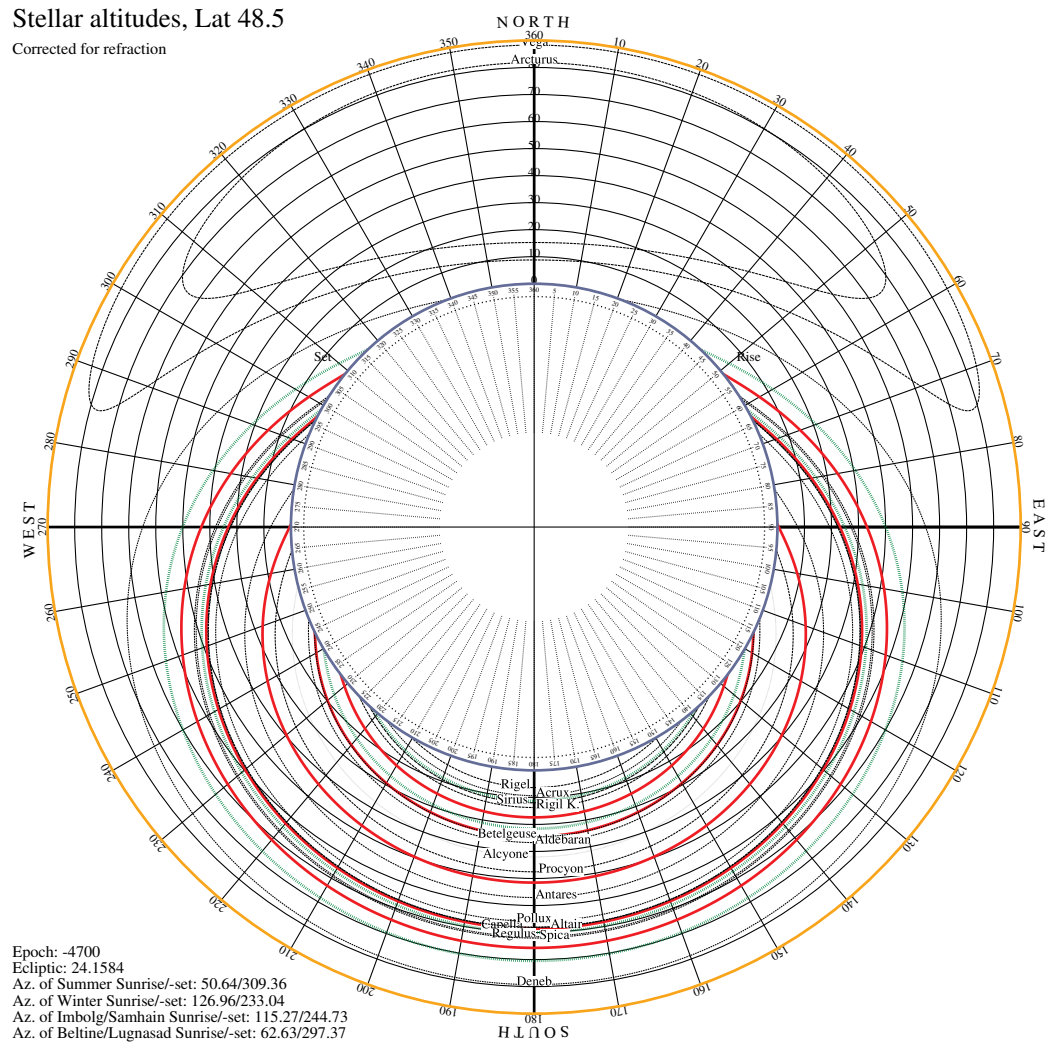


Figure 1.6: Flipped view of figure 1.4. The zenith (orange) is now mapped to the outermost circle, while the horizon (blue) encloses the inner area.

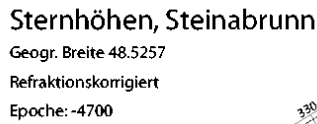


Figure 1.7: Combining the flipped star path map of figure 1.6 with data of the local horizon from GIS data (the thick irregular black zone along the horizon) and an archaeological map of the twofold *Kreisgrabenanlage* (KGA) of Steinabrunn [EDER-HINTERLEITNER *et al.* 1999] as example for an archaeological application. The radial lines indicate some of the plausible viewing directions along ditches, while the dashed lines indicate views through palisade gaps. Degree labels have been added where a line does not originate in the diagram’s center.

been marked with their respective orientations, allowing the identification of the intended orientation from the star map.

Orientation Histogram

All plausible orientation lines (views over earth bridges, along radial ditches or through palisade gaps from viewpoints close to the center) of 27 *Kreisgrabenanlagen* were entered in a circular histogram placed inside the mapping from figure 1.6. This histogram, in combination with the star path map lying immediately outward, allowed us to identify groups of alignments which indicate that these directions had been chosen so that the objects rising or setting in these directions can be observed by looking, *e.g.*, along a ditch or through a door or gap in the palisade (Figure 1.8).

North and south are clearly indicated in 2–4 respectively 4–5 KGAs, east and west only in 2–3 each. A few peaks indicate alignments to certain solar dates (marked with red ellipses): directions around 127° indicate Winter solstice sunrise, 115° and slightly southward (shifted by raised local horizons at several sites) apparently mark sunrise at start and end dates of a “Winter” season centered around solstice. A weak group near 64° and a larger group near 295° may indicate sunrise and sunset at beginning or end of a “Summer” season similarly centered around summer solstice, which is not strongly marked itself (at 50°). The strongest peaks however appear to be connected to stars (blue ellipses). The strongest concentration lies in the range 104–108° with in total 9 strong and 3 more weak hits, which indicates the rising point of the Pleiades star cluster, marked here by the path of its brightest star, Alcyone, which by itself is by far the dimmest star in this chart. Almost on the opposite side, the setting direction of Antares is pointed to by 8 or even 9 strong hits in the range 275–280°. The calendarical interpretation of these peaks is described in section 1.4.

Note that this histogram only works if the horizons are not highly elevated and if all sites approximately share geographical latitude. Due to the fact that an elevated horizon shifts both rising and setting points southward (on the northern hemisphere), the peaks in the histogram are a bit widened, but *towards the south only*. The widening is greater along the northern and southern parts of the horizon, caused by the shallow angles of the diurnal arcs in these areas.

1.3.5 Improving the Diagram

Improved Horizon Readability

Given that the horizon is the most interesting region, it can be enhanced to use more space in the diagram. For this, the mapping of the sky has to be made nonlinear to allow the stretching of the horizon. For a study of Celto-Roman temples [ZOTTI 2005a], the altitudes a were simply replaced by the arc cosines of the squares of their cosines ($r = r_0 + \arccos(\cos^2 a)$) (Figure 1.9; note the completely different stellar arcs, which have shifted from the positions in the other diagrams due to precession). Of course, other functions are usable and may be tried. On the other hand, stretching too much makes it harder to discern the diurnal arcs in the border of the diagram.

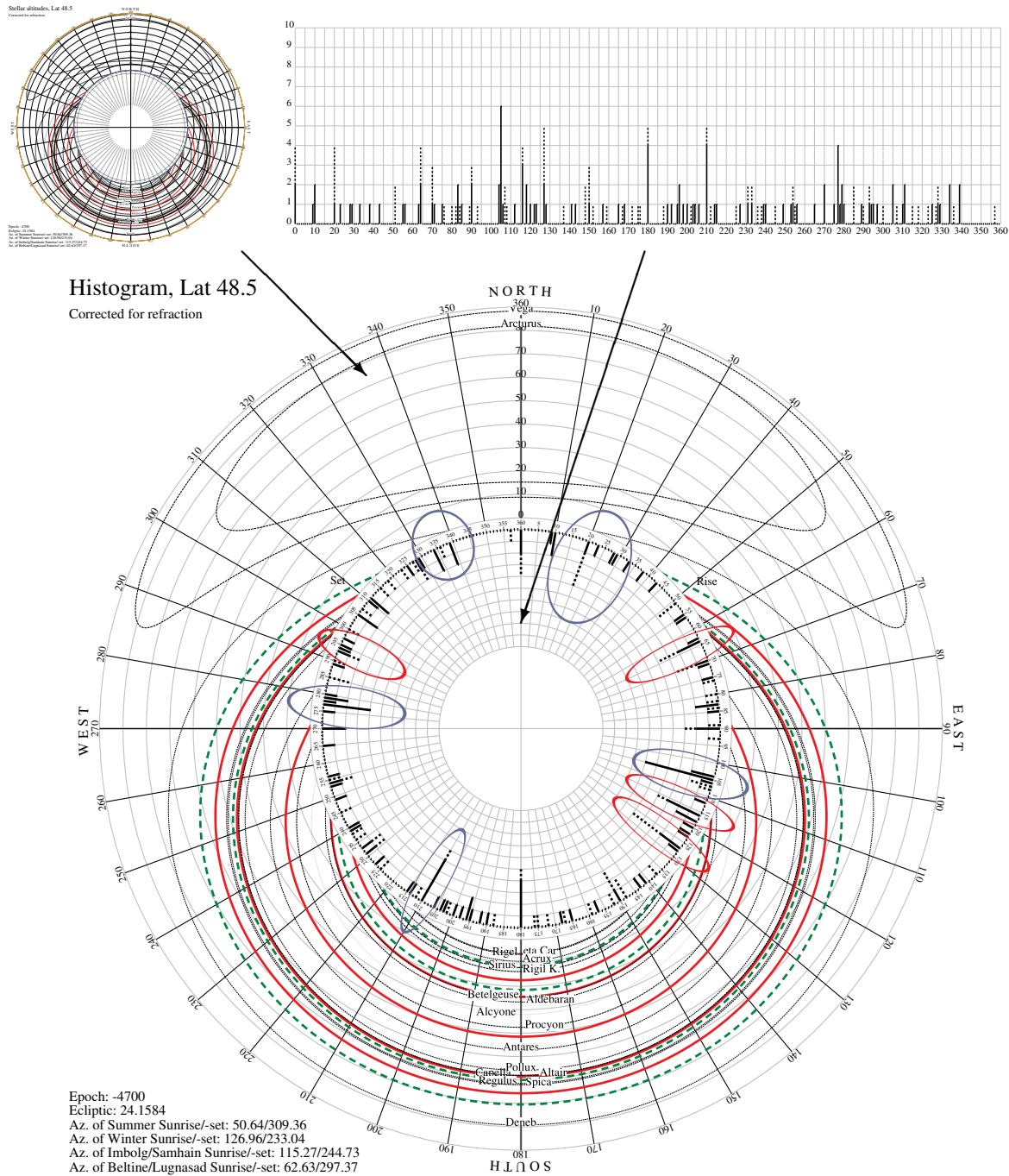


Figure 1.8: An ordinary rectangular histogram of all identified directions over azimuths of 27 *Kreisgrabenanlagen* (top right). The thick lines along the grid pointing from the horizon line towards the center indicate the number of orientation lines pointing toward the respective azimuth. Full lines indicate directions of radial ditches or earth bridges, dashed lines indicate less conclusive gaps in the palisades. The histogram shows some peaks, but is hard to understand without the celestial context. Putting the histogram inside the mapping of figure 1.6, with lines pointing from the horizon circle towards the center, immediately shows the possible astronomical connection of these directions.

Sternhöhen, Gurina

Geogr. Breite 46.667

Refraktionskorrigiert

Epoche: 0

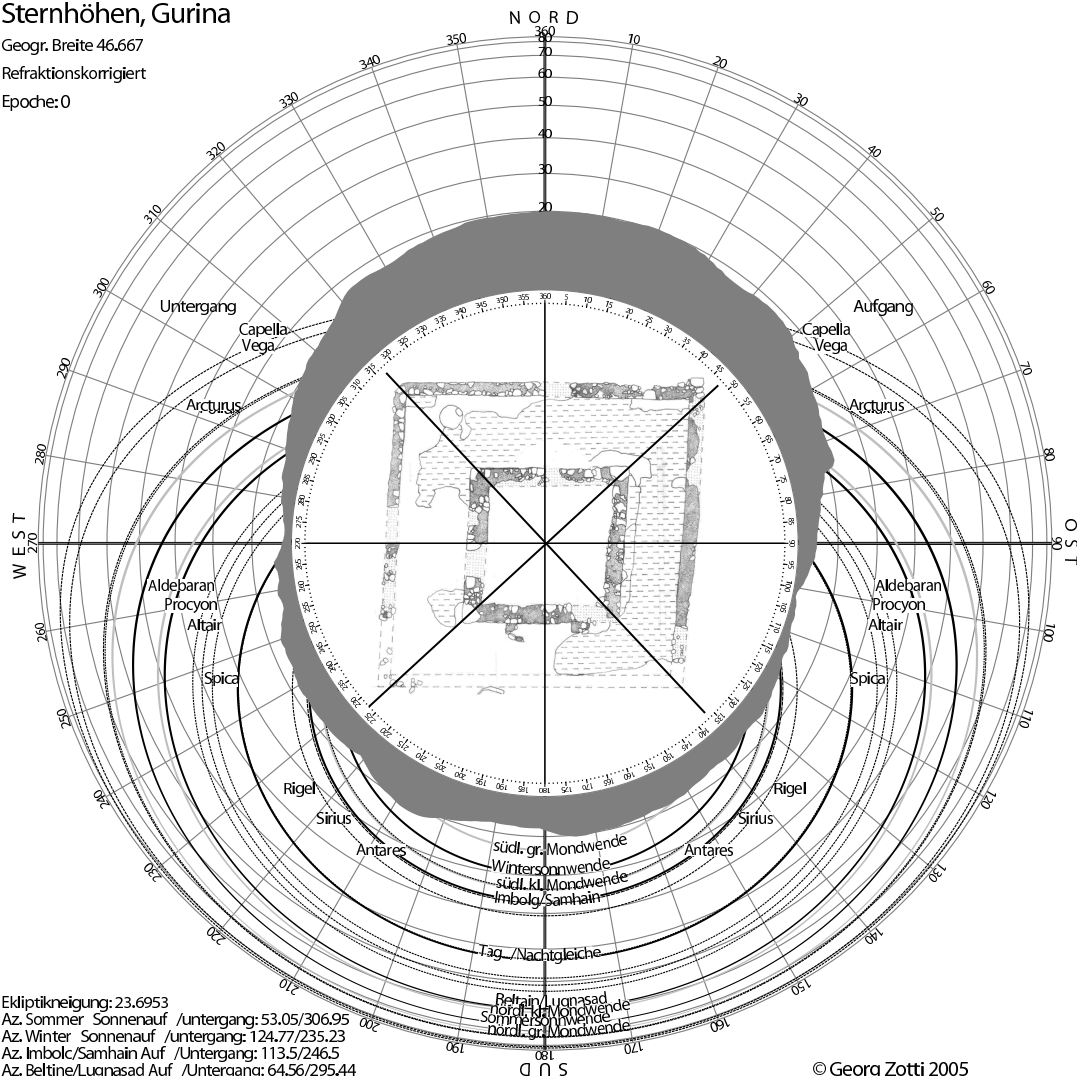


Figure 1.9: A nonlinear mapping of the altitudes improves readability along the horizon. Also, the arcs for the Sun and the Moon are computed for upper and lower limbs, then the region between is filled. This improves reliability over a simple thick line. The structure here lies in a valley running in a west-eastern direction with a high mountain ridge towards the north [ZOTTI 2005a].

Solar and Lunar Paths

Using simple lines for the Sun and the Moon will just show the trail of their respective centers. However, these bodies are approximately 1/2 degree in visual diameter, which can lead to a significant difference when investigating astronomical alignments. For a sunrise grazing upward along a distant hill, it can make a difference of several degrees in azimuth whether the first rays of sunlight (upper limb) should be pointed to, or the appearance of the complete solar disk. This difference also changes the calendar date found, because the Sun's rising azimuth moves northward ("left" as seen on the ground) between December and June solstices and southward in the other half of the year. So, diurnal arcs for these two bodies should be computed and plotted not for their centers, but for their upper and lower

Corrected for refraction

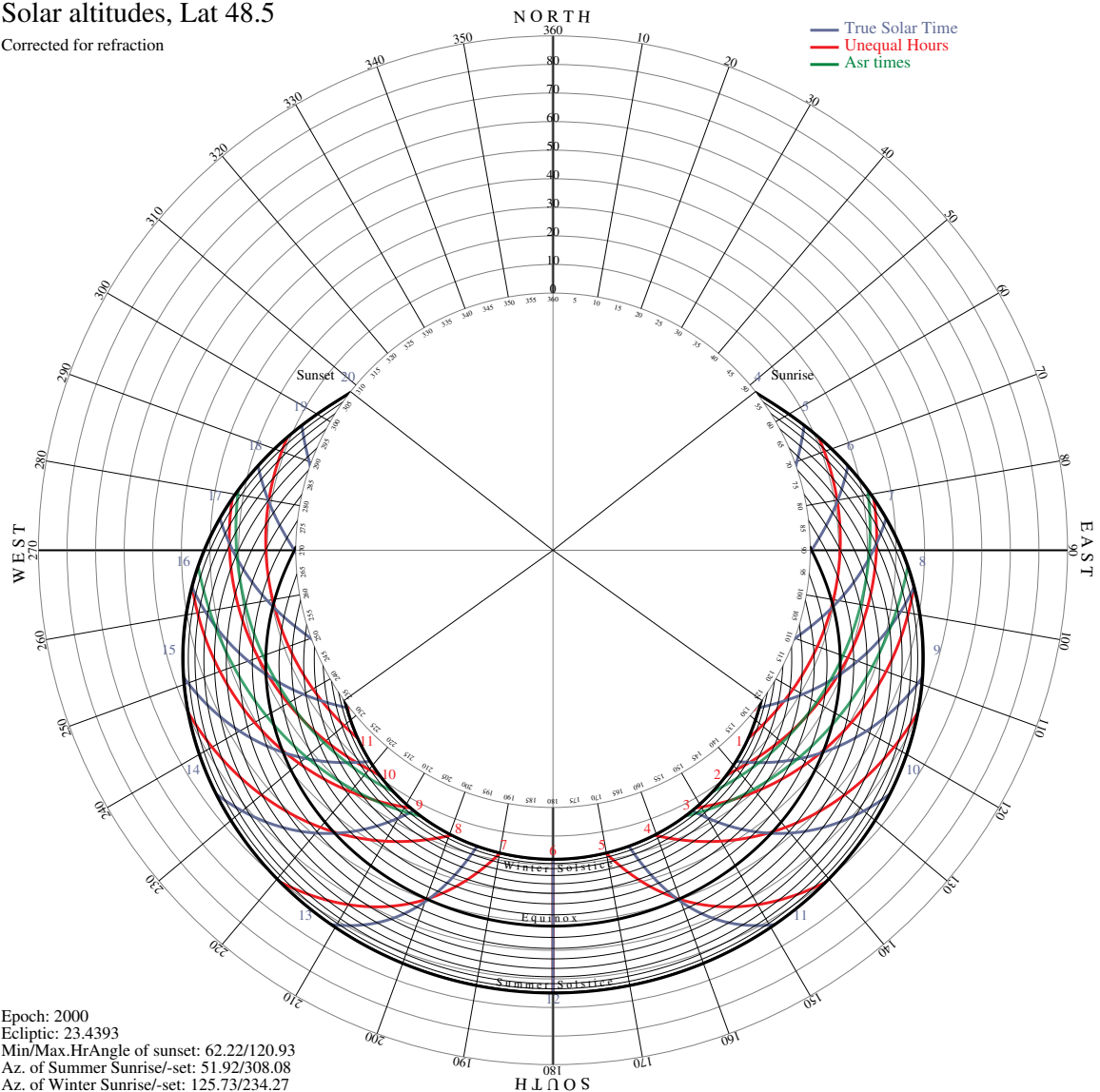


Figure 1.10: Flipped sky map showing diurnal arcs (daily paths) of the Sun, together with lines for equal hours (blue), unequal hours (red) and Islamic *ʿaṣr* times (green) as examples of interesting directions to look for in studies on solar orientation of buildings. The diurnal arcs now show the Sun’s daily motion for every tenth day.

limbs, and the region between these lines may be filled. Now it is possible to discern on an enlargement of the horizon whether, *e.g.*, the Sun's first light (upper limb crossing horizon line) or its full visibility (lower limb crossing) may have been the target of an alignment, and the thick line will at last have a valuable meaning. Of course, the line thickness will vary if the altitudes are scaled in a nonlinear way.

More Fun with the Sun

From diurnal arcs of the Sun drawn for various dates of the year in this kind of map (Figure 1.10), dates for zenith passages of the Sun can be estimated for sites between the tropics, which have been of interest, *e.g.*, to pre-Columbian peoples of Peru [KRUPP 1994, p.181]. It may also be of interest to show *hour lines*, *i.e.*, Sun positions at regular intervals from *true noon* (which is defined by the Sun reaching its highest altitude for the respective day). In the Alpine regions, many villages have their chain of “hour mountains”, where the Sun will be positioned roughly over these mountain tops at the respective hour, so they should stand out on the horizon plot.

Today we are familiar only with the concept of *equal hours*, dividing the day into 24 equal parts. However, in antiquity and medieval times, it seemed more natural to divide the day between sunrise and sunset into 12 hours, and to divide the night in a similar way. Because—except at the days of equinox—night and day are of different length, day and night hours were of unequal length, and the duration of these *unequal hours* varied during the course of the year. Early sundials show these hour lines, and the Spanish “siesta” still is the name of the sixth (unequal) hour of the day, *i.e.*, noon. Old building structures involving small windows and wall ornaments sometimes are said to be aligned to show these hours by light spots shining onto them.

Of course, when looking for solar alignments in prehistoric archaeological structures, we cannot assume the usage of a 12-partite day, still such lines can be used as guidelines to estimate the Sun’s motion through the sky.

Another example for a possibility of solar alignment has been inspired by the Islamic rules to find the afternoon prayer times (*‘aṣr*). Measured with a simple pole, these times are defined by the pole’s shadow length equaling the pole’s noon shadow length extended by the pole’s length (*‘aṣr* 1) or twice the pole’s length (*‘aṣr* 2) [AHMED 1996/1997]. Alignments towards the Sun’s position at these times would have to include a very high local horizon or also artificial wall tops or windows, however, and cannot be seen in archaeological structures if only foundation walls (or even less) remains.

1.4 Discoveries

A word of caution: Many azimuth directions one can find in an old building structure can provide some star that rises or sets there at some period in time. Therefore, investigations of singular buildings are always prone to the danger of overinterpretation. The histogram (Figure 1.8) shows many singular entries of gate directions, and many stars that seem to be pointed at. But not every door or wall was necessarily intended to be aligned towards some rising or setting point of a certain object. A current problem with the data is also the still incomplete set of horizon profiles, so that a complete evaluation cannot yet be made. However, it is possible to detect the largest accumulations of gate orientations, and the diagram can show us possible celestial objects that can explain the orientation. Here, an important point is that the visually most impressive accumulations are not *centered* around an object’s diurnal path, but have their peaks slightly southwards of, and are *limited* in the north by the intersection of the diurnal path and the mathematical horizon. This southward shift is expected as effect of an elevated horizon.



Figure 1.11: Virtual reconstruction of a look through one of the doors in the neolithic *Kreisgrabenanlage* of Steinabrunn in Lower Austria. The singular post appears to be aligned to the rising point of the Pleiades star cluster, which with their rising in the morning shortly after spring equinox possibly announced the beginning of the agricultural year. Astronomical alignments like this have been identified using the method described in this chapter. Screenshot from StarryNight Pro 4.5, foreground from virtual reconstruction courtesy of Imagination Computer Services, Vienna.

Combined with either interactive desktop planetarium software or a self-made planisphere for the neolithic period, it is possible to interpret a few of the detected accumulations of azimuth directions. In addition to the factual alignment visible from the diagram, we wanted to solve the question of *why* certain stars could have been so important that our far ancestors oriented their largest buildings towards them.

For the Sun, the most obvious direction accumulations are near azimuth 127° (Winter solstice) and south of 115° (Candlemas/All-Saints-Day), thus marking start, middle and end of a “Winter” season centered around the Winter solstice. On the northern side, an equally defined “Summer” appears to be marked mostly with begin/end dates, while the summer solstice seems to have been less important.

Still, it seems evident that not only solar directions have played a role in the orientations of *Kreisgrabenanlagen*. While the data currently do not offer a clear connection to lunar extremal risings or settings (green lines in figures 1.4 and 1.8, respectively), there are two striking peaks towards directions $104\text{--}108^\circ$ and $275\text{--}280^\circ$. Indeed, around 4700 B.C., there

have been two very conspicuous objects rising respectively setting at these directions: the Pleiades star cluster (rising) and the bright star Antares in Scorpius (setting). Moreover, the events of rising Pleiades and setting Antares took place *almost simultaneously*. Further investigation led to the conclusion that the Pleiades' heliacal rising (see section 1.2) took place just after spring equinox. It appears very likely that the neolithic farmers used this celestial event to start their agricultural year. Note that the Pleiades have been observed by many cultures worldwide in connection with the seasons [KRUPP 1994], although a star cluster like the Pleiades, which consists of dim stars, cannot be observed below an extinction angle of about $a_E = 4^\circ$, which is, however, a typical horizon elevation in Lower Austria.

Deneb, the Swan's tail star, joins the couple: just when Antares is setting and the Pleiades are rising, Deneb is highest in the sky, shining almost in the zenith. It is the northernmost bright star that sets below the northern horizon, and a wide group of doors and other sight lines appear to point towards it. Unfortunately, the intersections on the northern and southern horizon are very sensitive to elevated horizon lines, so the entries in the histogram, which cannot contain a horizon line, appear less concentrated. Figure 1.3 shows the scene where simultaneously Antares is setting near 275° , the Pleiades rise at 106° and Deneb culminates in the south in about 80° altitude (near center).

Also a frequently used southern gate direction (210°) required to look for a star setting there. Unfortunately, there are several stars sharing almost the same declination, but Rigel appears to be the brightest candidate. Further investigations in the field, taking measured horizon profiles, should clarify and narrow the error margins for this and all other directions.

1.5 User Reactions

Archaeologists, who are largely unfamiliar with astronomical problems, but interested in possible astronomical influence in the culture of a studied epoch, were asked for their understanding of the diagram when applied to a different study [ZOTTI 2005a]. Overall, the first reaction typically was that the diagram shows too many lines, and cannot stand without explanation. However, when properly described, they understood what can be seen, and accepted it as a tool for the solution of this specific type of investigation. The problem apparently consisted not so much of reading the diagram itself, but in the elementary astronomical knowledge necessary to understand it.

1.6 Conclusion and Future Work

In this chapter we have shown a simple, yet effective way to investigate buildings with known date of origin for astronomical orientations towards special rising and setting points of Sun, Moon and stars. The core item is a novel diagram combining a terrestrial map, *e.g.*, of a building or other archaeological structure, and a folded-apart representation of the sky dome showing daily paths of celestial objects and the local horizon. We have shown how this diagram has been applied to a certain class of neolithic circular enclosures (*Kreisgrabenanlagen*), and have pointed out interesting discoveries made with a variant of the diagram which includes a histogram of alignments of a larger number of KGAs. These discoveries allowed us to produce renderings for selected points of view inside virtual reconstructions. These were used as foreground panoramas for affordable commercial desktop planetarium soft-

ware to create astronomical vistas and animations (*e.g.*, Figure 1.4 from ZOTTI [2005b], where also the detailed astronomical results have been published).

Clearly, an optimal solution would be an interactive, navigable Virtual/Augmented Reality environment with an astronomically correct and visually convincing high quality sky simulation, which would allow immediate investigation of virtual reconstructions of archaeological sites. Unfortunately, only partial solutions of such systems seem to exist. One such system has been used at UCLA's Cultural VR Lab [UCLA], where research has been done on the solar orientation of the sacred Inca precinct of the Island of the Sun in Lake Titicaca, Bolivia [FRISCHER 2003]. One problem with current VR systems however is that 3D content development suitable for archaeo-astronomical research is very time consuming and costly and needs lots of interdisciplinary expertise.

The concept of analysing collected azimuth directions in a circular histogram could be extended to allow interactive work. Interactive brushing through a larger database of KGAs in a Geographical Information System (GIS) which includes their possible orientations and selecting, *e.g.*, only archaeological sites in a specific region, could for example probably identify local traditions, although the total number of known KGAs in Europe (about 120 [DAIM and NEUBAUER 2005, p.4]) may be too small to deliver reliable results. If data from a long temporal series (several centuries) are investigated, the star paths will be seen shifting due to precession, still, for example an interactive investigation of the orientation of burial sites could probably find long-lasting traditions. In any case, dating the archaeological findings is necessary for any investigation related to stellar positions.

Chapter 2

Using Virtual Reconstructions in a Planetarium for Demonstrations in Archaeo-Astronomy

Never before was an instrument created which is so instructive as this; never before one so bewitching; and never before did an instrument speak so directly to the beholder. The machine itself is precious and aristocratic [...] The planetarium is school, theater, and cinema in one classroom under the eternal dome of the sky, a drama with the celestial bodies as actors.

— ELIS STRÖMGREN, *Director of Copenhagen Observatory, 1923*

As described in chapter 1, in the last decades archaeologists in central Europe have found traces of enigmatic neolithic circular building structures (*Kreisgrabenanlagen*, KGA) buried in the soil. The orientation of many of their doorways may have been chosen with an astronomical background in mind.

This chapter explains the use of virtual reconstructions of these buildings from archaeological data, in combination with a simulation of the sky of that time in a Planetarium, to present the astronomical findings to the public. It is based on the paper and the talk given at CEMVRC 2006 [ZOTTI *et al.* 2006].

2.1 Introduction

While diagrams like the ones presented in chapter 1 are useful for communicating archaeoastronomical findings to scientists and lay-persons with prior astronomical knowledge, in this chapter we present a medium which is more suitable to deliver a compelling experience to members of the general public.

For an impressive, immersive presentation of these results we propose a combination of the high-quality sky simulation as projected by the current generation of Planetarium projectors with a horizon panorama created from virtual reconstructions of these ancient sites.

The rest of the chapter is structured as follows: first, some related work in virtual reconstruction is mentioned. After a short summary of the astronomical alignments which appear likely to have been built into the KGAs on purpose, a novel way to present these results to

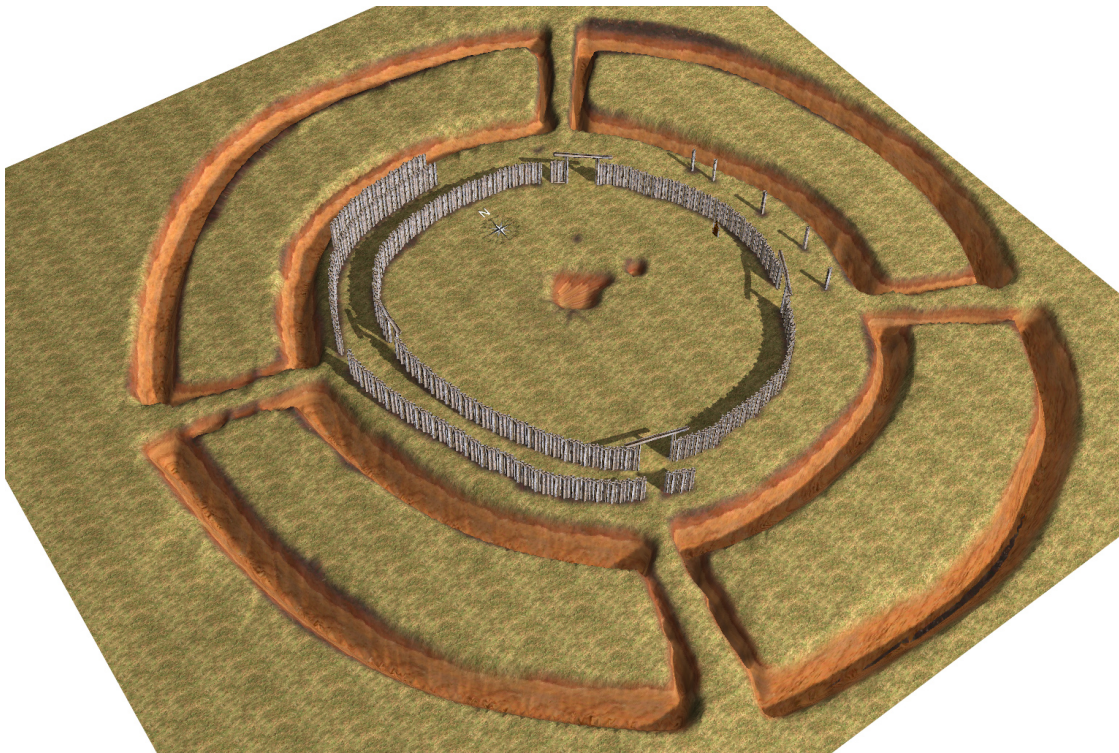


Figure 2.1: Virtual reconstruction of the Steinabrunn site.

the public inside a Planetarium will be presented. Problems and more alternatives will be discussed in the section on future work.

2.2 Related Work

Virtual reconstructions have become a standard practice for public demonstration of buildings and whole cities long lost in the course of history. Frequently the main interest lies in the proper reconstruction of the buildings and cities, without much consideration being given to the surrounding landscape. At best, such models may show a piece of landscape modeled after digital elevation data from a Geographical Information System (GIS), with either a simple blue or more realistic daylight sky [e.g., PREETHAM *et al.* 1999] as background. Alternatively, photographically captured HDR images of the daylight sky can be used for illumination of the scene (see STUMPFEL *et al.* [2004] and chapter 6).

Rarely, the different illumination effects of the Sun on an ancient temple dependent on time of day and year are studied [SUNDSTEDT *et al.* 2004]. In a larger, immersive VR system dedicated to virtual reconstructions of archaeological sites, the orientation of a south american temple with respect to certain rising and setting directions of the Sun on the local horizon has been investigated by FRISCHER [2003]. An accurate depiction of the visual appearance of an ancient site during night-time appears to currently be of little interest to the archaeological community, however; no such system is known to the author.

For public demonstration and explanation of the night sky, the last century has seen the development of Planetarium systems [MEIER 1992], which consist of a closed hemispherical dome (auditorium) with a special projector in its centre. This device is capable of projecting

the stars, planets, the Milky Way, and sometimes explanatory graphs, coordinate grids and mythological figures onto the dome, and thereby simulates the night sky in a highly immersive fashion. The projector can be rotated around several axes to simulate the sky for any time and location on Earth. Demonstrations and lectures can be enriched with additional slide and special-effect projectors. It is likely the best tool for astronomical demonstrations, and can be seen, in a certain sense, as a predecessor of computer-driven immersive Virtual Reality systems.

In the first generations of Planetarium projectors, large patches of the sky were projected with a technology similar to a slide projector, using a huge central light bulb and several projection optics outlets mounted on a sphere that use metal masks with star holes of different diameter. Actually, two part-spheres were used for the northern and southern hemispheres, connected by a lattice structure where moving planet projectors were mounted. This dumb-bell shape was typical for almost all Planetaria of the 20th century.

One of the problems of this type of device was the simulation of stars with different brightness. Given that the brightest stars are more than 100 times brighter than the dimmest naked-eye stars, the brightest stars had rather unrealistically large projected star blobs. Later projector generations used a dedicated projector with a brighter lamp for the projection of the brightest stars with a smaller dot size. The latest generation of projectors no longer have star field masks, but project each star individually through a glass fiber of different diameter, which gives much smaller and (where needed) brighter star images and provides a simulation of the sky with much more realism, also allowing to show the slight colour tint visible in a few bright stars. This latest generation of projectors even allows to simulate the scintillation, or twinkling, of the stars induced by turbulent air in the Earth's atmosphere, which adds to the overall impression of being under the "real" sky.

To simulate the horizon of the current observer location, a system of carefully aligned overlapping slide projections along the horizon is frequently used. By using different slide sets, different observing locations on Earth, or even on the surface of the Moon or Mars, can be simulated during a show.

Digital Planetarium systems [SkySkan 2003; EVANS&SUTHERLAND 2006] replace the classical Planetarium projector with a digital projection system also capable of full-dome projection, thus even allowing "interstellar travel experience", *i.e.*, the three-dimensional view of the sky from anywhere in a large area around the Sun's position in our galaxy, for a large auditorium [*e.g.*, Hayden Planetarium]. However, until recently, overlapping CRT projections were used, and stars were again usually drawn with diameters showing their relative brightness, which also limited the achievable realism by the need to draw oversized stars to compensate for the limited dynamic range of the CRT projectors. The recent development of Laser systems promise a wider dynamic range and a large increase in realism, however, being scanning systems, there is still the impression of a "big flickering monitor". Therefore, also the most modern Planetaria are usually equipped with a "conventional" star projector system.

For private use, in the last years "desktop planetarium" computer programs have become not only popular but gain ever more realism with each new release [*e.g.* StarryNight]. For example, the Milky Way is no longer shown as a flat gray area like on a printed atlas, but shows bright filaments and dark knots, stars vanish during twilight, and the daylight Sun may cause a "lens flare" artifact to indicate its brightness. The latest versions do not plot stars from a catalog, but make use of an all-sky photographic atlas. It is even possible (*e.g.* with Starry NightTM) to use a self-made panorama photograph as "local horizon", so a



Figure 2.2: Horizon Panorama for the center of the Steinabrunn site.



Figure 2.3: Horizon Panorama for a location near the south-east gate of the Steinabrunn site.

better estimate on object visibility or rise and setting times of objects can be given, especially if there are mountains on the horizon. Like in a Planetarium, these foreground panoramas are obviously valid for one viewpoint only.

Some other programs of that kind allow the user to select observing sites outside of the Earth, so, given the high-quality three-dimensional data of, *e.g.*, the ESA Hipparcos astrometry satellite [ESA Hipparcos], users can explore the sky from anywhere in the stellar vicinity around the solar position and, *e.g.*, study the changes in the constellations as seen from other locations in space [ESA Digital Universe 2004].

What is still missing is the combination of a desktop VR system, which allows a virtual walkthrough of a reconstructed archaeological structure, with an astronomically and physically correct sky model.

2.3 The Capability of a Planetarium to Simulate Celestial Phenomena Important in Archaeo-Astronomy

Unfortunately, neither refraction nor extinction (see section 1.2) can be properly simulated in a classical Planetarium. Stars are mechanically masked off at the mathematical horizon. Modern special effect projectors can at least simulate a flattened and reddened Sun close to the horizon. Usually, the Sun and the Moon are also projected with an exaggerated diameter, however, which simulates the effect that these celestial bodies look much larger than they are on the horizon. But also solutions found in popular desktop planetarium programs seem questionable, so that room for improvement is still there.

On the other hand, precession (see section 1.2.3) can usually be simulated by a rotation of the main projector, which is a key necessity for the simulation required here. The neolithic sky was shifted by precession by about 90° from today's sky, so that even with real reconstructions of archaeological structures *in situ*, as done at KGA Goseck, Germany, it would no longer be possible to verify or photograph any intended stellar orientation using today's sky. (However, KGA Goseck appears to be only solar-oriented.)

In rare cases even proper motion of a few stars can be simulated by a special-purpose projector. In a Digital Planetarium, both effects are easily shown if the computational model is correct.

Sight lines inside the KGAs cannot currently be given to sub-degree accuracy, because the exact positions of, *e.g.*, post tops above the surface is lost and can only be inferred from post hole positions, admittedly leaving some room for speculation about the practical use of one or another stellar alignment. Also, some sight lines are difficult to set down, *e.g.*, where the ditch or palisades are not really circular and some door axes do not meet on one spot, so that defining a single point of observation is hardly possible. It would be fortunate to be able to interactively look for the best spot, *i.e.*, take a walk through a virtual model in combination with the sky, explore the most impressive sight lines on the ground and look whether they can be seen in combination with some celestial view which originally could have motivated the respective construction.

2.4 Our Work

The astronomical investigation of 28 KGAs in lower Austria [ZOTTI to appear, 2005b, 2006, 2008] indicated that several doorways and gates are not oriented randomly, but appear to be oriented so that for an observer in or close to the center of the KGA the Sun will appear to rise or set there on one of the 8 *key dates* (see section 1.2.1), with the winter solstice as most prominent solar direction.

In addition, three groups of door and ditch alignments have been identified which appear to point towards the rising point of the star Deneb (α Cygni) and that of the most prominent of all star clusters, the Pleiades, and the setting direction of Antares (α Scorpii) as they have been around 4700 B.C. (see section 1.4).

For a rapid presentation in time for the exhibition mentioned on page 2, horizon panoramas (Figures 2.2, 2.3) for different observing locations inside several KGAs had been created from the virtual reconstructions, which could then be loaded into desktop planetarium software [StarryNight]. With this combination, some interesting snapshots of sky vistas have been taken, *e.g.*, Figure 2.4 (a).

In the wake of the successful exhibition and rising public awareness of these remarkable structures, a television documentation on *Kreisgrabenanlagen* is currently under production. A part of the film will contain the topic of astronomical alignments. Now, in the course of a year, rising and setting alignments of the Sun with horizon features on the solar key dates are being filmed *in situ*, even if there are no building remains visible. Due to the Earth's slightly different axis tilt (23.44° today *vs.* 24.15° then), the solstitial extremes of previous times can no longer be reached and are missed by 1.2° , which is more than two apparent solar diameters. This means that any special phenomena that could have been visible from some locations at that time, like the solar disk "scratching" along a distant mountain slope, or diving slightly below the slope during the days of solstice can no longer be observed today. Still, such recordings give a good impression about why KGAs may have been built at their respective locations, and equinoctial events indeed have the same horizon point, so they can (and should!) be proven by documented observation, *i.e.*, film. On the other hand, trying to record stellar risings and settings *in situ* is completely pointless: Precession has shifted the stellar sky so that the rising and setting points today are totally different from those in the neolithic period. To create video content for this part of the TV documentation, we had to resort to simulation.



Figure 2.4: Sunrise over a hill, seen from KGA Steinabrunn on a date which is early November or February in our modern calendar. These dates are right between equinoxes and the Winter solstice, thus marking a calendrical key date. The Sun rises in a direction pointed to by the doorway. – (a) Simulation with *Starry Night Pro 4.5* [ZOTTI 2005b]. – (b) The same scene, captured in the Planetarium, where only the part of the panorama above the mathematical horizon can be shown. The Sun rises as reddened ball over the hill (appearing rather yellowish due to overexposure – quite natural for the Sun!). The Planetarium dome is tiled, so any twilight simulation in the Planetarium is unfortunately rather poor. The sky gradient has therefore been added during image postprocessing.

The first idea was to simply use the program mentioned above, which also allows the creation of video clips (Quicktime format). However, the resolution of the animations is rather low and not very well suited for presentation on television.

Therefore, we proposed to use the currently best artificial sky as available with a Zeiss Mark IX Universarium “star ball” projector installed at the Zeiss Planetarium Vienna, Austria. This Planetarium is also equipped with overlapping slide projectors to create a horizon panorama display, and a Zeiss Universal Laser Image Projector (ZULIP), which is used for special effects and as video projector which can be rotated, tilted and zoomed.

To create a horizon panorama for the Planetarium dome, the horizon image is exposed with proper pre-distortion on a set of several slides to be used with carefully aligned slide projectors. Typical panoramas in a Planetarium presentation show a city skyline (combined with a sky view of just the brightest stars and lots of background light to simulate the urban light pollution), a mountain panorama (combined with a dark rural sky), maybe some exotic destination to show the sky of a tropical location on Earth, or a Lunar panorama created from Apollo image data. Of course, being projected in the same way as the starry sky, bright stars sometimes appear to sit in front of the skyscrapers or mountain tops, which is one of the shortcomings of this approach. To cut off the stars, a mask of similar shape like the horizon line would have to be set up around the star projector, which is however impractical because the stars are not projected from the true center, but from an extended sphere, so that a border of parallax mismatch remains. Also, changing the horizon panorama would mean having to change the mask, so this is not done in practice.

When the Planetarium sky was set for the epoch of the Kreisgrabenanlagen (4700 B.C.), the vistas previously found only on a custom-made planisphere and visualised in *Starry Night* could be replayed in unprecedented realism, and the added impression of the fully immersive Planetarium sky dome with the Milky Way spanning a high arc through the zenith and the bright Milky Way center setting on the Western horizon together with Antares was

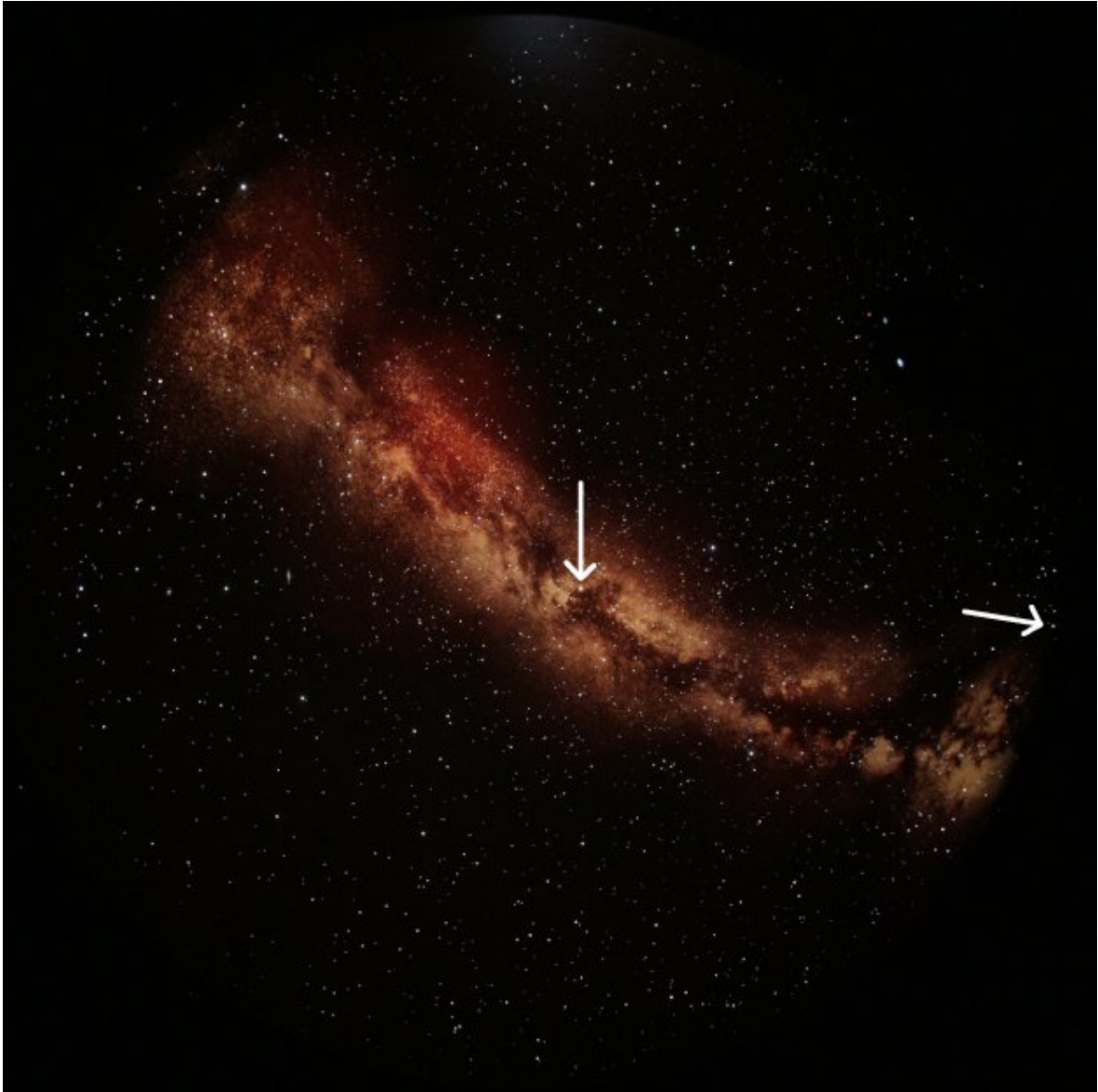


Figure 2.5: “Archaeo-Astrophotography”. A fish-eye photograph taken in the Planetarium, showing the Milky Way spanning the whole sky through the zenith when Antares was setting (right edge) and the Pleiades were about to rise, with Deneb close to the zenith. This photograph can no longer be produced in nature in the same orientation, because the sky has shifted due to precession. Compare with Figure 1.3 for a star map.

almost an eye-opener as to the (possible) “magical moment” the people of that time may have felt (Figure 2.5).

Test shots with the HDTV camera used for the documentary showed that the camera was unfortunately not sensitive enough to capture the Planetarium sky with a wide-angle lens, so that the capturing of the immersive look of the sky in the Planetarium with a full KGA panorama is not possible. However, with a mild telephoto setting, stars and even the Milky Way could be recorded. Therefore, it was decided to record only important views, *i.e.*,



Figure 2.6: From the same location as Figure 2.4, shortly after spring begin, the Pleiades appear above the hill in the morning twilight for the first time after having been invisible for several weeks. Photograph taken from the Planetarium dome (causing the curved horizon line), combining the small star dots from the “star ball” with the foreground from the ZULIP. The twilight effect has been added during image postprocessing, where also stars overlaid on the foreground were removed. Compare also with Figure 1.4.

views through doors or along ditches, with the applicable part of the foreground panorama projected by the ZULIP, to save the cost of producing the slides for the full panoramas.

Because the “star ball” projector is centered in the Planetarium dome, the ZULIP is placed off-center, and the projection area least influenced by projection distortions is obviously on the same side of the star ball as the ZULIP. Fortunately, unlike older Planetarium projectors, the star ball can be rotated in azimuth, so that the cardinal points in the dome can be set arbitrarily. So, for the TV shots, the ZULIP projection direction was frozen towards this region of least distortion, showing one of the interesting doors of the KGA panorama, and the azimuth match was made with the central projector, so that the sky geometrically matched the view from Starry Night.

To counteract the abovementioned problem of stars projected onto the foreground panorama, we tried to mask off the stars from the star ball where they would project on the palisade walls with cardboard masks mounted on tripods. Unfortunately, the star fields of the star ball projector apparently overlap, so while stars of one star field could be masked off on the correct line, other star fields still cast stars on the foreground, so the idea had to be fi-

nally abandoned, and for the TV production, post-processing the shots using video overlays of shots taken with only the KGA doors are necessary to have a star-free foreground.

The simulation of twilight in the Planetarium is unfortunately a problem: around the horizon, several groups of coloured light bulbs can be activated, but of course their light mixes with the images projected along the horizon, deteriorating the otherwise splendid view. Also, the inside of the dome of this Planetarium is not smooth but covered with painted sheet metal tiles from the 1960s which show their age by warping. While this is still not too problematic for the audience in a live show, twilight-type illumination of the background does not look very good in a video closeup, and again, therefore, twilight effects should rather be added in a post-processing step, or right into the projected horizon panorama. Figures 2.4 (b) and 2.6 were created from combining photographs of the doorway projected with the ZULIP with and without the sky, and a layer showing a gradient for the twilight or sky colours as could be optimally simulated in a Planetarium.

2.5 Discussion and Future Work

Compared to the simulation in *Starry Night*, the main differences with simulating the celestial vistas in a Planetarium are

- + fully immersive feeling of being right under the stars
- + much smaller star points of much more intense brightness
- only the part of the panorama above the mathematical horizon can be shown on the dome.

The last point is however indeed a severe shortcoming for this kind of simulations, for which the Planetarium has originally not been invented (see Figure 2.4). Nowadays, the Planetarium is frequently used for show effects which include horizon features like mountain chains or foreground houses. In case particular stars over a building are important in a show, the current solution is to lift the projected sky upwards so that the house can be projected in full size. Of course, this ruins correct stellar altitudes, and the sky on the other side of the dome will be much too low. It is obviously impossible to do this with a full 360° horizon panorama.

The requirements for the provision of the necessary subhorizontal context would unfortunately include a change in the auditorium infrastructure to include a cylindrical horizon zone and a projection system that could project slightly below the horizon. While the ZULIP has a technical barrier built in that prevents casting Laser radiation downwards and possibly into the audience, it appears possible to re-align the slide projection system so it could also add more of the horizon on the cylindrical gallery just below the sky dome.

For computer graphics applications outside of a Planetarium, a physically and astronomically correct twilight and night sky model has to be developed and integrated in a system allowing virtual walk-throughs, allowing the demonstration of astronomical alignments in a desktop VR or CAVE setting.

The digital age has also entered the Planetarium world. While the star projection quality of a modern fiber glass projector is still unsurpassed, all-dome projection systems at least for special effects are becoming more common. Using such projectors, it should soon be possible to allow for continuously changing horizons, so that a complete walk through a virtual

reconstruction, together with a sky with twilight effects [*e.g.* HABER *et al.* 2005], could be projected by digital image projectors and combined with the superb quality of the star projector, or the whole scene could be generated on the computer and projected on the dome with an all-sky projection system. Also, digital projection systems consisting of overlapping projectors currently mask of the subhorizontal area, which however could be reactivated by changing these masks and extending the dome projection area below the horizon. This would allow interactive exploration and demonstration of possible stellar alignments in a properly reconstructed virtual scene, and promises to become an exciting way to demonstrate the astronomical knowledge and the role of celestial events for people of the distant past.

Chapter 3

Tangible Heritage: Production of Astrolabes on a Laser Engraver

Once upon a time, the famous astronomer Ptolemaios was riding on the back of his mule over a bad road, his mind occupied with his armillary sphere. Suddenly the mule stumbled over a rock. Startled, Ptolemaios dropped the precious instrument, and the mule trodded on it. Sadly, the scientist picked up the flattened sphere, but miraculously, it still moved. It was even simpler to use now! Ptolemaios attached an altitude meter, and thus had invented the astrolabe.

— *anonymous legend*

The astrolabe, an analog computing device, used to be the iconic instrument of astronomers during the Middle Ages. It allowed a multitude of operations of practical astronomy which were otherwise cumbersome to perform in an epoch when mathematics had apparently almost been forgotten. Usually made from wood or sheet metal, a few hundred instruments, mostly from brass, survived until today and are valuable collectors' items and museum showpieces. This chapter explains a procedural modelling approach for the construction of the classical kinds of astrolabes, which allows a wide variety of applications from plain explanatory illustrations to 3D models, and even the production of working physical astrolabes usable for public or classroom demonstrations.

This chapter extends a paper and presentation given in the Cultural Heritage track at Eurographics 2007 [ZOTTI 2007a]. In this chapter, the geometrical construction of the astrolabe, which had to be largely omitted due to space reasons, has been added.

3.1 Introduction

The Planispheric Astrolabe, an ingenious computing device which origin lies somewhere in the Near East of the later 4th century, used to be the representative instrument of astronomers and astrologers alike in the later medieval and renaissance period, and is frequently seen on contemporary paintings of scholarly environments and scientific activity. Unlike the Armillary Sphere, which was a three-dimensional model of the (geocentric) universe, the astrolabe maps the sky onto a flat disk that rotates over another disk with an intricate pattern of arcs that represents local horizontal coordinates, so that the sky situation for a specific date can be seen. On the reverse side, the instrument provides an altitude

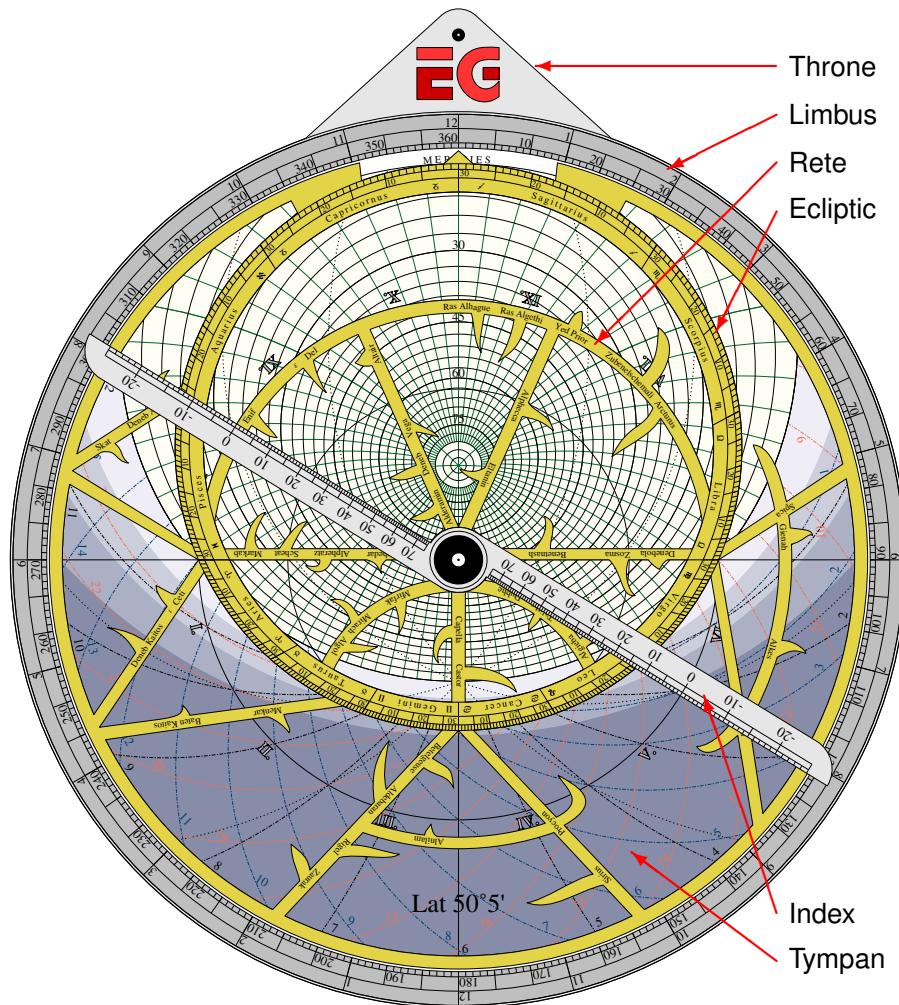


Figure 3.1: Front of a Planispheric Astrolabe. The parts are described in section 3.3.

meter, and this combination allows many practical astronomical operations, of which the determination of time from a single altitude measurement of the Sun or a star appears to have been the most common. Its name derives from the greek words *ἄστρον* (*astron*, star) and *λαμβάνειν* (*lambanein*, take, grasp), i.e., star-taker.

After further development by early Arab mathematicians and astronomers, the astrolabe saw wide distribution in the cultural region of early Islam, where the practical determination of prayer times depending on solar altitude was important for every believer. It was then introduced to Europe via Moorish Spain around the year 1000. Rare until about 1300, it has seen a sharp production peak in Europe in the late 16th century, but was quickly thereafter replaced by the telescope as observing instrument, while its quick, but not overly accurate results were abandoned in favour of those available by the then rapidly emerging mathematical procedures. In Europe, it was rarely used after about 1650, but still described in books on astronomical instrument making well into the 18th century. In Islam countries, it was widely used until the late 19th century, and has been manufactured there until only a few

decades ago. Today tourists are sometimes offered instruments which are sold as astrolabes, but which are unfortunately usually badly constructed and therefore useless.

Astrolabes are frequently shown in exhibitions as masterpieces of early Islam or European Renaissance instrument making. In all its strict construction and functionality, there was some artistic freedom for ornaments, dedications, or adorations. Original instruments are typically unaffordable, however, and also good brass reproductions are difficult to make and therefore costly.

For most of the applications the astrolabe has been in use, it has been superseded by more modern instruments, and some of the questions of everyday life it helped to answer in the medieval period are no longer even posed today. So visitors in a museum usually are confronted with an instrument that looks appealing to most, but is hard to understand because the basic astronomical applications are no longer commonly used or even common knowledge in today's mechanised world.

The seemingly complicated arrangement of lines and circles on most astrolabes is mostly derived directly from the stereographic projection. Traditional construction manuals typically contain long tables of precomputed values like circle centers and radii in case that the executing craftsman is not interested in the construction principles [e.g. LORCH 2005].

If we nowadays want to draw an astrolabe on a computer, of course, these old manuals can still be followed to manually add up all the lines and circles in a CAD drawing, a process which however appears rather tedious and repetitive. Also, a manually drawn instrument will only show one instance of an astrolabe, usable for a given period, and would have to be redone for another to take, e.g., the precessional shift (motion) of the fixed stars into account.

This chapter describes a procedural modelling approach for the astrolabe, which is in its essence an analog computing device around a 2D map of the sky, in an expressive, widely available graphics language: PostScript™. Almost all of the classical diagrams and scales from original instruments found in the literature have been analysed and implemented and are again available for practical study. For explanations, variants of the finished diagrams can be shown which add the necessary construction lines, so that the construction process will be immediately clear from figures in the same style as the finished drawings. The resulting astrolabe figures can be printed, or used as basis for a working virtual 3D instrument for cultural heritage applications in a medieval setting, and even physical models have been created from the same code by controlling a laser engraver/cutter. These real-world instruments are usable for, e.g., museums, where visitor groups could be demonstrated hands-on how to operate these instruments. The year 2009 has been declared "International Year of Astronomy" by UNESCO, and we expect a series of exhibitions and seminars on the history of astronomy, where these instruments can be used.

The rest of the chapter is structured as follows: the section on related work focuses on procedural modelling in the domain of cultural heritage applications, followed by some pointers to construction descriptions for astrolabes. Then follows a functional description of the instrument which explains the various features that may be available and the advantages of using a programmed approach. Some construction details and their implementation are described afterwards, followed by a section on practical production of astrolabes with a laser engraver/cutter. The discussion concludes with potential other applications and future work.

3.2 Related Work

3.2.1 Procedural Modelling

Procedural modelling is frequently used in large scenes like urban visualization, when (mostly artificial) structures are too complex to be modelled completely in detail, and where on the other hand lots of buildings share similar structure. A limited set of rules for building construction can yield a wide variety of visually acceptable buildings that overall results in an acceptably realistic model of a large urban area.

In the area of cultural heritage, BIRCH *et al.* [2001] describe such a system that allows the rapid generation of simple house models. These can be used as “vernacular” buildings that fill the scene between more interesting buildings which have to be modelled in detail.

WONKA *et al.* [2003] describe the modelling of buildings and MÜLLER *et al.* [2006] of complete large urban areas with the help of shape grammars. These allow the generation not only of buildings and cities with simple ground plans, but MÜLLER *et al.* also show a large model reconstruction of ancient Pompeii that can be encoded in a limited set of rules.

Another application of procedural modelling is the encoding of regularly structured architectural detail. The traditional way of creating a detailed model in multiple resolutions would start with a highly detailed mesh, and automatic polygon reduction schemes would provide different levels of detail, probably losing the architectonic intent and providing a non-optimal mesh. HAVEMANN and FELLNER [2004] explain the procedural construction of gothic church windows and their efficient implementation in their Generative Modeling Language (GML). Later, from the same group, BERNDT *et al.* [2005] present their overall solution for an extremely compact shape representation that encodes 3D shapes with only a few control polygons plus functions in GML, which is capable of creating the final mesh in the required resolution by Catmull-Clark subdivision. Their solution is thus optimal for transferring complex geometric 3D models also in a web application if bandwidth is limited, and if the models are reasonably regular to be described by geometric procedures. BERNDT *et al.* present again windows of gothic cathedrals as excellent examples where this approach works very well. The GML syntax is very similar to Adobe PostScript™ [ADOBE SYSTEMS, INCORPORATED 1990], a stack-based programming language mostly used for high-quality printers or as graphics file format best suited for vector graphics.

The current role of procedural modelling for digital cultural heritage is also described by ARNOLD and GESER [2007, section 5.1].

3.2.2 Astrolabes

From medieval times, several manuscripts and printed texts on astrolabe construction survived and are topic of high interest by linguists and historians of mathematics and astronomy alike [e.g. LORCH 2005; CHAUCER ca. 1391; STÖFFLER 1513].

The first modern large study on surviving astrolabes, and still a valuable reference, has been collected by GUNTHER [1932]. MICHEL [1947] is often cited as best 20th-century source of construction details, although some issues remain open. SAUNDERS [1984] also explains construction and use of the most common planispheric and also of other variants of the astrolabe. Good photographs of old instruments can be found in the works of WEBSTER and WEBSTER [1998] or GUÉNA and TALEB-BENDIAB [2005].

Recently, the Web allows access to images of collections of old instruments [OXFORD MUSEUM OF THE HISTORY OF SCIENCE 2006], general information [MORRISON 2005] and even a Java application [POWELL]. An online catalogue has been under construction for years [KING *et al.* 2002]. Also, there are several individuals who build brass replica of certain instruments, or metal astrolabes in classical style without copying a specific model.

3.3 Description of the Astrolabe

The astrolabe consists of several distinct parts which must be present on any usable instrument. Their fabrication allows some artistic freedom, although their construction must adhere to strict mathematical rules. The construction of the astrolabe is based on the stereographic projection which was invented by HIPPARCHOS (2nd ct. B.C.).

The front side (Figure 3.1) is a predecessor of the planispheric star map which is still widely used by today's amateur astronomers. On a modern planisphere, a transparent plastic sheet with a horizon mask rotates over a map of the sky visible for a certain geographical latitude, with the celestial pole of the respective hemisphere as map center. Scales on the borders of both disks allow the user to align a time of day with the date of interest, and the horizon mask then shows the sky visible at that date and time. In contrast, on the astrolabe, the horizon table is on the lower, fixed disk, while the star map rotates above. Durable transparent materials were not available for astrolabes, so the star map was constructed in a grid-like fashion, hence its name *rete* (lat. "(spider-)net"; yellow in Fig. 3.1). The star map must include the annual path of the Sun (ecliptic), which by the stereographic projection is mapped onto a circle that lies excentric on the *rete* and shows degree marks for the signs of the zodiac. The stars are marked as end points of pointers, arrows, flames, leaves or similar shapes which grow from the struts of the *rete*. A disadvantage of the stereographic projection is the high degree of distortion far from the center of projection, so the star map on the astrolabe was almost always limited to the range of declinations the Sun can reach, and the (usually) southern part of the sky was missing.

The horizon tablet had to be constructed for the geographic latitude of the observer, so most astrolabes have several interchangeable plates, or *tympan*s, which are all stored inside the flat cylindrical body, or *mater*, of the instrument. Only one *tympan* is visible at a time, and can show an — at first glance — exceedingly rich assortment of circle arcs, which are explained in section 3.4.2 below.

On European instruments, above the *rete* there was a rule, or *index*, helping to read the various marks.

On the back, astrolabes showed a variety of additional scales and nomograms. The only compulsory scale was an *altitude scale* on the outer border, which together with the backsight, or *alhidade*, allowed measurements of stellar or solar altitudes. Other scales are described in section 3.4.4. Almost always, inside this there is a diagram consisting of two circles: zodiac and calendar, which allows to read the Sun's position in the zodiac for every date of the year. Also standard inventory, the *shadow square* in the lower part allowed simple trigonometric distance or altitude measurements for terrestrial surveys. Additional nomograms allowed the direct determination of the *unequal hour* (see section 3.4.2) from a measurement of solar altitude, or a conversion between *equal* and *unequal hours*.

To determine time, a stellar or solar altitude was measured, then the *rete* was rotated until the star pointer or solar position on the zodiac was on the correct *almucantar*. The *index* was placed on the solar position on the ecliptic and pointed to the correct time on the *limbus*.

The original astrolabes were typically made from wood, pasteboard or, for wealthier customers, brass plate. The plain drawings were transferred and engraved or etched on the plate, then the outlines had to be cut, and the parts were assembled on a central axis, so that *rete*, *index* and *alhidada* could be rotated.

3.4 Implementation of the Astrolabe Construction

All parts of the astrolabe have been implemented as a set of native EPS (Encapsulated PostScript) graphic files. Aside from still being a *de-facto* standard in the printing domain, PostScript is a Turing-complete programming language in its own right, and is reasonably simple to be used directly, without the help of another program that would precompute auxiliary values, for the generation of 2D graphics when nothing more is required and the final image is mostly prepared for print. The astrolabe is in its essence a flat model of the heavens and is entirely constructed of straight lines and circle segments, which are also available as native PostScript operators. Moreover, PostScript provides clip and fill operators, so that an area bounded by a defined path can be either excluded from further change, or filled with a single colour (or a colour gradient, or even a pattern). Native PostScript programming is in fact everything that is required to create the intricate line art typical for this kind of instrument.

Typical EPS files consist of two parts: A preamble which defines *dictionaries* (collections) of higher-level drawing functions typically provided by an application's EPS export filter and *font dictionaries* (typeface descriptions), which may be repeated in every EPS exported from that application, and then the *page description* (commands for drawing the actual image) itself.

In our case, the EPS files consist of three parts: at the start of the file, a configuration block allows the setting of a wide variety of parameters that activate the required features and influence their final appearance. For example, geographic latitude is the key parameter that controls the final result of the horizon plate (see Fig. 3.5). Or, depending on whether the user wants to create a "Western" (European) or "Eastern" (Islamic) instrument, different diagrams can be selected for the back, with some more switches that influence details in the finally drawn diagrams. Star positions and the calendar will be computed for the epoch requested. The pastel colouring, if activated, emulates the 17th century style of coloured copperplate-printed astrolabes. Also linear distortions caused by some printers can be compensated by prescaling factors, so that circles will be printed correctly.

Then follows the part where numerous procedures are defined. Some are purely general astronomical computations after MEEUS [1998], others fulfill generalised high-level PostScript drawing operations like typesetting of letters along a circle, and finally there are plotting functions that draw the required diagrams and make use of the previously defined functions.

The final part is again the actual page description, which, by evaluation of the configuration variables, calls the required plotting functions with the correct parameters.

From today's point of view, the construction is simple and requires only secondary-school mathematical capabilities. Modern descriptions on the geometrical construction can

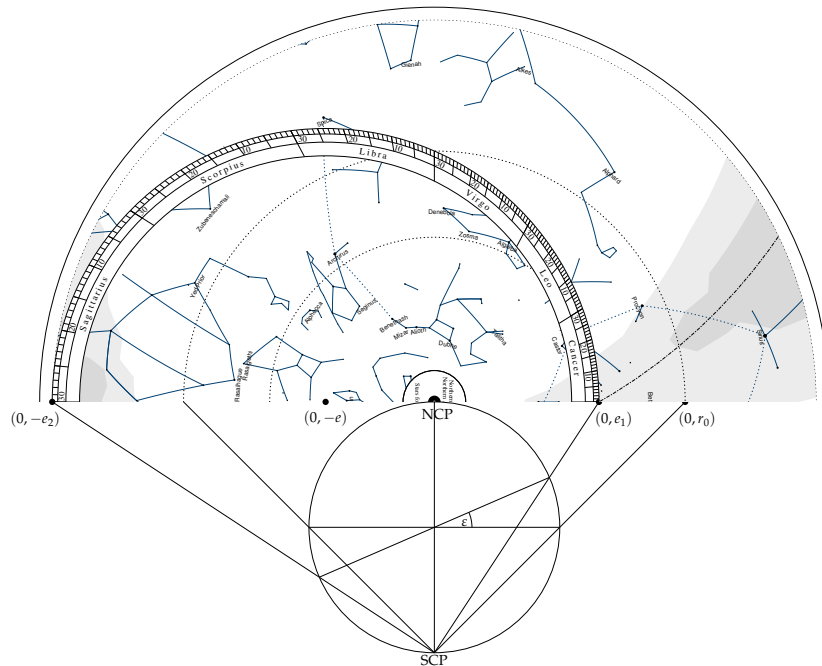


Figure 3.2: *Rete*: Stereographic construction. For demonstration, the image is rotated clockwise, and half of the tangential plane is also shown face-on with a modern-style star map.

be found in the books by MICHEL [1947] and SAUNDERS [1984]. Still, for the sake of completeness, in this section, many of the necessary formulae, dimensions and procedures are also given. Because the instrument is constructed geometrically, the conceptually simple projection of the star map (*rete*) will be the first part described, followed by the horizon plate (*tympa*) and the rear side. The combination of all elements was the ingenious invention of late antiquity whose creator is not known.

3.4.1 The star map, or *rete*

The construction is performed with the aid of a sphere (the celestial sphere) and a tangential plane, usually on the North Celestial Pole (Fig. 3.2; the rare *southern projection* uses a tangential plane on the South Celestial Pole, and such an instrument can be created as well. Medieval astronomical clocks like the Prague Orloj usually used this kind of projection). The celestial sphere is seen from the outside, and from the point where the Sun is placed at the beginning of spring (vernal equinox). The ecliptic (annual path of the Sun) therefore is shown projected as an inclined line. The angle of inclination is the *obliquity of the ecliptic*, about $\varepsilon = 23.44^\circ$, but slowly changing in time, with a value closer to 24° seen in antique sources. (See e.g. MEEUS [1998, ch. 22] for details.)

With the eye point on the South Celestial Pole (SCP), draw lines through the equator endpoints to mark radius r_0 , and to the extrema of the ecliptic diameter to mark radii e_1 and e_2 on the tangential plane. These three radii are the most important sizes on the astrolabe, and their ratio depends on the exact value of ε . When the projection sphere has radius $r = 1$,

the other dimensions can be derived from triangular relations as

$$r_0 = 2 \qquad e_1 = \frac{2 \cos \varepsilon}{1 + \sin \varepsilon} \qquad e_2 = \frac{2 \cos \varepsilon}{1 - \sin \varepsilon}. \quad (3.1)$$

Next, we draw the projection of the ecliptic, *i.e.*, a circle of radius $r_e = \frac{e_1 + e_2}{2}$ around point $(0, -e)$ where $e = \frac{e_2 - e_1}{2}$. Along this circle, the Sun moves during the year by about one degree per day. The ecliptic has to be partitioned into the 12 signs of the zodiac and marked for each degree of *ecliptical longitude* λ . However, because the circle is not centered in the center of projection, the partition is irregular. The coordinate that is mapped regularly as polar angle around the center of projection is the *right ascension* α , which is the longitudinal coordinate of the celestial equatorial coordinate system. So, for each $\lambda \in [0...359]$ we set a mark on the ecliptic circle at $\alpha = \arctan \frac{\sin \lambda \cos \varepsilon}{\cos \lambda}$. Every 30 degrees represent one sign of the zodiac, which are labeled accordingly with names and/or symbols (Table 3.1), if available.

Because the stereographic projection causes strong distortions for areas on the sphere far from the tangential point, the star map usually is cut off at the southern solstice radius e_2 .

Stellar Positions

A star map would be incomplete without stars. While their *right ascension* α maps directly to polar angle counterclockwise from the First Point of Aries Υ , their *declination* (latitudinal coordinate) δ maps to radius $r_\delta = \frac{2 \cos \delta}{1 + \sin \delta}$. If we just want a functional model and print the *rete* on transparent material, we can now draw a star map in today's usual style, representing the constellations with stick figures and star symbols of different sizes, depending on their magnitudes (brightness), like in the top half of figure 3.2. Note that also the lines connecting the stars are parts of great circles and thus project as circular arcs, not simply straight lines.

However, the classical astrolabe was made from metal or wood, so we must construct a *rete* as fretwork or tracery that allows to see the underlying *tympan* for operation. Depending on instrument size, about 10 to 30 stars should be included on such a *rete*. This is the part that allows most artistic freedom but needs most manual decisions, however, so that many different styles of *rete* artwork are possible.

As a design aid, we first can print the modern star map that includes the ecliptic circle. As mechanical requirement, we have to find a way to connect the ecliptic circle to the rotational center (pole). Most classical instruments therefore provide a horizontal strut from Υ to the First Point of Libra Ω . Also frequently seen are an outer circle along e_2 , and a part of a circle that follows the equator. Apart from these elements, we can now freely add struts that should run through parts of the sky map so that no bright stars are occluded. The struts can be straight or form a complicated tracery, but they should be balanced so that the center of gravity is still the center of rotation, because a disbalance will cause errors when the astrolabe is used for an altitude measurement and should hang vertically.

Table 3.1: Symbols for the Signs of the Zodiac

Υ	Aries	Ram	\mathcal{Q}	Leo	Lion	\nearrow	Sagittarius	Archer
δ	Taurus	Bull	\mathfrak{M}	Virgo	Virgin	ζ	Capricornus	Capricorn
Π	Gemini	Twins	Ω	Libra	Scales	\mathfrak{A}	Aquarius	Waterman
\mathfrak{C}	Cancer	Crab	\mathfrak{M}	Scorpio	Scorpion	✶	Pisces	Fishes

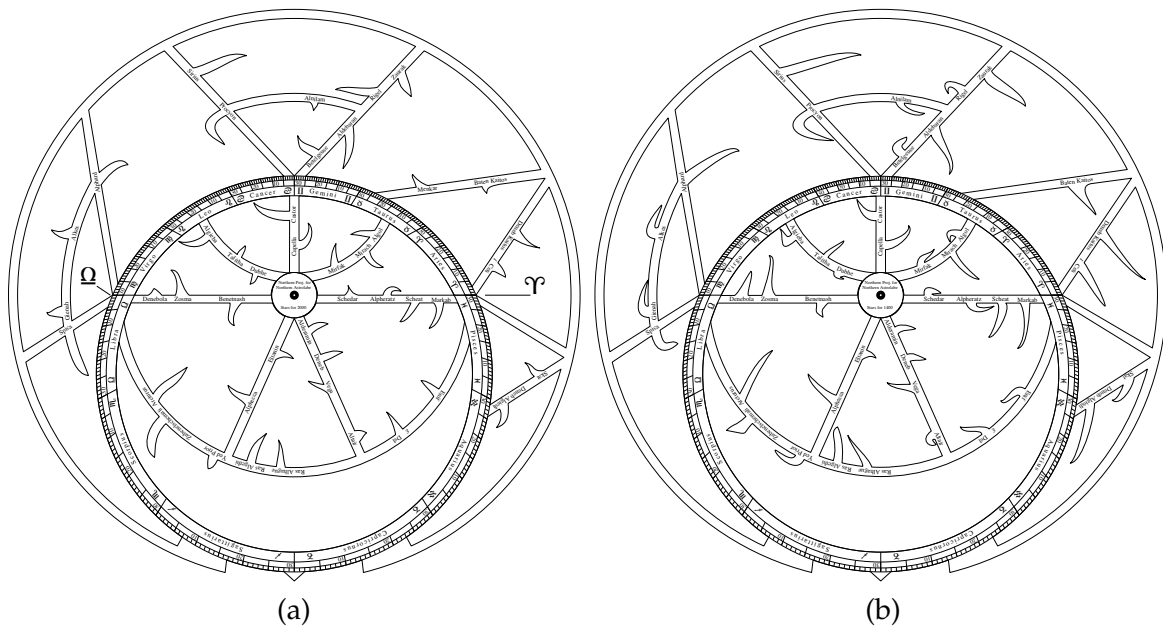


Figure 3.3: *Rete*: (a) designed for the epoch 2000. – (b) with star positions automatically subject to precession, the basic *rete* design can be used for several centuries (here: 1400), but with some aesthetical limitations. Note, *e.g.*, the elongated star pointers on the right side, where also some stars have crossed the carrier fretwork. Some star pointers must be deactivated while stars hide behind the carrier fretwork.

From the auxiliary struts or tracery, we can now grow the star pointers, which, depending on the overall style, are usually formed as flames or leaves.

Precession

As already mentioned in section 1.2.3, stellar positions are not fixed for eternity, but over decades and centuries change, due to the stars' proper motion, but much stronger and faster mostly due to precession, caused by the wobble of the Earth's axis and visible as slow shift (1 degree in about 72 years) of all stars parallel to the ecliptic. Therefore, any *rete* will be outdated within a few decades after production. Here a key advantage of the procedural modelling approach comes into play: The star positions are computed from stellar coordinates which are stored inside the EPS file for a standard epoch, and a configuration variable in the file header is set to the year of interest, so that coordinates for that year are computed by the PostScript interpreter, from which the points on the *rete* are finally derived. The pointers on the instrument presented here are defined as pairs of native PostScript spline curves, where the roots are at fixed locations on the *rete* struts (a manual design decision), the end-points are the star positions which are subject to precession, and the control points, which are chosen with artistic freedom so that the whole star pointer shows an elegant sweep, are subject to half the precession effect.

But even with this generalisation, a single *rete* tracery design can only work for a few centuries at best: if we leave the roots of the star pointers at fixed positions on the struts, precession would for epochs too far from the design epoch distort the star pointers into an unelegant shape (Fig. 3.3(b)), and sometimes the star positions cross the *rete* struts. For an

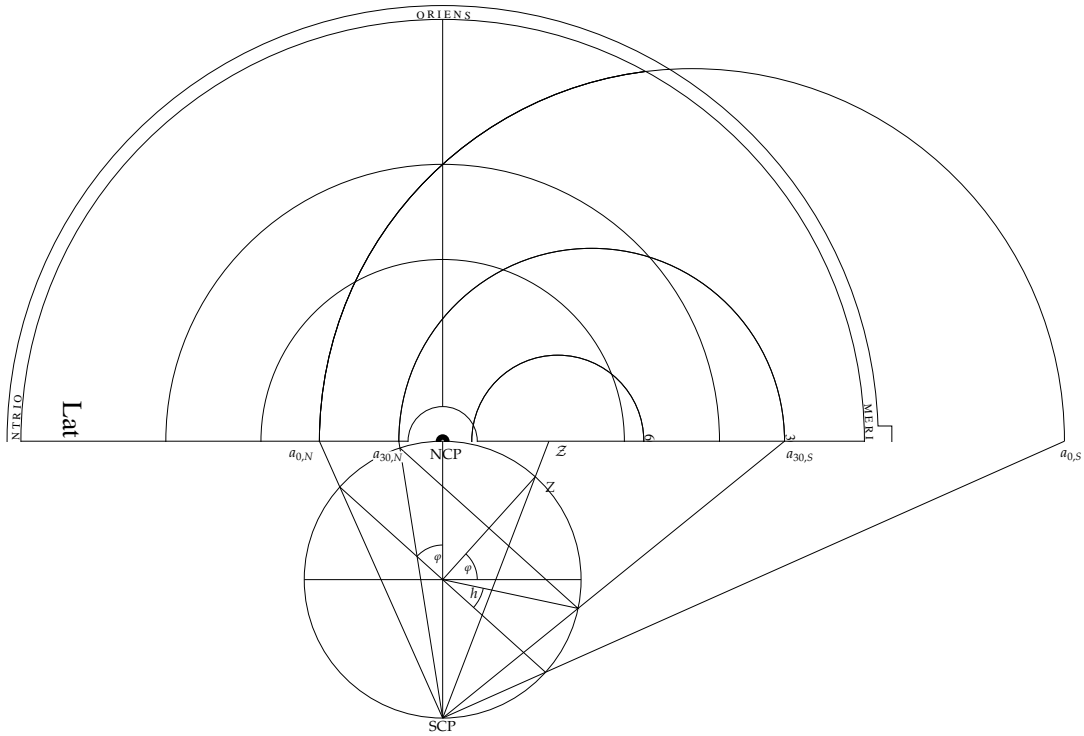


Figure 3.4: *Tympan*: Stereographic construction of altitude circles.

instrument far from the design epoch, the star pointers must therefore have to be rooted at different positions on the struts, and even some struts may have to be relocated to avoid occlusion of a star. Obviously, selection of the respective root points depends on the epoch parameter.

3.4.2 The horizon plates, or *tympan*s

The astrolabe's second essential part is the horizon tablet or *tympan*, which has to be constructed depending on the geographical latitude φ where the instrument shall be used. All lines on classical *tympan*s are constructed geometrically, so individual instruments differ only in the selection of line categories and their densities, which can also be selected in the file header. For classical instruments, the execution of this drawing required mathematical-geometrical skills and care from the craftsman, and has also been very time consuming and therefore costly. To increase usability, most astrolabes contain several exchangeable plates constructed for different latitudes, further increasing the work effort. In contrast, because the line art is encoded in constructional procedures, the program presented here will immediately “draw itself” to provide a correctly constructed plate for any latitude required.

Horizon, altitude and azimuth circles

The basic construction of the horizon plate starts in the same way as the construction of the *rete* to find circles r_0 , e_1 , e_2 . The observer is located on the surface of the Earth, which is seen in the center of the celestial sphere. Because the latter sphere is regarded to be of infinite

radius, the observer's horizon, a tangential plane on the Earth's surface, is reduced to an inclined plane through the sphere's center (Fig. 3.4).

Again, we draw lines through the extreme points of this horizon diameter on the sphere to reach points $a_{0,N}$ and $a_{0,S}$, the north and south points, respectively, of the horizon circle. Note that the southern point of the horizon usually lies outside of the final figure.

From figure 3.4, we find

$$a_{0,N} = -\frac{2 \sin \varphi}{1 + \cos \varphi} \quad a_{0,S} = \frac{2 \sin \varphi}{1 - \cos \varphi} \quad (3.2)$$

$$a_0 = \frac{a_{0,S} + a_{0,N}}{2} \quad r_{a_0} = \left| \frac{\sin \varphi}{1 - \cos \varphi} + \frac{\sin \varphi}{1 + \cos \varphi} \right| \quad (3.3)$$

and draw the part of the circle that lies inside e_2 . Similarly, to draw a circle, or *almucantar*, for altitude h above the horizon, we first draw its projection in the celestial sphere, then project its extreme points from the SCP towards the projection plane to find the intersections from which the circle can be drawn.

$$a_{h,N} = \frac{2 \sin(h - \varphi)}{1 + \cos(h - \varphi)} \quad a_{h,S} = \frac{2 \sin(h + \varphi)}{1 - \cos(h + \varphi)} \quad (3.4)$$

$$a_h = \frac{a_{h,S} + a_{h,N}}{2} \quad r_{a,h} = \left| \frac{a_{h,S} - a_{h,N}}{2} \right| \quad (3.5)$$

Usually, only positive altitudes are drawn with a step width fitting the instrument's size. However, traditionally, up to three *twilight lines* for $h \in [-6^\circ, -12^\circ, -18^\circ]$ can be found below the horizon circle, defining the civil, nautical or astronomical times of twilight. In PostScript, it is easy to not only draw these circles as lines, but we can fill the regions with approximate twilight colours (Fig.3.5 (a)).

Unequal Hour Lines

Today one hour is understood as 1/24 of the mean solar day. In antiquity and the Middle Ages, however, several systems of reckoning time were used in parallel. The hours we use today were called *equal hours* or *equinoctial hours*. In the system of *unequal hours*, the bright day (from sunrise to sunset) was split in twelve parts of equal length, as was the night. In summer, daylight hours were thus longer than nighttime hours, and *vice versa* in winter. At the equinoxes, day and night hours were of equal length, hence the names *equal hours* or *equinoctial hours* for the hours that we use today. The *unequal hours* of day or night were counted from sunrise or sunset, respectively, and were the more important system for daily life. The astrolabe is capable of determining at least these two systems of time. Only when mechanised clocks were introduced and were usually capable of displaying only the equal hours, the other traditional systems were abandoned within a few decades [ZINNER 1967, p.17].

Although the Sun is needed to determine the unequal hour, the lines are usually drawn not in the part of the *tympan* above the horizon, but in the lower part, to avoid further cluttering of the already dense mesh of arcs in the area representing the sky. To read the daytime, the *solar nadir* (antisolar point) was found on the ecliptic opposite the real position with the use of the *index*.

The traditional way of construction for the unequal hour lines was as follows: first, the parts of the circles e_1 , r_0 and e_2 that lie below the horizon were split in twelve parts of equal

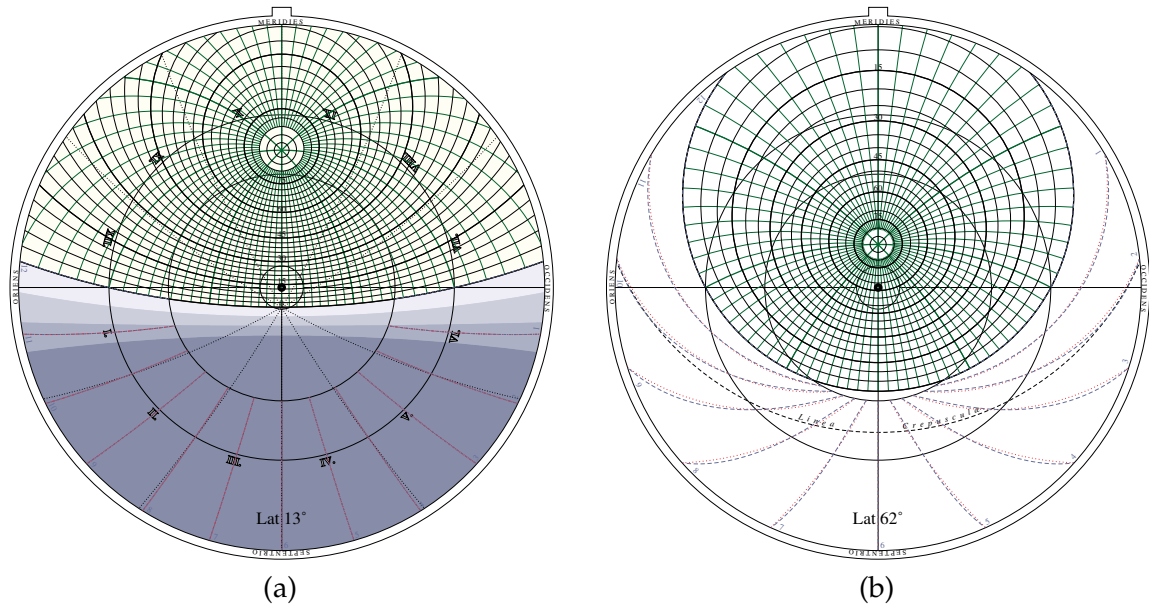


Figure 3.5: *Tympans* examples for latitudes 13° and 62° , with different features activated. (a) The traditional engraved line art is enhanced by background areas that indicate the twilight zones. The shape of the fill areas results from successive applications of the PostScript clip operator with simple circular paths that also produce the almucantarats (altitude circles). — (b) this figure shows the different results for the Unequal Hour lines for traditional approximate (dotted red) and correct (dashed blue) construction for latitudes $\varphi > 50^\circ$.

length. Then, each corresponding triplet of split points was connected with a circular arc. Although this is just an approximation of the correct solution where the diurnal circle for every declination should be split in twelve parts, the error is in the range of the line width up to about latitude $\varphi = 50^\circ$. This similarity can be best shown by comparing approximate and correct lines on the same *tympans* (see Fig.3.5 (b)).

Two other time reckoning styles counted equal hours from sunrise (*horae ab ortu*), or sunset (*horae ab occasu*), respectively. Such hour lines are just copies of the horizon rotated by 15 degrees per hour and can be seen as red and blue arcs in the lower part of Figure 3.1.

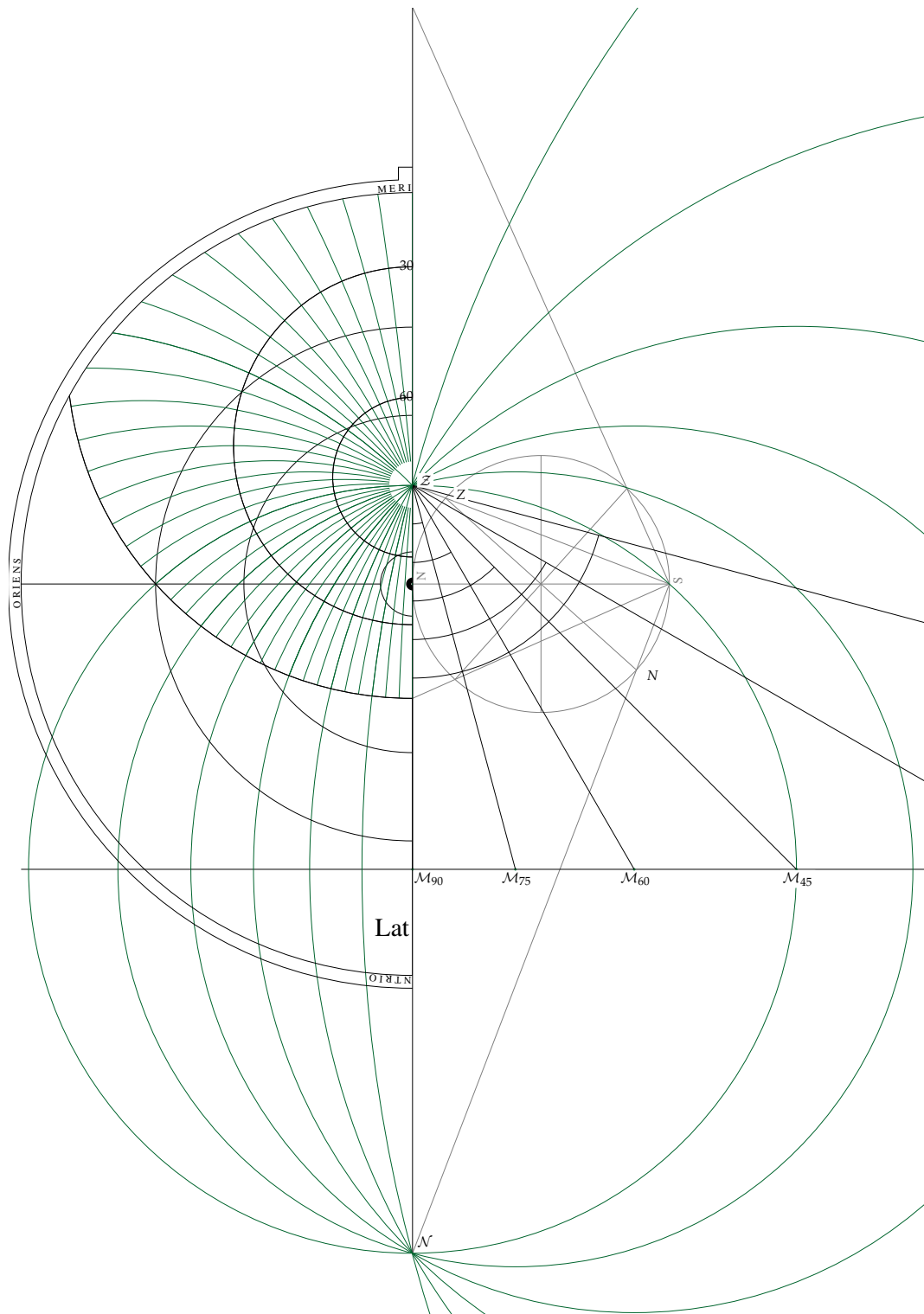
Azimuth Circles

The construction of the azimuth circles is a bit more complex (see Figure 3.6).

All azimuth circles A run through zenith and nadir, intersect the almucantarats at right angles, and therefore are centered along a line orthogonal to the meridian line and bisecting it between zenith $\mathcal{Z} = (0, \mathcal{Z}_y)$ and nadir $\mathcal{N} = (0, \mathcal{N}_y)$. With the lengths found by projection:

$$\mathcal{Z}_y = \frac{2 \cos \varphi}{1 + \sin \varphi} \quad \mathcal{N}_y = -\frac{2 \cos \varphi}{1 - \sin \varphi} \quad \mathcal{M}_{A,y} = \frac{\mathcal{Z}_y + \mathcal{N}_y}{2} \quad r_{90} = \mathcal{Z}_y - \mathcal{M}_{A,y}$$

we draw circles around $(\mathcal{M}_{A,x}, \mathcal{M}_{A,y})$ with $\mathcal{M}_{A,x} = r_{90} \tan(90^\circ - A)$ and radius $r_A = \sqrt{r_{90}^2 + \mathcal{M}_{A,x}^2}$.

Figure 3.6: *Tympan*: Construction of azimuths.

Astrological House Circles

The astrolabe was also the tool of astrologers who determined the location of celestial objects in sections of the sky named *houses*. One system which is easily constructed on the astrolabe, is usually attributed to REGIOMONTANUS (1436–76), although its construction has been described already 200 years earlier [ZINNER 1967, p.141].

The equator circle is partitioned in 12 equal parts of 30 degrees (see Fig 3.7). Now, we plot circles through each of the partition points, and the north and south point on the horizon. One of these circles is equivalent with the horizon. The houses are usually labeled with roman numerals, and their order is against the daily apparent rotation of the sky.

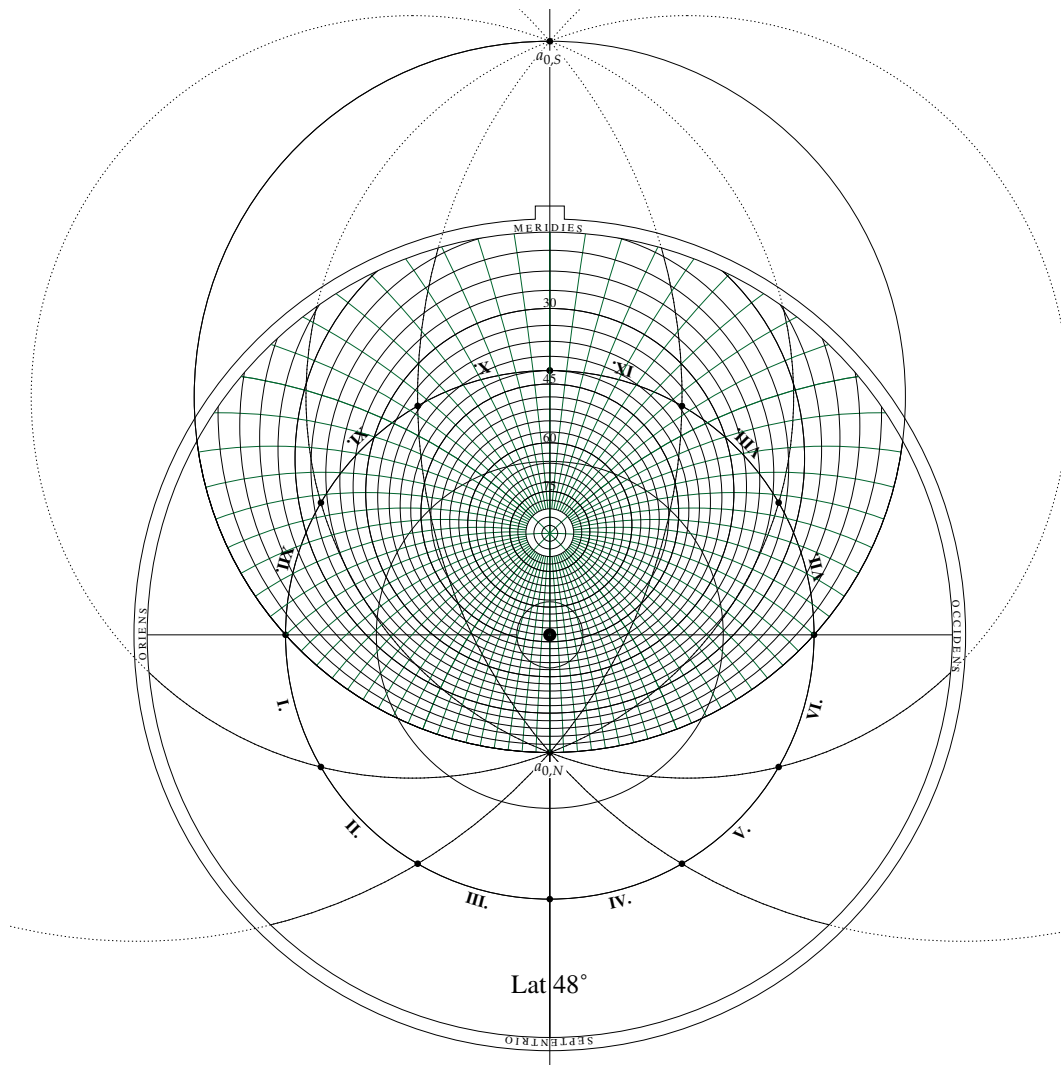


Figure 3.7: *Tympan*: Construction of *houses* after REGIOMONTANUS.

3.4.3 The case, or *mater*

This part consists of a flat disk and a thicker ring (*limbus*) with degree or time scales mounted on its outside. The flat disk serves as carrier for the engravings of the back, see section 3.4.4. The *limbus* is circular, but with a decorated protrusion (*throne*) where a shackle is attached, so that the astrolabe can be hung vertically for altitude measurements. This *throne* is often simple on European instruments, but very large and richly decorated with adorations or dedications on Islamic instruments. On the front side of the astrolabe, the *limbus* carries degree or time scales, or both. The time scale usually counts clockwise two times 1...12, with 12 on top. It is quite likely that the “clockwise” direction itself derives from the daily motion of the heavens on this instrument!

As a flat empty cylinder, the *mater* provides space for usually several *tympans*, or horizon plates (see section 3.4.2). The *tympans* should not rotate inside the *mater*, so they are fixed either by an additional peg or by a tongue that is inserted in a recession in the *limbus*. Over the topmost *tympant*, the *rete* rotates freely. Sometimes, the bottom of the cylinder is also engraved, and to work with this plate, the *tympans* have to be removed.

3.4.4 The back, or *dorsum*

The back of the astrolabe may carry a wide range of diagrams, and differs strongly between European and Persian instruments. We will describe the classical European diagrams shown in figure 3.8 and again refer to MICHEL [1947] or SAUNDERS [1984] for more details.

Altitude Scale

The *altitude scale* runs on the outer border of the astrolabe back and is used in combination with the *alhidade* (backsight) to measure altitudes. Usually all four quadrants are labelled in degrees, with zero on the right and left edges, and 90 degrees at both poles.

Calendar Circle

Inscribed, there is the *zodiac* with its regular partition into 12 signs, where each sign is labelled [1...30] separately. Typically, the beginning of spring where the Sun is located on the “head” of Aries Υ is drawn on the right edge, and the signs of the zodiac are counted counterclockwise.

Further inside, a *calendar circle* is drawn, which can be either concentric with irregular day marks, or excentric with regular day marks, to map the irregular speed of the (geocentric) Sun during the year. The placement of the excentric circle is determined from the length of the seasons [MICHEL 1947, p.76; NEUGEBAUER 1975, IB 1, 3B], and is also variable over the centuries.

The calendar and ecliptic have to be aligned properly so that for every day of the year the Sun’s position on the zodiac (ecliptic longitude λ) can be determined. For an instrument that shows the Julian calendar (*i.e.*, all instruments built before 1582, and still many built after that year), spring begin ($0^\circ\Upsilon$) was not on March 21, but up to 10 days earlier. The exact amount of the required rotation is again computed from astronomical literature [MEEUS 1998].

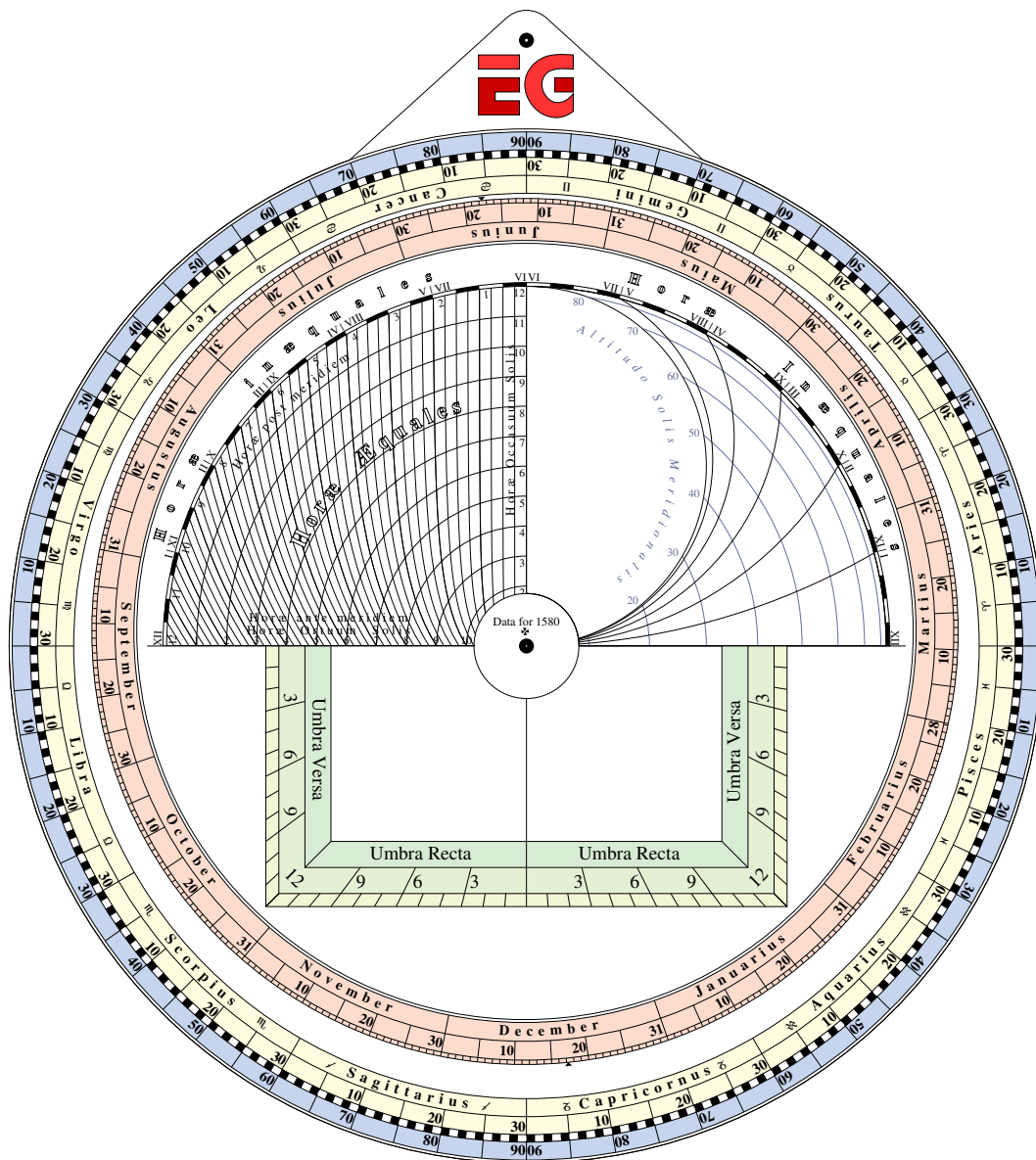


Figure 3.8: *Dorsum*: Typical late-16th century instrument.

Shadow Square

The *Shadow Square* (green in Figure 3.8), with its sides usually split regularly in 12 or 7 parts, basically is a tangent scale for altitude measurements, and illustrated instructions for simple trigonometric surveys can be found in contemporary literature [e.g. STÖFFLER 1513].

Unequal/Equal Hour diagrams

The *Unequal Hours Diagram* in the right upper quadrant provides a direct way to determine the unequal hour from a single measurement of solar altitude. Sometimes, this diagram alone was drawn on a quadrant to form an instrument of its own. The quadrant for *Unequal/Equal Hours Conversion* (Figure 3.8, upper left) can be found mostly on later instruments.

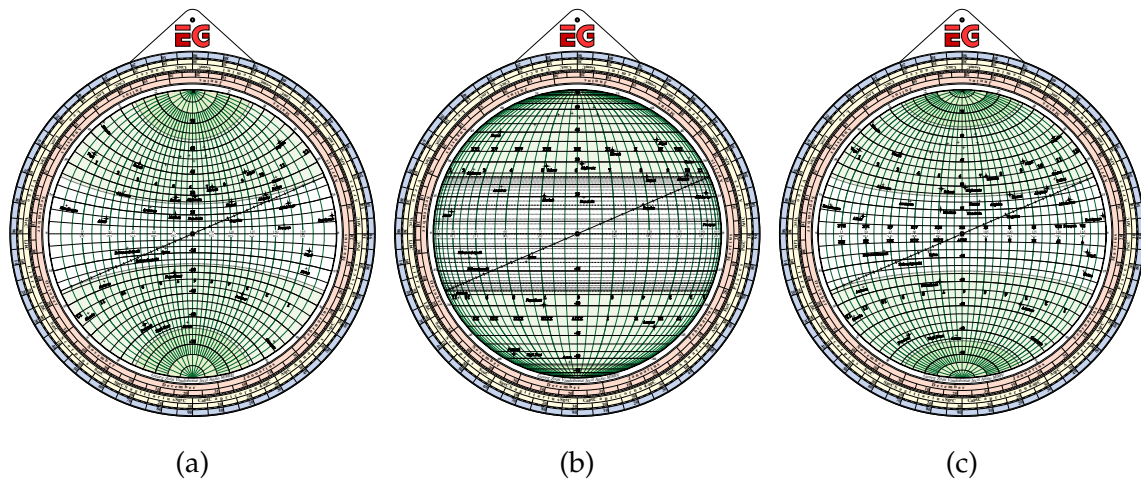


Figure 3.9: Universal astrolabes: (a) Saphaea Arzachelis (stereographic) – (b) orthogonal projection after DE ROJAS – (c) optimally spaced grid after DE LA HIRE.

3.4.5 Universal Astrolabes

An important group of instruments with modified backs are *Universal Astrolabes* which come in 3 different versions and do not need a tympan for every latitude, but are capable of solving problems for any latitude, although they are generally more difficult to operate (Figure 3.9). The projection generally is executed with the celestial sphere seen from the First Point of Aries Υ , but with different eyepoint distances.

3.4.6 Persian Astrolabes

The classical Persian astrolabe design includes several other diagrams that suited everyday needs of Muslim believers, like determination of prayer times and the prayer direction (Figure 3.10).

3.5 Applications of the Model

The diagrams described in the previous chapter were programmed as PostScript graphics files (EPS), promising high portability in other graphics applications, and computational precision for all mathematically constructed lines, which is hardly achievable by manual construction in a common graphics editor. Also, by tweaking the provided configuration variables, it is possible to produce a variety of horizon plates (*tympan*s) for any latitude, or an instrument with star positions for any period within several centuries around 2000.

For practical demonstrations of such instruments to a wider audience, the cheapest solution is a simple print on cardboard as has also been done in the original period, where the *rete* can now also be printed on an overhead slide. For higher durability, such an instrument can be laminated. Better for handling and practical experience, however, is the production of rigid instruments.

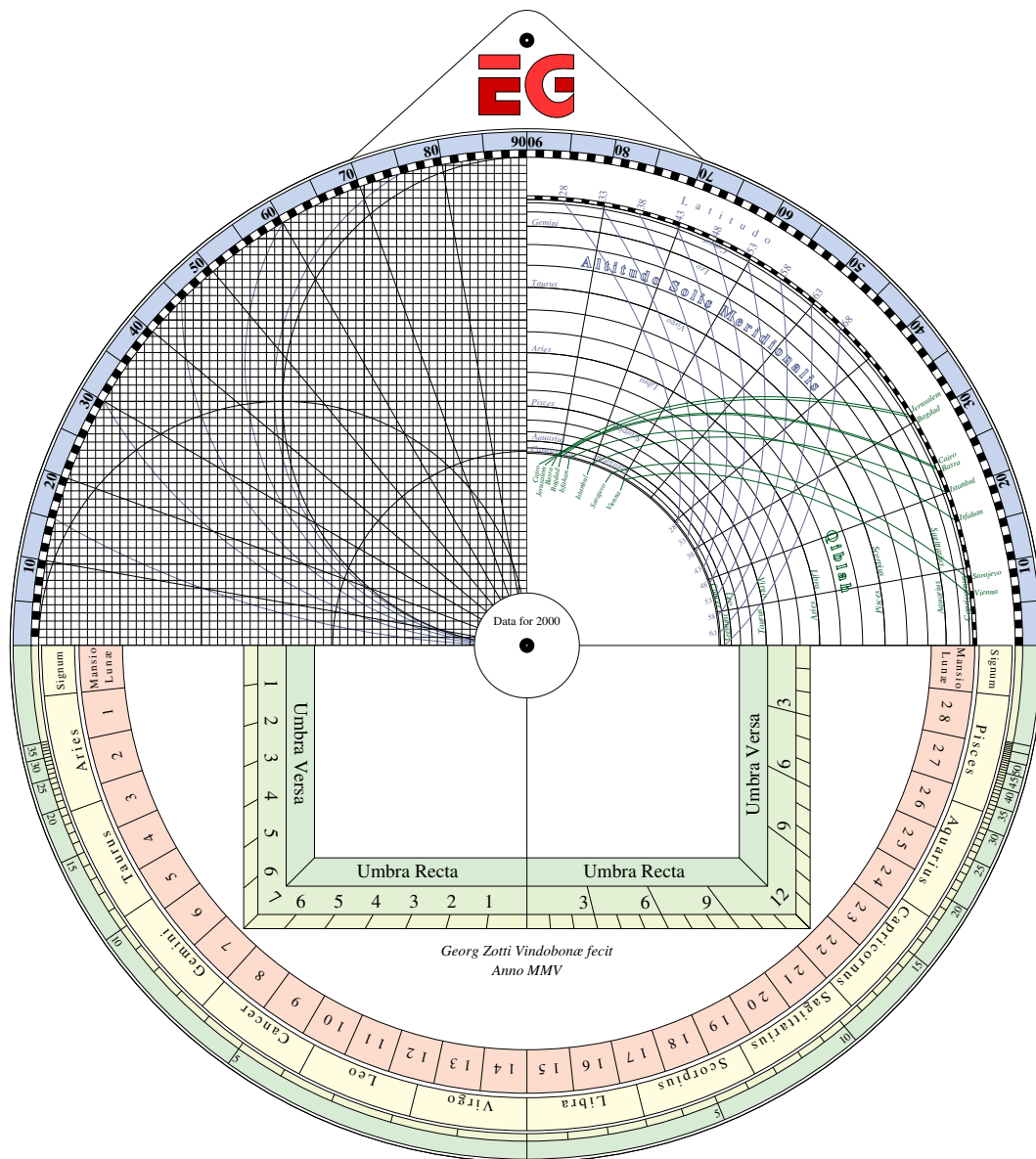


Figure 3.10: Persian back. The top right quadrant allows the determination of solar noon altitude from date and latitude, and – for a selection of locations – the determination of the time (expressed as solar altitude) when the Sun is visible towards the direction of Mecca. The top left quadrant provides a sine tablet, and the bottom half shows a solar calendar (yellow), lunar mansions (red), and the shadow square with extended tangent scale (green).

3.5.1 Production for Hands-On Experience: Cardboard and Laser Woodcutting

A 2kW CO₂ laser engraver/cutter with xy table proved to be an ideal tool for our purposes. It works in two modes of operation: First, the line art is burned into the material in a scanline mode, then the contours of the parts (with a certain colour code) are cut in direct xy pen plotter mode. The line style of contour lines of the astrolabe are defined in the cutlines procedure, which is redefined when the lasercut switch is active. Also, the setting of lasercut invalidates any colour settings or fill operations. Unfortunately the machine is not powerful enough

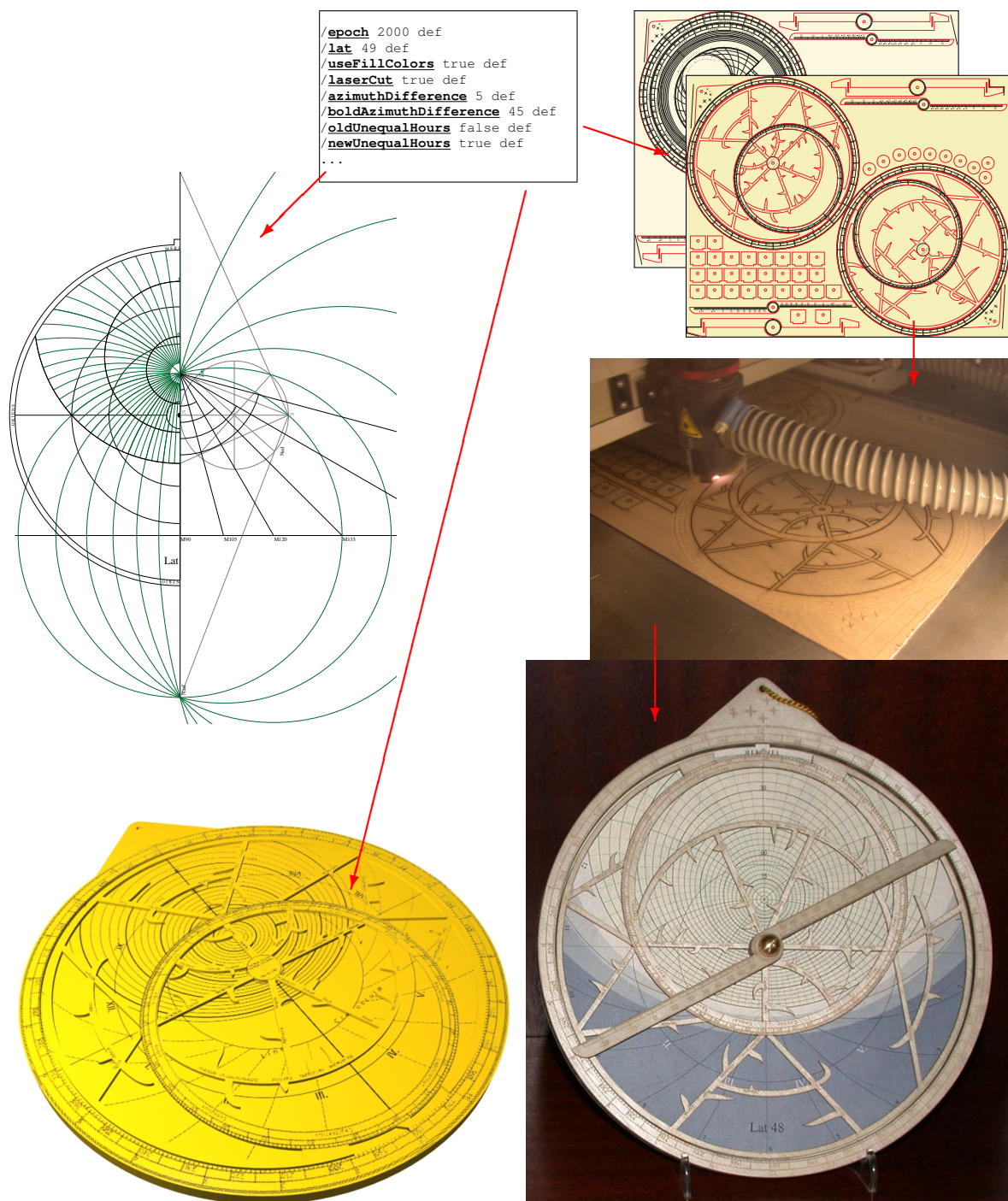


Figure 3.11: The procedural astrolabe implementation can be used for a multitude of purposes, from technical illustrations to 3D models and even to control a laser engraver/cutter for the production of working instruments.

to cut metal, so it was decided to use modelling plywood as base material. All parts were imported into a standard vector graphics drawing program, and the machine was used as printer, where the driver dialogue in this case also controls different laser power and pulse settings for different materials. The sequence of cutting operations is directly taken from the EPS file, so that the necessary care can be taken that the machine first cuts holes, then the outline. The engravings are done in quite high resolution (300 or 600 dpi), which takes however more than an hour for an A3 sized wood plate. The lasercut wood parts have to be further assembled: the *mater* is produced by gluing the *limbus* onto a spacer ring of equal size and further to the back plate, then the outer border is smoothed with abrasive paper. All wooden parts are painted with wax varnish, then polished, giving an esthetically pleasant shimmer and protection from dirt.

The *tympan*s are printed on a regular colour laser printer on decorative paper, so that many different tympan for different latitudes can be provided inside the *mater*. A decorative screw is used as polar axis to keep all parts together.

3.5.2 3D Modelling

The EPS programs can also be used as basis for 3D models for various computer graphics applications in the cultural heritage domain, from interactive scientific museum installations to applications in games in a medieval setting. The transformation into a 3D model is currently done in standard 3D modelling software, where bitmaps of the drawings can be used as textures and bump/displacement maps alike (the engraved lines were usually filled with dark ink), and the outline curves are extruded into flat objects (Figure 3.12). The components are joined along the axis, where *rete*, *index* and (on the reverse side) *alhidada* can rotate.

3.6 Discussion

In this chapter a procedural modelling approach was presented for a computer graphics reconstruction of the most important astronomical instrument of the Middle Ages. This approach, based on a functional implementation of the required diagrams, provides several advantages over a more traditional construction that would follow the classical construction manuals with their tabulated values and would typically be performed with a graphical editor.

The instruments presented here are not reproductions of existing old instruments. They show an original design, which however must follow the basic construction principles of the stereographic projection. For simpler use or explanatory purposes, a modern star map on overhead transparency can replace or augment the classic *rete*, and a wide variety of printed paper horizons (*tympan*s) can be included in the *mater*.

In case an artist would want to recreate an old instrument or a particular design of his own, the procedural approach can still help to construct the lines and dimensions required by the mathematical construction. The detailed artistic execution for a particular instrument, e.g., ornamenting of the *throne* or a particular *rete* design, may then be done in a graphical editor after the procedural EPS file has been imported.

To test star coordinates for instruments of medieval times, old star catalogues from the literature [BRUNOLD 2001; KUNITZSCH 1966] have been entered, and a modern-style star map can easily be plotted for any of them, so that a researcher of old manuscripts could

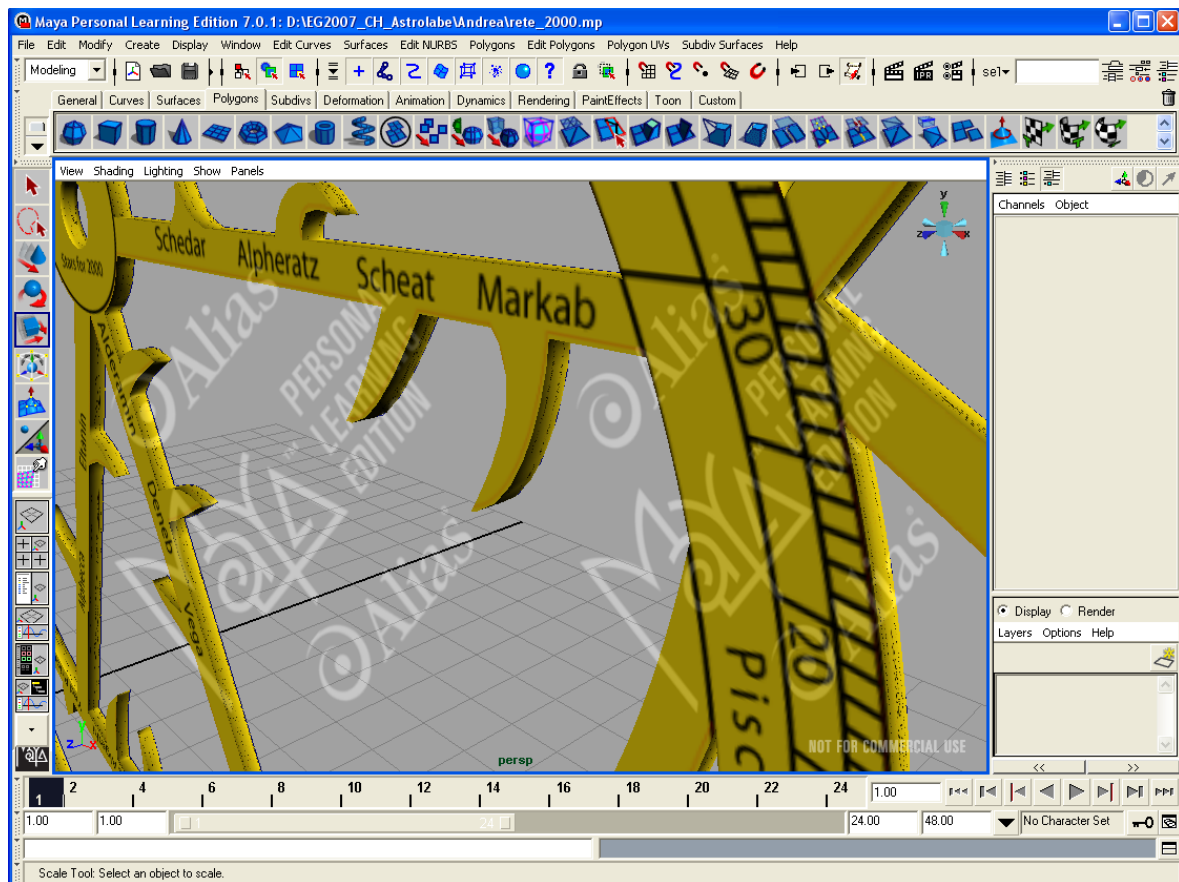


Figure 3.12: The *rete* in a 3D modelling program.

have an instrument at hand that provides the same functionality, coordinates and data (albeit different appearance) as the original author probably had when writing.

The procedural modelling approach is of course not limited to astrolabes, but applicable to all similar devices, like quadrants or sundials. Obviously, when done in PostScript, the astronomical functions can be re-used, and only the page description must be adapted to the respective instrument.

Chapter 4

Modelling Skylight with Computer Graphics

The eye is very forgiving with regard to variations in absolute color, but much more demanding of correct relative colors; hence the base color of the sky is of little importance, as long as it is a reasonable shade of blue.

— R. VICTOR KLASSEN [1987, p.226]

The blue sky must have fascinated humans since prehistoric time, and early philosophers and artists have proposed countless descriptions and theories to explain the reasons for its appearance [HOEPPE 1999]. Frequent and less frequent phenomena have been described in textbooks [e.g., MINNAERT 1993; LYNCH and LIVINGSTON 1995].

However, the physical cause of its blue colour, *i.e.*, scattering of light on air molecules, could be explained no earlier than in the late 19th century with the works of Lord RAYLEIGH [1871, 1899]. His work was a fundamental requirement for all physically based skylight models. Since then, in the optics and physics literature, countless works have been presented on various topics of atmosphere physics, physical atmosphere modelling and of optical effects in the Earth's atmosphere, and, ultimately, this literature must be consulted also when we want to provide a physically based sky background for computer generated *images* of outdoor scenes.

On the other hand, there exist a few *analytical approaches* to skylight models, which try to provide a fast solution while still looking reasonably good, or fulfill practical purposes in illumination estimation.

The third possibility to include the sky into a computer graphics scene is based on *photography*, where the sky is captured with ultra-wide angle lens systems, and the photograph is then used as background and also to estimate illumination.

In this chapter, first the physical processes that most influence the appearance of the clear sky are presented also with papers from the atmosphere physics literature that seem relevant for the development and understanding of the topic, and then several important clear-sky models and methods of handling the sky as light source from the computer graphics literature are presented. Also, several papers on special atmospheric phenomena will be presented. The simulation of atmospheric effects caused by macroscopic particles like smoke, clouds or halos, is mostly out of topic, however.

4.1 Spectral Power Distribution of Sunlight

Many daylight models for computer graphics only provide tricolour (*e.g.*, RGB or CIE XYZ or Yxy) data. However, for applications in colour vision and rendering of industrial colours which may show metamerism, the spectral power distribution of sunlight and daylight has to be taken into account. An approximate solution is to model the Sun as black body of about $T = 5800$ K. However, the Sun is no real black body, and an accurate solar spectrum outside the atmosphere [*e.g.*, KURUCZ *et al.* 1984; KURUCZ 2005] (Fig. 4.1) should be preferred over a black-body spectrum. Then, all wavelength-dependent computations have to be performed for as many wavelengths as possible and required for the application.

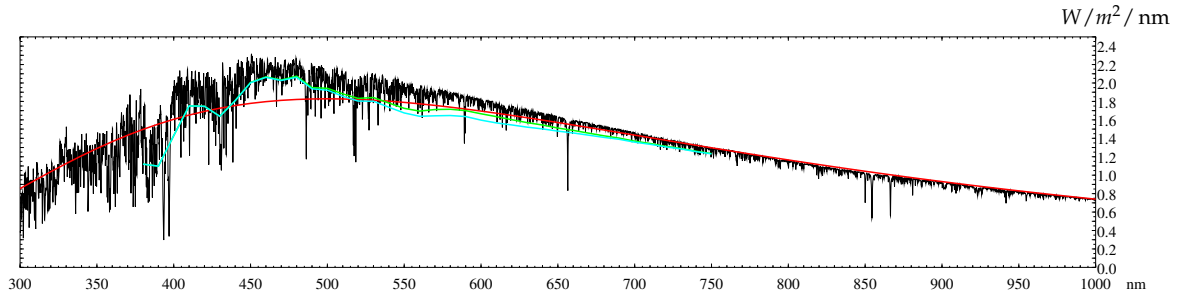


Figure 4.1: High-resolution solar spectrum with data from KURUCZ [2005] (black), compared to values from NAGEL *et al.* [1978] before (green) and after (blue) ozone absorption and a blackbody spectrum at $T = 5800$ K (red).

4.2 The Atmosphere

The Earth's atmosphere can be described as a shell of gas consisting of a mixture of about 78% Nitrogen, 21% Oxygen, Argon, water vapour, carbon dioxide, and traces of other gases. The mixing ratio of the main components (except water vapour, which is concentrated in the troposphere, *i.e.*, the lowest 11 km or so) can be regarded constant in all altitudes for our purposes.

Air can be approximated as ideal gas with

$$p = \frac{\rho \mathcal{R} T}{\mathcal{M}} \quad (4.1)$$

with mass density ρ , gas constant $\mathcal{R} = 8.314510$ J/mol K, the mean molecule mass for air $\mathcal{M} = 28.96 \cdot 10^{-3}$ kg/mol, and temperature T [K]. On the surface of the Earth, standard values used for many applications are $T = 288.15$ K and pressure $p_0 = 101325$ Pa [BRUTON 1996, p.11f].

The vertical concentration of pressure, molecule number density or dust can be described with an exponential density profile for altitude z ,

$$N(z) = N_0 e^{-\frac{z}{H_0}} \quad (4.2)$$

with the respective quantity at sea level N_0 and a *scale height* H_0 where the respective quantity has decreased by $1/e$. Models for the Earth's atmosphere usually use a scale height near 8000m for molecules (air) and near 1200m for aerosol particles.

The temperature profile of the US Standard atmosphere is shown in table 4.1.

Table 4.1: US Standard Atmosphere Temperature Gradients [after BRUTON 1996, p.34]

Height [km]	Temperature Gradient [K/ km]	Temperature difference from ground [K]
0	−6.5	−
11	0.0	−71.5
20	1.0	−71.5
32	2.8	−59.5
47	0.0	−17.5
51	−2.8	−17.5
71	−2.0	−73.5
84.8520	−	−101.2

4.3 Light and the Atmosphere

The atmosphere is the largest body of participating media that we can observe daily. Usually, we experience the air as transparent with hardly any interaction with light that falls through it. Only on longer distances, we detect its presence by colour shifts of distant objects caused by scattering (*aerial perspective*) or blurring and mirages by effects of *refraction* in the turbulent hot air near the ground. The most prominent effect of light interaction is however the blue colour of the daylight sky itself. Light passing through the atmosphere is influenced by several processes which are not easily computed, and, for the exact computation of radiation transfer, methods pioneered by CHANDRASEKHAR [1960] should be applied. However, the Earth's atmosphere is optically thin, and so several approximations are usually allowed that are described in this section.

4.3.1 Scattering, Absorption and Extinction

Scattering is the physical process of the interaction of electromagnetic radiation with matter, where a particle in the path of an electromagnetic wave takes energy from the incident wave and re-radiates it in all directions [LIOU 2002, p.6]. The accurate explanation is based on the Maxwell equations, but many effects can be described in a simpler way. Note that many of the terms described here depend on the wavelength, adding to the computational complexity.

Particles of different size cause different phenomena. The *size parameter* for spherical particles of radius a is

$$x = 2\pi a / \lambda \quad (4.3)$$

and helps to differentiate *Rayleigh Scattering*, where $x \ll 1$, from *Lorenz-Mie Scattering* (often just called Mie scattering), where $x \gtrsim 1$.

The scattered energy is usually not distributed isotropically. Spherical particles re-radiate the energy in an angular pattern symmetrically around the direction θ of the incoming wave. The angular distribution of the scattered energy is then expressed by the *scattering phase function* $P(\theta)$ [LIOU 2002, p.90], which is dimensionless and normalised so that

$$\int_0^{2\pi} \int_0^\pi \frac{P(\theta)}{4\pi} \sin \theta d\theta d\varphi = 1 \quad (4.4)$$

The *scattered intensity* of a single particle can be generally defined as

$$I(\theta) = I_0 \frac{\sigma_s}{r^2} \frac{P(\theta)}{4\pi} \quad (4.5)$$

with the incoming intensity I_0 , observer distance r , and the *scattering cross section* σ_s (units of area) describing the amount of incident energy removed from the incident direction by a single scattering event.

The loss of directed energy by scattering of light transiting a medium of *particle number density* N_s (number of molecules per unit volume) is governed by the *volume scattering coefficient* [m^{-1}]

$$\beta_s = \sigma_s \cdot N_s \quad (4.6)$$

In the visible range of wavelengths, air molecules instantly re-radiate all of the incident energy at the same wavelength. Larger particles like aerosol droplets also scatter energy, but also absorb some of it and re-radiate it in the infrared. For visual purposes, the light can be regarded as lost and be described similarly by the *absorption cross section* σ_a and *volume absorption coefficient* β_a . These values are tabulated in the literature [e.g. HESS *et al.* 1998a].

The *extinction cross section* is then given as

$$\sigma_e = \sigma_s + \sigma_a, \quad (4.7)$$

and the *volume extinction coefficient* as

$$\beta_e = \beta_s + \beta_a. \quad (4.8)$$

The *optical depth* is defined as [LIOU 2002, p.103]

$$\tau = \int_{s_0}^{s_1} \beta_e ds \quad (4.9)$$

and describes the total attenuation of incoming radiation I along a path s , so that

$$I_{s_1} = I_{s_0} \cdot e^{-\tau} \quad (4.10)$$

A measure of the clearness of the atmosphere is the *atmospheric turbidity* T , defined here as the ratio of the vertical optical depth of the atmosphere including aerosol to that of a pure-air molecular atmosphere:

$$T = \frac{\tau_m + \tau_{aer}}{\tau_m} \quad (4.11)$$

A (hypothetical) perfectly clean atmosphere has $T = 1$.

It is comparatively easy to compute optical depths between any two points in plane layered atmospheres, and many problems in radiative transfer are presented only for plane problems in the literature. However, the Earth's atmosphere is (roughly) spherical with exponentially decreasing density profile, and so typically optical depths have to be computed by numerical integration.

Rayleigh Scattering

Rayleigh scattering describes the scattering process by air molecules [RAYLEIGH 1871]. Incident radiation produces an electric field which generates a dipole configuration on the molecule and further causes oscillation of this dipole, which then emits a plane-polarised electromagnetic wave, so this light is inherently strongly polarised. Shorter wavelengths are scattered much more efficiently, which, together with the human visual system's rather low sensitivity to violet light, finally explains why the sky appears blue.

The scattering cross section of air molecules is given as

$$\sigma_s = \frac{24\pi^3}{\lambda^4 N_s^2} \left(\frac{m^2 - 1}{m^2 + 2} \right)^2 \frac{6 + 3\delta}{6 - 7\delta} \approx \frac{8\pi^3 (m^2 - 1)^2}{3\lambda^4 N_s^2} \frac{6 + 3\delta}{6 - 7\delta} \quad (4.12)$$

with the refractive index of air m , molecule number density N_s ($N_s = 2.54743 \cdot 10^{19} \text{ cm}^{-3}$ for standard air [BUCHOLTZ 1995]) and an *anisotropic factor* (or *depolarisation factor*) of $\delta = 0.035$ [LIOU 2002, p.93].

The Rayleigh phase function for unpolarised light is [LIOU 2002, p.90]

$$P_R(\cos \theta) = \frac{3}{4}(1 + \cos^2 \theta) \quad (4.13)$$

and is illustrated in Figure 4.2 (a).

The total scattered intensity of unpolarised sunlight of intensity I_0 incident on a molecule is then given as

$$I(\theta) = I_0 \frac{\sigma_s}{r^2} \frac{P(\theta)}{4\pi} = \frac{I_0}{r^2} \alpha^2 \left(\frac{2\pi}{\lambda} \right)^4 \frac{1 + \cos^2 \theta}{2} \quad (4.14)$$

where the *polarizability* is given as

$$\alpha = \frac{3}{4\pi N_s} \left(\frac{m^2 - 1}{m^2 + 2} \right) \approx \frac{1}{4\pi N_s} (m^2 - 1) \quad (4.15)$$

with the molecule number density N_s and the refractive index of molecules m close to 1 [LIOU 2002, p.89-93]. The *degree of linear polarisation* can further be given as

$$LP(\theta) = \frac{\sin^2 \theta}{\cos^2 \theta + 1} \quad (4.16)$$

and from this it is obvious that the maximum of polarisation is in the plane 90° from the incident direction.

Absorption is negligible in the visual wavelength range, and so the *extinction cross section* is

$$\sigma_e = \sigma_s \quad (4.17)$$

BUCHOLTZ [1995] provides more detailed derivations of Rayleigh-scattering related quantities like cross section, volume-scattering coefficient, optical depth, wavelength-dependent depolarisation factor (anisotropic factor) computation and a slightly improved phase function for standard air, improving the works of PENNDORF [1957] and FRÖHLICH and SHAW [1980]. The differences to the approximations given above are in the range of upto a few percent. TOMASI *et al.* [2005] further improve these results by studying the influence of water vapour on the mentioned quantities.

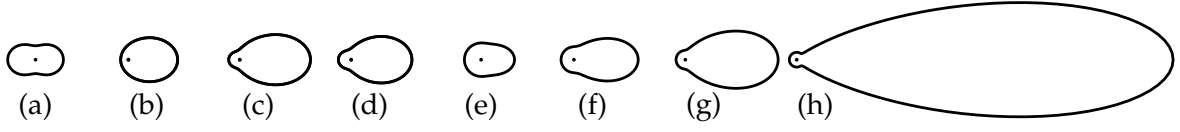


Figure 4.2: Scattering phase functions for unpolarized light coming from the left: (a) Rayleigh. (b) HENYEY and GREENSTEIN [1941] (c) CORNETTE and SHANKS [1992] (d) HG-Rayleigh [LIU and WENG 2006] (e) GIBBONS [1958] “extremely clear” (f) GIBBONS [1958] “dusty” (g) GIBBONS [1958]/NISHITA *et al.* [1987] “hazy” (h) GIBBONS [1958]/NISHITA *et al.* [1987] “murky”. Asymmetry factor $g = 0.3$ for (b)–(d).

Mie Scattering

Usually, the atmosphere is not clear, but shows some pollution consisting of dust, aerosols, haze, and, especially in industrial areas, soot. The respective particles are much larger than molecules (size parameter $x \gtrsim 1$), so Mie scattering theory has to be applied.

The proper description of Mie (or Lorenz-Mie) scattering has to be derived from the Maxwell equations, is rather involved even for spherical particles, and is described in physics textbooks, *e.g.*, by LIOU [2002, p.176ff]. A simplified expression for the scattering cross section of non-absorbing spherical particles is given by LIOU [2002, p.96ff]:

$$\sigma_{s,Mie} = \frac{8\pi a^2 x^4}{3} \left(\frac{m^2 - 1}{m^2 + 2} \right)^2 \left(1 + \frac{6x^2}{5} \left(\frac{m^2 - 1}{m^2 + 2} \right) + x^4 \left(\frac{3}{175} \frac{m^6 + 41m^4 - 28m^2 + 284}{(m^2 + 2)^2} + \frac{1}{900} \left(\frac{m^2 + 2}{2m^2 + 2} \right)^2 (15 + (2m^2 + 3)^2) \right) + \dots \right) \quad (4.18)$$

with size parameter x (4.3) and index of refraction m .

The phase function $P(\theta)$ even for spherical particles according to Mie theory is very complicated to evaluate and typically shows several peaks. The phase function for typical cloud water droplets shows strong forward and lesser backward scattering peaks and another peak around the rainbow direction of 138° . Typical terrestrial aerosol particles mostly show a forward scattering peak. In most cases, particles of many different sizes are mixed, and the exact shapes of the phase function average out, so for many applications it is enough to work with simple analytic approximations (Figure 4.2 (b)–(h)): A classical approximation to the Mie phase function has been presented by HENYEY and GREENSTEIN [1941]:

$$P_{HG}(\mu, g) = \frac{1 - g^2}{(1 + g^2 - 2g\mu)^{3/2}} \quad (4.19)$$

with $\mu = \cos \theta$ and an *asymmetry factor* $g \in [-1, 1]$, where $g \rightarrow -1$ indicates back scattering and $g \rightarrow +1$ forward scattering. This function is however adequate only for scatterers without a strong forward peak [LIOU 2002, p.313].

GIBBONS [1958] found similarly looking functions (Fig. 4.2 (e–h)), with the scaling factors given here selected to fulfill eq. (4.4):

$$P_G(\theta) = \begin{cases} \frac{9}{10} (1 + \cos^{16}(\theta/2)) & \text{(extremely clear)} \\ \frac{9}{13} (1 + 4 \cos^{16}(\theta/2)) & \text{(dusty)} \\ \frac{1}{5} (1 + 9 \cos^{16}(\theta/2)) & \text{(hazy)} \\ \frac{33}{83} (1 + 50 \cos^{64}(\theta/2)) & \text{(murky)} \end{cases} \quad (4.20)$$

Ideally, the phase function used for an approximation to Mie scattering should reduce to the Rayleigh phase function for small symmetric particles. CORNETTE and SHANKS [1992] presented an improved analytic phase function which provides a better result and reduces to P_R for $g \rightarrow 0$:

$$P_{Cs}(\mu, g) = \frac{3}{2} \frac{1 - g^2}{2 + g^2} \frac{1 + \mu^2}{(1 + g^2 - 2g\mu)^{3/2}}. \quad (4.21)$$

Another combination into an HG-Rayleigh phase function with similar result has been presented by LIU and WENG [2006]¹:

$$P_{LW}(\mu, g) = \frac{4}{2 + G^2} \frac{3}{8} (1 + \mu^2) \frac{1 - G^2(g)}{(1 + G^2(g) - 2G(g)\mu)^{3/2}} \quad (4.22)$$

$$\text{where } G = \frac{5}{9}g + \sqrt[3]{\frac{1}{2} \left(\frac{10}{9}g + \frac{250}{729}g^3 \right) + \sqrt{\Delta}} - \sqrt[3]{\sqrt{\Delta} - \frac{1}{2} \left(\frac{10}{9}g + \frac{250}{729}g^3 \right)}$$

$$\text{and } \Delta = \left(\frac{1}{2} \left(-\frac{10}{9}g - \frac{250}{729}g^3 \right) \right)^2 + \left(\frac{1}{3} \left(4 - \frac{25}{27}g^2 \right) \right)^3$$

The scattered radiation intensity for a particle at distance r from the observer is then

$$I(\theta) = I_0 \left(\frac{\sigma_{s,Mie}}{r^2} \right) \frac{P(\cos \theta, g)}{4\pi} \quad (4.23)$$

For atmosphere physics, esp. meteorology, climatology and remote sensing, several studies on the aerosol constituents in the Earth's atmosphere have been performed in the last decades. HESS *et al.* [1998a] presented OPAC, a software package (in FORTRAN) that is capable of providing the typically required quantities like extinction, scattering and absorption coefficients (σ_e , σ_s , σ_a , resp.), asymmetry parameter g , phase function $P(\theta)$ or aerosol optical depths τ for a variety of atmospheric compositions. Several standard mixtures are provided, but the user can also create own aerosol compositions. Later, HESS *et al.* [1998b] provided data for the worldwide distribution of aerosol composition on a 5×5 degree-grid, so that typical conditions can be derived for any place in the world. GONZI *et al.* [2002] report recent aerosol property measurements over many observing stations in Europe.

Mie scattering is responsible for some very interesting atmospheric phenomena. Not only aerosol and dust are modelled with Mie scattering, also the interaction of light with small water drops, such as fog, clouds, and even the rainbow, can be described. For rainbows, however, LEE [1998b] compared Mie theory with the older and much simpler Airy rainbow theory. For most natural drop sizes, Airy theory appears to be adequate, and Mie theory not necessary for the computation of rainbows with typical water droplet size distributions. However, phenomena that can properly only be explained with Mie theory include:

Multiple rainbows: When the droplet size is very homogeneous, not only the two main arcs of the rainbow, but a wide zone of colourful arcs is visible around the rainbow angle.

Glories: Often visible from airplanes when watching the aircraft's shadow on the clouds. The zone around the shadow appears bright with coloured fringes.

¹ A scaling factor of $\frac{1}{2}$ given in the paper was removed here to fulfill our normalization (4.4)

Aureole or (atmospheric) *corona* can be seen as bright glare around the Sun. It is caused by atmospheric particles, like dust, smoke, pollen or even insects [LYNCH and LIVINGSTON 1995]. Each type of particle produces a different effect, but they all are related to Mie scattering.

Bishop's Ring: This effect can be seen as a bluish ring of light with pale narrow red borders around the Sun. It is difficult to observe and was first reported after the eruption of the Krakatoa in 1883. The effect is related to scattering of dust in the stratosphere, which originates from volcanic eruptions. It is different from the aureole because the size of the particles is restricted around $1\mu\text{m}$, and therefore only certain wavelengths of light are scattered [LYNCH and LIVINGSTON 1995].

Blue Sun, Blue Moon: This effect, like the Bishop's Ring, is also related to volcanic activity and was first reported after the eruption of the Krakatoa in 1883, when large amounts of volcanic ash were blown into the stratosphere. When the particle size in such clouds averages near $0.7\mu\text{m}$, Mie scattering eliminates most of the red of the sunlight, so the Sun has a lavender or blue tone, and the moon likewise appears blue. This effect can also occur when great forest fires may produce particles with the critical size of $0.7\mu\text{m}$.

4.3.2 Refraction

Besides scattering and absorption, the light that reaches the ground unscattered is still subject to another effect: *atmospheric refraction*. The classical formulation of refraction on a region boundary is SNELL's law:

$$\frac{\sin \eta_i}{\sin \eta_t} = \frac{v_i}{v_t} = \frac{m_t}{m_i} \quad (4.24)$$

Here, η_i is the angle of incident light with the boundary normal, η_t the angle between transmitted ray and boundary normal, v_i and v_t the velocities of light on the incident and transmitted side, respectively, and m_i and m_t the respective indices of refraction.

For standard air and wavelength λ in μm , LIOU [2002, p.92] gives

$$(m - 1) \cdot 10^8 = 6432.8 + \frac{2949810}{146 - \lambda^{-2}} + \frac{25540}{41 - \lambda^{-2}} \quad (4.25)$$

The index of refraction of air depends on the wavelength, pressure, temperature, and the exact mix of gases, which for the main components (N_2 , O_2 , Ar) can be seen as constant ("standard air"). Only the CO_2 constituent is usually specified explicitly. Also, water vapour influences the index, while the traces of other gases can be safely neglected for our purposes. An exact, modern formulation for the refractive index of air is given by CIDDOR [1996], improving previous work by EDLÉN [1953] and OWENS [1967].

As a gas shell that shows a decrease of density with altitude, the index of refraction is strongest close to the ground and diminishes successively towards the top of the atmosphere. The effect of refraction is indeed small and often insignificant for objects not far from the viewer. On the other hand, it is important for astronomical objects: the setting Sun is usually lifted by slightly more than its diameter, or about $34'$ (see also page 5). Sometimes the exact shape of the distorted Sun or other effects of refraction are of particular interest. The index of refraction in the troposphere is strongly dependent on temperature. Inversions in the temperature profile near the ground cause effects such as inferior (Fig. 4.3 (a)) and superior



Figure 4.3: Refractive near-horizon phenomena: (a) Inferior Mirage: hot air immediately above the ground bends light rays upward towards the observer. — (b) Green Flash: Setting Sun with slightly greenish upper limb. (Photographs by the author)

mirages of objects far away on the horizon. Extreme examples like the Novaja Zemlya effect, where the solar image is lifted by atmospherical *ducting* by up to 5° , have been studied with ray tracing methods by atmosphere physicists [e.g. FRASER 1977; VAN DER WERF 2003; LEHN 1979; VAN DER WERF *et al.* 2003a,b; NENER *et al.* 2003; DAVIDSON and VAN DER WERF 2005].

Refraction is a phenomenon that affects the accuracy of positions in astronomical observations, and tables for the reduction of observations can be found in astronomical and also nautical literature. Usually, however, observations below 10 or even 15 degrees are avoided due to hardly correctable effects of extinction. Overviews of older models are given by MAHAN [1962] and recently by YOUNG [2004]. Simple, approximate formulae for the standard reduction of ground-based observations are given by MEEUS [1998, p.105ff]. HOHENKERK *et al.* [1992, p.141] provide a recipe for the computation of the effect of refraction using numerical integration and iterative refinements with straight path segments of decreasing length, and also simplified solutions. Another numerical method has been proposed by AUER and STANDISH [2000].

The refractive index of air depends also on the wavelength, and so all astronomical objects are subject to *differential refraction*, especially apparent if they are low in the sky, so that they show an upper green-blue limb and a lower red limb. The most prominent of these phenomena is the *green flash* of a rising or setting Sun, where the upper limb of the Sun shows a distinct green hue (Fig. 4.3 (b)). Sometimes the lower half of the Sun is below the horizon or behind clouds, leaving only the green limb visible. A gallery of images is available on the web by PARVIAINEN. A *blue flash* has been observed by the author in May 2004 visually, caused by the setting planet Venus when it vanished on the horizon in Namibia's extremely clear air, which of course all of these phenomena require to be seen.

LEHN and EL-ARINI [1978] presented a program to simulate and analyze atmospheric refraction effects such as mirages on the visible shape of distant simple objects by a temperature inversion layer close to the ground using step-wise ray tracing. BRUTON [1996] developed methods to derive temperature profiles from photographs of the Sun close to the horizon and satellite observations of star positions through the atmosphere. In the process, he also modelled the view of the Sun as seen through an atmosphere with layers of inverted temperature gradient, simulating phenomena such as mirages, distorted solar images, or the

green flash. He used curved ray tracing in a physically correctly modelled atmosphere and a multilayer model for temperature inversions, which also allowed him to derive expressions for extinction and air mass in a multilayer model. His atmosphere model is however aerosol-free, and only Rayleigh scattering and extinction are modelled. Based on this work, SAMPSON *et al.* [2003] compared ground-based photography of the setting Sun to a computed shape of the setting Sun that considered refraction values computed with atmosphere profiles from rawinsonde (“weather balloon”) measurements.

A whole series of papers on mirage geometry, green flashes and low-altitude refraction has been published by YOUNG *et al.* [YOUNG *et al.* 1997; YOUNG and KATTAWAR 1998; YOUNG 2000, 2004]. Optical refraction in the troposphere is also described by NENER *et al.* [2003].

4.4 Rendering of the Sky Dome and Physically-Based Skylight Models in Computer Graphics

This section deals with the practical approaches towards skylight modelling and using an extended light source like the sky dome for rendering in computer graphics. Numerous papers from the atmospheric optics domain are also mentioned to put an eye on observations and activities in this domain which should be much closer observed by researchers in computer graphics than it currently still is.

Skylight modelling has seen enormous progress in the last decades, and many researchers have published papers too numerous to mention them all. State-of-the-art reports have been given previously by NISHITA [1998], who concentrated on the numerous incremental works of his own group but also explained scattering by water, and SLOUP [2002], who also explained most of the physical processes important for skylight simulation in computer graphics.

Usually the sky is modelled as large, but finite, solid hemispherical light source centered around the observer, with no participating medium between this sky dome and the “interesting” scene objects. A typical assumption is that the skylight distribution is laterally symmetrical around the solar vertical, so only half of the sky directions will usually be evaluated and the result mirrored to the other half of the celestial hemisphere.²

NISHITA and NAKAMAE [1986] use the CIE [1973] skylight distribution (see section 4.5) and describe a way to compute outdoor and indoor illumination levels. They slice the sky into series of narrow spherical belts (“bands”) that are centered around inclined planes through the eye point. The luminance is assumed constant along the band width, so that only the center line of each band (*i.e.*, the projection of the plane on the sphere) has to be sampled. To estimate visible sky coverage, they add all areas of each band proportional to the unobstructed part of each centerline (intersection of radial rays in the projecting plane with the scene). They also take interreflection from other surfaces into account. Later, DOBASHI *et al.* [1994a] present an adaptive method to select a proper width for the band light sources to minimize sampling artifacts.

MÜLLER *et al.* [1995] split the sky dome into 145 “shooting” patches for a radiosity renderer and compute patch radiosity either from simple models, *e.g.* the CIE [1973] sky light

² However, HERNÁNDEZ-ANDRÉS *et al.* [2003] noted from digital image analysis of scanned slide images that the natural sky is often subtly asymmetric and interpret these findings as indications of asymmetric aerosol distribution.

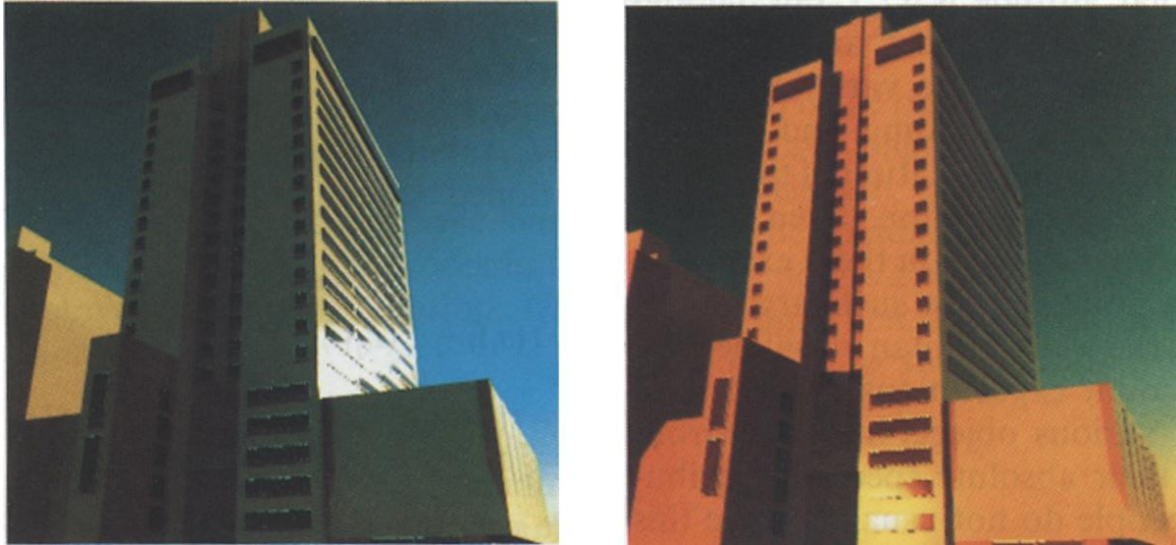


Figure 4.4: Results by KANEDA *et al.* [1991]. Note the unrealistic greenish hue in the evening scene, indicating an incomplete skylight simulation.

distribution, or data measured with standardised sky scanners. They present a practical estimate for the minimum size of the modelled sky dome to avoid any noticeable parallax effect. Their approach to colours seems however overly simplistic: The Sun is modelled as bright yellow, and the sky patches are simply painted blue.

KLASSEN [1987] presents a physically based approximative solution for sky colour computation. After an introduction about the physics of scattering, he models the Earth's atmosphere as just two spherical shells consisting of a pure-air layer and a haze-filled layer below. Both are of constant density, and refraction is not considered. He provides solutions for extinction and first-order scattering on haze particles with tabulated phase functions. Rayleigh scattering is not considered, and the sky colour is a mix of the Mie-scattered solar radiation and a uniform blue that is computed or visually estimated. The scene is computed for 33 wavelengths in intervals of 10 nm and then converted to RGB.

KANEDA *et al.* [1991] improve KLASSEN's model with an exponential density distribution with scale heights of 7994m for molecular density and 1.2 km for aerosols, and also fog and clouds can be modelled with single scattering, so direct sunlight through fog casts shadows. The band light source approach of NISHITA and NAKAMAE [1986] is again used to collect skylight illuminance onto a surface point and extended to allow specular reflection with a Cook-Torrance surface model. The images in their paper (Fig. 4.4) show a green hue for a sunset scene, indicating an incomplete simulation.

TADAMURA *et al.* [1993] use a similar atmosphere model and the GIBBONS [1958] phase function (4.20) for haze and compare their sky model to the CIE model. Instead of the band source approach to compute sky visibility and illumination onto a surface point, they propose to set up a parallelepiped over the point of interest, aligned towards the Sun, and use graphics hardware to render the scene onto the sides of the parallelepiped, to create an obstruction map as seen from that point. Illuminance is then simply computed from the sum of unobstructed pixels, their respective projected size and sky luminance value of the respective pixel center. They show how to optimize the sizes and resolutions of the faces

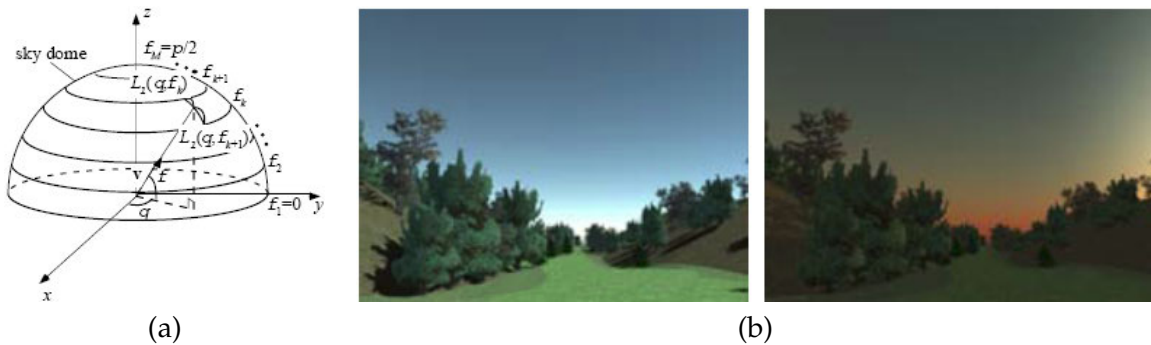


Figure 4.5: DOBASHI *et al.* [1994b, 1997] (a) The sky dome divided in the direction of f . – (b) examples of daytime and evening conditions.

of the parallelepiped depending on the relative illuminance differences. Compared to the band light source approach, they report a significant speed-up for illumination calculation, even more pronounced with increasing scene complexity. Furthermore, they split their objects into quadrilateral meshes and sample the sky illuminance for the mesh vertices only, then apply a linear interpolation scheme for illuminance calculation for each pixel to further reduce computing time.

As another improvement for the rendering performance of KANEDA *et al.*'s [1991] model, DOBASHI *et al.* [1994b, 1997] present a method to rapidly compute sky colours for any solar altitude from tabulated values of weight functions for basis functions precomputed for discrete solar altitudes. They observe that the sky luminance is laterally symmetric to the solar vertical and discuss three approaches to store the precomputed values:

Regular Grid The sky dome is partitioned into altitude zones which are vertically divided. The luminance is computed for all vertices, and linear interpolation is applied for values within the cells. This approach takes impracticable amounts of storage.

Spherical Harmonics The luminance distribution is stored with the spherical harmonics approach. The circumsolar luminance peak poses a problem, however, so that many functions are required for proper reconstruction. Also, the reconstruction is much more time demanding than their favourite,

Fourier Series The sky is partitioned into altitude zones (Fig. 4.5 (a)), and luminance along the azimuth is encoded into weights of a Fourier series, *i.e.*, a cosine basis, which is especially well suited for the laterally symmetric values. The number of weights (and thus, cosine terms required), depends on solar altitude and can also differ for each zone and is computed by estimating the error introduced by truncating the Fourier series. The sky colour is then reconstructed by linear interpolation in the weight table for different solar altitude and points in between the sampled altitudes, providing results visually equivalent to the original model (Fig. 4.5 (b)).

This last approach seems in principle applicable for all sky models that take long to evaluate, and the weight table nowadays would fit easily on graphics hardware.

In another paper targeted to outdoor scenes for architecture, DOBASHI *et al.* [1996] also use a Fourier approach to precompute weights for sky visibility (sampled again with the

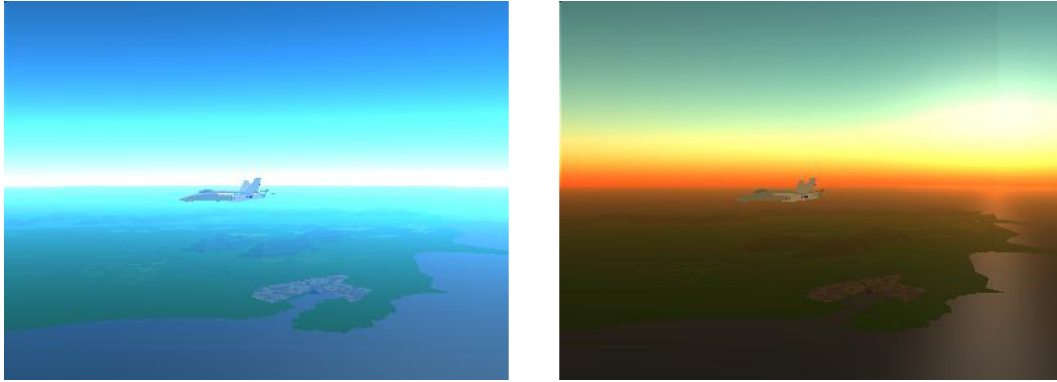


Figure 4.6: Examples of the multiple scattering algorithm by NISHITA *et al.* [1996a].

abovementioned band light approach) for each pixel in a scene, so that scenes can be rerendered much faster if sky conditions or surface properties are changed.

NISHITA *et al.* [1996a] present the first computer graphics skylight model that includes an approximative solution for secondary scattering. They model molecular (Rayleigh) and aerosol (Mie) scattering (with their Mie phase function approximation from NISHITA *et al.* [1987], eq. (4.20)) and provide solutions for the path integrals through the atmosphere with exponential density distributions, neglecting refraction and ozone absorption (Fig. 4.6). The atmosphere around the observer is partitioned into radial cells that help later to accumulate skylight intensities along radial view rays. For computation of the optical depths, they apply cylinder coordinates with the cylinder's z -axis pointing towards the Sun and the usual parallel Sun ray approximation, and observe that optical depths from the Sun to points of equal distance r from the Earth's center and z -coordinate in the cylinder are identical. These values are precomputed separately for Rayleigh and Mie extinction and stored incrementally into 2D lookup tables $T(r, z)$ which are constructed from the sunward top of the atmosphere towards decreasing z values. Low r values have to be sampled more frequently due to the higher density of the atmosphere there. The intensities of single-scattered sunlight then have to be accumulated along the viewing ray through the atmosphere cells towards the observer. NISHITA *et al.* also propose a fast approximation for secondary scattering: for each sample point along the view ray, a few important directions are sampled for primary scattering like above, and the cumulative intensity is added to the first-order scattering intensity as seen from the observer. Also reflectance from the ground is taken into account, where ground luminance is computed from direct sunlight and skylight. For higher orders of scattering, a recursive scheme is proposed if really needed. For increased performance, they recommend a combination with the basis function display method of DOBASHI *et al.* [1997].

A quite different approach is presented by JACKÈL and WALTER [1997]. The main topic of their work is the simulation of skylight by means of Mie scattering computed with the proper phase function from Mie theory (no simplifications) for different mixtures of particle sizes found in the meteorological literature. The authors use an atmosphere model with clear-air and aerosol with respective exponential density profiles, ozone in stratospheric layers and (optional) raindrop shells (near the ground). An optional sulfur-acid shell in the stratosphere is used to simulate the purple light in twilight. They use a 41-channel spectral rendering system to reconstruct accurate colour values. To improve rendering speed, the values of the phase function are precalculated and stored in lookup tables, and the continuous

density profile is approximated by using large scattering volumes of constant density. The authors make however no mention of refraction, and they only mention to have a simplified approximation towards double scattering without giving details. The model and more background information is explained in the Master thesis by WALTER [1996].

The most ambitious physically based skylight model for computer graphics until now has been presented by HABER *et al.* [2005]. Although titled a twilight model, the simulation also works with the Sun above the horizon. The authors however specifically address phenomena visible especially in twilight (see page 72). The atmosphere with a scale height of 8 km is partitioned into layers of increasing thickness adapted so that the mass in a vertical column of air is equally distributed between layers. Aerosol data from the meteorological software OPAC [HESS *et al.* 1998a] is used, which provides optical properties of different aerosol and dust mixtures, so that atmospheric conditions for different grades and types of pollution (*e.g.*, maritime, mountain, urban, desert air) can be selected, or a custom mixture can also be created. From temperature and humidity, also the refractive index of air based on CIDDOR [1996] is computed. Conditions in a layer are constant. The sky around the viewer is partitioned into spherical shells of increasing radius, with the maximum radius selected so that the Sun at the border of astronomical twilight can just illuminate the outermost shell. The shells are partitioned into volumetric cells with radial edges. Because twilight shows smooth patterns, the cells can be 3° wide in azimuth and altitude. To model light transport, first the direct irradiation of sunlight is computed for each cell. Here, refraction and absorption through each atmosphere layer and the absorption by stratospheric ozone are taken into account. Then first-order scattering is computed and stored for each cell. Then, cell-to-cell energy transport is computed, taking into account the extinction along each ray between the cells, but neglecting refraction and scattering anisotropies. After about five iterations, equilibrium in the distributed energy is established with sufficient accuracy, and the skylight intensity can be “collected” for the observer by summing the energies along the viewing cells (reduced by absorption along the view ray). The sky radiation for each direction can then be interpolated between cell centers. The authors present several optimizations, but still the computation takes several hours with their 8-channel spectral renderer on a contemporary PC.

4.4.1 Special Topics of Atmospheric Effects

Aerial Perspective, Haze and Fog

Aerial Perspective (also called *airlight*) is the bluish tint an observer can see when looking at objects in great distance and is an important clue for distance estimation. More distant mountains appear in a bluer and brighter tint than mountains close to the observer (Figure 4.7). Airlight is sunlight in-scattered between the mountain and the observer. This effect depends mainly on the distance between the observer and the mountains. The longer the distance, the higher is the amount of light from the mountains which is scattered out of the line of sight by Rayleigh scattering and replaced by in-scattered airlight [LYNCH and LIVINGSTON 1995; MINNAERT 1993].

The effects of thin fog, clouds of dust and haze are frequently confused with airlight. Their main difference to airlight is their high amount of Mie scattering, especially close to the solar direction. But, instead of blue, the effects caused by haze appears gray, white or brown. Again, a strict separation is difficult, and often the terminology is not as strict.



Figure 4.7: Airlight, visible as the increasing blueness of far mountains. (a) far view through almost haze-free air — (b) More haze decreases object visibility. (Photographs by the author)

The computer graphics literature is rich with models for rendering scenes including *participating media*, as all transparent, but scattering media collectively are called. In this section, only a few atmosphere-related papers are presented. Papers on effects like smoke, steam, clouds or halos are not considered.

The earliest and simplest computer graphics approaches towards haze and fog just mixed colour values computed for a vacuum scene with an arbitrary grayish fog colour, thus at least providing a depth cue and also a cheap way to hide the far clipping plane and other limitations in the amount of objects that could be displayed in real-time systems. The mixing coefficient depends on object distance.

BLINN [1982] describes scattering in clouds and Saturn's rings using the HENYEY and GREENSTEIN [1941] phase function (4.19).

MAX [1986] proposes a method to display sunbeams cast into fog through holes in occluders by an extension of the shadow volumes technique [CROW 1977]. He models the fog as layer of constant density near the ground and works with only single scattering. NISHITA *et al.* [1987] model the appearance of anisotropic light sources in fog, using the experimental approximations to the haze phase function (4.20) from GIBBONS [1958].

KLASSEN [1987] provides in his sky model a likewise single-scattering solution for the influence of a thin fog layer near the ground on the sky colour. The terrain is modelled flat, a fog layer of constant density covers the ground, and a layer of clear air of constant density is above. The flat-earth assumption is valid for solar altitudes above about $h_{\odot} > 15^\circ$. Sunlight is attenuated by the clean air, then by air and haze, before illuminating an object. The reflected light is then attenuated by haze on its way to the observer, and some in-scattering adds light from the Sun.

WILLIS [1987] presents a similarly simple model based on absorption and mixing-in of a background radiation value, usable to add haze effects in flight simulators.

KANEDA *et al.* [1991] model single scattering in a fog with exponential density distribution.

The skylight model by PREETHAM *et al.* [1999] also contains a model for aerial perspective which is applicable for terrain rendering with a flat-earth approximation (Figure 4.8):

The atmosphere here is modelled also flat with different exponential density falloff rates for molecules and aerosol particles and without refraction. Light from the surface point L_0

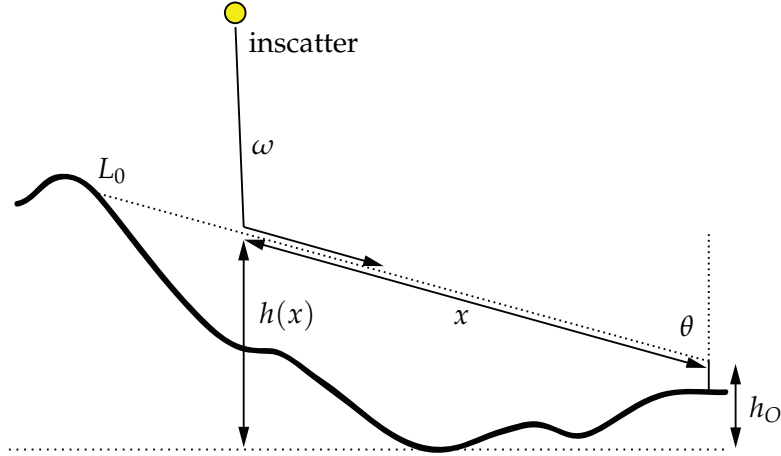


Figure 4.8: Geometry for aerial perspective after PREETHAM *et al.* [1999].

is attenuated by extinction along the way, and some more light is added by in-scattering, so $L(s) = L_0\tau + L_{in}$. The scattering coefficients β decrease exponentially along with the densities with altitude, so $\beta(h) = \beta_0 e^{-h/H}$ with surface-level coefficient β_0 , altitude h and the respective scale heights $H_{aer} = 1.2\text{km}$ and $H_m = 8.8\text{km}$. For a target location L , h depends on its distance as $h(x) = h_O + x \cos \theta$ with observer height h_O . So,

$$\beta(h(x)) = \beta_0 \cdot e^{-\frac{h_O + x \cos \theta}{H}} \quad (4.26)$$

The *extinction factor* for either molecules or aerosol/haze along a path s is $\tau = e^{-\int_0^s \beta(x) dx}$, so that

$$\tau = e^{-\int_0^s \beta_0 \cdot e^{-\frac{h_O + x \cos \theta}{H}} dx} = e^{-\left(\frac{H\beta_0}{\cos \theta} \cdot e^{(-h_O/H)} \cdot (1 - e^{(-s \cdot \cos \theta/H)})\right)} \quad (4.27)$$

and the total extinction factor is computed as $\tau_{tot} = \tau_m \cdot \tau_{aer}$.

For L_{in} we give here the approximation from PREETHAM [2003] that assumes almost horizontal viewing rays close to the surface of the Earth, so that τ reduces to $\tau = e^{-\beta_0 s}$ and

$$L_{in} = \int_0^s e^{-\beta_0(s-x)} \int_0^{4\pi} L^s(\omega') \beta(\omega, \omega') d\omega' dx \quad (4.28)$$

with the spectral radiance $L^s(\omega)$ of the sky and the Sun as viewed in direction ω and the angular scattering term $\beta(\omega, \omega')$. With a further assumption that primarily direct sunlight is in-scattered, the second integral reduces to $E^s \beta(\omega, \omega_s)$ with solar irradiance E^s from direction ω_s , and so

$$L_{in} \approx \int_0^s e^{-\beta_0(s-x)} E^s \beta(\omega, \omega_s) dx = E^s \beta(\omega, \omega_s) \frac{1 - e^{-\beta s}}{\beta} \quad (4.29)$$

A more rigorous computation is in the original paper [PREETHAM *et al.* 1999].

DOBASHI *et al.* [2002] present a hardware-based volume rendering approach based on a number of sampling planes placed in front of the viewpoint and subdivided into meshes. Light scattering in a uniform medium is approximated by computing the scattering in the sampling planes and accumulating the brightness in a second, back to front, rendering pass. Projective shadows can be created by rendering visibility maps from the light source onto the planes with hardware shadow mapping. Sub-planes are used to increase sampling accuracy (Figure 4.9).

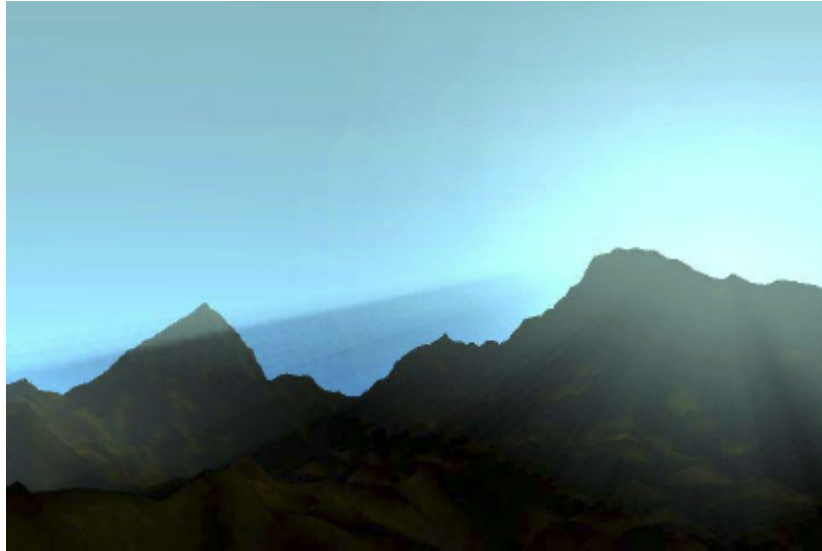


Figure 4.9: Interactive atmospheric scattering [DOBASHI *et al.* 2002].

Effects of Refraction

All general all-sky models presented so far except that of HABER *et al.* [2005] ignore the effect of refraction in Earth's atmosphere.

In the field of computer graphics, BERGER *et al.* [1990] seem to be the first to deal with atmospheric refraction. They put a box with discrete horizontal atmosphere slices (layers of constant index of refraction) between scene and observer and apply Snell's law at each layer boundary with their ray tracer. Using discontinuities in the index of refraction, they showed how to produce mirages. STAM and LANGUÉNOU [1996] applied the concepts of geometric optics for the handling of media with continuously varying index of refraction, like "blobs" of hot air emanating from heat sources and dissipating in the surrounding. They limit their method however to bounded environments that act as container for the blobs of hot air and compute a first-order approximation, *i.e.*, only one refraction that is computed as summary term of all the blobs in the environment. In a second approach, they use a precomputed table of perturbations. For animations, such a perturbation table would have to be varied over time as well to simulate the effect of the moving blobs of hot air.

Using the methods of BRUTON [1996], SLOUP [2003] introduced the approximation of the curved ray path equation into the computer graphics literature to show the distorted Sun on the horizon. The atmosphere is divided into spherical layers. The boundaries of the layers are isothermal surfaces (so there is no refraction discontinuity on the boundaries), and the temperature gradient is constant in each layer. Thus, the ray path is split into circular arcs along layer boundaries. The intersection point of each arc with the next layer is found progressively, and in each layer the next layer where the ray intersects can be above or below the current layer. The ray is followed through the atmosphere until it either reaches the top of the atmosphere (from where it escapes as straight ray) or hits an object within. His approach is demonstrated with images of the setting Sun followed through an atmosphere with up to several inversion layers, similar to the images in BRUTON's work.

These studies are applicable for scenes where the Sun is shown in closeup, so that there is a considerably high probability that a ray shot from the eye will ultimately hit the Sun. If most rays leave the scene without hitting the Sun, the solution is inefficient. GUTIERREZ *et al.* [2004] describe a global illumination approach for the rendering of the setting Sun based on their *curved photon mapping* [GUTIERREZ *et al.* 2003]. They argue that the computational effort of the classical approach of shooting rays backwards from the eye into the scene and then towards light sources (*i.e.*, backward ray tracing) through inhomogeneous media would be too high to allow a general solution, and the same goes for direct (forward) ray tracing (shooting light from the light sources and trying to hit the eye) and bidirectional path tracing (starting rays both from eye and light sources). So they add photon maps [JENSEN 1996] into the scene, and start to shoot photons from the light sources, *i.e.*, the Sun for daylight scenes. The photons follow (in general) curved paths through the atmosphere until they hit an object in the scene. If the object is diffuse, the photon is stored in the photon map, if the photon is reflected, it further follows curved paths, until ultimately all photons are stored in photon maps. The second pass then is similar to classical backwards ray tracing, so the eye rays are shot into the scene along potentially curved paths and finally hit an object. The radiance at the surface there is reconstructed from the photons stored in the vicinity of the hit point. Unfortunately, the images in the paper that should show natural scenes only demonstrate the second pass (using textures instead of the photon maps), and the very simple photon tracing test scene takes very long to compute (several minutes for a small image). The authors also present a model of the human visual system, taking into account the influence of retinal bleaching on the enhancement of the Green Flash effect, which had also been studied by YOUNG [2000] before. In related papers, SERON *et al.* [2004] use their curved raytracing system to render sunsets as seen through inhomogeneous atmospheres with very simple scene setups, and GUTIERREZ *et al.* [2005b] use textured billboards with arctic atmosphere profiles to simulate several types of arctic mirages. All these papers only show refraction, and no extinction. Finally, GUTIERREZ *et al.* [2005a] present their combined solution for participating media such as air with haze or fog, or water with elastic and also inelastic (fluorescent) scattering particles and refraction, applying *volume photon mapping*. Refraction is applied both for the photon shooting pass and for the gathering pass.

LINȚU *et al.* [2005] describe solar disc rendering again based on BRUTON [1996], combined with the atmosphere model of HABER *et al.* [2005] (see page 68), so that both Rayleigh and Mie scattering and extinction are taken into account for different climate types as well as refraction. In their case, up to 30000 atmosphere layers are used. They also model the solar disc with the limb darkening caused by absorption in the solar atmosphere.

Twilight

The appearance of twilight is usually governed by rapidly changing brightness and colours, which are strongly dependent on aerosol and dust in the sky. With the Sun just below the horizon, the horizon sky can take colours from pink to brown (*cf.* Fig. 4.10(a), (c) and (d)).

The earliest simulation models for twilight again can be found in the optics and physics literature. For example, ADAMS *et al.* [1974] present computations that showed the importance of the ozone layer for the blue zenith sky at twilight. About the same time, BLÄTTNER *et al.* [1974] simulate the twilight sky along the solar vertical considering molecule (Rayleigh) scattering and sky polarization using a Monte Carlo method for multiple scattering compu-

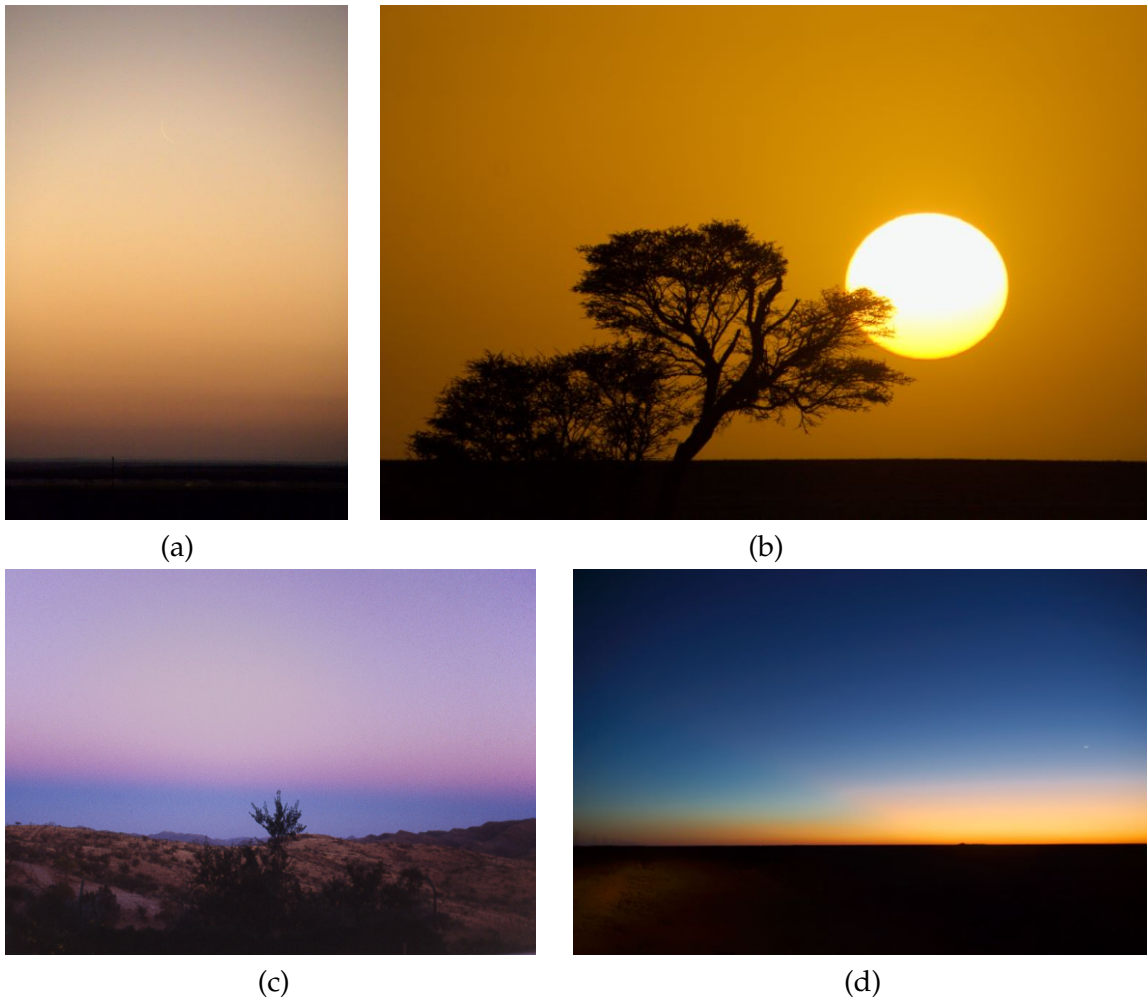


Figure 4.10: (a) Desert twilight, shortly before sunrise — (b) Desert sky at sunset: the large amount of dust causes strong absorption, and the Sun is slightly compressed due to differential refraction. — (c) Earth's shadow rising as gray-green stripe below the pink twilight in the east after sunset under extremely clear sky (Namibia) — (d) Colourful twilight in the desert after sunset, including purple light. (Photographs by the author)

tations in a spherical shell atmosphere. They note the importance of multiple scattering especially for twilight polarisation computation.

LEE [1994b] describes colour measurements from digitised film slides. Later, LEE and HERNÁNDEZ-ANDRÉS [2003] take note of a short-lived feature visible at twilight called *purple light* (Figure 4.10 (d)). Usually, strong purple light is explained with volcanic dust in the stratosphere, but by modelling the radiative transfer through the atmosphere with software from the geophysics domain, they found that the ordinary purple light is caused by low-stratosphere aerosol (mostly sulphuric acid droplets) illuminated by sunlight reddened by its passage through the troposphere.

The skylight model of HABER *et al.* [2005] is the only model in the computer graphics literature that specifically addresses problems visible during twilight. The direct atmosphere insolation takes refraction into account, several scattering passes (distribution of energy between the atmosphere cells) are performed, which is essential for twilight simulation [BLÄTTNER *et al.* 1974], and also the effect of ozone absorption in a higher atmosphere layer is taken into account, so that there is no unnatural green hue in the model during twilight.

This model has been used by LINȚU *et al.* [2005] to add the sky colours around the setting Sun. However, it does not show stars in the dimmer twilight sky. A combination of a twilight model with stars would have to take studies on stellar twilight visibility into account, *e.g.* by TOUSEY and KOOMEN [1953].

The night sky model of JENSEN *et al.* [2001] seems also to include twilight, but no images are shown that would clearly demonstrate significant twilight effects.

Skylight Polarisation

A typical simplification in all computer graphics skylight models hitherto mentioned is that the polarisation caused by Rayleigh scattering is usually neglected, with the usual notion that the human visual system is not responsive to effects connected to polarisation.

However, scattered sunlight is strongly polarised around the sun/anti-sun axis, with the strongest polarization occurring at 90° from the Sun. This polarization is an important phenomenon in nature, and many insects are able to recognize it. Austrian biologist KARL VON FRISCH found out that bees are able to recognize the polarization pattern in the sky in the near ultraviolet spectrum and can use it for navigation even if the Sun is covered by thick clouds and only 10–15% of sky is free of clouds [PYE 2001, p.103f].

PYE [2001, p.66f] mentions that in Vikings legends there is mention of a device called “sunstone” used for navigation and cautiously suggests that this may have been a polarising crystal with which the Viking navigators could recover the position of the Sun from the polarisation pattern of the sky.

But even without instruments, with the naked eye, it is possible to detect a weak pattern on the clear sky caused by polarised light which is called *Haidinger’s Brush* [O’MEARA 2005a,b].

The strongest effect of skylight polarisation, however, appears in images where skylight is reflected on smooth surfaces like water or glass, so that close to Brewster’s angle the light wave component parallel to the surface is reflected strongest while the orthogonally oscillating component is partially absorbed.

The proper simulation of skylight polarisation requires a polarisation-aware rendering system [WOLFF and KURLANDER 1990; FRENIERE *et al.* 1999] and a physics-based simulation of Rayleigh scattering. In the physics literature, already COLLINS *et al.* [1972] presented a

complete physically modelled backward Monte Carlo simulation (*i.e.*, with the ray starting from the eye point) that included a spherically layered atmosphere, refraction, absorption, multiple molecular and aerosol scattering and polarization computation based on the Stokes vector formalism. In computer graphics, this work has not successfully been repeated yet, but see section 4.5.1 for an analytical model of skylight polarization.

Night Sky Rendering

The night sky shows several differences from the daylight sky. The primary light source, if available, is the Moon, reflecting sunlight towards Earth. In principle, the distribution of moonlight in the atmosphere works identical to the daylight computation with light from the Sun. However, there are additional light sources:

Twilight: see page 72.

Stars and Planets: Of the 6000 or so stars visible with the unaided eye, about half are above the horizon. However, no single star is bright enough to cast a discernible shadow, so the total starlight can be integrated over the hemisphere. Planets look like stars at first glance. Most planets can just be handled as stars, but Venus can be bright enough to cast a shadow and would have to be treated separately. Spectral irradiance from stars and planets has been studied by RAMSEY [1962].

The Milky Way is the soft-whitish band of light seen in dark rural skies. Again, no directional computation is necessary, just an integrated increase of total light.

Airglow: A feeble emission caused by photochemical processes in the upper atmosphere. This is the sky background brightness visible even in the darkest of astronomical observing sites, far away from sources of artificial light pollution.

Zodiacal Light is sunlight reflected off interplanetary dust. It concentrates in the ecliptic plane and is confined to an arc about 60 degrees on both sides of the Sun. It is best visible on the border of astronomical twilight and about equal in brightness to the Milky Way.

Aurorae: A phenomenon of the upper atmosphere visible at night usually only in higher geographical latitudes, caused by particles of the solar wind that enter the Earth's upper atmosphere along the Earth's magnetic field lines. They then collide with atoms and excite them, and the energy is shortly thereafter re-radiated in a characteristic wavelength, so that the aurorae emit light of very distinct wavelengths. BARANOSKI *et al.* [2005] present a method to simulate the appearance and also dynamics of this spectacular phenomenon.

Light Pollution: An unfortunate fringe effect of civilisation is the ever increasing level of light pollution caused by artificial light directed or at least reflected or scattered skywards. This light causes many ecological problems and destroys the majesty of the natural night sky.

Moving Objects: Phenomena that disturb the “visual silence” of the night sky include meteors (shooting stars), which in rare cases can become brighter than the Full Moon, and — again effects of civilisation — airplanes and satellites.

An older survey of papers on sources of nocturnal light sources is given by INGHAM [1971].

JENSEN *et al.* [2000, 2001] present a physically-based night sky model usable with a Monte Carlo spectral ray tracer that covers stars and planets, zodiacal light, airglow, diffuse galactic and extragalactic light, and the Moon, which is modelled with a retro-reflective BRDF that is able to model the Moon's disk-like appearance with no brightness falloff towards the limb. They also model the Earth's atmosphere similar to NISHITA *et al.* [1996a], so bright light sources like the Moon are shown surrounded with a corona of scattered light, and all celestial objects show atmospheric extinction. Refraction is not mentioned, however, and scenes in bright twilight are not shown.

Another aspect is important for night scenes: at the low levels of light available at night, colour vision is disabled. A photograph with long exposure time shows that moonlight is just reflected sunlight with even an *enhanced red* component, and that such long-time exposures almost look like daylight scenes (Figure 4.11). However, most people experience a *blue shift* in night vision when the Moon is shining. In particular, JENSEN *et al.* [2000] describe the use of a mixed psychophysical and empirical model for *tone mapping* of night scenes. This model deals with loss of colour vision, blue shift and loss of visual acuity under mesopic viewing conditions, which is why their work takes much care to perform all computations exactly and in physical units to be able to apply models from colour vision research.

Targeting the same problem, KHAN and PATTANAIAK [2004] describe a model of the human visual system where the rod and blue-sensitive S cone cells in the retina interact to cause this perception of blue.



Figure 4.11: Comparison of a daylight landscape photograph and a long-time exposure of a nearby scene at night under moonlight. The night scene shows almost daylight colours, which are however not visible for the human visual system under the low nocturnal light levels. The slight reddening of colours may be an effect of the Moon's light being reddened by its specific reflection spectrum, but more likely is also caused by differences of the film's sensitivity for different colours in case of long-time exposures. (Photographs by the author in Namibia)

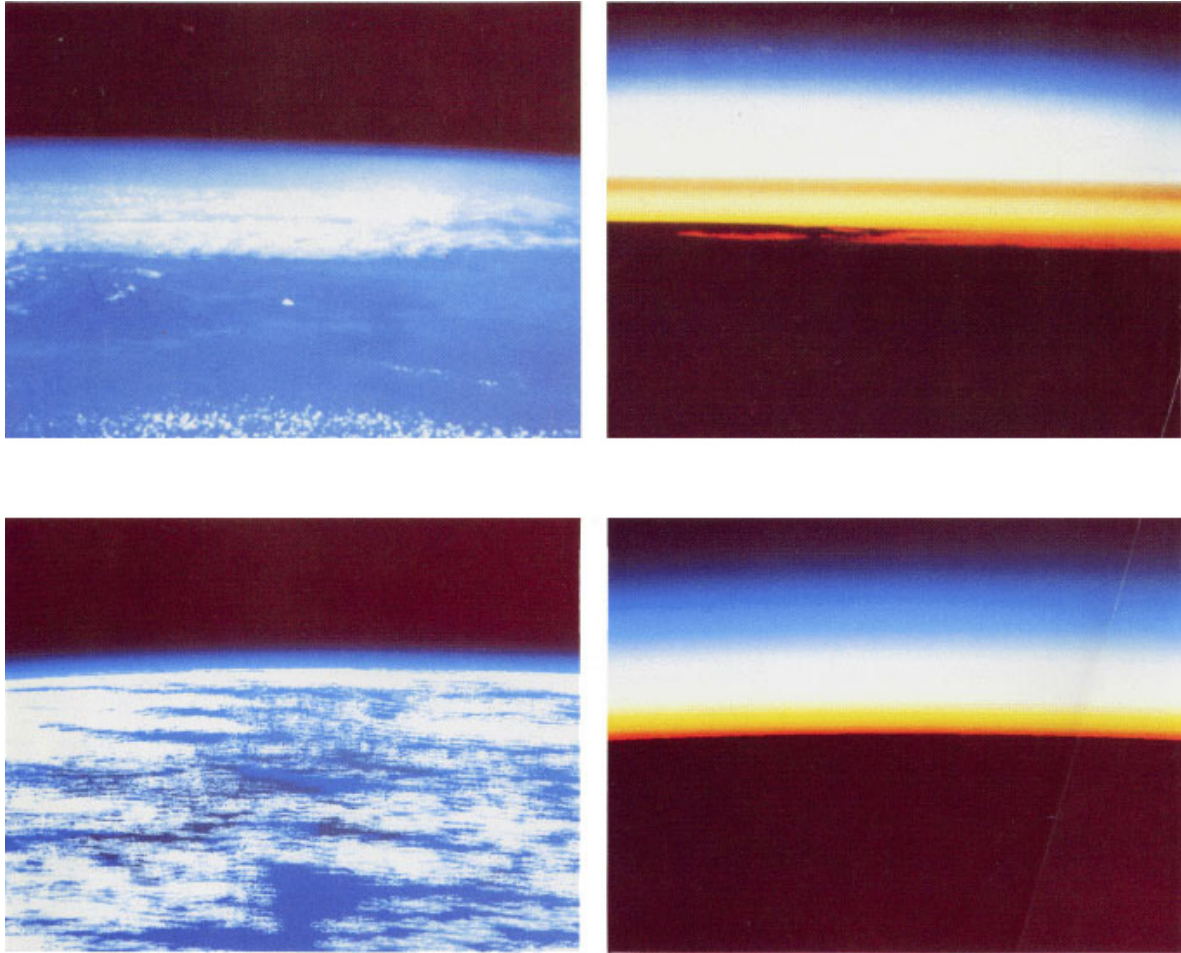


Figure 4.12: Real photographs of the Earth viewed from outer space (top) and results of the algorithm for the same scene (bottom; images from NISHITA *et al.* [1993]).

Earth from Space

NISHITA *et al.* [1993] explore the appearance of the planet Earth as seen from space, *i.e.*, outside the atmosphere (Figs. 4.12 and 4.13). They present a model based on KLASSEN's [1987] work, including a spherical atmosphere with exponential density and different, reasonable molecule and aerosol scale heights and single Rayleigh and Mie scattering, but without refraction. They consider attenuation of sunlight before it hits the ground and between ground and observer, and sunlight that is scattered into the view direction so the Earth shows a bluish shell. The ground is illuminated by direct sunlight and integrated skylight, which can be precomputed into a lookup table and is also computed for locations in twilight, *i.e.*, where the Sun is below the horizon. Ground reflection that illuminates the sky dome is ignored. The paper also discusses a simple single-scattering approach for clouds, which however don't cast shadows onto the planet's surface, and for light reflection and scattering in the oceans. The model is also usable for ground views, and later, NISHITA *et al.* [1996b] also add clouds with anisotropic scattering.

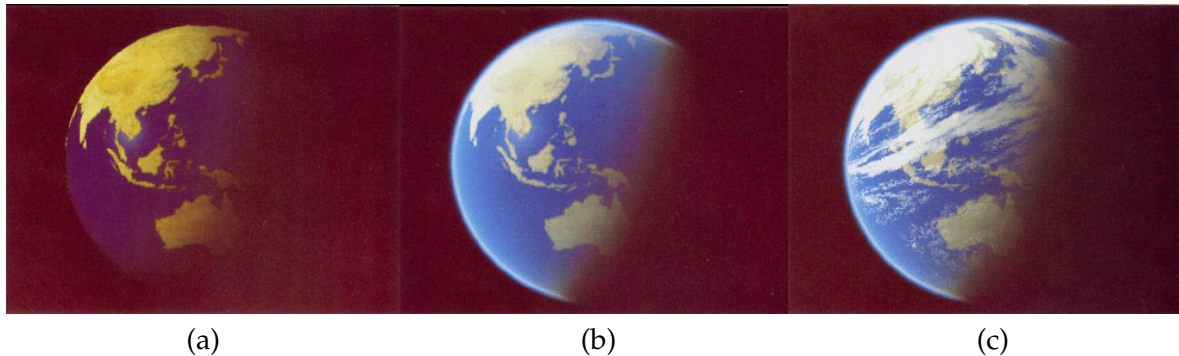


Figure 4.13: Results of the algorithm by NISHITA *et al.* [1993]: (a) The Earth viewed from outer space: the colour of the sea, direct sunlight and skylight are taken into account. – (b) adding the colour of the atmosphere by taking into account atmospheric scattering and absorption. – (c) adding clouds. (Images from NISHITA *et al.* [1993]).

IRWIN [1996] presents a similar model, restricted to a purely molecular atmosphere (Rayleigh scattering only), but extended by using a spectral rendering system instead of the usual RGB approach also used by NISHITA *et al.* [1993]. He also shows images of sunset colours from *inside* the atmosphere. O'NEIL [2004] presents a real-time solution of NISHITA *et al.*'s [1993] model, making extended use of lookup tables, and a demo program with source code on his website.

DOBASHI *et al.* [2002] also present a way to produce near-realtime views of the Earth from outside the atmosphere by adding texture shells around the Earth that are sampled for scattering effects, and also includes clouds consisting of small spheres.

4.5 Analytic Skylight Models

The methods presented in section 4.4 based on integration of scattered light usually take very long for evaluation. For many applications, it is sufficient to create a skylight distribution which just looks believable, if possible at low cost or, important for computer graphics, even in real-time. Some ad-hoc models just use an arbitrary blue colour with a brightness or whiteness gradient towards the horizon³, which is more an artist's solution than a simulation of natural colours. Providing fast and still accurate results is the domain of analytic models, and numerous models have been created mainly for illumination planning for applications in architecture and planning of solar power plants. Older models frequently mentioned are the CIE [1973] and CIE [1994] models.

Typically, the computation of sky luminance in analytic models is split in two parts: Finding zenith brightness Y_z , and then applying a skylight distribution pattern that relates skylight of any point of the hemisphere to zenith brightness. The latter expression typically uses the angles depicted in figure 4.14.

Even if this chapter's focus is on clear-sky physics, measurement and simulation, for completeness the traditional CIE [1994] Overcast Sky luminance model (by MOON and

³ However, LEE [1994a] pointed at the fact that the brightness maximum is usually slightly above the horizon.

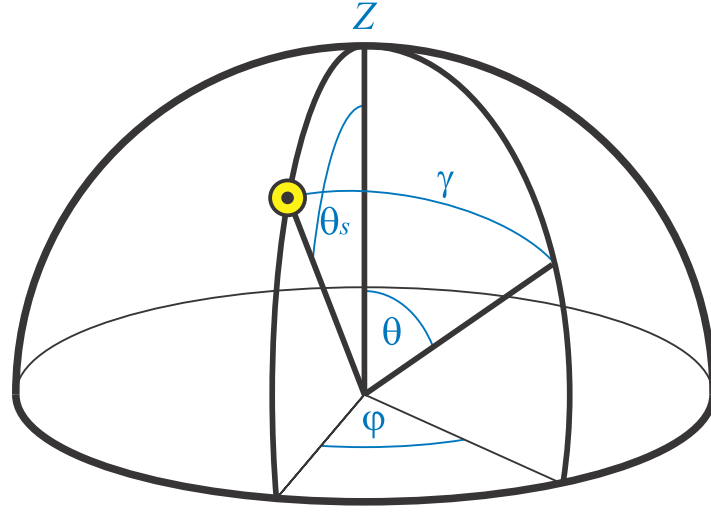


Figure 4.14: Angles and directions on the sky dome used in the analytical models.

SPENCER) shall be mentioned first, which describes a simple model for overcast sky luminance:

$$Y_{OC} = Y_{z,o} \frac{1 + 2 \cos \theta}{3} \quad (4.30)$$

The CIE [1973] and CIE [1994] Clear-Sky Models have been recommended until recently:

$$Y_{CIE94} = Y_{z,c} \frac{(0.91 + 10e^{-3\gamma} + 0.45 \cos^2 \gamma)(1 - e^{-0.32/\cos \theta})}{(0.91 + 10e^{-3\theta_s} + 0.45 \cos^2 \theta_s)(1 - e^{-0.32})} \quad (4.31)$$

Zenith luminances for overcast and clear skies, $Y_{z,o}$ and $Y_{z,c}$, respectively, can be obtained from tables or from formulas that depend on solar altitude h_{\odot} and turbidity T also from the CIE [1994]: $Y_{z,o} = 123 + 8594 \sin h_{\odot}$ and $Y_{z,c} = (1.376T - 1.81) \tan h_{\odot} + 0.38 [\text{kcd}/\text{m}^2]$. ZANINETTI *et al.* [1999] use $Y_{z,o} = 90 + 9630 \sin h_{\odot}$ and $Y_{z,c} = 100 + 63h_{\odot} + h_{\odot}(h_{\odot} - 30)e^{(h_{\odot}-68)0.0346}$, apparently from the CIE [1973].

The ASRC-CIE model [LITTLEFAIR 1994] uses a linear combination of four luminance models: the standard CIE [1994] cloudless sky (4.31), a high turbidity version of the latter, a realistic formulation for intermediate skies proposed by Nakamura and the standard CIE [1994] overcast sky (4.30).

An all-weather sky luminance model based on eq. (4.31) has been formulated by PEREZ *et al.* [1993]. Based on 5 parameters (darkening or brightening A of the horizon, luminance gradient B near the horizon, relative intensity C of the circumsolar region, width parameter D of the circumsolar region, and relative backscattering intensity E), this model has been found to be more accurate than the CIE [1994] model [PREETHAM *et al.* 1999]. The key expression is given as

$$\mathcal{F}_P(\theta, \gamma) = (1 + Ae^{\frac{B}{\cos \theta}})(1 + Ce^{D\gamma} + E \cos^2 \gamma) \quad (4.32)$$

The distribution coefficients A, B, C, D, E must be chosen carefully for a realistic luminance distribution. The sky luminance $Y(\theta, \theta_s, \varphi)$ is then given as

$$Y = Y_z \frac{\mathcal{F}(\theta, \gamma)}{\mathcal{F}(0, \theta_s)}, \quad (4.33)$$

This model has been further improved and has been recently adopted in the CIE-2003 models [CIE 2004], changing the 5-parameter equation to

$$\mathcal{F}_{CIE2003}(\theta, \gamma) = (1 + Ae^{\frac{B}{\cos \theta}})(1 + C(e^{D\gamma} - e^{D\frac{\pi}{2}}) + E \cos^2 \gamma). \quad (4.34)$$

with values for $A \dots E$ tabulated for 15 standardised distributions from overcast to clear and polluted conditions (see Table 5.2). The CIE 2003 Standard Clear Sky #12 has been parameterised to be virtually indistinguishable from the older CIE 1994 model. The standard does not provide absolute zenith luminances Y_z , but one of the authors has provided another five-parameter equation and a table of typical values for the 15 sky types [KITTLER and DARULA 2006; DARULA and KITTLER 2002]. See section 5.4 for more details.

All of the models mentioned so far however only model luminance and therefore are not directly applicable for colour computer graphics, where spectral radiance would be required.

TAKAGI *et al.* [1990] use analytical luminance functions for various weather conditions and compute the *correlated colour temperatures* T_{cp} of skylight from an empirical formula found by their own measurements of sky luminance L [cd/m²] and colour temperature:

$$T_{cp} [K] = \frac{1.1985 \cdot 10^8}{L^{1.2}} + 6500 \quad (4.35)$$

The spectral distribution is then computed after JUDD *et al.* [1964]. For direct sunlight, they also take extinction by air, aerosols and ozone into account.

PREETHAM *et al.* [1999] present a practical (and up to now the only widely used) analytic skylight model for computer graphics, which models spectral solar and sky radiance and colour dependent on solar altitude and view direction. Their goal was to present a formula that returns the spectral radiance for an input direction, viewer's position, date and time under certain conditions. The Sun's position can be computed from latitude, longitude, time and date with the formulas described in the paper, which by its overall completeness allows a fast implementation.

Atmospheric conditions are controlled with a single parameter, the turbidity T (eq. 4.11). The model uses the formulae from PEREZ *et al.* [1993] (eq. (4.32)–(4.33)) for sky luminance Y and CIE chromaticity values x and y , and the three groups of values $A \dots E$ are computed with simple linear expressions in T . The authors further describe how to convert the CIE Yxy values to spectral radiance.

The model has been created as data fit against the model of NISHITA *et al.* [1996a] computed with 12 solar altitudes and turbidity values of $T \in [2 \dots 6]$. Unfortunately, it clearly fails for low turbidities, as will be described in more detail in chapter 5 [ZOTTI *et al.* 2007]. The model also incorporates the effects of aerial perspective, see section 4.4.1.

Figure 4.15 shows a comparison of the luminance distribution relative to zenith brightness for the mentioned models.

A further extension to this paper is made by HOFFMAN and PREETHAM [2002]. Absorption calculations and Rayleigh and Mie scattering calculations are performed on the vertex and fragment shaders of graphics hardware to achieve real time performance (Fig. 4.17).

RILEY *et al.* [2004] provide another analytic expression for single-scattered skylight, which is derived from first principles and suited for hardware implementation, but with a simplified flat-earth assumption.

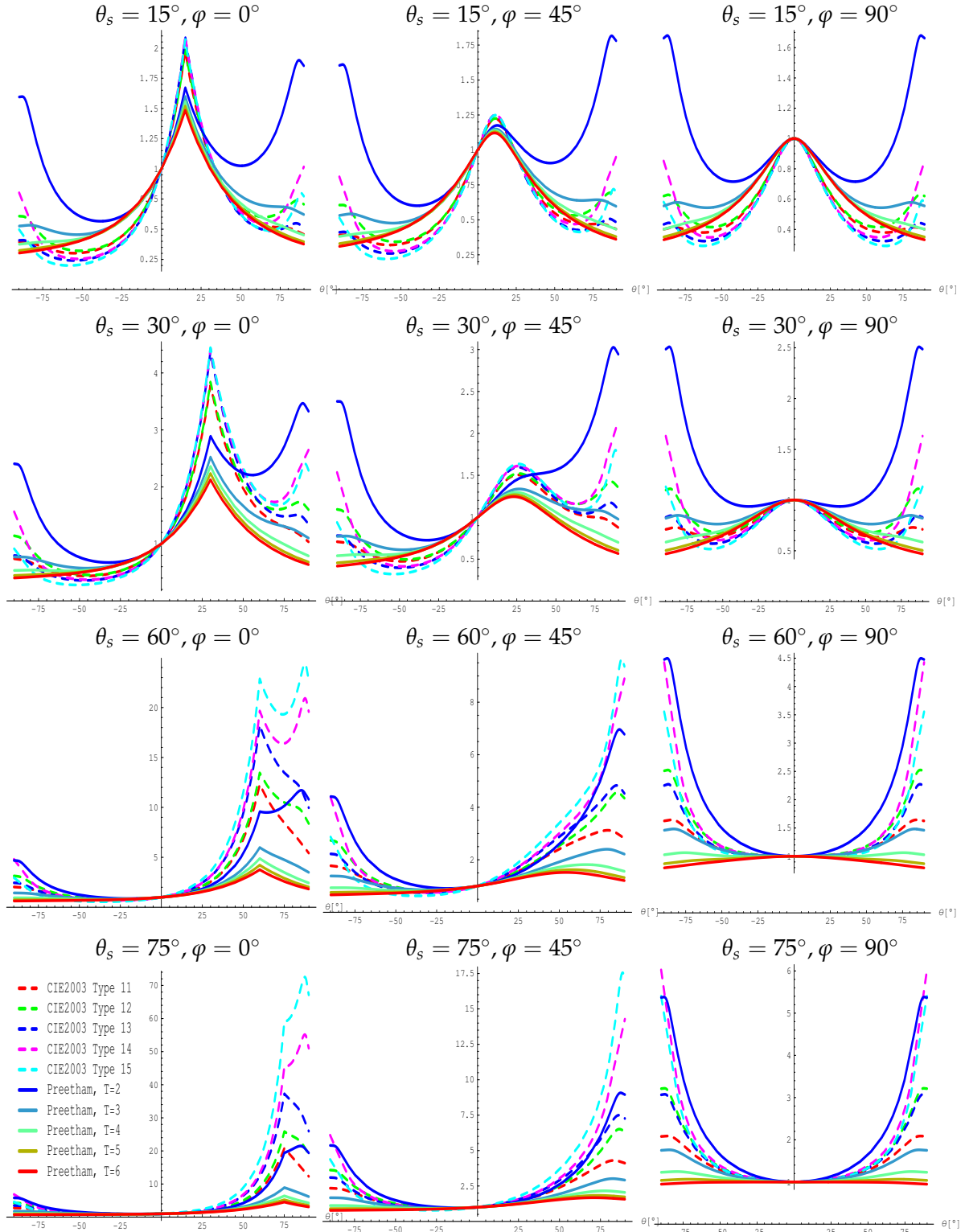


Figure 4.15: Comparison of vertical slices through zenith-relative sky luminance distributions following the CIE [2004] analytic skylight models 11 to 15 compared to the model of PREETHAM *et al.* [1999] for turbidities $T \in [2, 3, 4, 5, 6]$. The curve for the CIE 1994 clear-sky model is indistinguishable from CIE [2004] Type #12 and is not explicitly plotted.

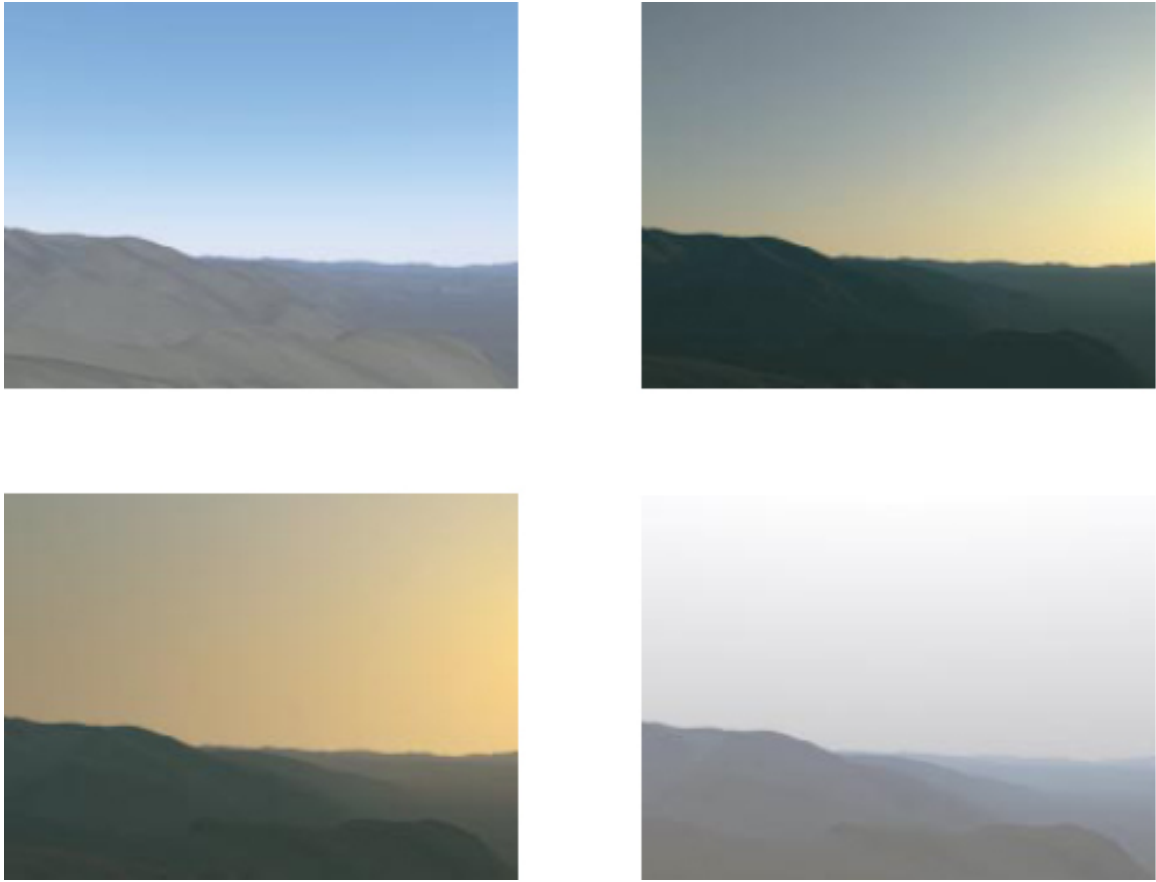


Figure 4.16: A scene at different times/turbidities T rendered with Preetham's model [from PREETHAM *et al.* 1999]: Upper left: morning, $T = 2$; Upper right: evening, $T = 2$; Lower left: evening, $T = 6$; Lower right: overcast, $T = 10$.

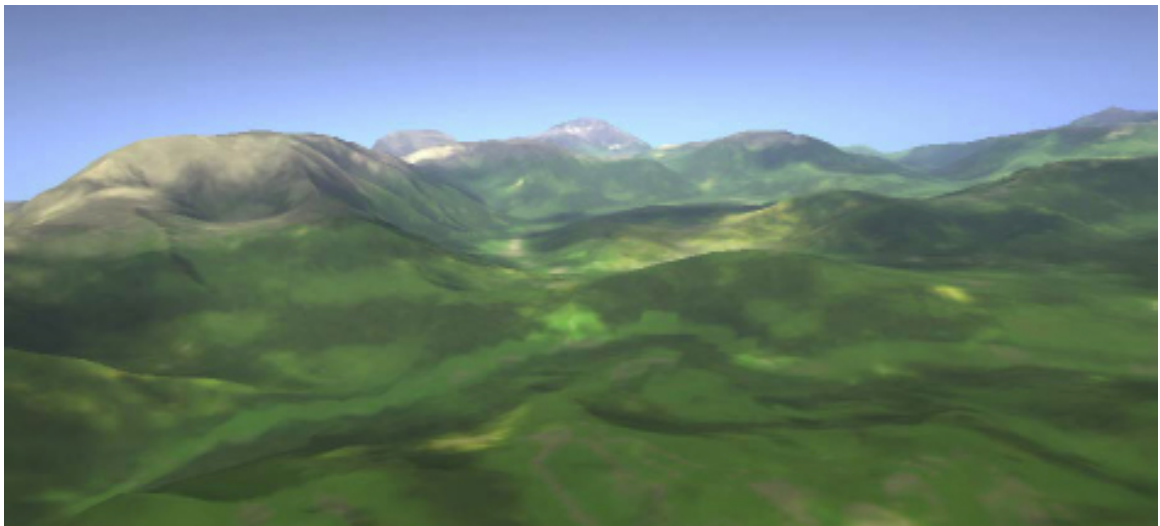


Figure 4.17: Real time atmospheric scattering [HOFFMAN and PREETHAM 2002] (from [PREETHAM 2003])

4.5.1 Polarisation

WILKIE *et al.* [2004] present an analytical model for skylight polarisation and describe how to use polarised light in a photorealistic rendering system. The authors make use of the Stokes vector mechanism known from the physics literature, where the radiation is not just described as scalar intensity, but as 4-component vector consisting of intensity and horizontal, vertical and circular polarisation components which have to be handled properly in all components of the rendering system. This model is not a complete skylight model, but an add-on description which could in principle be used with any clear-sky model, and the model of PREETHAM *et al.* [1999] is used for the illustrations in the paper. Unfortunately, skylight polarisation is strongest when the sky is very clean and dry (low turbidity), and here this carrier model in particular fails (*cf.* chapter 5). However, the differences in reflected views of polarised *vs.* unpolarised skylight are clearly demonstrated.

4.6 Photographic Methods for Skylight Capturing and Modelling

We can conclude that realistic clear-sky models are difficult to create, and approximations still often look artificial. Also, even if the models contain simulated clouds, usually they lack photorealism: the most striking outdoor scenery still is provided only by nature.

For computer graphics applications, *environment maps* have a long tradition, where the whole scene is surrounded by a textured sphere or box with some scene background. This background can also be used as scene illumination, however, traditional photographs suffer from a lack of dynamic range (discernible brightness values), so that scenes often look dull. In the last years, digital cameras have largely simplified the combination of several photographs made with different exposure settings into *High Dynamic Range* (HDR) images [DEBEVEC and MALIK 1997], which are able to store the full dynamic range of daylight scenes including the Sun. If used for scene illumination in a global illumination rendering system, *importance sampling* has to be used so that the area of the Sun, or bright clouds, is sampled more densely [*e.g.*, AGARWAL *et al.* 2003].

STUMPFEL *et al.* [2004] describe a system that is capable of capturing 17 photographic f-stops and thus the full dynamic range of a sky dome of 1:100000, including the Sun. Their digital single-lens reflex (D-SLR) camera is equipped with an 8 mm fisheye lens capable of capturing 180° of view. It is remote controlled by software that captures images which are analysed during download. The exposure time and/or aperture are changed and exposures taken until the whole sky dome has been captured with no region under- or overexposed in all images. To deal with the extremely bright Sun, which would cause saturated pixels even for the shortest possible exposure time, they use an ND3 neutral density filter, allowing only 0.1% light transmission. They have to correct their photos because of a colour shift introduced by the “neutral” filter. The image is further degraded due to vignetting, *i.e.*, increased brightness in the image center, which is dependent on the aperture setting (f-stop) and has to be corrected (this would be one of the corrections applied by “flat-fielding” scientific CCD images). The photographs are then stacked with appropriate scaling values derived from the exposure data (stored in the images’ EXIF information) to create HDR images which can be used both as scene background (with proper tone mapping to bring the brightness values in the range of computer screens!) and for image based lighting. However, to avoid bad sampling and therefore noise, they replace the brightest pixels (*i.e.*, the Sun) by an additional

directional light source which correctly simulates sunlight attenuated by the atmosphere depending on solar altitude and atmospheric conditions.

STUMPFEL [2004] and DEBEVEC *et al.* [2004] describe another approach towards sky capturing: photographing an aluminised dome mirror and a diffuse white sphere side by side, and then undistorting the reflected image from the spherical mirror. The reflection of the Sun is of course overexposed, but the missing energy can be reconstructed from analysing the diffuse reflection on the white sphere.

For practical applications in architecture and the building industry, the simulation with analytic models mentioned in section 4.5 is also constantly being verified and improved. For example, SPASOJEVIĆ and MAHDAVI [2005] apply luminance data retrieved from fisheye photographs calibrated with photometric measurements to an illumination simulation of a building interior and compare the results against measurements inside the physical room and an illumination simulation with the classical CIE overcast sky model. In their work, they show that the correlation between the indoor measurements and simulation with photo-based luminance values is much better than between indoor measurements and CIE overcast sky simulation, even if in both simulations the total integrated horizontal illumination is identical.

Traditionally, atmosphere physicists take spectra of the skylight with spectrometers. However, the required devices are expensive, and these measurements often take too much time if the spectral density over the whole sky has to be assessed, and therefore an attempt to use electronic cameras that show broadband sensitivity (CCD, CMOS) and an optimised selection of filters has been proposed by HERNÁNDEZ-ANDRÉS *et al.* [2004]. Later, LÓPEZ-ÁLVAREZ *et al.* [2005] describe a method how an optimal set of 3–5 filters can be selected using a simulated annealing algorithm (minimising of a penalty or cost function) to be able to reconstruct the spectral power distribution from only a few channels.

Also skylight polarisation is a topic where photographic methods have been applied. NORTH and DUGGIN [1997] use a 4-lens stereoscopic camera with four linear polarising filters oriented in multiples of 45° in combination with an aluminized dome mirror to capture the skylight polarisation. A difficulty here is the effect of the reflection on the dome mirror, which in itself changes the polarisation plane. Another problem was parallax image misalignment between the four images. LEE [1998a] uses a normal lens to acquire images of only parts of the sky, but with simplifications that require only two images. Both authors describe the use of conventional film-based cameras and digitise their colour slides.

Also STUMPFEL [2004] describes an extension to their basic setup with the aluminized dome mirror, so that with a polarising filter it is possible to capture sky polarisation with at least 3 exposures. A systematic approach should likely use an automatic filter rotator in front of the lens for reproducible results.

Using a camera with fisheye seems also to be possible at first thought if the whole camera is rotated, because the filter can only be mounted in a tiny slot between optics and sensor. On the other hand, polarisation results from the fisheye solution appear to suffer from reflection effects inside the lens [STUMPFEL 2004].

Chapter 5

A Critical Review of the Preetham Skylight Model

Every user of a model should be aware of its limitations.
And every creator of a model should publish them.

— *Anonymous Engineer's Wisdom and Dream*

The PREETHAM *et al.* [1999] skylight model is currently the most widely used analytic model of skylight luminance in computer graphics. Despite its widespread use, very little work has been carried out to verify the results generated by the model, both in terms of the luminance patterns it generates, and in terms of numerical reliability and stability.

We have implemented the model in Mathematica™, and we visualise and discuss those parameter ranges which exhibit problematic behaviour and compare the computed luminance values with references from the literature, especially the 15 standard skylight distributions published by the CIE. We have also performed luminance measurements on real cloudless skies, and compare these measurements to the predictions of the model. This chapter extends a paper from WSCG 2007 [ZOTTI *et al.* 2007].

5.1 Introduction

Over the past 20 years, the representation of the clear blue sky in computer graphics has been improved tremendously, from the then-common simple blue backgrounds to physically-based spectral models of skylight distribution.

A brute-force numerical simulation of radiation transport in the atmosphere still takes several hours on contemporary fast PCs, so for most practical applications, a fast approximate model of some sort is commonly used.

This chapter discusses the sky luminance values in the widely used skylight model published by PREETHAM *et al.* [1999]. We contrast its luminance distributions to comparable distributions of the latest CIE skylight models. It appears that the range of atmospheric conditions Preetham's model can represent is more limited than previously assumed.

The task of this chapter is not to completely invalidate Preetham's model. We want to demonstrate, however, that it is not a bullet-proof, complete, generally valid model and should always be used with its limitations in mind.

The rest of the chapter is organised as follows: For brevity's sake, we do not repeat the entire state of the art in skylight models (see chapter 4), but only mention the works immediately used in this chapter. We then concentrate on the Preetham model instead, introduce the key components of the model, and in the largest section we show numerous colour-coded illustrations which help to identify where this model is applicable, and also how it compares to the recent CIE models, as well as to our own measurements.

5.2 Related Work

For applications in the computer graphics domain, PREETHAM *et al.* [1999] has published a simple analytic skylight model that promised to simulate daylight luminance and colour values very fast, and has seen wide acceptance as the current *de-facto* standard model for computer graphics.

For illumination planning purposes, the CIE and ISO committees recently have released a joint standard series of analytic models for skylight luminance of clear and overcast skies [CIE 2004], which supersede previous standards. These models lack both spectral and colour information, so their immediate application to computer graphics is not possible; however, they still provide a valuable reference and are discussed in section 5.4.

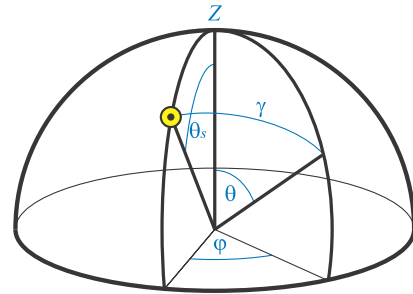
5.3 Preetham's Model

This analytic model [PREETHAM *et al.* 1999] was created by fitting simulation data from the skylight model of NISHITA *et al.* [1996a] to the sky luminance approximation formula of PEREZ *et al.* [1993], which has also been adopted by the CIE in a modified form [CIE 2004]. In the appendix of Preetham's paper, all necessary formulae are given for the implementation of the model. However, no comparison to measurements taken in nature seems to have been performed, and the paper is rather silent on limitations of the model. The only hint towards limitations is the statement that simulation and fitting only took turbidities in the range 2...6 into account.

5.3.1 Coordinate System

In the model, several angles are required:

- θ_s solar angle from zenith
- θ view angle from zenith
- φ view azimuth from solar azimuth
- γ angle between solar and view direction, where



$$\cos \gamma = \begin{pmatrix} \sin \theta_s \\ 0 \\ \cos \theta_s \end{pmatrix} \cdot \begin{pmatrix} \sin \theta \cos \varphi \\ \sin \theta \sin \varphi \\ \cos \theta \end{pmatrix}. \quad (5.1)$$

For simplicity, the solar azimuth is always taken as 0° , and the sky obviously is symmetric around the solar azimuth.

5.3.2 Turbidity

The key parameter to describe the influence of haze and aerosols in Preetham's model is the atmospheric turbidity T , defined as the ratio of the optical thickness of the atmosphere including haze to that of a pure-air molecular atmosphere:

$$T = \frac{\tau_m + \tau_h}{\tau_m} \quad (5.2)$$

A (hypothetical) perfectly clean atmosphere has $T = 1$, and (rare, but observable) values of about 1.25 can be called "exceptionally clear", and 1.6 "very clear", as seen in figure 3 of Preetham's paper. Haze has $T \gtrsim 10$, and at this point at the latest we should also stop using a "clear-sky" model. Preetham concedes that turbidity is only a rough estimate for atmospheric conditions; it is quite a useful parameter nonetheless, since it offers an intuitive way of controlling the appearance of outdoor scenes.

5.3.3 A problem with zenith luminance Y_z

PREETHAM *et al.* [1999, A.2] give zenith luminance as

$$Y_z [\text{kcd/m}^2] = (4.0453T - 4.9710) \tan \chi - 0.2155T + 2.4192 \quad (5.3)$$

where

$$\chi = \left(\frac{4}{9} - \frac{T}{120}\right)(\pi - 2\theta_s) \quad (5.4)$$

Figure 5.1 shows values of Y_z dependent on solar zenith angle θ_s and turbidity T . As can be seen in the plot, there are regions (marked red) near the border of seemingly feasible input values where *the model yields negative zenith luminance!* So, from this figure alone, it is obvious that Preetham's model should not be used for very clear air ($T \lesssim 1.6$), and also values near sunrise/sunset ($\theta_s > 85^\circ$) are apparently problematic for high turbidities, where the model fails for turbidities $T \gtrsim 10$.

5.3.4 Sky luminance Y

The sky luminance $Y(T, \theta, \theta_s, \varphi)$ is given as

$$Y = Y_z \frac{\mathcal{F}(\theta, \gamma)}{\mathcal{F}(0, \theta_s)}, \quad (5.5)$$

where

$$\mathcal{F}(\theta, \gamma) = (1 + Ae^{\frac{B}{\cos \theta}})(1 + Ce^{D\gamma} + E \cos^2 \gamma) \quad (5.6)$$

and A, B, C, D, E are given as functions of T .

Table 5.1 shows plots of Y in the solar/antisolar vertical, and the vertical 90 degrees from the solar azimuth. It can be seen that, for turbidities $T < 2$, luminance values below zero, or extremely high values (reddish brown) are regularly found close to the horizon. Also, for low Sun angles (large θ_s) and large values of turbidity T , sky luminance would be negative according to this model.

Tables 5.10 and 5.11 show skylight distributions relative to the zenith brightness and absolute luminance values for different values of T and θ_s .

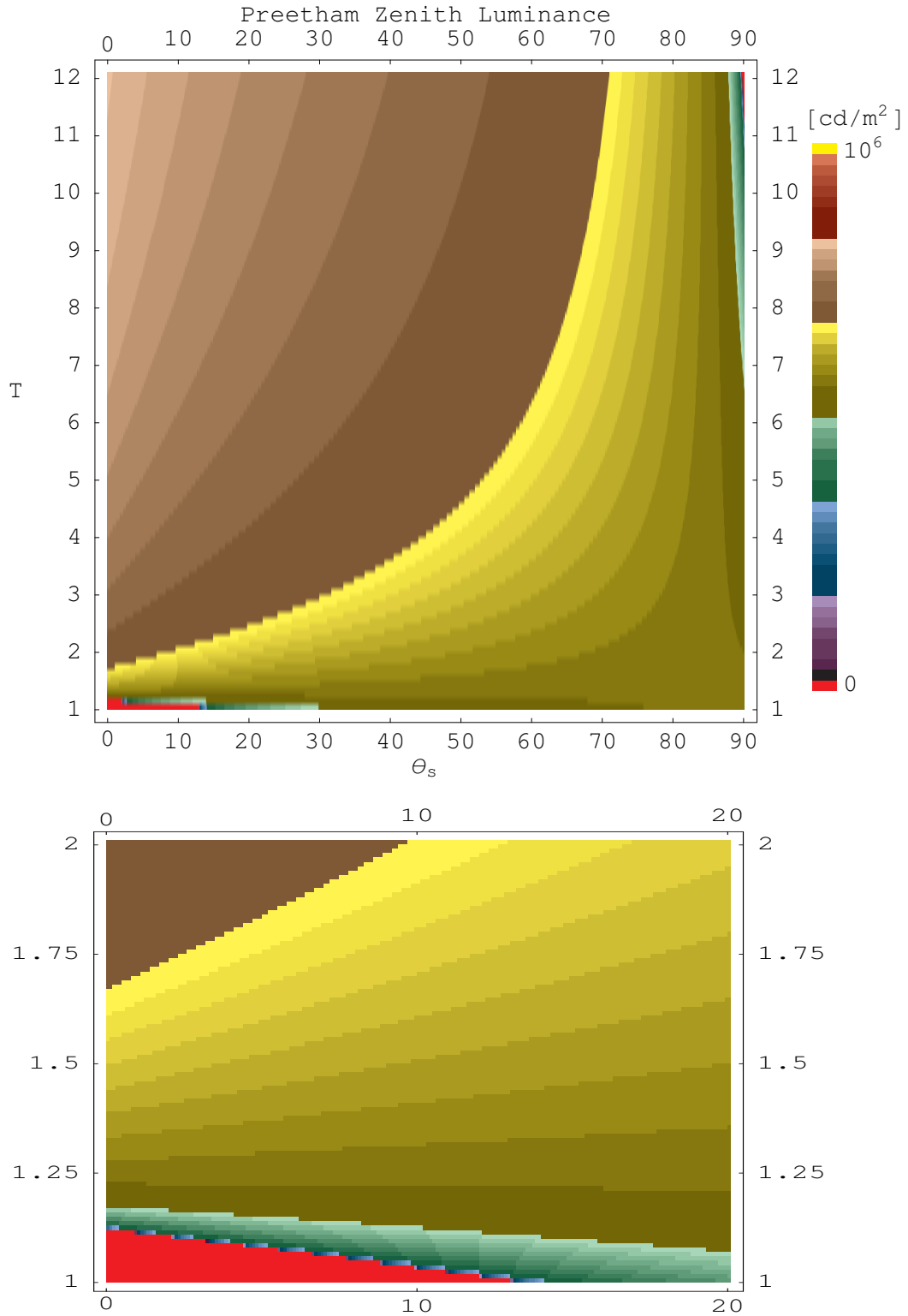
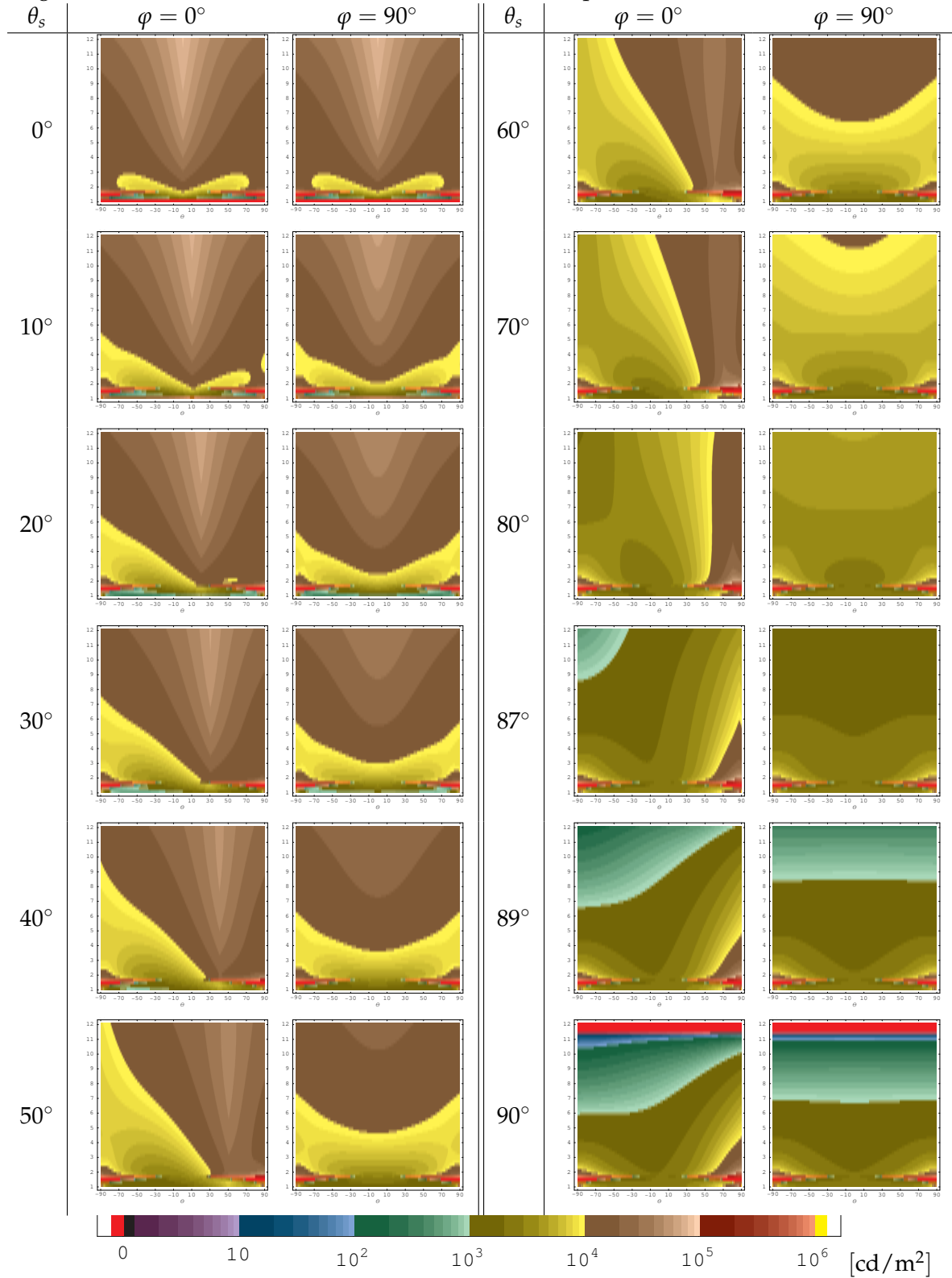


Figure 5.1: Preetham zenith luminance Y_z (5.3) as function of solar zenith angle θ_s and turbidity T . Negative values (physically meaningless) are depicted in red. The lower image magnifies the bottom left corner.

Table 5.1: Absolute sky luminance Y in the Preetham model for various Solar zenith angles θ_s , as function of view angle θ and turbidity $T \in [1 \dots 12]$. Each left column shows data in the solar vertical, the right columns show the vertical 90° sideways from the solar vertical. Negative values, *i.e.*, areas where the model fails, are depicted in red.



5.4 CIE Standard Sky

The CIE, together with the ISO, has recently published fifteen standard sky luminance distributions [CIE 2004], which are described in Table 5.2. These distributions were created and refined from a long series of skylight measurements and previous standards. A sixteenth type describes the “traditional” overcast sky.

The typical application of the CIE Standard General Sky models is illumination estimation for architectural design [KITTLER and DARULA 2006]. Unfortunately the model only provides luminance data, so that direct application to (colour) computer graphics is not possible.

From the descriptions it appears that the only CIE skylight distributions comparable to the Preetham model are CIE Types 11–15. Note that the CIE skylight distribution type designations are in no way related to Preetham’s turbidity! The CIE models do not have a single intuitive parameter to describe atmospheric conditions. However, they also use eq. (5.5), but with a modified form of the Perez equation (5.6), which, using the symbols from above, is:

$$\mathcal{F}_{CIE2003}(\theta, \gamma) = (1 + Ae^{\frac{B}{\cos \theta}})(1 + C(e^{D\gamma} - e^{D\frac{\pi}{2}}) + E \cos^2 \gamma). \quad (5.7)$$

The values A, B (luminance gradation parameters) and C, D, E (scattering indicatrix parameters) are tabulated for the 15 standardised distributions [CIE 2004; DARULA and KITTLER 2002; KITTLER and DARULA 2006]. The sixteenth distribution is the classic formula of MOON and SPENCER [1942]:

$$Y_{CIE2003, \#16}(\theta) = Y_z \frac{1 + 2 \cos \theta}{3} \quad (5.8)$$

Table 5.8 shows skylight luminance distributions of the 16 CIE 2003 Standard General Skylight distributions relative to the zenith luminance.

The standard does not provide absolute zenith luminances Y_z , but KITTLER and DARULA [2006] and DARULA and KITTLER [2002] provide another five-parameter equation and a ta-

Table 5.2: The CIE 2003 Standard General Sky models [CIE 2004]

-
- | | |
|----|--|
| 1 | CIE Standard Overcast Sky: Steep luminance gradation towards zenith, azimuthal uniformity |
| 2 | Overcast, with steep luminance gradation and slight brightening towards the Sun |
| 3 | Overcast, moderately graded with azimuthal uniformity |
| 4 | Overcast, moderately graded and slight brightening towards the Sun |
| 5 | Sky of uniform luminance |
| 6 | Partly cloudy sky, no gradation towards zenith, slight brightening towards the Sun |
| 7 | Partly cloudy sky, no gradation towards zenith, brighter circumsolar region |
| 8 | Partly cloudy sky, no gradation towards zenith, distinct solar corona |
| 9 | Partly cloudy, with the obscured Sun |
| 10 | Partly cloudy, with brighter circumsolar region |
| 11 | White-blue sky with distinct solar corona |
| 12 | CIE Standard Clear Sky, low luminance turbidity |
| 13 | CIE Standard Clear Sky, polluted atmosphere |
| 14 | Cloudless turbid sky with broad solar corona |
| 15 | White-blue turbid sky with broad solar corona |
| 16 | CIE Traditional Overcast Sky |

ble of typical values for sky types 1–15, which are applicable for solar zenith angles $10^\circ \lesssim \theta_s < 90^\circ$ [DARULA and KITTLER 2002]. With the symbols from above, it is

$$\gamma_z = \frac{D_v}{E_v} \left(\frac{B' \cos^{C'} \theta_s}{\sin^{D'} \theta_s} + E' \cos \theta_s \right). \quad (5.9)$$

Here, D_v is the exterior diffuse/sky horizontal illuminance, E_v the extraterrestrial horizontal illuminance (both in lux), and D_v/E_v is tabulated with maximal and minimal values, if applicable both for sunny and clouded conditions. B', C', D', E' are parameters tabulated for the 15 distributions and not related to A, B, C, D, E above. Also note that equation (5.9) obviously provides dubious results with a very low Sun.

Table 5.9 shows all 15 “regular” CIE 2003 Standard General Skylight distributions with their given maximum and minimum recommended values.

5.5 Measurements

For comparison with the Preetham model, we made several measurement cycles of skylight distributions on cloudless skies using a Minolta LS-110 Luminance Meter on a leveled photography tripod with coordinate indications. Tables 5.3–5.7 show 5 typical results for bright, sunny days, taken on the outskirts of Vienna.

The indicated solar zenith distance θ_s was valid at the begin of each measurement cycle, and measurement started in the solar vertical, which points towards the right side in each all-sky plot, and measurements were performed in a grid with steps of 30° in azimuth and 15° in altitude. The Sun was sinking during the half-hour measurements, causing an apparent discontinuity in the solar vertical. However, what can be clearly seen is the bright area around the Sun, the size of which depends most on atmospheric conditions, a distinct dark zone on the hemisphere opposite the Sun and a slight overall horizon brightening.

To estimate the turbidity, we tried to invert Preetham’s equation for zenith brightness (eq. 5.3) with the measured zenith luminance values as input. From Table 5.1, the resulting turbidities would have been in the range 1.2 . . . 1.8, respectively, when the Sun’s altitude was 40° , however, turbidity values for the quite low zenith brightness at the lower solar altitudes are entirely unattainable by the model.

5.6 Comparison

Table 5.10 shows skylight distributions of the Preetham model for various values of turbidity T and solar zenith angle θ_s , relative to the zenith luminance. Each small circle represents a full 180° hemisphere in stereographic projection, which best shows the horizon area. With increasing θ_s , the Sun sinks towards the right horizon.

To show the possible effect of the different variants of the Perez equation for \mathcal{F} (eq. 5.6 vs. eq. 5.7), the Preetham model was also evaluated with the CIE 2003 formula for \mathcal{F} , and the result is shown in the lower half of each plot. The difference appears to be very small, but does nothing to improve the shortcomings described in the next paragraphs, so we cannot recommend using it in this context.

Table 5.11 shows skylight distributions for the same data, again with both variants of the function \mathcal{F} , but providing absolute luminance values from the Preetham model. Compared

to the CIE standard with recommended values from KITTLER and DARULA [2006] (Tables 5.8 and 5.9) and real-world measurements (Tables 5.3–5.7) we note the following shortcomings:

- The results for low turbidities $T < 2$ are definitely wrong: A very clear atmosphere only has a moderate brightening along the horizon (*cf.* esp. Table 5.6), and not the wide, extremely bright zone visible in Figure 5.11 and the azimuthal slice plots in Tables 5.3–5.7, leading to a totally unrealistic “horizon glow”. Even for $T \lesssim 2.4$ the horizon is shown unnaturally bright when the Sun is low ($\theta_s \gtrsim 60^\circ$), and the brightening around the Sun is too weak.
- The Preetham model does not properly reproduce the noticeable darkening of the sky in the antisolar hemisphere when the Sun is low, with luminance values about 2–5 times too high.
- Also, the brightness peak towards the Sun is not as steep as it can be measured or is modelled by the CIE Clear-Sky models.

The CIE Clear Sky (Type 12) is best approximated with $T \approx 2.3 \dots 2.5$, however, differences remain, esp. the mentioned darkening is too weak when $\theta_s \gtrsim 60^\circ$. Comparing Preetham and CIE models for higher turbidities, we found some potentially usable similarities, but with different absolute luminances (with values from KITTLER and DARULA [2006]):

Preetham T	10	5	2.9
CIE Type	6	7	10
$Y_{Pr}/Y_{CIE} _{15^\circ < \theta_s < 70^\circ}$	> 2	$\gtrsim 1$	$\lesssim 1.25$

5.7 Conclusion and Future Work

We have provided comparisons between the sky luminance values of the popular Preetham skylight model, the ISO/CIE 2003 Standard General Sky luminance distributions and several measurements taken by ourselves.

Our measurements of typical mid-European early autumn clear sky luminance distributions yielded luminance patterns which are not reproducible by the Preetham model, but which are reasonably close to those from the CIE Clear Sky models.

From the way it was created, the Preetham model can at most be as good as the numeric skylight model by NISHITA *et al.* [1996a] with simulation of (at most) second order scattering. The data fit was done for turbidities 2...6, so outside this range, it should not be used. We showed it even breaks down numerically for $T \lesssim 1.9$ and $T \gtrsim 10$.

A truly universal analytic skylight model certainly would be desirable for outdoor scenes, when the skylight should be used as light source, and the sky as visible background. A better simulation of atmospheric scattering such as that by HABER *et al.* [2005] should be used as base to improve or replace Preetham’s model, so that a data fit will hopefully provide more natural results.

5.8 Figures and Tables

The following tables of figures show the Mathematica™ plots comparing the Preetham model with the CIE2003 General Standard Sky models and our own measurements of sky luminance.

Table 5.3: Comparison of the sky luminance distribution of a very clear sky measured in Vienna on 23.9.2006 12:55 to 13:37CEDT starting with solar zenith angle $\theta_s = 50^\circ$ with values from Preetham's model and values from CIE Type 12. Values recommended by DARULA and KITTLER [2002] are in the gray range. According to eq. (5.3), turbidity was $T = 1.3$, where the model fails in most parts of the sky.

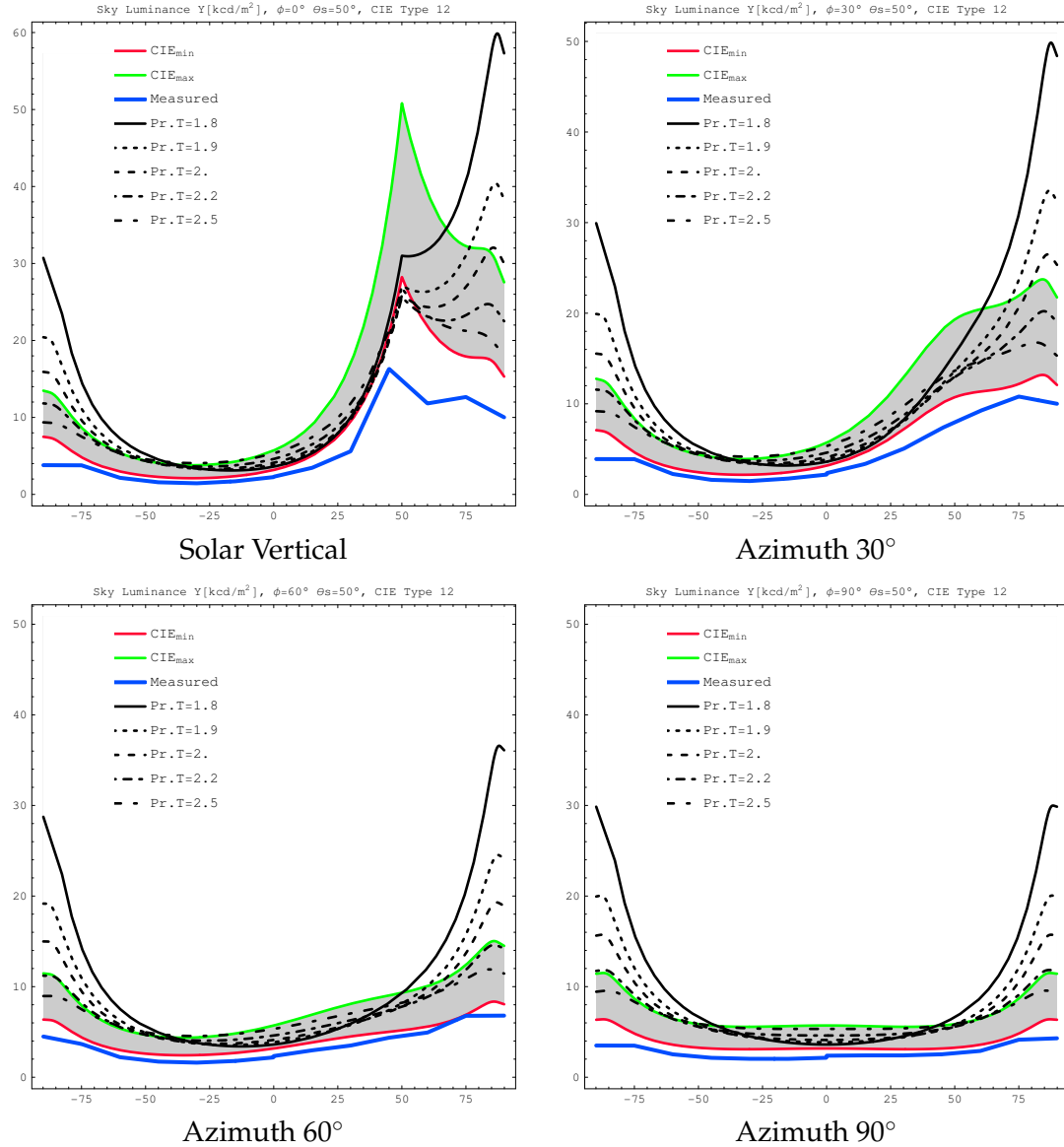
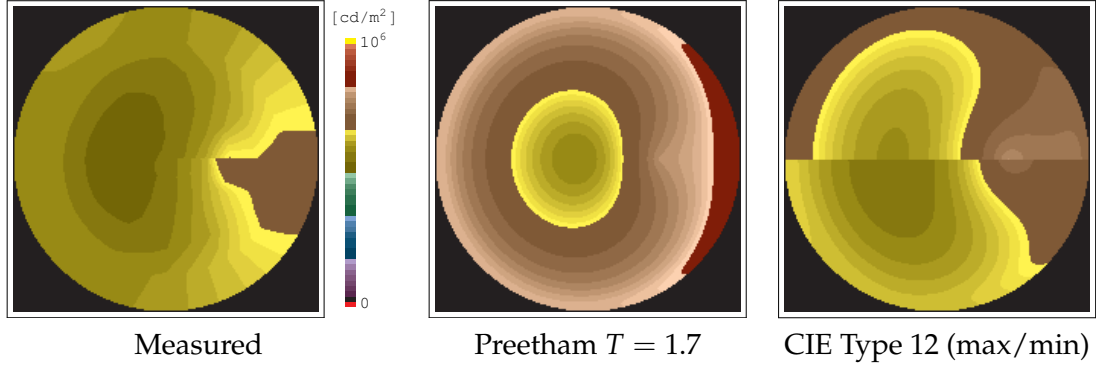


Table 5.4: Comparison of the sky luminance distribution of a very clear sky measured in Vienna on 23.9.2006 16:54 to 17:22CEDT starting with solar zenith angle $\theta_s = 72^\circ$ with values from Preetham's model and values from CIE Type 12. Values recommended by DARULA and KITTLER [2002] are in the gray range. According to eq. (5.3), turbidity was as low as 1.3, where the model fails in most parts of the sky.

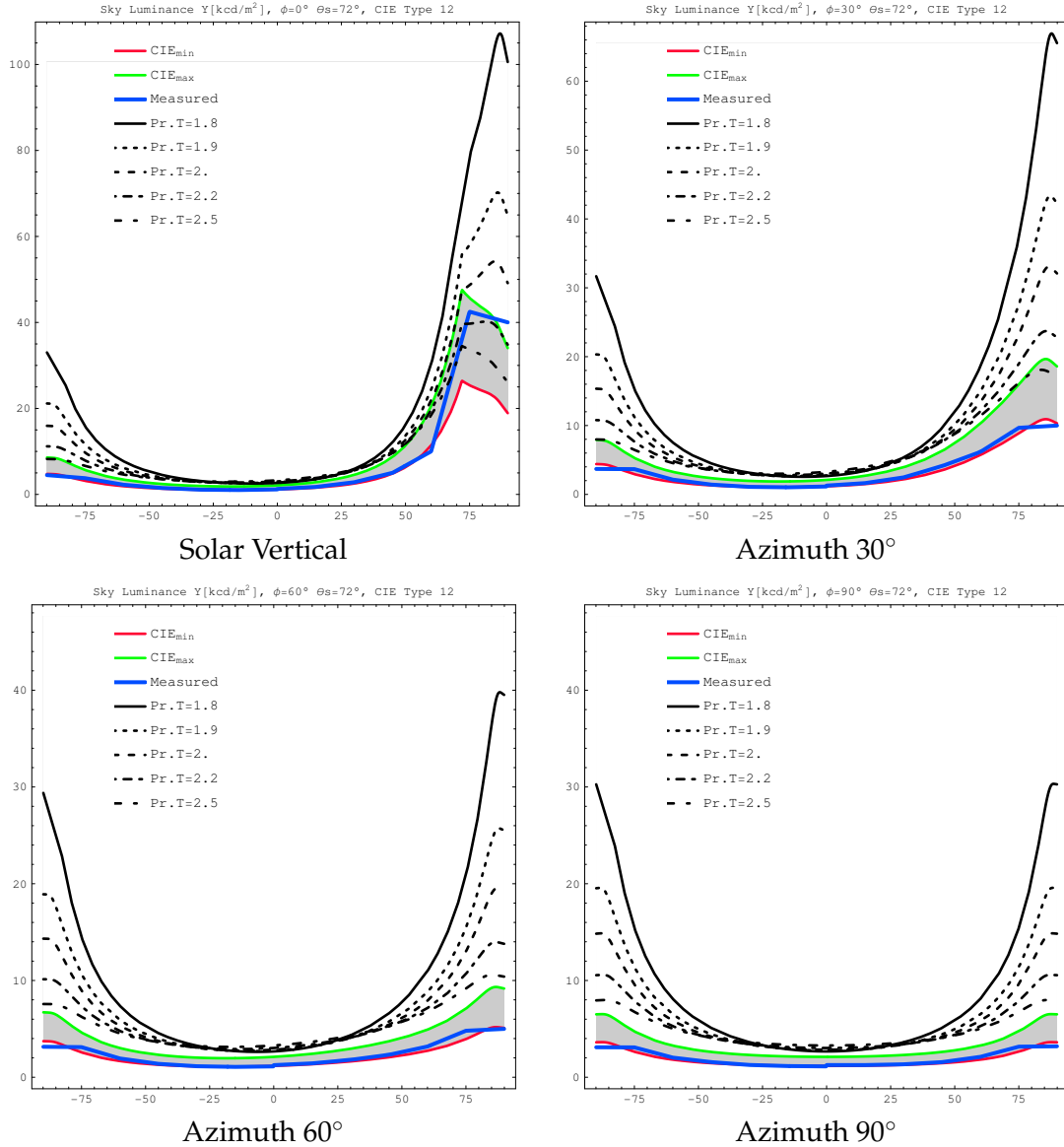
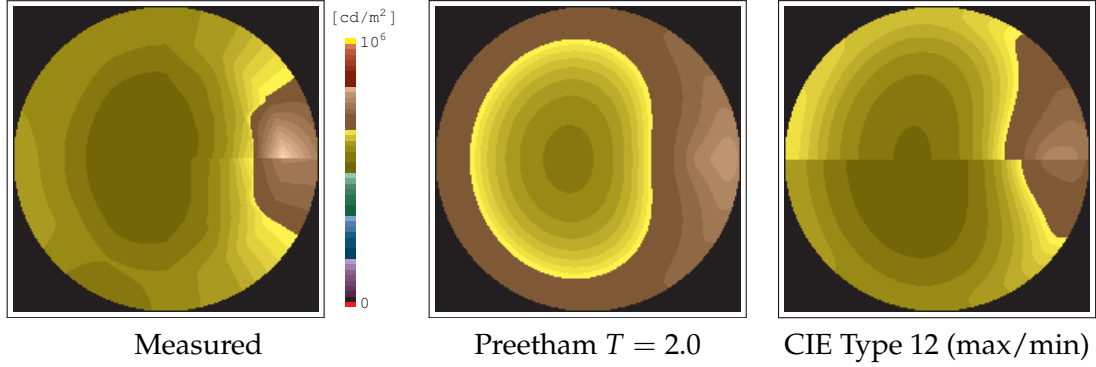


Table 5.5: Comparison of the sky luminance distribution of a slightly hazy sky measured in Vienna on 24.9.2006 at solar zenith angle $\theta_s = 50^\circ$ with values from Preetham's model and values from CIE Type 12. Values recommended by DARULA and KITTLER [2002] are in the gray range.

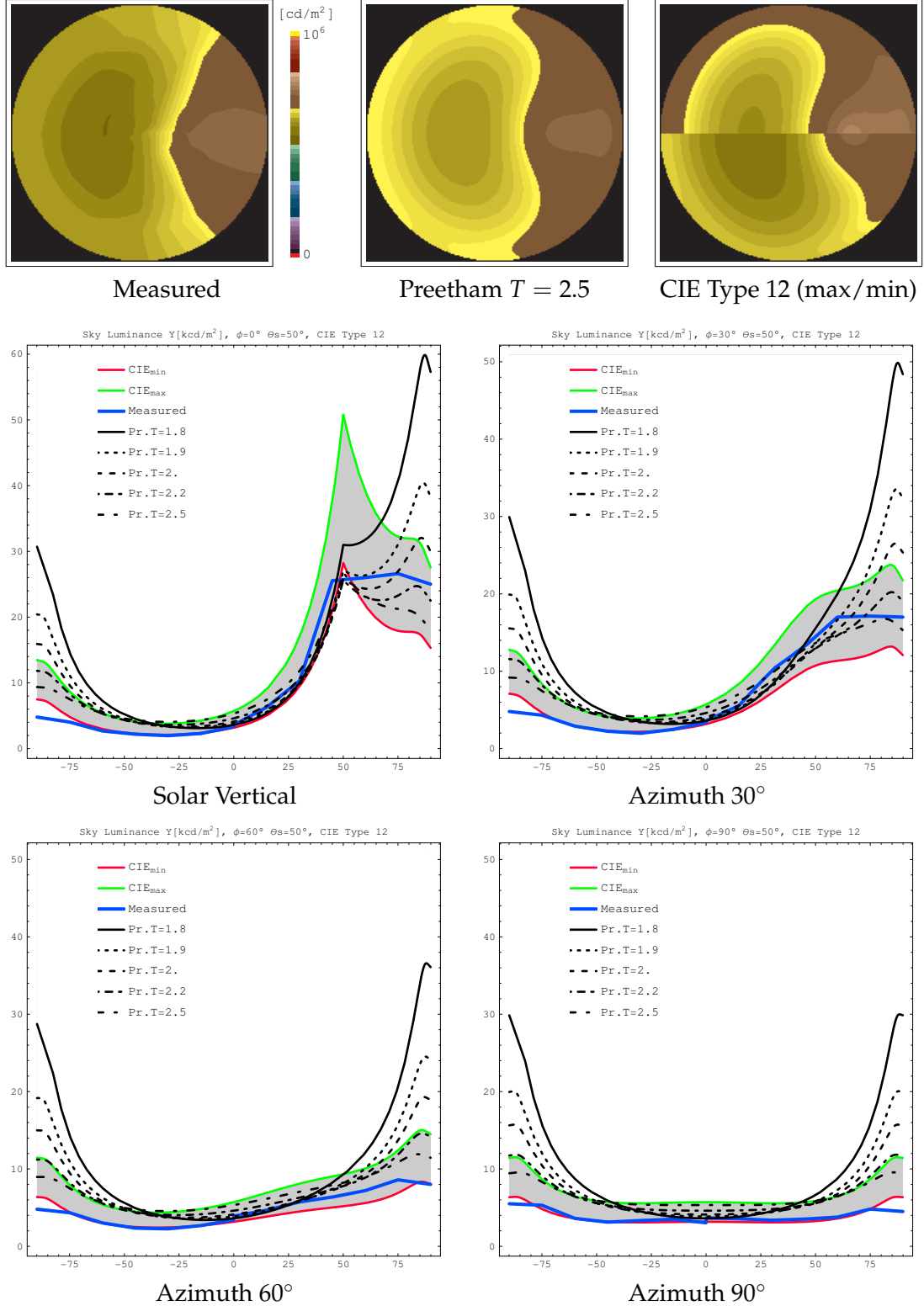


Table 5.6: Comparison of the sky luminance distribution of a clear sky measured in Vienna on 24.9.2006 starting at 17:38CEDT at solar zenith angle $\theta_s = 80^\circ$ with values from Preetham's model at $T = 2.2$ and values from CIE Type 12. According to eq. (5.3), turbidity would be as low as 1.2, where the model fails in parts of the sky. We show a comparison with the Preetham model at $T = 2.2$. The distribution is of similar shape, but far too bright.

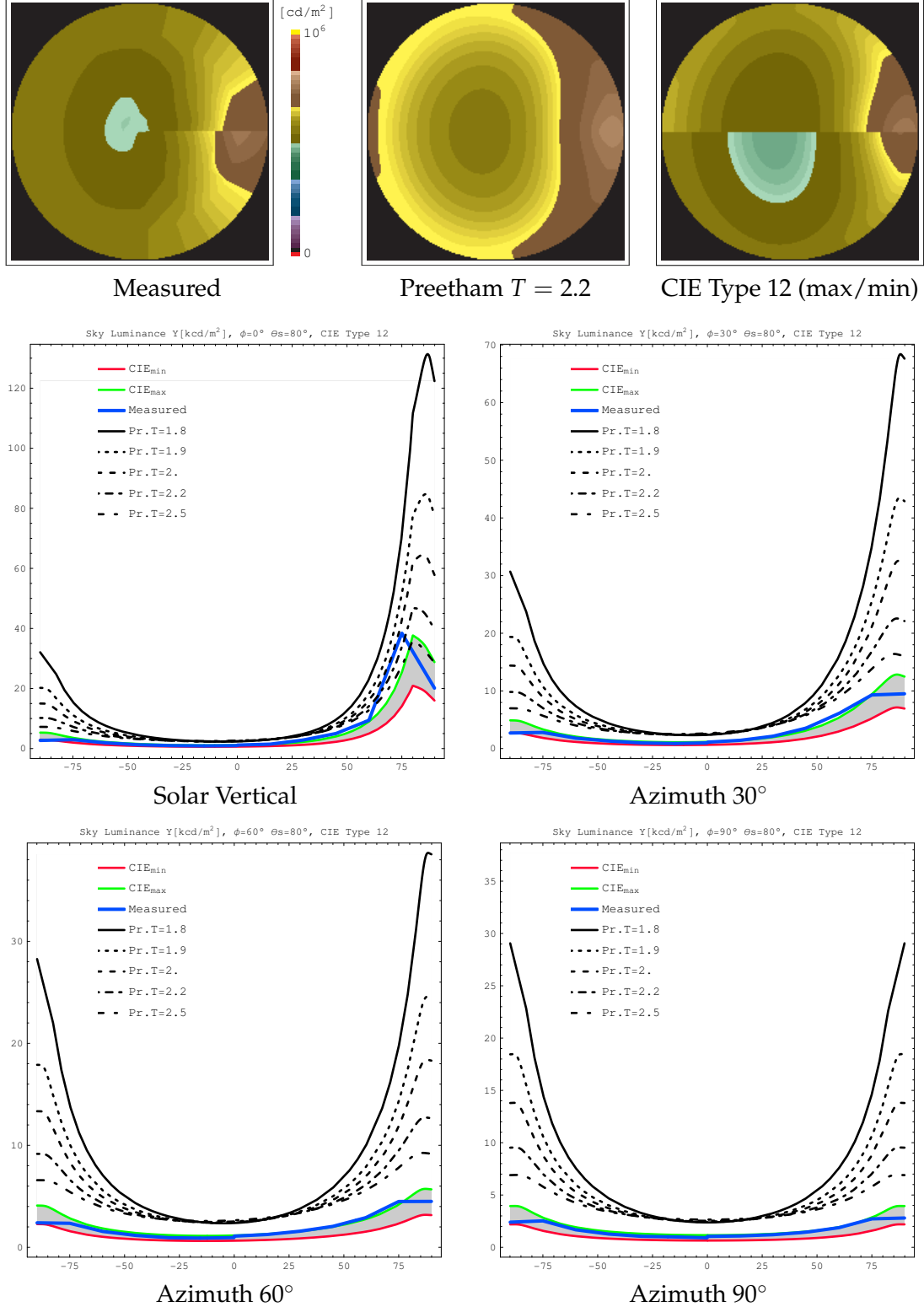


Table 5.7: Comparison of the sky luminance distribution of an extremely clear sky measured in Vienna on 6.10.2006 at solar zenith angle $\theta_s = 60^\circ$ with values from Preetham's model and values from CIE Type 12. According to eq. (5.3), turbidity was $T = 1.5$, where the model fails in parts of the sky. We show a comparison with the Preetham model at $T = 1.8$, which already shows completely unrealistic values.

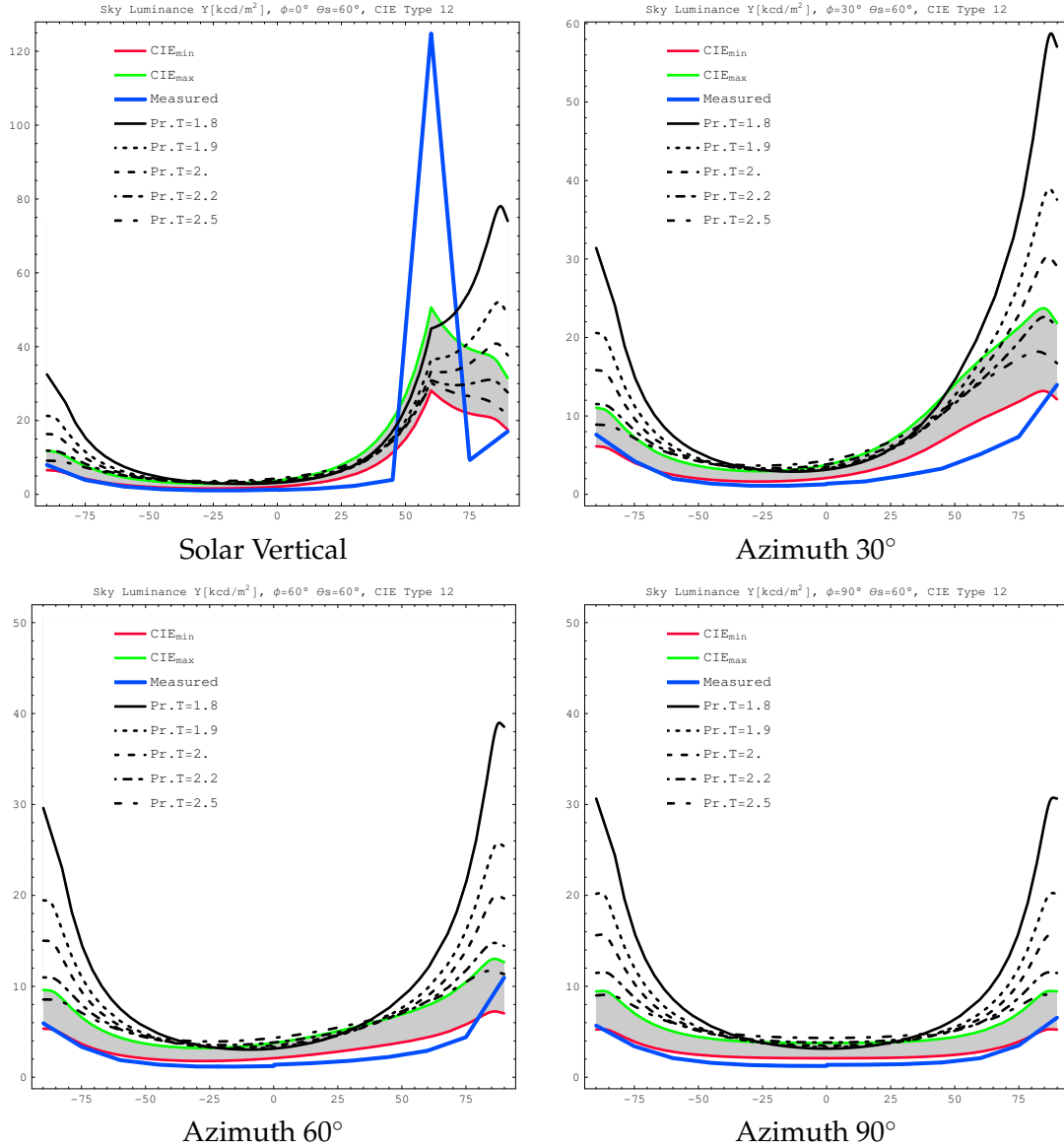
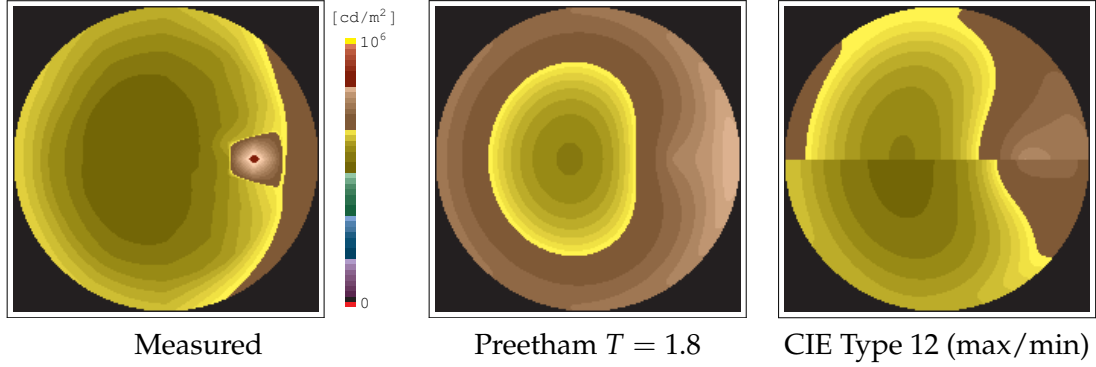


Table 5.8: Relative sky luminance distributions of the 16 CIE 2003 Standard General Sky models [CIE 2004], for various solar zenith distances θ_s . The scale is logarithmic in percent of zenith luminance, and colour hues are used to separate the decades of magnitude.

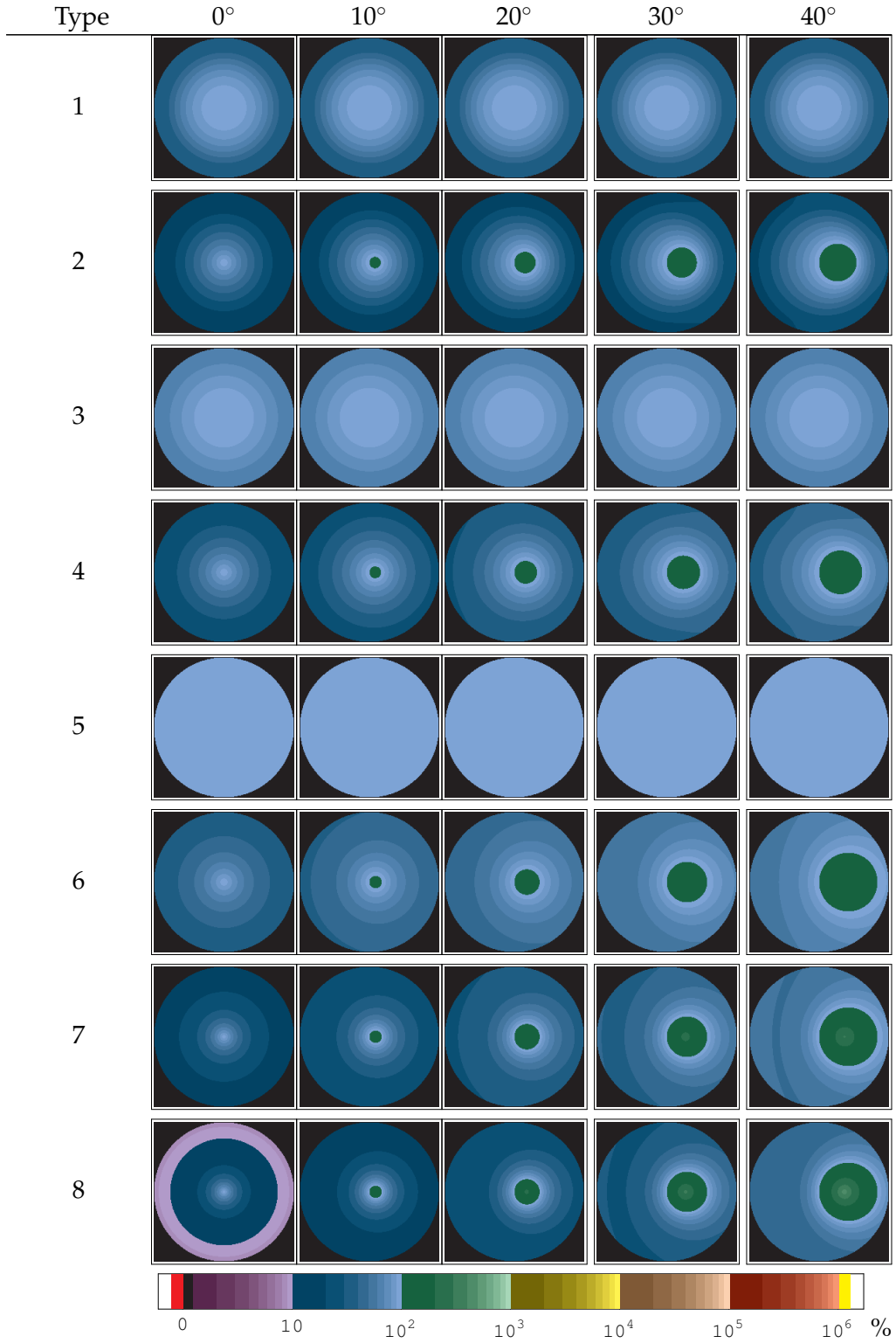


Table 5.8: (cont.) Relative sky luminance distributions of the 16 CIE 2003 Standard General Sky models [CIE 2004], for various solar zenith distances θ_s . The scale is logarithmic in percent of zenith luminance, and colour hues are used to separate the decades of magnitude.

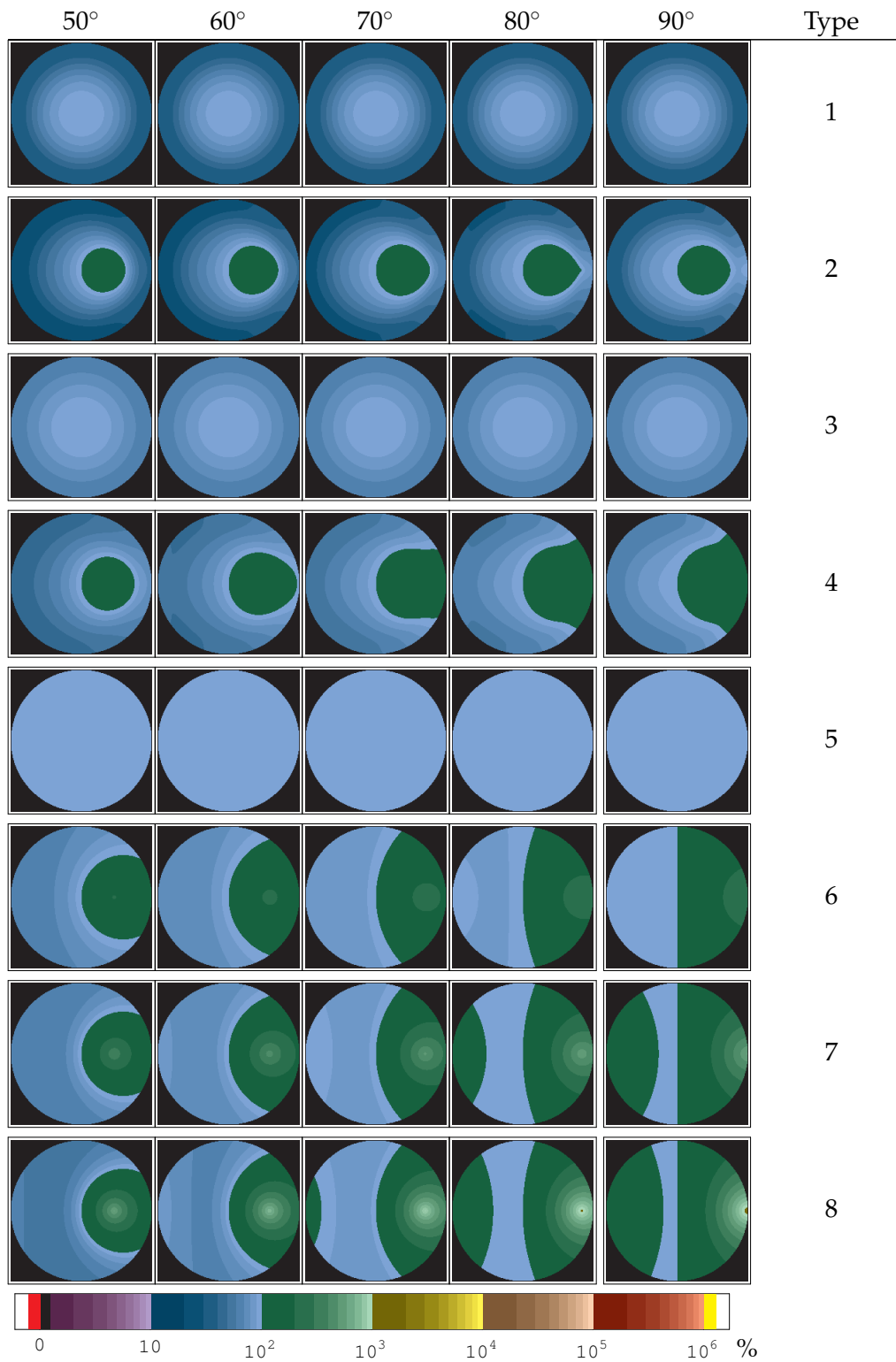


Table 5.8: (cont.) Relative sky luminance distributions of the 16 CIE 2003 Standard General Sky models [CIE 2004], for various solar zenith distances θ_s . The scale is logarithmic in percent of zenith luminance, and colour hues are used to separate the decades of magnitude.

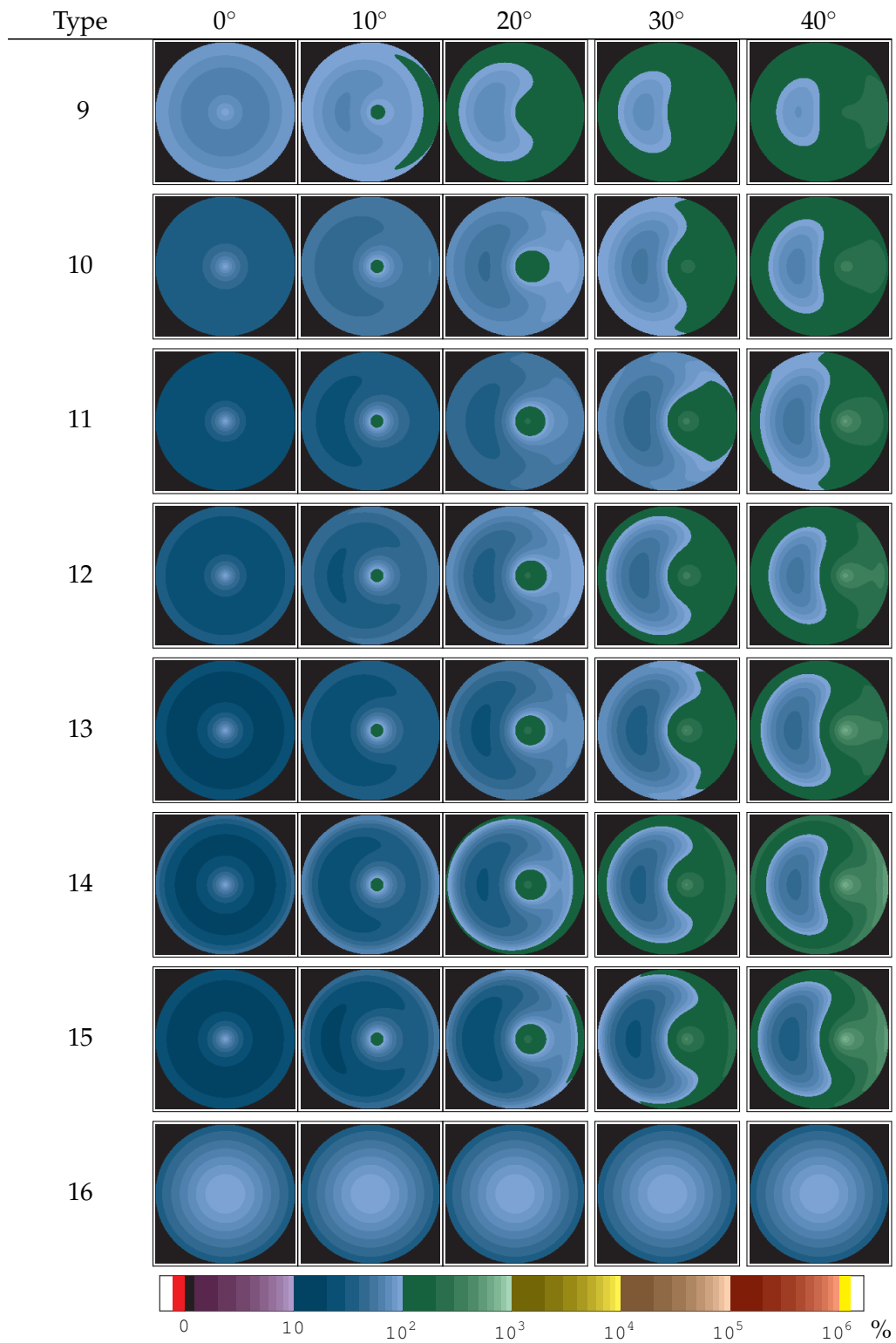


Table 5.8: (cont.) Relative sky luminance distributions of the 16 CIE 2003 Standard General Sky models [CIE 2004], for various solar zenith distances θ_s . The scale is logarithmic in percent of zenith luminance, and colour hues are used to separate the decades of magnitude.

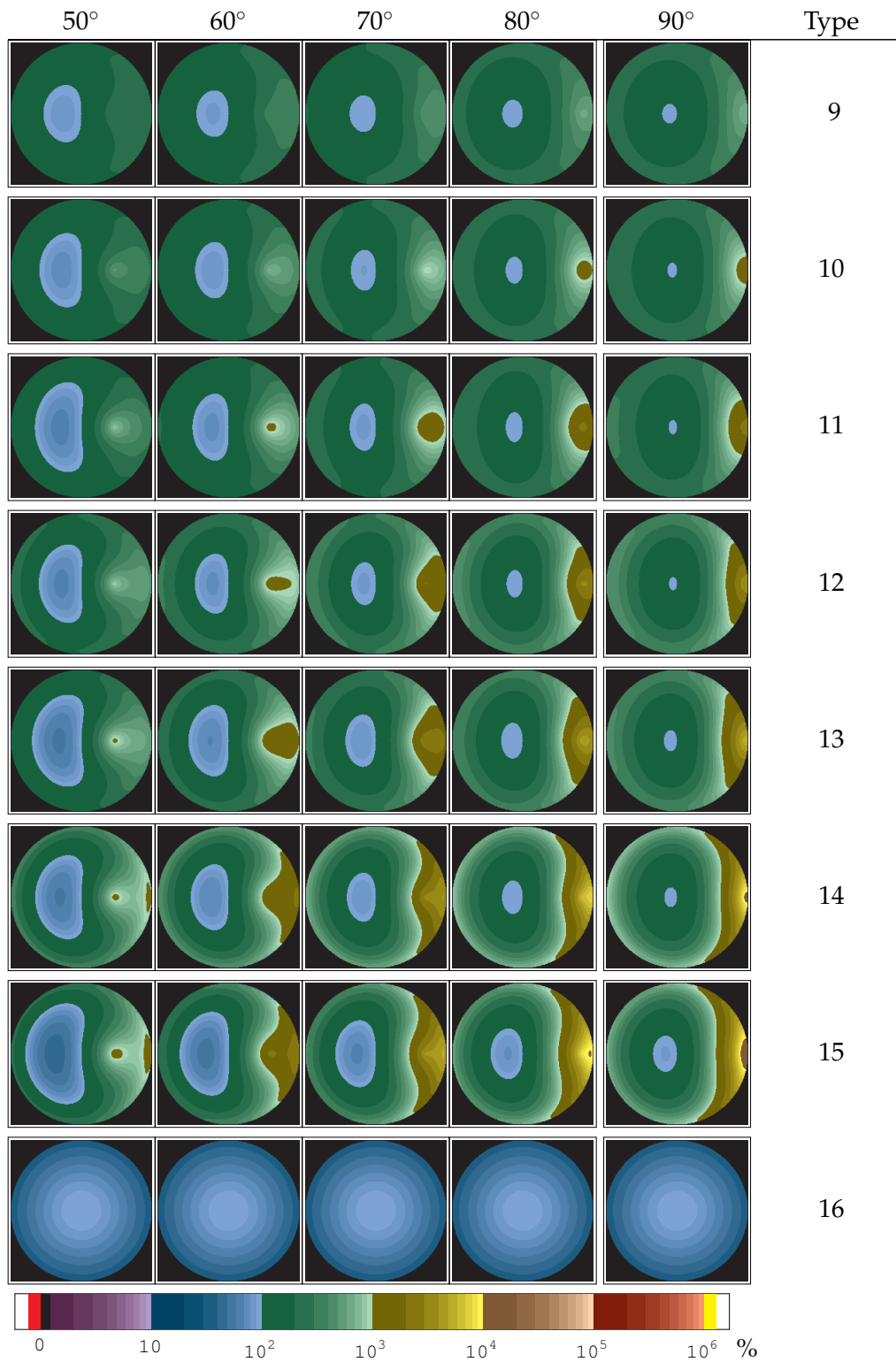


Table 5.9: Absolute sky luminance distributions based on the CIE 2003 Standard General Sky models, for various solar zenith distances θ_s . Each upper half-image shows the approximate maximum, the lower half the minimum recommended values after KITTLER and DARULA [2006]. The scale is logarithmic in $[\text{cd}/\text{m}^2]$.

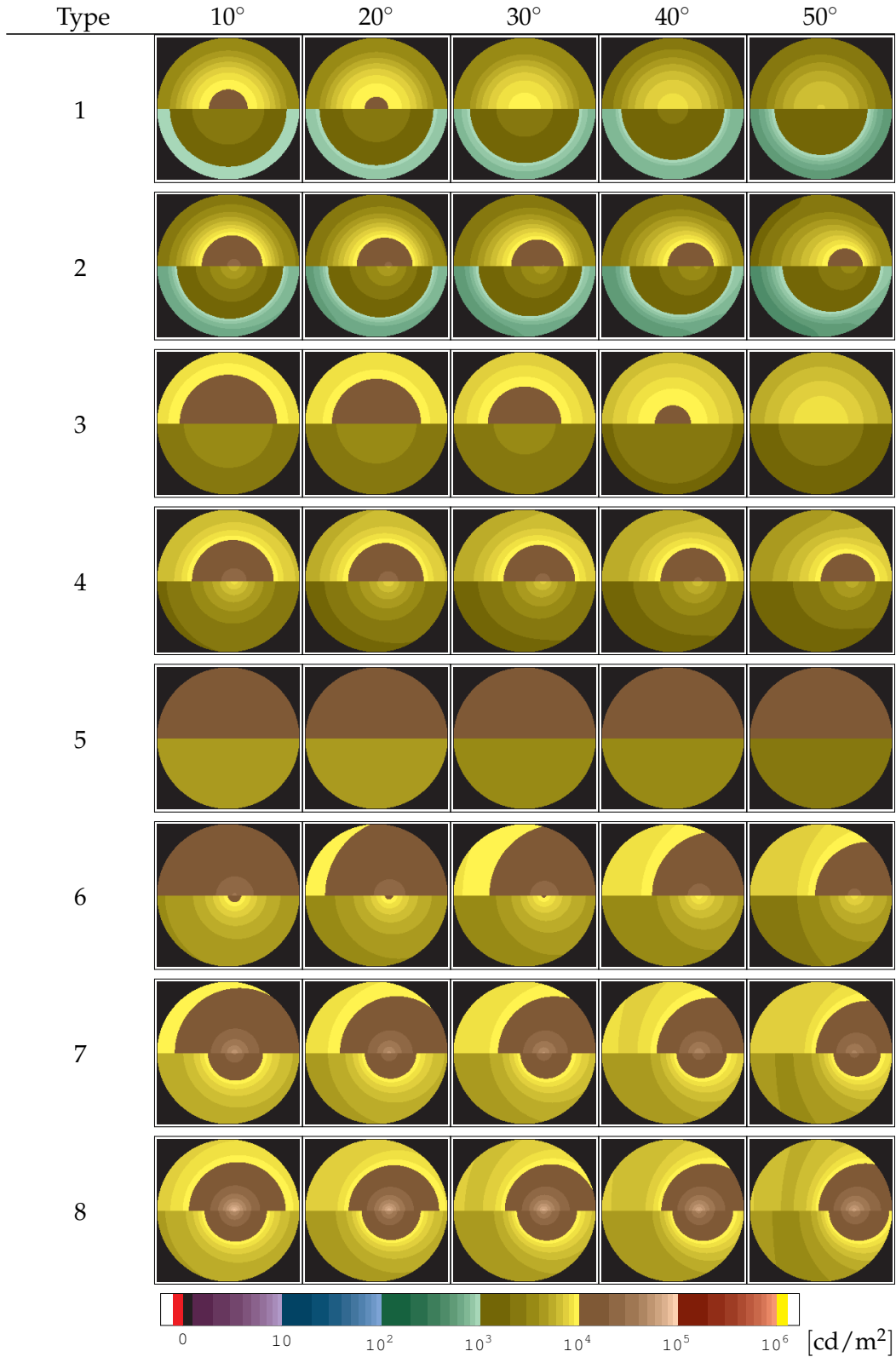


Table 5.9: (cont.) Absolute sky luminance distributions based on the CIE 2003 Standard General Sky models, for various solar zenith distances θ_s . Each upper half-image shows the approximate maximum, the lower half the minimum recommended values after KITTLER and DARULA [2006]. The scale is logarithmic in $[\text{cd}/\text{m}^2]$.

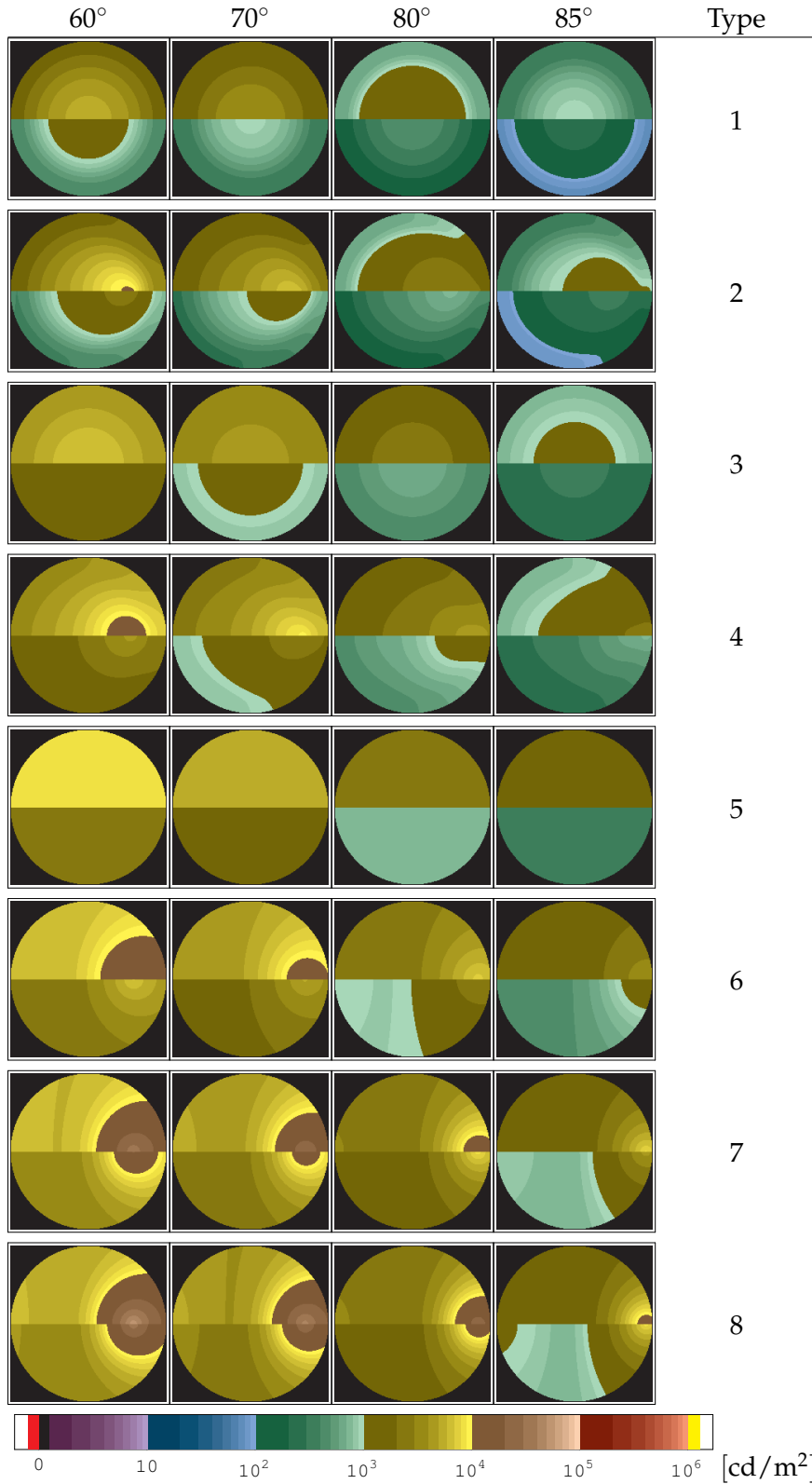


Table 5.9: (cont.) Absolute sky luminance distributions based on the CIE 2003 Standard General Sky models, for various solar zenith distances θ_s . Each upper half-image shows the approximate maximum, the lower half the minimum recommended values after KITTLER and DARULA [2006]. The scale is logarithmic in $[\text{cd}/\text{m}^2]$.

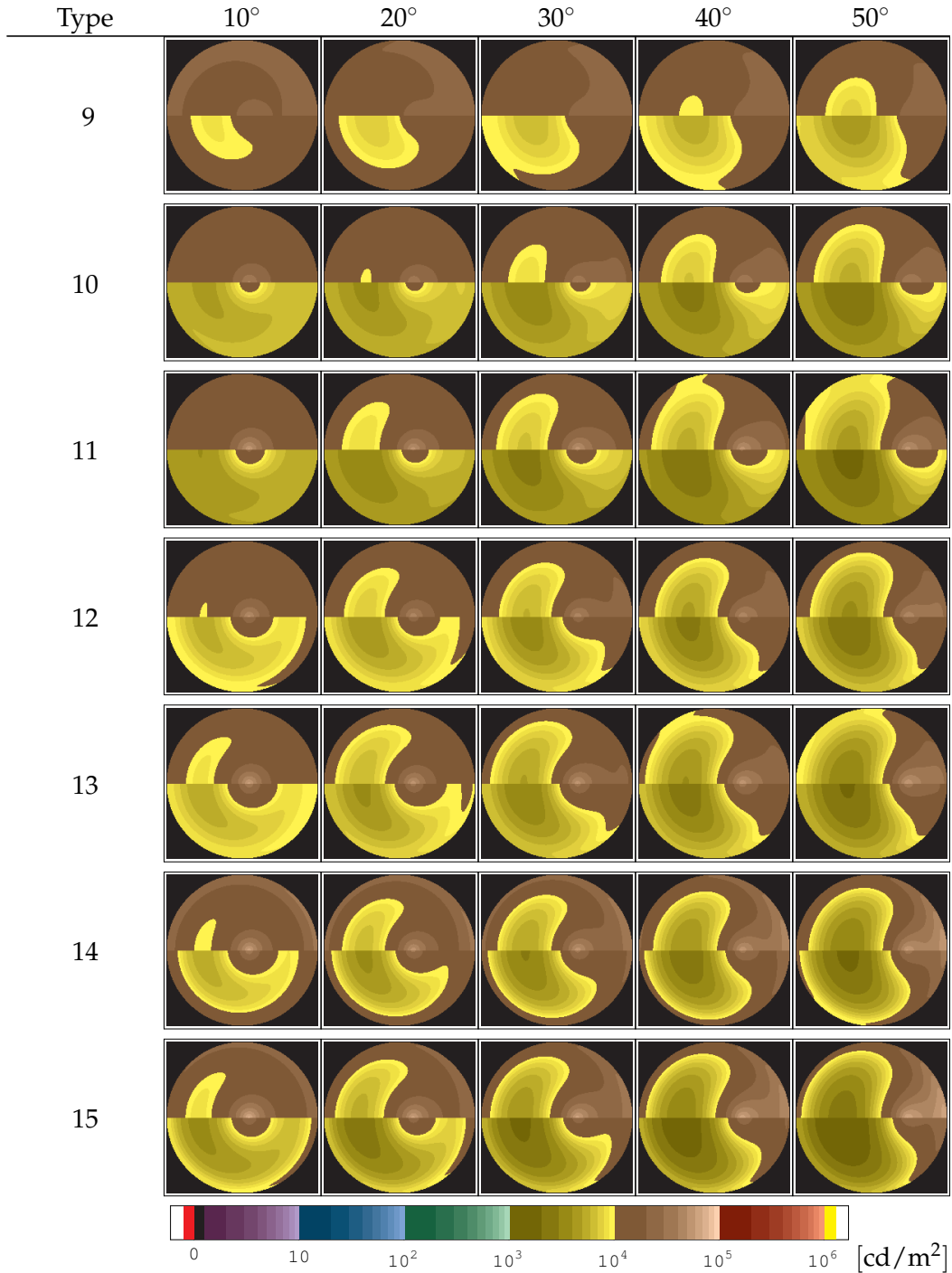


Table 5.9: (cont.) Absolute sky luminance distributions based on the CIE 2003 Standard General Sky models, for various solar zenith distances θ_s . Each upper half-image shows the approximate maximum, the lower half the minimum recommended values after KITTLER and DARULA [2006]. The scale is logarithmic in $[\text{cd}/\text{m}^2]$.

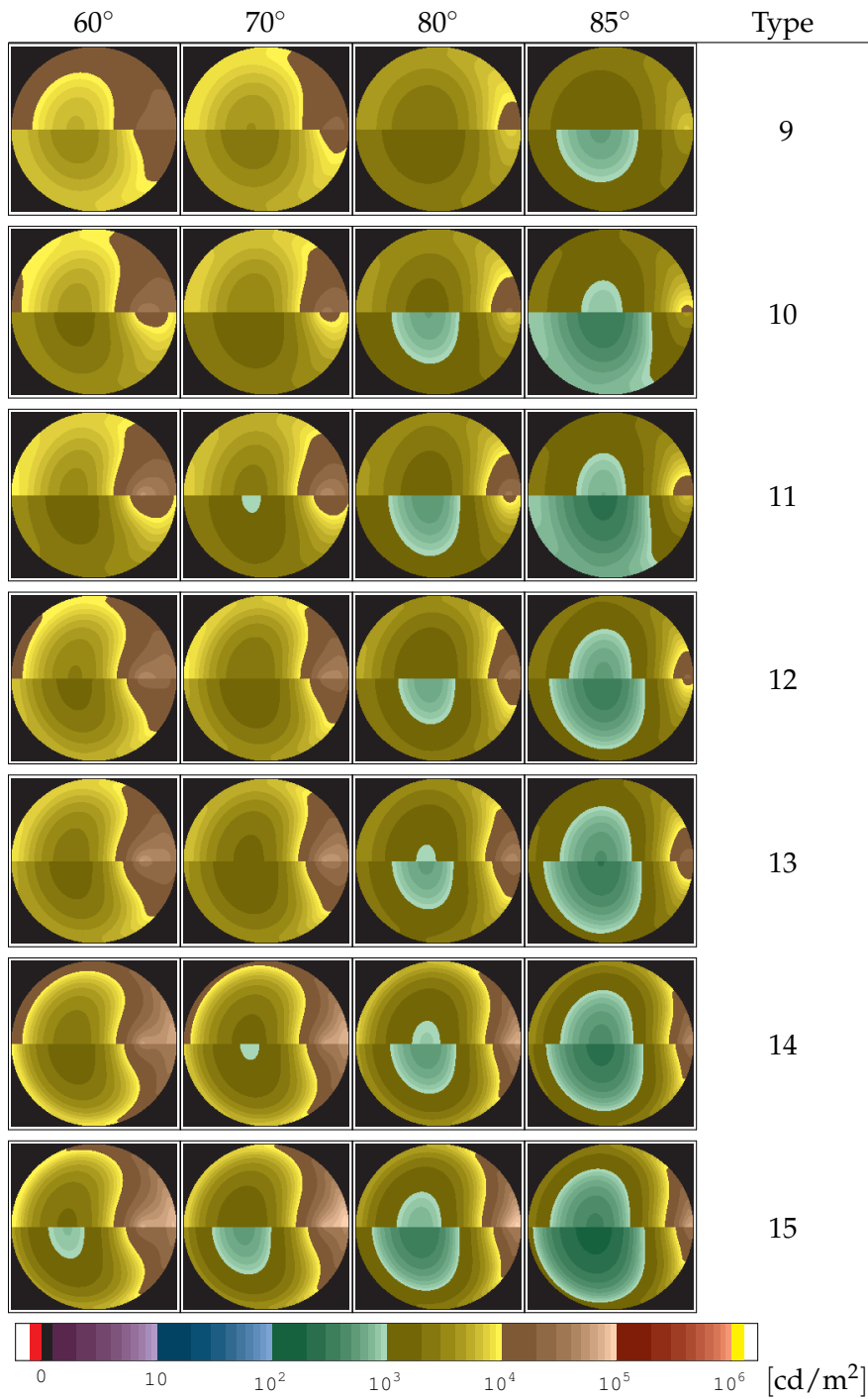


Table 5.10: Relative sky luminance distributions of the Preetham model, for various solar zenith distances θ_s and turbidities. The upper half-images show values from the original model, the lower show values achieved by replacing equation (5.6) by (5.7), which however does not significantly improve the results and was just done for trial purposes. The scale is logarithmic in percent of zenith luminance.

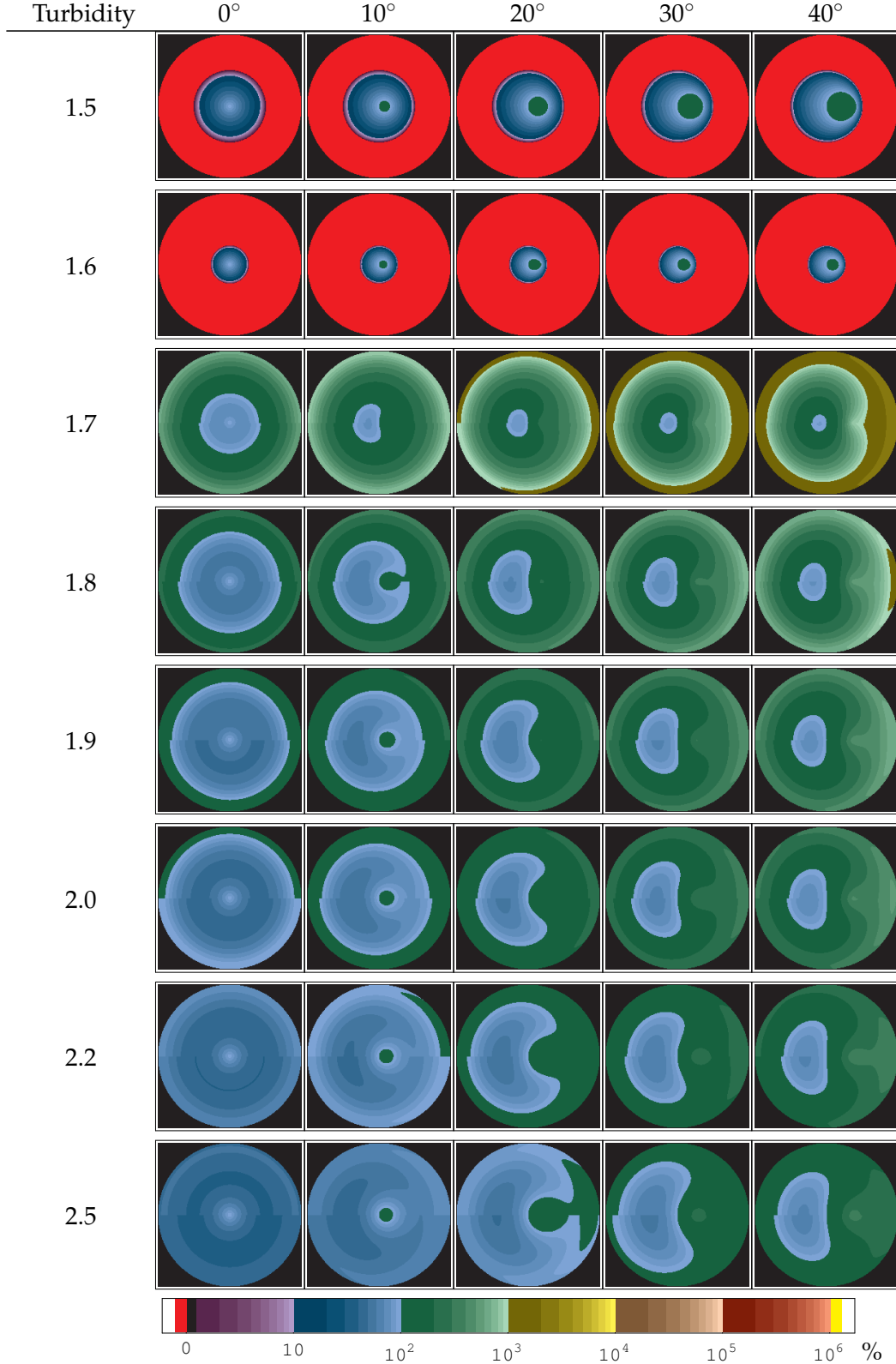


Table 5.10: (cont.) Relative sky luminance distributions of the Preetham model, for various solar zenith distances θ_s and turbidities. The upper half-images show values from the original model, the lower show values achieved by replacing equation (5.6) by (5.7), which however does not significantly improve the results and was just done for trial purposes. The scale is logarithmic in percent of zenith luminance.

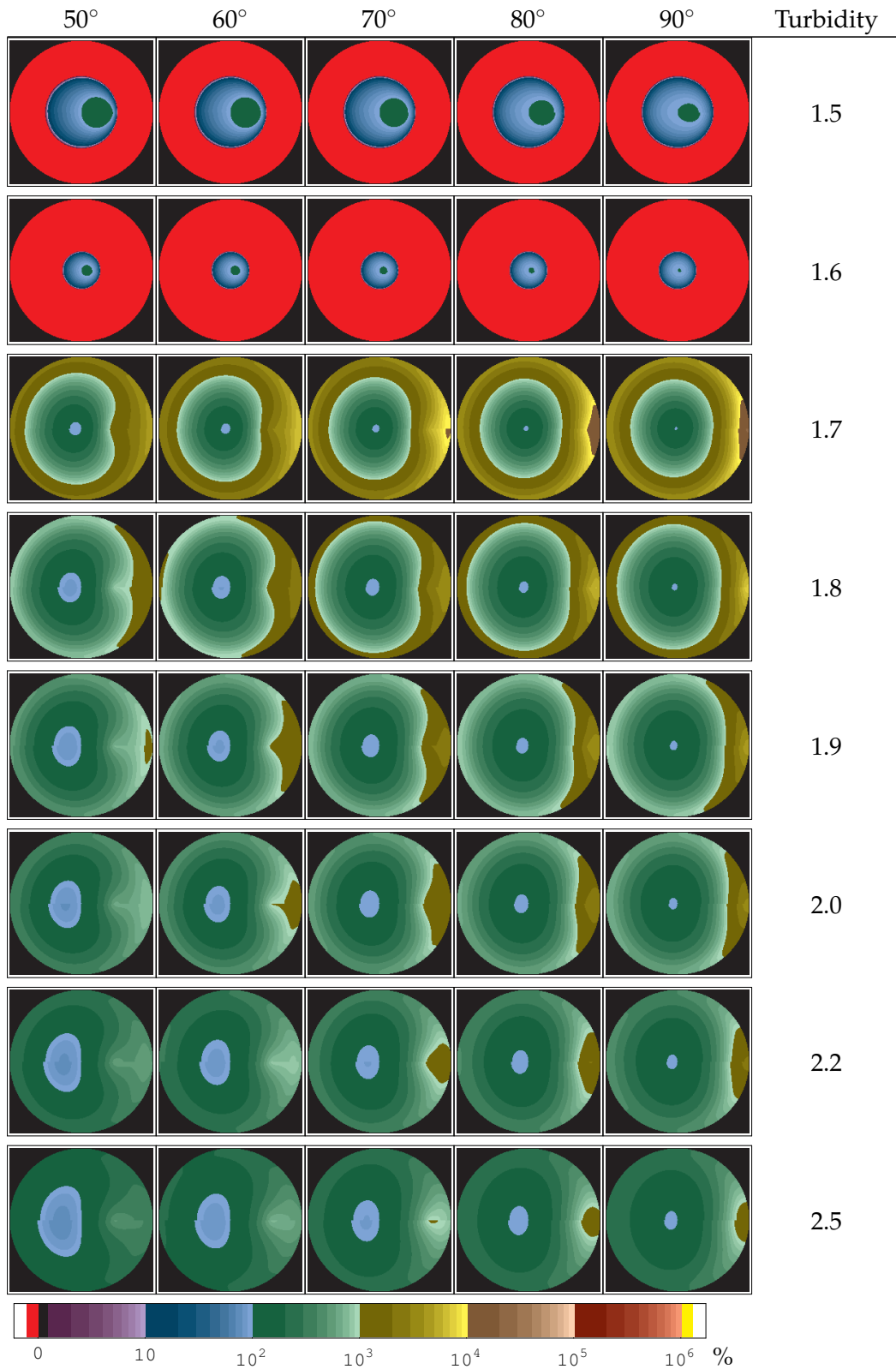


Table 5.10: (cont.) Relative sky luminance distributions of the Preetham model, for various solar zenith distances θ_s and turbidities. The upper half-images show values from the original model, the lower show values achieved by replacing equation (5.6) by (5.7), which however does not significantly improve the results and was just done for trial purposes. The scale is logarithmic in percent of zenith luminance.

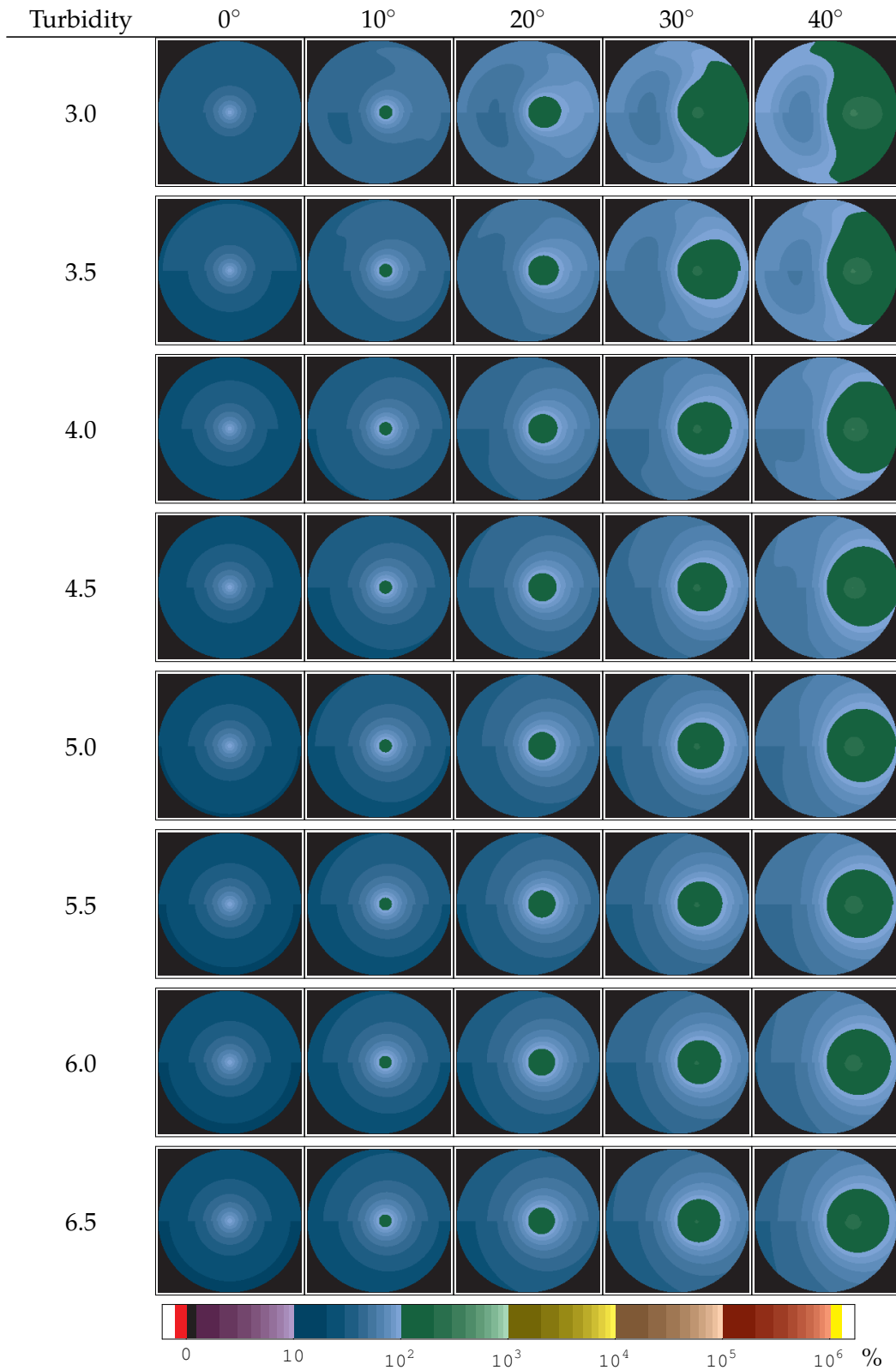


Table 5.10: (cont.) Relative sky luminance distributions of the Preetham model, for various solar zenith distances θ_s and turbidities. The upper half-images show values from the original model, the lower show values achieved by replacing equation (5.6) by (5.7), which however does not significantly improve the results and was just done for trial purposes. The scale is logarithmic in percent of zenith luminance.

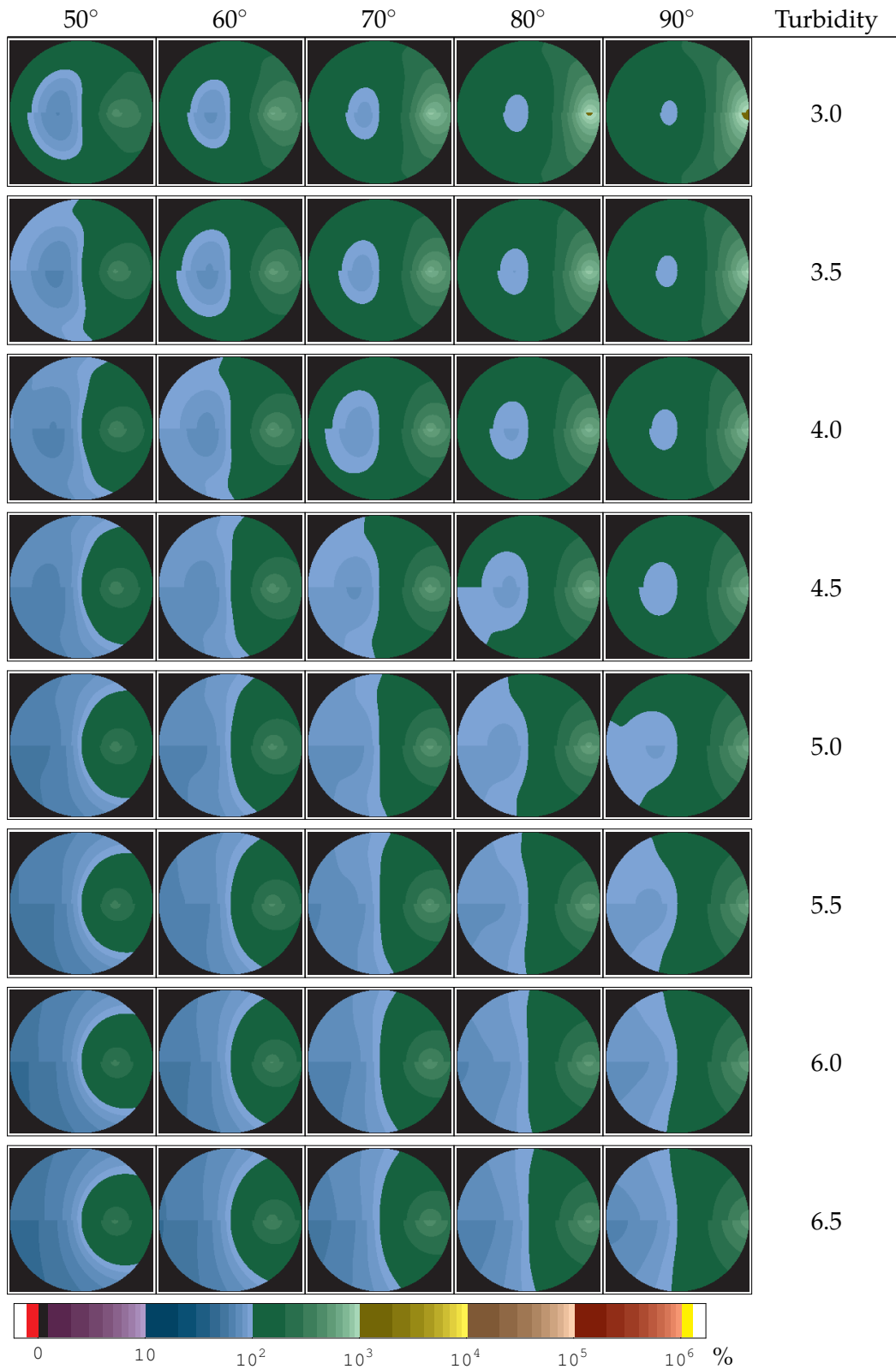


Table 5.10: (cont.) Relative sky luminance distributions of the Preetham model, for various solar zenith distances θ_s and turbidities. The upper half-images show values from the original model, the lower show values achieved by replacing equation (5.6) by (5.7), which however does not significantly improve the results and was just done for trial purposes. The scale is logarithmic in percent of zenith luminance.

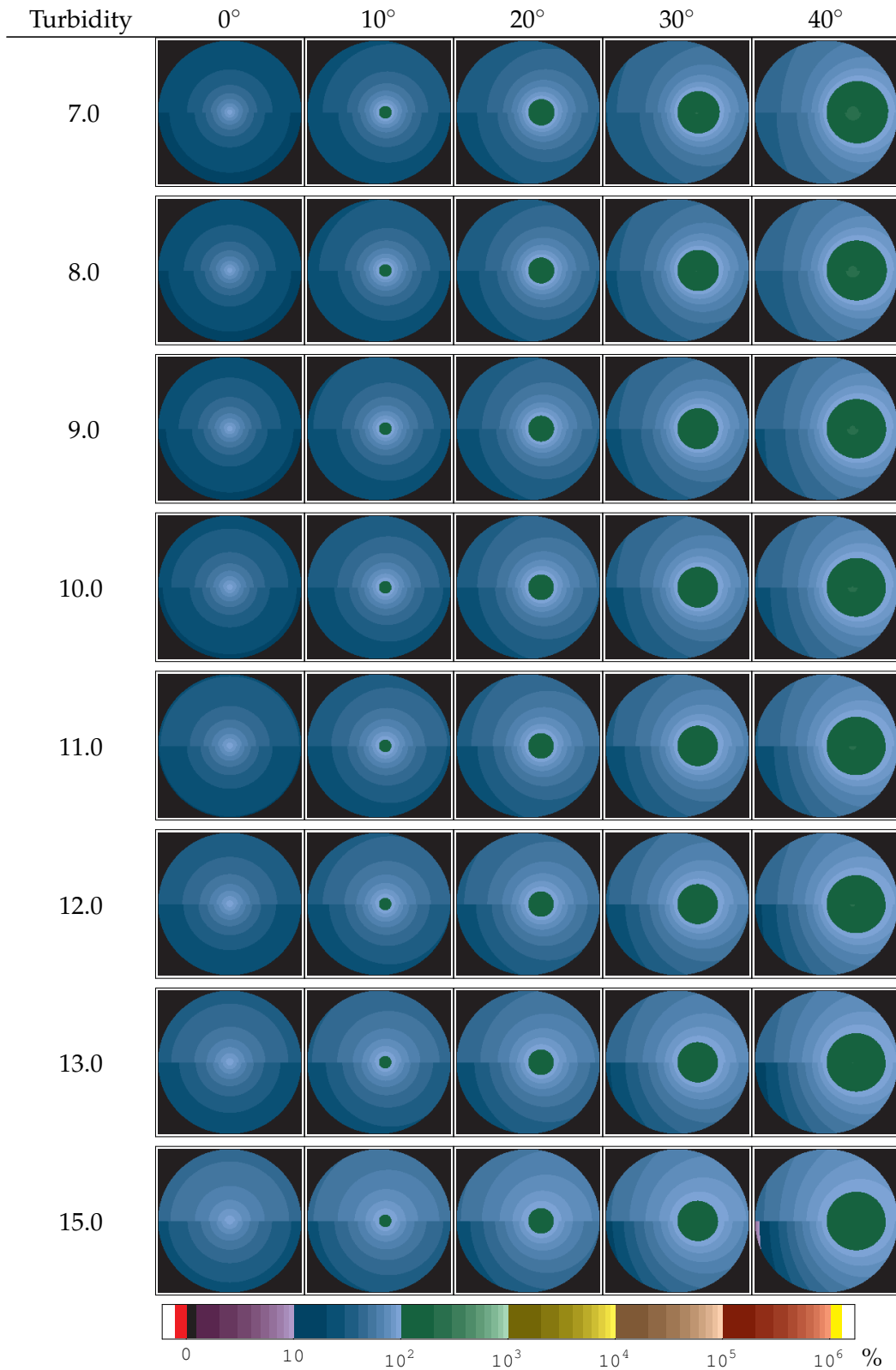


Table 5.10: (cont.) Relative sky luminance distributions of the Preetham model, for various solar zenith distances θ_s and turbidities. The upper half-images show values from the original model, the lower show values achieved by replacing equation (5.6) by (5.7), which however does not significantly improve the results and was just done for trial purposes. The scale is logarithmic in percent of zenith luminance.

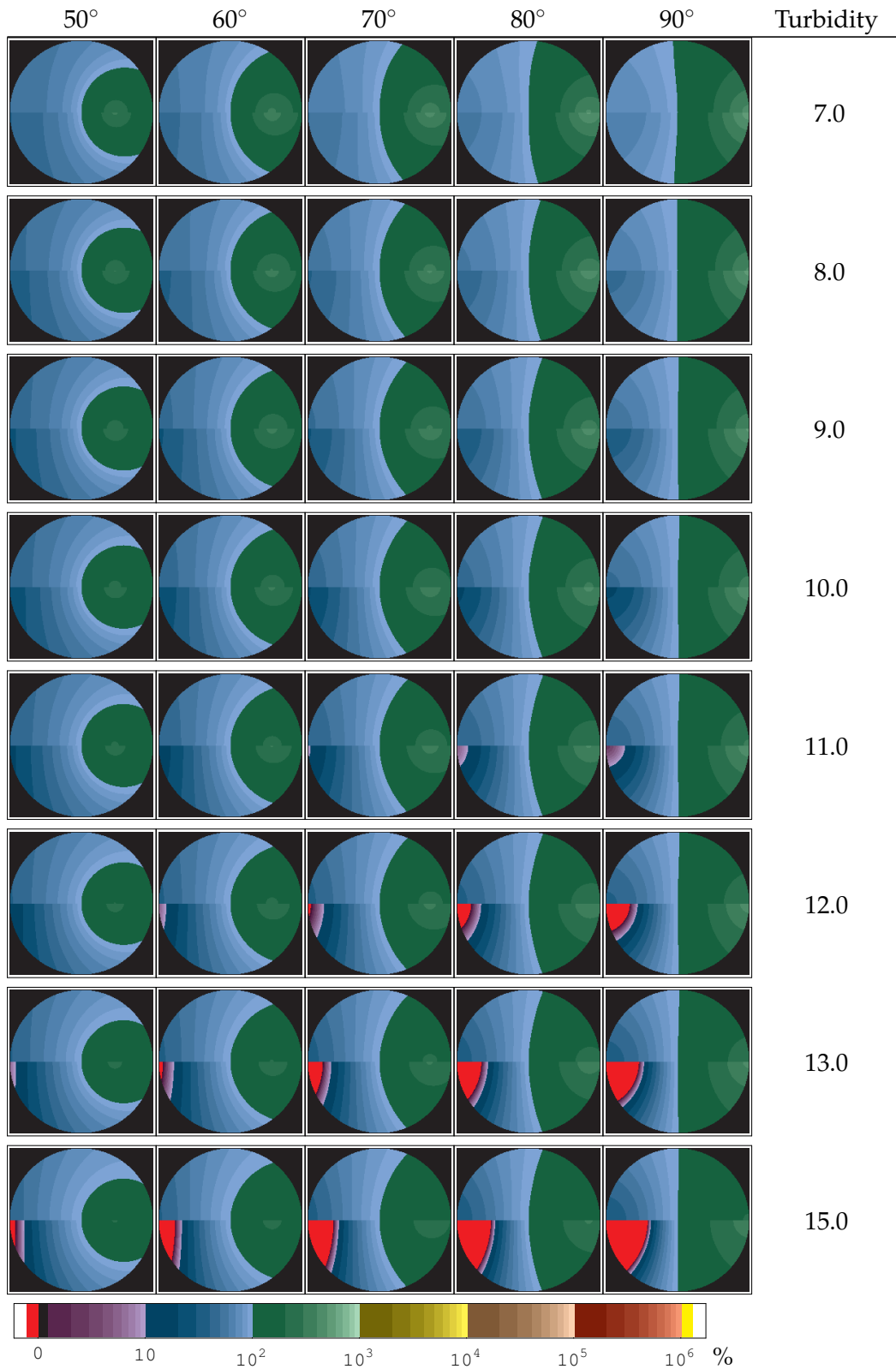


Table 5.11: Absolute sky luminance distributions of the Preetham model, for various solar zenith distances θ_s and turbidities. The upper half-images show values from the original model, the lower show values achieved by replacing equation (5.6) by (5.7), which however does not significantly improve the results and was just done for trial purposes. The scale is logarithmic in $[\text{cd}/\text{m}^2]$.

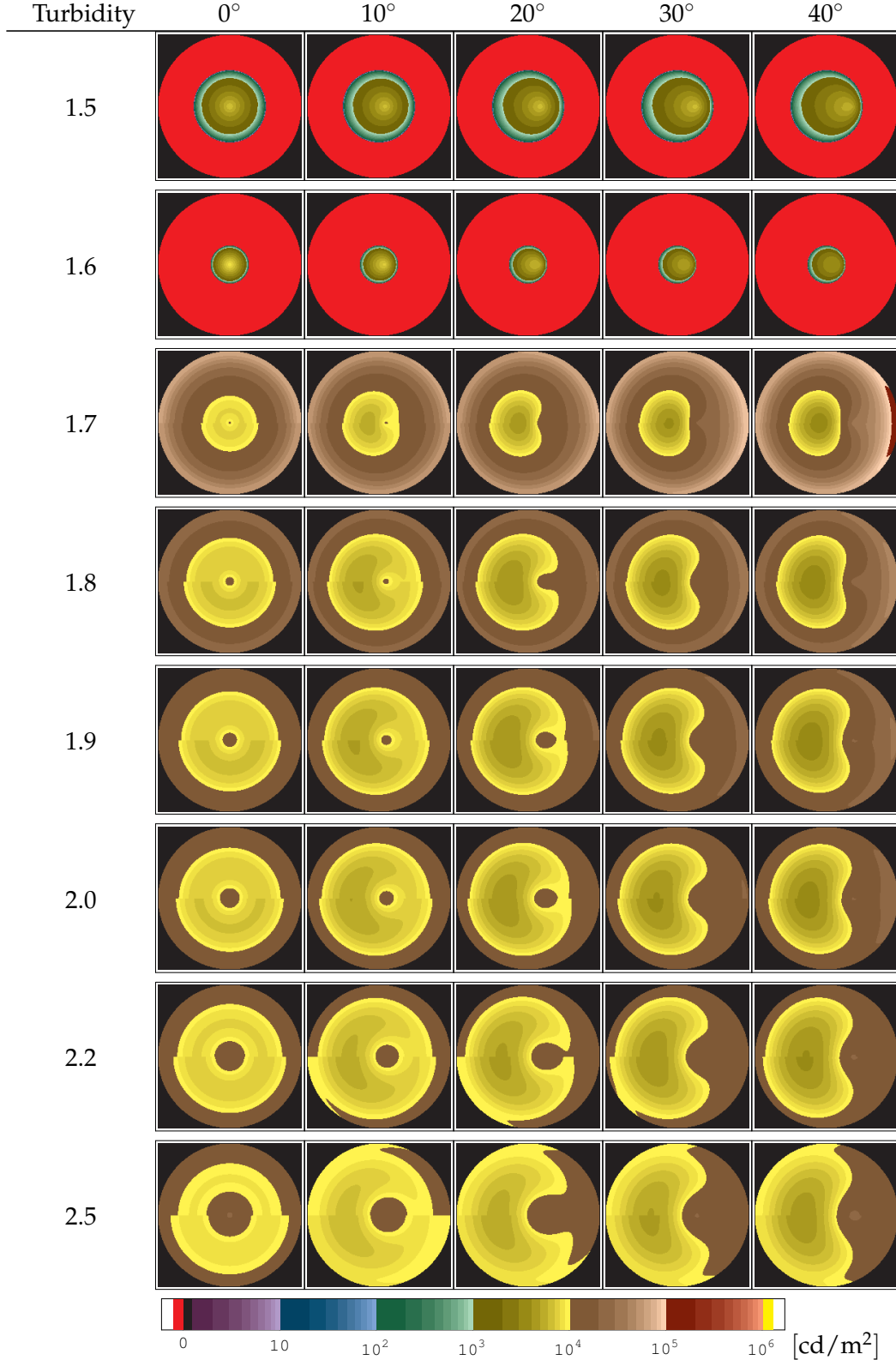


Table 5.11: (cont.) Absolute sky luminance distributions of the Preetham model, for various solar zenith distances θ_s and turbidities. The upper half-images show values from the original model, the lower show values achieved by replacing equation (5.6) by (5.7), which however does not significantly improve the results and was just done for trial purposes. The scale is logarithmic in $[\text{cd}/\text{m}^2]$.

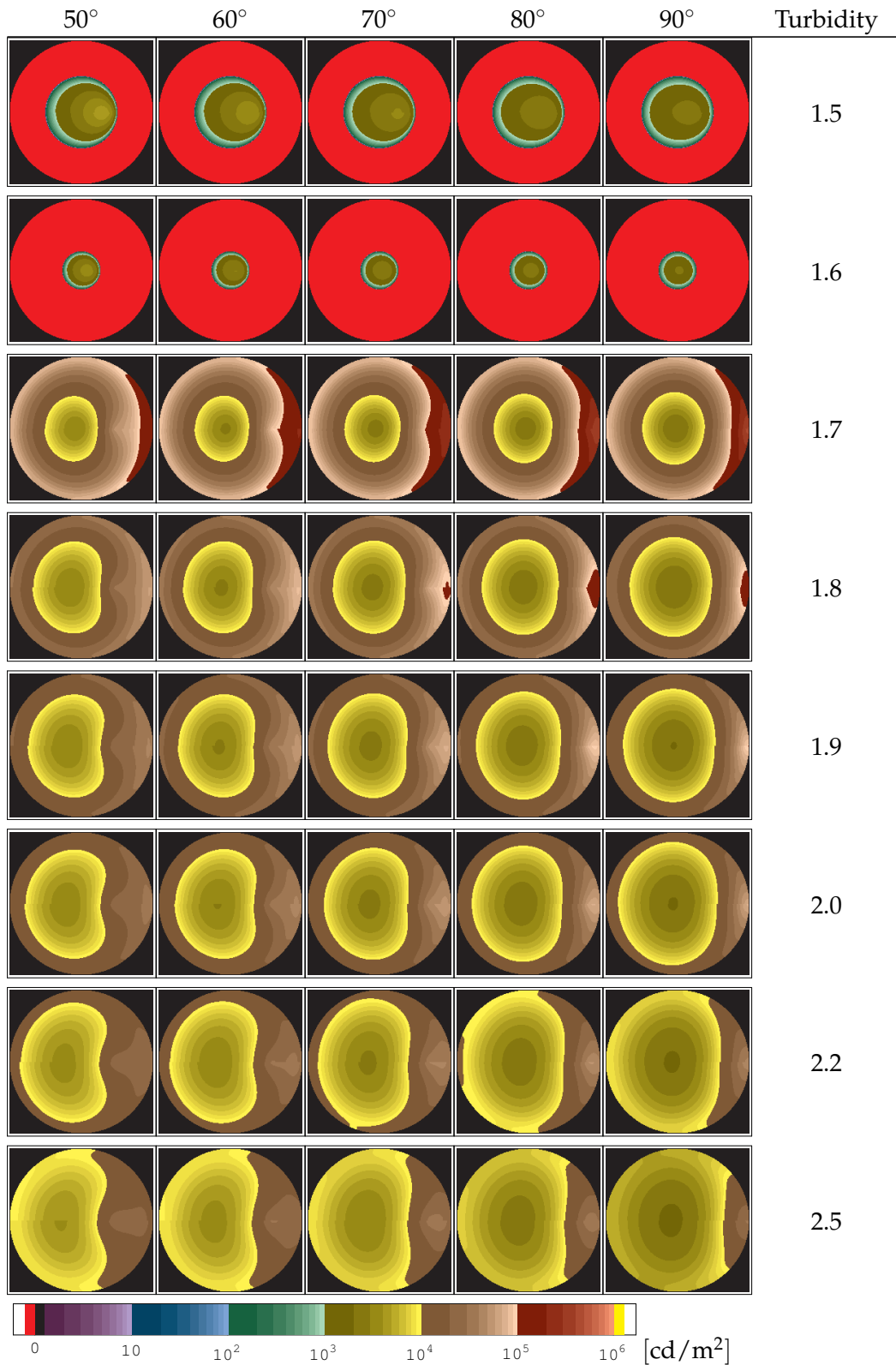


Table 5.11: (cont.) Absolute sky luminance distributions of the Preetham model, for various solar zenith distances θ_s and turbidities. The upper half-images show values from the original model, the lower show values achieved by replacing equation (5.6) by (5.7), which however does not significantly improve the results and was just done for trial purposes. The scale is logarithmic in $[\text{cd}/\text{m}^2]$.

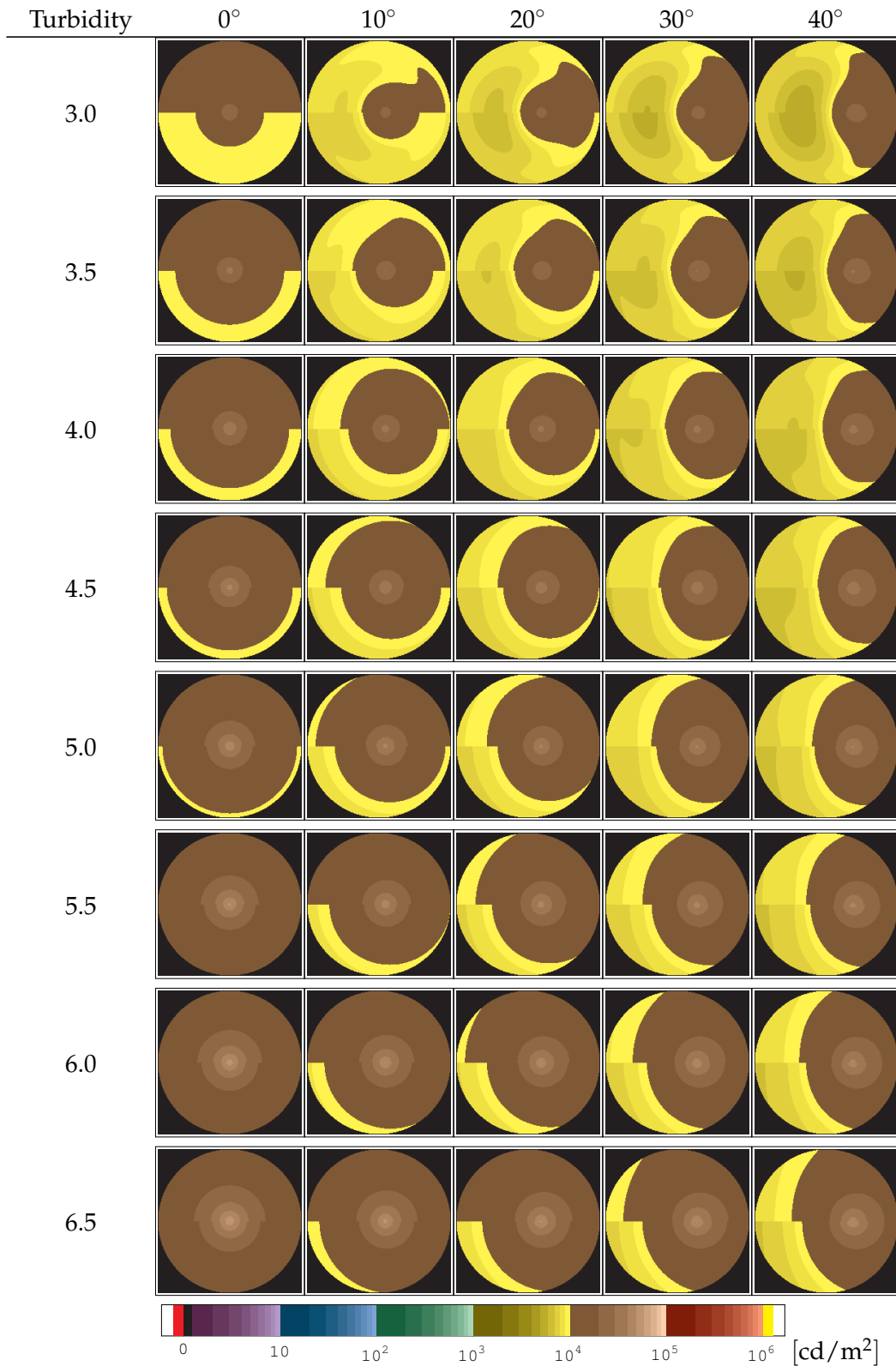


Table 5.11: (cont.) Absolute sky luminance distributions of the Preetham model, for various solar zenith distances θ_s and turbidities. The upper half-images show values from the original model, the lower show values achieved by replacing equation (5.6) by (5.7), which however does not significantly improve the results and was just done for trial purposes. The scale is logarithmic in $[\text{cd}/\text{m}^2]$.

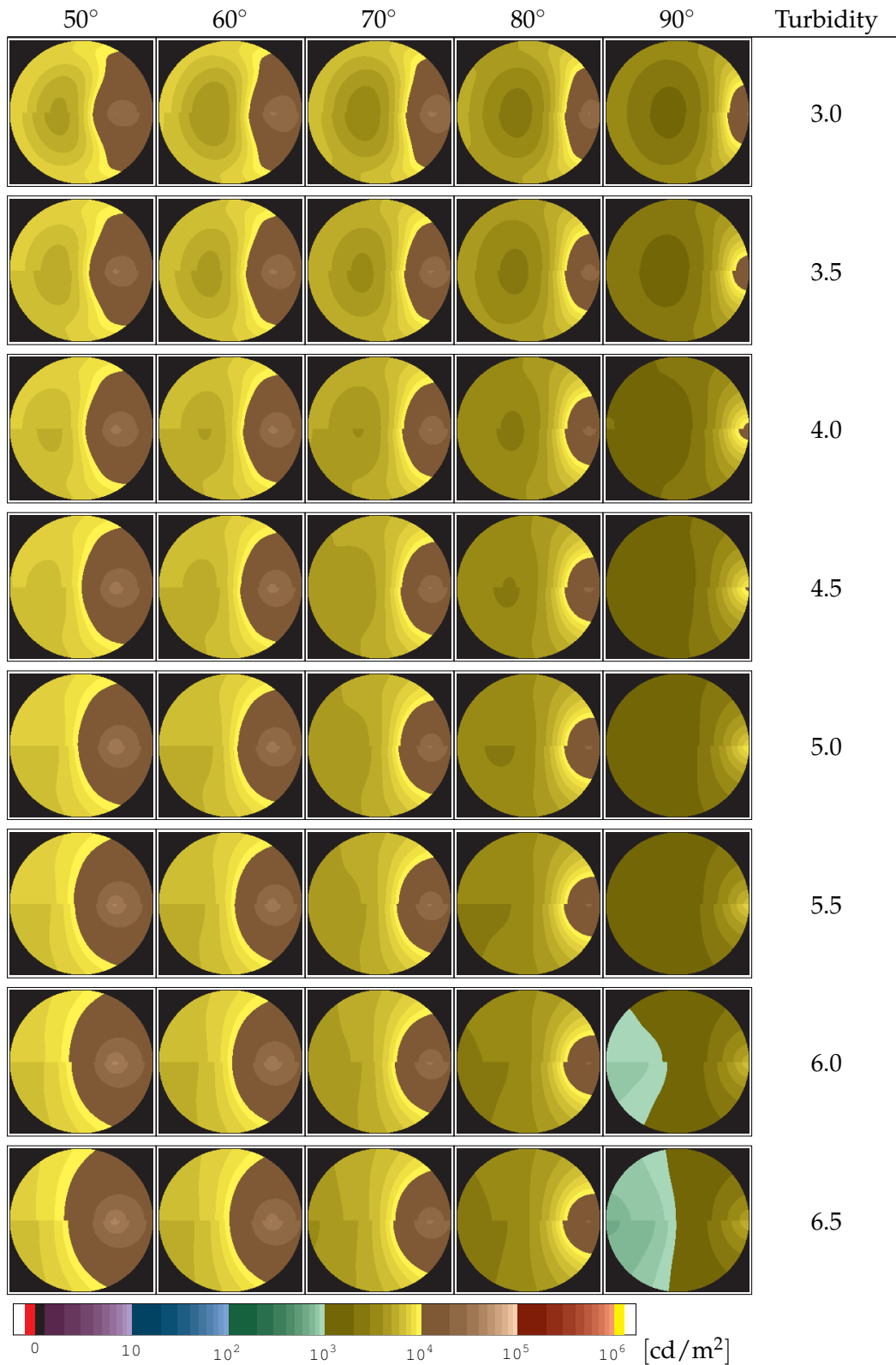


Table 5.11: (cont.) Absolute sky luminance distributions of the Preetham model, for various solar zenith distances θ_s and turbidities. The upper half-images show values from the original model, the lower show values achieved by replacing equation (5.6) by (5.7), which however does not significantly improve the results and was just done for trial purposes. The scale is logarithmic in $[\text{cd}/\text{m}^2]$.

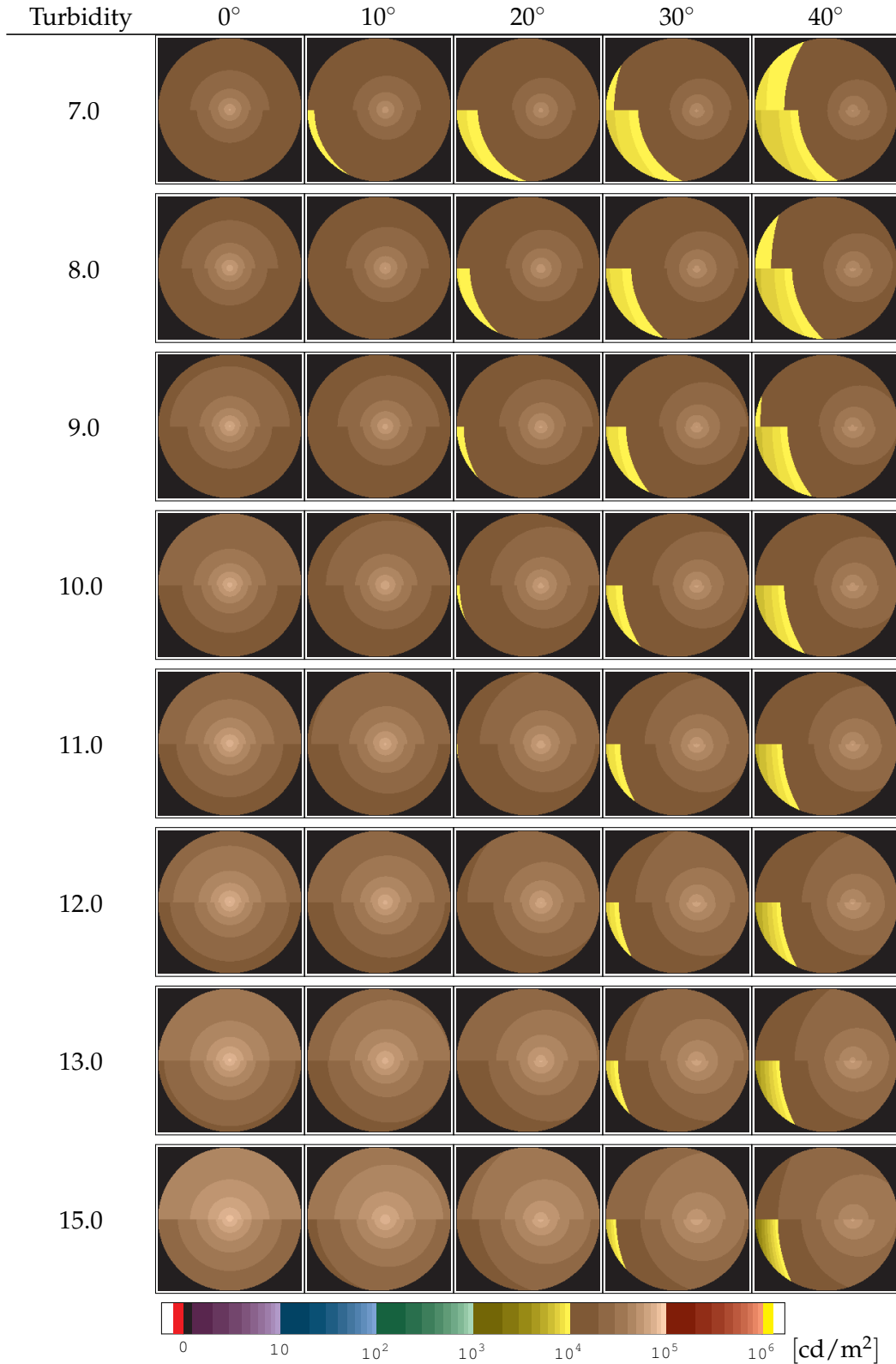
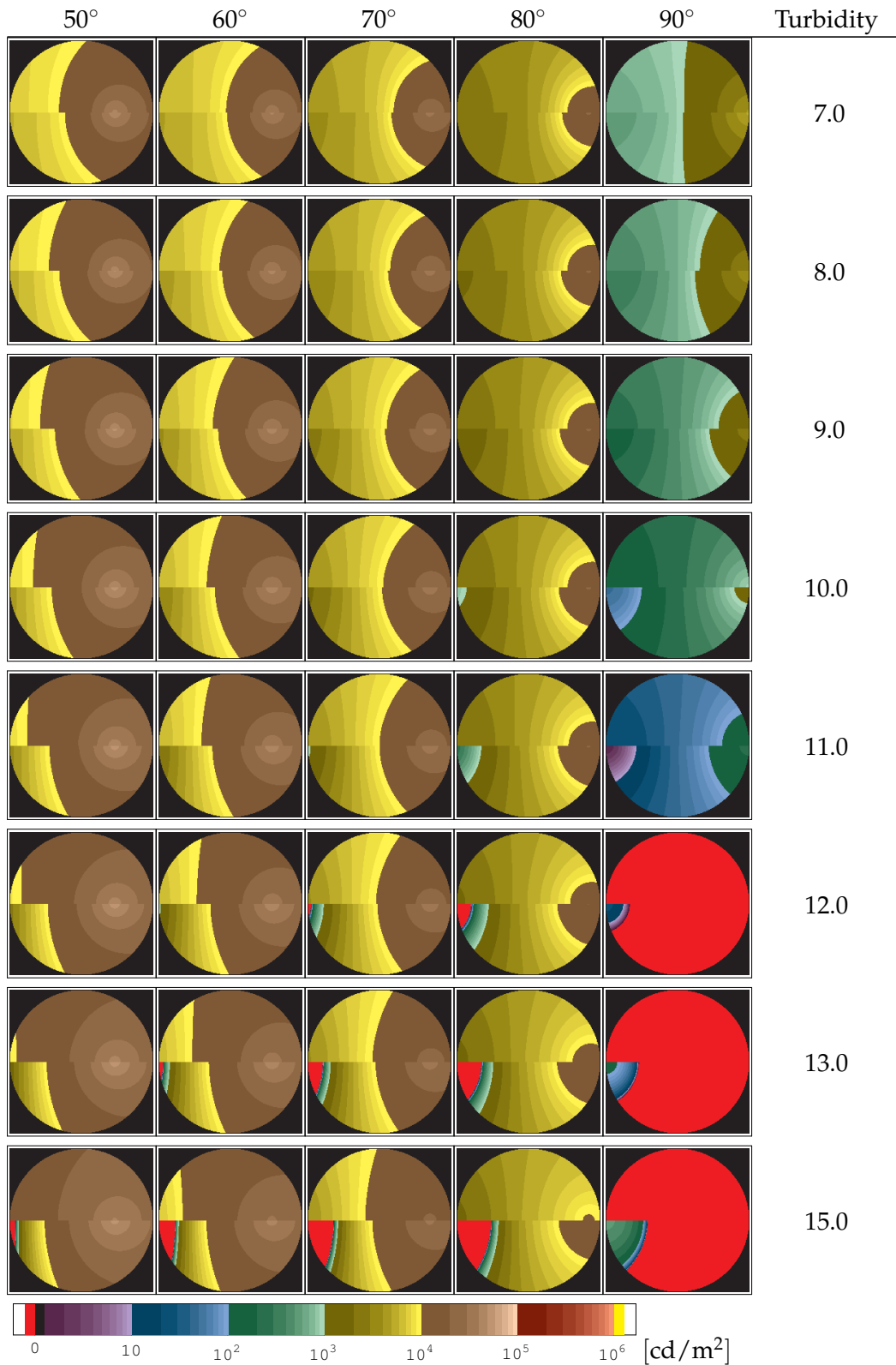


Table 5.11: (cont.) Absolute sky luminance distributions of the Preetham model, for various solar zenith distances θ_s and turbidities. The upper half-images show values from the original model, the lower show values achieved by replacing equation (5.6) by (5.7), which however does not significantly improve the results and was just done for trial purposes. The scale is logarithmic in $[\text{cd}/\text{m}^2]$.



Chapter 6

Skylight Acquisition and Measurements with a Digital Camera

The advent of CCD imaging has made photometry easier and more practical than ever before for observers both professional and amateur, not only because the CCD is both sensitive and highly linear, but also because it captures a two-dimensional “virtual sky” for careful analysis at a later date.

— BERRY AND BURNELL [2000, p.241]

This chapter describes a system for High Dynamic Range (HDR) skydome image acquisition using advanced consumer-grade digital cameras and free software. The acquired photographs are actually *radiance maps* usable as naturalistic skylight source (potentially with clouds and other dramatic natural effects) in a rendering system, but the fact that the chosen software is capable of providing images with absolute luminance values also allows us in principle to scientifically analyse the images, for example in studies of nocturnal light pollution by urban sky glow [ZOTTI 2007b]. The photographic method and the selected HDR image format allow the user to cover the full dynamic range of natural scenes. For daylight scenes, a filter must be used to capture the solar disk without overexposure even with the shortest exposure time. At night, long-time exposures and higher sensitivity (sensor gain) are required. A few demonstrative results are given.

6.1 Introduction

In the 1970s, CCD technology was first applied in electronic imaging sensors for astronomy. In the following decades this technology has been enormously improved in quality, pixel size, sensitivity, full well capacity (the number of photons that can be counted, *i.e.*, the range of linear dynamic response) and detector size. The big advantages over classical film are the much higher quantum efficiency (requiring shorter exposure times), linear response to exposure time and light intensity, *i.e.*, the lack of reciprocity failure (Schwarzschild effect) inherent to film, and the possibilities of electronic image processing, some of which (*e.g.*, unsharp masking) model processing methods pioneered in technical and astronomical photography.

Meanwhile, CCD and CMOS sensor technology has reached the mass market as core technology for digital cameras. There are however notable differences between consumer cameras and scientifically used CCD cameras:

Colour Scientific cameras provide only monochromatic output corresponding to their spectral sensitivity curve which usually is provided by the manufacturer. Their natural sensitivity to infrared is generally high. Typical images are created by combination of several long-time exposures. Colour images, if needed, require combination of several such images made through filters. Astronomical colour images usually don't intend to show natural colours, but are combined to either enhance scientifically interesting aspects of the depicted object, or just to give an aesthetically pleasing image.

Consumer cameras provide RGB colour images, usually via a filter mask with an interwoven colour pattern (*Bayer mask*) applied over the sensor cells. Values for the colours different from the respective pixel filter are interpolated from the surrounding pixels with the correct colour filter. To prevent image degradation by chromatic aberration in photographic lens systems, an infrared cut-off filter is usually placed over the sensor. The final colour values result from the detector's true spectral sensitivity, Bayer filter and infrared filter transmissions, and series of manufacturer-defined values to white-balance the raw RGB image. These scaling values are individual to each camera model and take colour temperature for various typical scene illuminations into account.

Cooling Scientific CCD cameras are usually equipped with a cooling system to reduce dark current and related dark noise which are most apparent with the long exposure times typical for astronomical applications.

Consumer cameras are typically handheld devices with battery power supply and thus cannot be cooled. Daylight and handheld exposure times are typically short, so that this shortcoming usually does not pose a problem. Advanced consumer cameras provide a noise reduction mode for long-time exposures, where a *dark frame* of equal exposure time is made after the image and subtracted from the image.

File format Astronomical images use the FITS file format, which is largely unknown outside that community. It consists of a file header providing metadata (timestamp, instrument, exposure and target data, ...) and the pixel values in either 8 or 16 bit integer or 16 or 32 bit floating-point formats.

Consumer cameras typically provide images in JPEG format with the EXIF extension, a header likewise storing metadata like camera type, timestamp and exposure data. The significant difference is that JPEG is a file format limited to 8 bits (256 values) per colour channel, so that usually some image processing is performed by the camera's on-board firmware to map the image captured by the sensor, which typically provides an ADC resolution of currently 10–14 bits, to an 8-bit image. Professional-grade cameras also can provide 16-bit TIFF or manufacturer-dependent RAW formats, which can be regarded as digital equivalents of film negatives and typically include the unprocessed, linear image data in full ADC resolution of the camera. The Adobe DNG ("Digital Negative") format is an attempt to provide a meta-standard to RAW formats.

Processing Images of science-grade cameras look terrible to the uninitiated. Visible sensor defects are absolutely normal and can include whole columns of dead pixels. Some pixels have largely different sensitivity characteristic than others ("hot" or "cold" pixels). The overall image brightness usually falls off towards the image borders due to *vignetting*, and any dust particle on the sensor creates dark spots or ringlets ("dust

donuts"). The exposure value in each pixel is expected to be a function of target luminance, exposure time, and sensitivity. Adding to this, there is a small *bias* value, which is required to ensure that all pixel values are positive, a systematic *dark signal* which depends on detector temperature, and several noise terms. There exists a chain of standardized processing steps to get rid of all systematic defects and to minimize and quantify the noise effects [BERRY and BURNELL 2000]. In addition, the usual ADC resolution is 16 bits, providing 64k gray levels, which have to be mapped somehow to an 8-bit workstation screen. Typically, after image calibration, image data are analyzed with the safe assumption of linear sensor response, and only few images are processed with aesthetic aspects in mind.

Consumer cameras are built to make images that typically resemble classical photographs, with colours balanced to match human vision. All image processing is done on-board, and any failure in this process, and every single dead or hot pixel visible in the final image, is a reason for complaints. Also consumer camera chips are not perfect, so every camera receives an individual *error map* to remove image errors caused by (tolerable) hardware defects, so the originally bad pixels are not even apparent in the RAW images. Also, anti-blooming gates, which prevent the leakage of charge from saturated CCD cells into neighbouring cells, cause nonlinear response in the higher levels of exposure, which has the effect of reducing sensitivity. Due to the onboard processing, linear response cannot be assumed for JPEG images. The RAW format can however be expected to be linear in a range of intermediate values, with noticeable nonlinear response in the low exposure range due to a small bias, and nonlinearity near saturation levels caused by the abovementioned reduced sensitivity.

6.2 Related Work

The system described here makes use of the concepts of High Dynamic Range Imaging. *Dynamic Range* in this context means the relation between maximum and minimum luminance in a given scene. Contrary to conventional photographic images, which try to provide an optimal resulting image for print on reflective paper or display on a monitor or screen of severely limited dynamic range, HDR imaging attempts to capture the full dynamic range of natural scenes without allowing under- or overexposed image areas. The processing for display on any conventional or also HDR-capable screen can then be performed from the HDR image data. HDR images can also be used as area light sources for illumination of computer graphics scenes. HDR processing methods and many applications for HDR images for computer graphics are extensively described by REINHARD *et al.* [2006].

Our skydome acquisition setup described here is very close to the approach of STUMPFEL *et al.* [2004], also described by REINHARD *et al.* [2006]. They used a setup consisting of a Canon 1Ds digital SLR camera and Sigma 8mm fisheye lens capable of capturing the whole sky (180°). The sky is photographed with a series of different exposures until all regions in the image have been imaged with no saturated and no underexposed pixels. The Sun is too bright even for the shortest exposure time, so they had to use an ND3 filter (transmission 0.1%), which however caused a colour shift in the images that had to be removed by a colour transform computation.

Their approach was targeted towards daylight HDR image acquisition for display as scene background and image-based lighting, but they did not give details about absolute photometric values, and the available HDR images seem not to be calibrated.

6.3 Creation of HDR Images with PFSTools

Over the last years, HDR imaging [REINHARD *et al.* 2006] has entered the professional market with products such as HDRshop or Photogenics, and even leading general image processing products have started to support HDR images, although still on a very basic level.

To create our HDR images, we decided to use the PFSTools [MANTIUK *et al.* 2007; PFSTools 2006]. This suite of (mostly) command-line programs, which is still under development, is freely available for download in source code form and is intended to be a toolbox of small programs that can be chained via UNIX pipes to create, modify, store and display HDR images in several formats. A programming extension towards GNU Octave allows analysis or simple modifications like devignetting or application of specialized filters to HDR images in shell scripts or even from the command line.

For many applications of HDR images in computer graphics (*e.g.*, “radiance maps” for illumination, scene backgrounds), absolute values of scene luminance are often not of critical importance, because in the end all scenes will be *tone mapped* to low dynamic range to be displayed on a screen or printed, so the luminances stored in many available HDR images are often only relative in some arbitrary scale factor. Some HDR image formats, *e.g.*, OpenEXR, are also not designed to store, and not capable of storing the full dynamic range of luminance occurring in nature but are still well suited for artwork and the movie and game industry. The PFSTools however include a program to calibrate the final images with measurements taken with a luminance meter to provide absolute luminance values in units of $[\text{cd}/\text{m}^2]$. While the PFSTools are capable of finding at least approximate luminance values for unfiltered images by evaluating the EXIF image metadata, the filtered images clearly require correct calibration. The native image format (`.pfs`) uses IEEE 754 32-bit floats for each of the channels containing CIE XYZ colour values, resulting in huge HDR image files of 94MB for the skydome images in full resolution, cropped to 2800×2800 pixels. Following the observation that typical natural scenes have RGB (or XYZ) values of similar order of magnitude, the Radiance XYZE (`.hdr`) format, which uses 8 bits per component and a common exponent for the three components (totalling 32 bits per pixel), appears to be a more storage-efficient candidate for the permanent storage of larger numbers of (typical) HDR images.

Our skydome capturing system consists of a Canon EOS 5D digital SLR with 8mm Sigma fisheye lens (originally the f/4.0 EX model improved for Digital SLR, later the f/3.5 EX DG model, which showed less internal reflections), operated in tethered mode via USB connection to a notebook that runs a remote-control application. Typically, every few minutes a skylight capture sequence is triggered which gathers a series of exposures with different exposure time, which are immediately analyzed after download to detect whether additional longer or shorter exposures are required to cover the whole range of luminance values on the skydome, including the solar disk, so that every image area is imaged at least once without over- or underexposure. Given the enormous brightness of the Sun, up to ten images are required per scene, and an ND3 neutral density filter is used as long as the Sun is above the horizon to keep the exposures in the range manageable by the camera.

Given the considerable processing requirements, the RAW images are combined offline on a more powerful PC into PFS images, which can then be further analysed. Appendix A contains a description of the programming work done for the sky capture and analysis and provides more detailed usage information.

6.4 Results and Applications

With the setup described above, several series of afternoons and evening twilights have been captured from a rooftop in the western outskirts of Vienna. The sky on the selected days was mixed from clear to almost overcast, with some dramatic cloud situations and also an emergency break required by a thunderstorm.

As described by REINHARD *et al.* [2006], HDR images typically have to be tonemapped for display on a conventional device like a monitor or print. Table 6.1 shows the images of 2006-07-05 processed with the `pfstmo_fattal02` tonemapper. North is up and east is left in the images. It shows the effectiveness of the required colour correction of the not-so-neutral density filter described in section A.3.4, and also provides a good impression of sky colours (but not the luminance development) during suburban nightfall, when urban light pollution from the east (left) replaces twilight and causes an unnatural orange cast in the images, while the setting Moon is surrounded with a bluish aureola (lower right). In this series, captured with the original setup with the $f/4.0$ EX fisheye lens, the location of the Sun is framed by two reflection features created inside the optical system, deteriorating the image fidelity.

Table 6.2 shows the results of a similar session with the newer $f/3.5$ EX DG fisheye lens. The Sun's shape is now round without distortions. The captures of this day show dramatic cloud scenery with light rays shining through the clouds before a thunderstorm required a break. During twilight, there is only a shortish phase in civil twilight where clouds appear dark. During nautical twilight, urban light pollution (sky glow) reaches noticeable levels and illuminates the clouds.

These images can be used as sky background and also area light source in a photorealistic rendering system. Care must be taken when sampling the image to detect the brightest light sources. Methods described by REINHARD *et al.* [2006] include separating the Sun as directed light source and uniform sampling of the remaining image, and importance sampling.

6.4.1 Measurements of Sky Luminance and Colours

Using automatic exposures in conventional photography or (correctly applied) tone mapping for processing HDR images usually results in images that look “correctly exposed”, so that most of the image shows scene details that also are visible to an observer adapted to the same observing conditions. This however is only one application of HDR photography. As mentioned previously, HDR photography is intended to capture the full scene luminance, and so images store valuable data that can also be evaluated numerically.

Figure 6.1 (a) shows the zenith luminance (black dots) for 2006-07-05 (see images in Table 6.1) derived from averaging a small area around the zenith, and a curve of the solar altitude during that afternoon (red). From the data plot it can be seen that the zenith luminance during the day varies by a factor of 10 until the Sun is at an altitude of about $h_{\odot} = 5^{\circ}$. During twilight, luminance levels rapidly drop by more than 5 orders of magnitude, and zenith luminance already almost reaches minimum after nautical twilight ($h_{\odot} = -12^{\circ}$). During

Time	00	10	20	30	40	50
15						
16						
17						
18						
19						
20						
21						
22						
23						
0						

Table 6.1: Sky captures of 2006 July 5. Although the ND3 filter was removed after 20:20, there appears no colour shift, showing the effectiveness of the process described in section A.3.4.

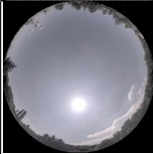
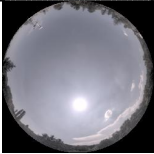
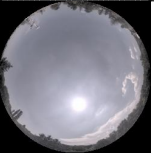
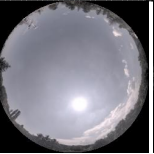
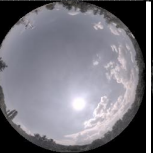
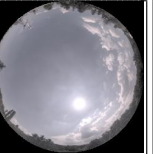

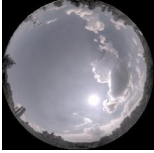


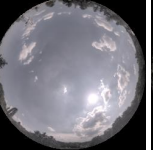
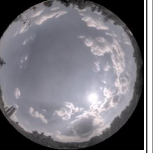
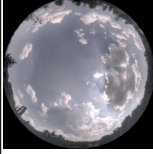

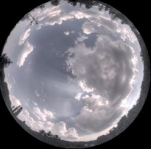

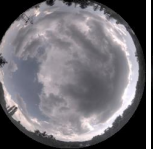
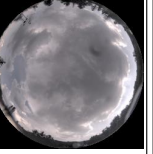
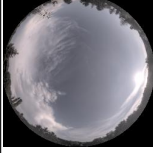
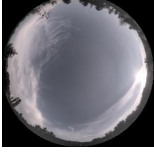
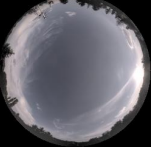

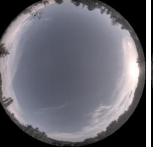
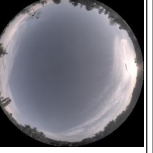
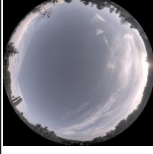








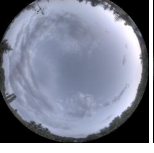
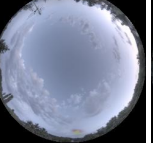
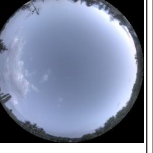
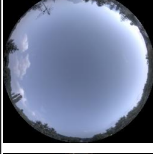

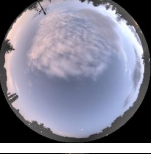
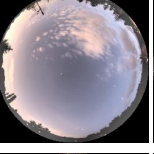
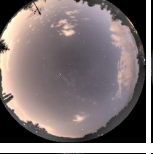
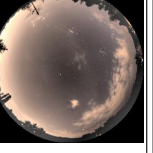
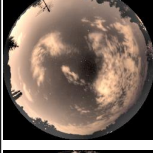
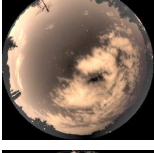
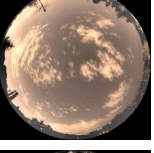
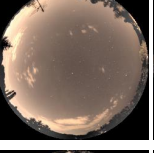
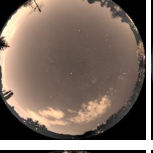
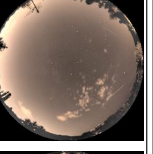
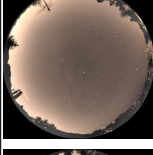
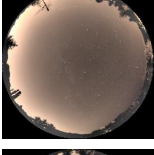
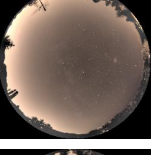
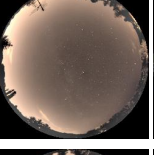
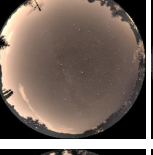
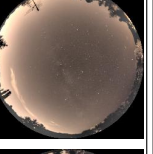
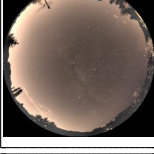
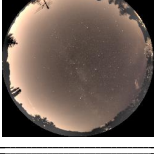
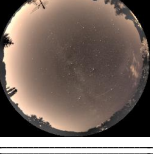

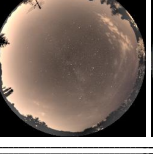
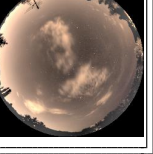
Time	00	10	20	30	40	50
13						
						
						
18						
						
						
21						
						
						
0						

Table 6.2: Sky captures of 2007 August 7. The ND3 filter was removed after 19:20. Rain caused a break from 15:55–17:40. The twilight and night captures were optimized by addition of longer exposures. During nautical twilight, urban sky glow (light pollution) takes over cloud and sky illumination with its orange cast. For luminance levels, see figure 6.2.

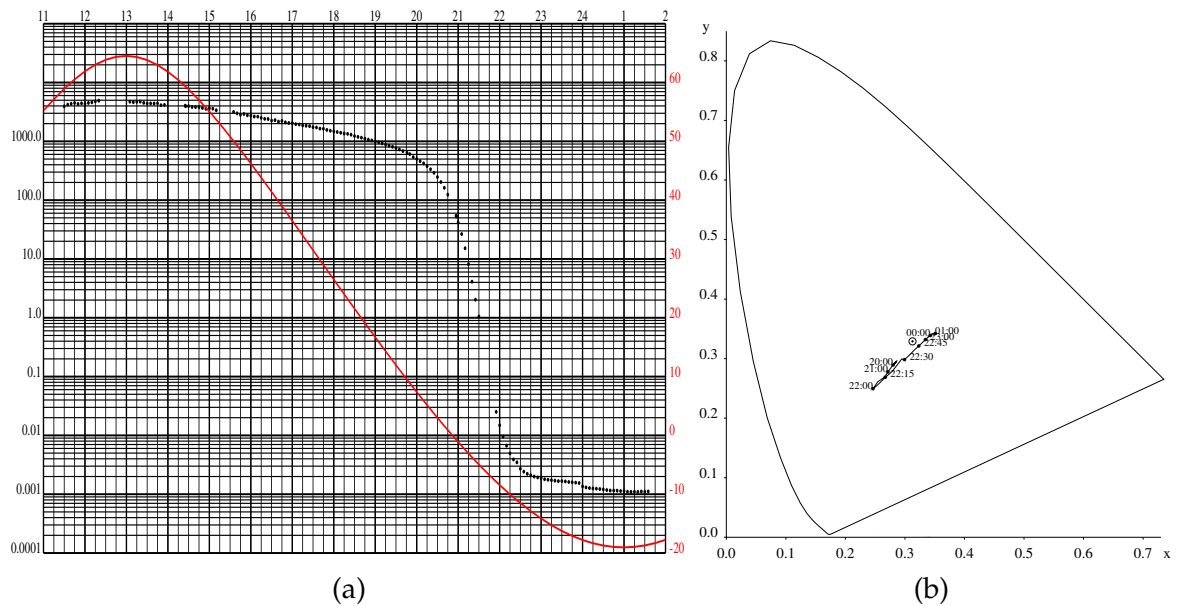


Figure 6.1: Zenith data measured from the HDR sequence of 2006-07-05: (a) luminance (black dots, logarithmic scale on the left) and solar altitude (red curve; labels in degrees on the right side). (b) Colours in the CIE xy chromaticity diagram. Nocturnal values are disturbed by artificial illumination.

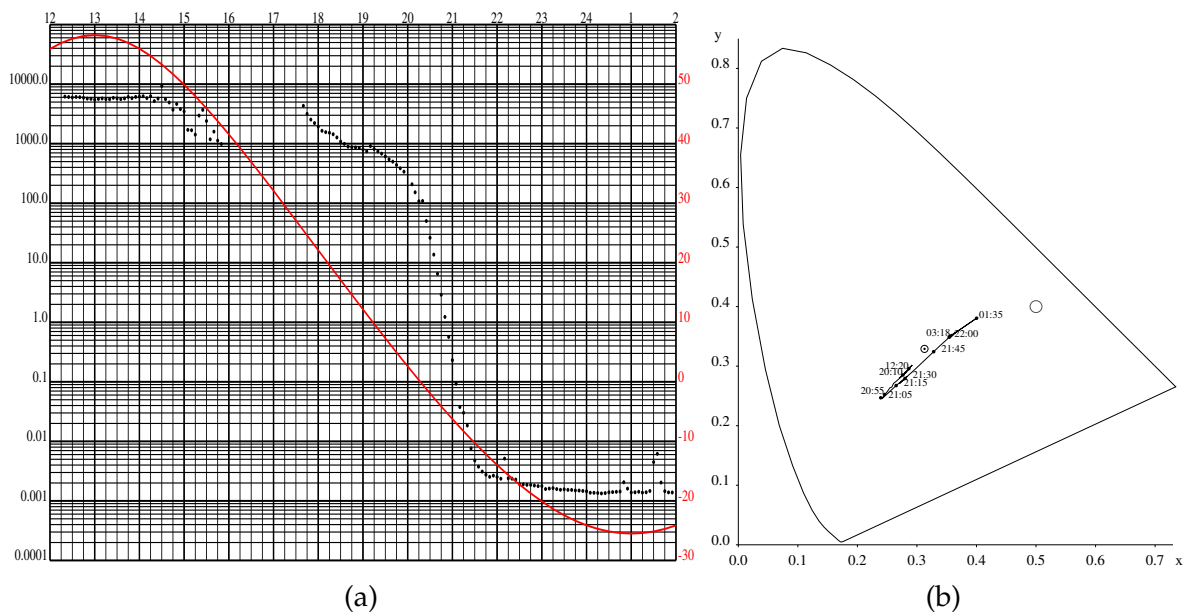


Figure 6.2: Zenith data measured from the HDR sequence of 2007-08-07: (a) luminance (black dots, logarithmic scale on the left) and solar altitude (red curve; labels in degrees on the right side). Clouds cause the jittered values from 14:30–18:15, and rain the break from 15:55–17:40. (b) Colours in the CIE xy chromaticity diagram. Values with zenith clouds during the day (which move sky chromaticity towards the neutral point) have been removed to show clear-sky data only. At night, clouds further pull the chromaticity towards that of street lamps (open circle), else the final position is reached with the end of nautical twilight.

the twilight phase, the instantaneous capturing of the whole sky is certainly the greatest advantage over sequential scanning methods that require at least several minutes to scan the skydome with automatically pointed measuring heads, even if those may provide more accurate results. At midnight, when the public illumination was reduced, zenith luminance immediately dropped by about 20%.

Figure 6.2 (a) is a similar curve for zenith luminance from the image sequence depicted in Table 6.2, which was much higher during the day due to the much higher turbidity. In Vienna, public illumination of most areas is reduced to half power already at 23:00 since 2007-02-01, and this drop is again noticeable in the light curve. Still, the amount of sky glow due to urban illumination is significant.

The zenith luminance values for daylight and twilight skies derived from evaluating the HDR photographs closely match measurements made with a Minolta LS-110 luminance meter, which however can only measure down to 0.01 cd/m^2 , and sky luminance values given by SCHAEFER [1993], indicating the usability of this approach. Sky luminance in other regions of the sky can be measured after properly flat-fielding (removing especially vignetting in) the images, which must also be done for image-based lighting applications.

Sky Colorimetry

The HDR images can also be evaluated with a different aspect in mind: colorimetric measurements, and the development of sky colour dependent on solar altitude. Such studies have been performed by atmosphere physicists, *e.g.*, LEE [1994b], who compares chromaticity values derived from data taken with a spectroradiometer to chromaticities taken from scanned film slides and notes the speed advantage of the photographic method, even if accuracy usually is not as high.

For the two days described before, Figures 6.1 (b) and 6.2 (b) show curves for sky colour in the CIE xy colorimetric diagram. The sky colour is shown to be largely constant during the day, but during twilight, the blueness rapidly increases. The suburban night sky is dominated by the colours of street lamps. It must however be noted that the spectral sensitivity of the camera system should be better known to produce reliable results.

Desert Skies, and a Solar Eclipse

To compare our measurements with unpolluted sky conditions, a series of twilight and night shots taken in the Libyan desert on 2006-03-28 was processed with the same tools. The zenith luminance data start at sunset with values comparable to European skies, but the values rapidly decrease towards only 1/10 of those, confirming the splendid visual impression of a dark desert sky. From the darker site, the Milky Way and especially zodiacal light is excellently visible (Fig. 6.3). To achieve exposure values that can be meaningfully analysed under so dark skies, exposure times of several minutes are required. The numerical values achieved from the images closely match data for optimal conditions (see Figure 6.7 and Table 6.4).

Finally, Figure 6.4 shows zenith luminance during the Total Solar Eclipse observed near Waw-an-Namus in the Libyan desert on 2006 March 29. This observing session was unfortunately plagued by a firmware bug of the camera which resulted in a failure of the automatic capture system just after start of totality, so that data of the most important phase was lost.

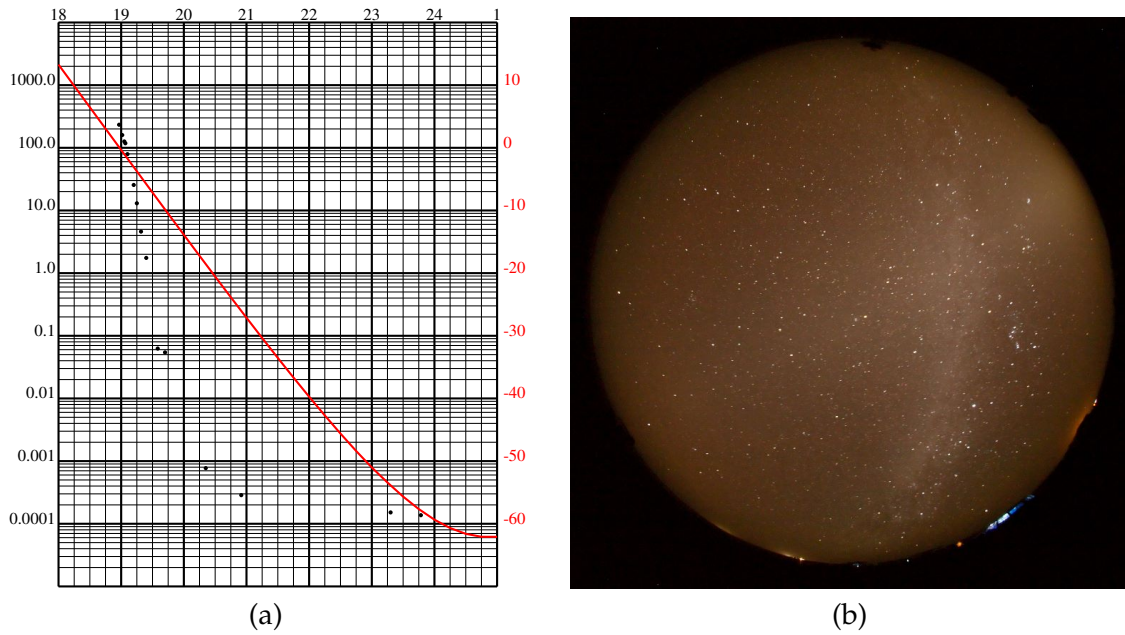


Figure 6.3: (a) Twilight curve in the Libyan desert. (b) Dark sky with Milky Way and Zodiacal light.

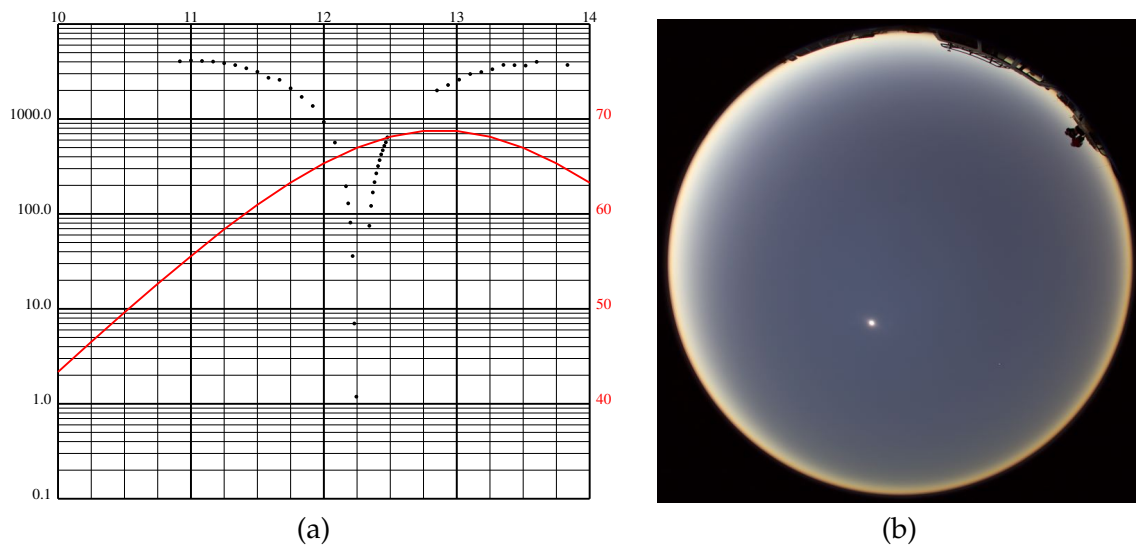


Figure 6.4: Total Solar Eclipse of March 29, 2006, photographed near Waw-an-Namus in southern Libya. (a) Luminance levels dropped to about 1/4000 of daylight levels. Moreover, the duration of the phase with sky luminance lower than at sunset (100 cd/m^2) is only about 15 minutes. (b) Totality at 10:14:46 UT, the last image before the capture system stalled due to camera malfunction.



Figure 6.5: Lake Bled, Slovenia, on 2007-10-05 during the day and at night. A high number of glaringly powerful globe lamps emit light wastefully into the sky. (Photographs by the author)

6.4.2 Measurements of Nocturnal Light Pollution with HDR Images

A negative effect of human civilisation is the ever increasing level of wasteful outdoor illumination which leads to an artificial increase of diffuse nocturnal sky luminance. This *light pollution* has been observed for decades with concern by astronomers, but increasingly the effects of light pollution has also become the subject of environmentalists who study the effects of artificial illumination on animals and also humans, and develop possibilities in decreasing the waste of energy caused by carelessly designed or installed luminaires, examples of which are shown in Figures 6.5–6.6. In many areas, more than 30% of the energy used could be saved without lowering downwards-directed light levels [CINZANO 1997; LANDESUMWELTANWALT and UMWELTANWALTSCHAFT 2003].

Nocturnal sky luminance values are obviously of interest for astronomers, but several units of measurement are in use concurrently, making the comparison of studies somewhat

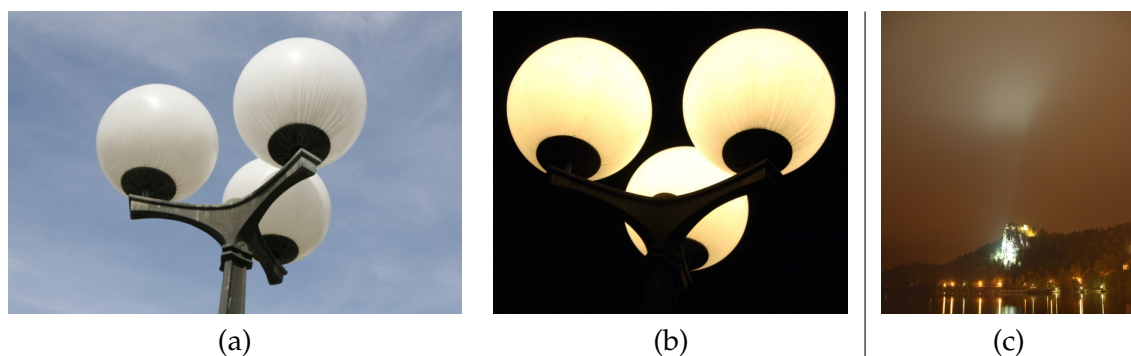


Figure 6.6: Examples of bad lighting: (a-b) Unshielded globe lamp. More than 50% of the light is emitted directly into the sky, and absorption by dirt and occlusion by the lamp pole prevent the remaining light from reaching the ground, where it was intended to go. (b) Illumination of the historical Bled castle, Slovenia. Improper floodlight orientation causes a high amount of light spill into the sky. (Photographs by the author)

difficult. Figure 6.7 tries to combine several of the frequently found units or pseudo-units. The x axis provides logarithmic scales of $[\text{cd}/\text{m}^2]$ and the older unit Nano-Lambert ($[\text{nL}]$, dotted lines), where $1\text{cd}/\text{m}^2 = \pi \times 10^5 \text{nL}$.

Yet another scale is the number of stars of 10^{th} magnitude per square degree that provides equivalent luminance, S_{10} , with $b [\text{nL}] = 0.22 b [S_{10,\text{vis}}]$ [CINZANO 1997, Section 3.1.5].

In his model of artificial night sky illumination, GARSTANG [1986] quotes the relation between sky luminance b in Nano-Lamberts (nL) and the unit of $\text{mag}/\text{arcsec}^2$ frequently used in the astronomical literature [GARSTANG 1986, Eq.(19)]:

$$b [\text{nL}] = 34.08 \exp(20.7233 - 0.92104 b [\text{mag}/\text{arcsec}^2]) \quad (6.1)$$

from which, with the relation $b [\text{nL}] = \pi \cdot 10^5 b [\text{cd}/\text{m}^2]$, CINZANO [1997, Eq. (3.24)] derived

$$b [\text{mag}/\text{arcsec}^2] = 12.603 - 2.5 \log_{10} b [\text{cd}/\text{m}^2] \quad (6.2)$$

This relation is presented in the lower straight line in Figure 6.7.

GARSTANG [1986] also quotes a relation between sky luminance $b [\text{nL}]$ and limiting visual stellar magnitude V , given by WEAVER [1947]:

$$V = \begin{cases} 7.930 - 2.171 \ln(1 + 0.1122b^{1/2}) & b \leq 1479 \text{ nL} \\ 4.305 - 2.171 \ln(1 + 0.001122b^{1/2}) & b > 1479 \text{ nL} \end{cases} \quad (6.3)$$

which is shown as solid line in the upper part of Figure 6.7. The curve indicates that truly dark-adapted vision only takes over at luminance values lower than $0.005 \text{cd}/\text{m}^2$, and only at these low values the abundant numbers of dim stars begin to become visible, as indicated on the right scale (after CINZANO [1997, Tab. 4.2]). Under optimal conditions, the limiting visual zenith magnitude can be around $\text{mag} 6.5$ (and even better on high altitudes), which is however beyond all hope near larger cities.

Later, GARSTANG [2000] derived another formulation for limiting visual magnitude m in dependence of object size θ [arcmin] and background luminance $b [\text{nL}]$ that lacks the sharp discontinuity, which in its basic form for $\theta = 0$ is shown in the dashed curve in the upper part of Figure 6.7.

$$i_1 = 3.451 \cdot 10^{-9} (1 + 0.109b^{1/2})^2 (1 + 2.35 \cdot 10^{-4}\theta^2 + 2.0 \cdot 10^{-5}b^{0.174}\theta^2) \quad (6.4)$$

$$i_2 = 4.276 \cdot 10^{-8} (1 + 1.51 \cdot 10^{-3}b^{1/2})^2 (1 + 5.81 \cdot 10^{-3}\theta^2 + 1.29 \cdot 10^{-3}b^{0.0587}\theta^2) \quad (6.5)$$

$$i = i_1 i_2 / (i_1 + i_2) \quad (6.6)$$

$$m = -13.98 - 2.5 \log i \quad (6.7)$$

A multitude of factors, such as observer age or experience, object spectrum, or glare effects, can further influence the visibility of stars, and a thorough review of this topic has been given by SCHAEFER [1993].

Comparing zenith luminance data from the HDR image analysis (Figures 6.1-6.2) with the upper curves in Figure 6.7, it can be seen that the limiting zenith magnitude for the light-polluted suburban skies measured by the HDR capture system was about $\text{mag} 5$, which matched a visual estimate: the Milky Way was barely visible near the zenith. CINZANO [1997] lists visibility estimates for the Milky Way depending on sky luminance (Tab. 6.3), and the description for 500nL supports the results of the measurement.

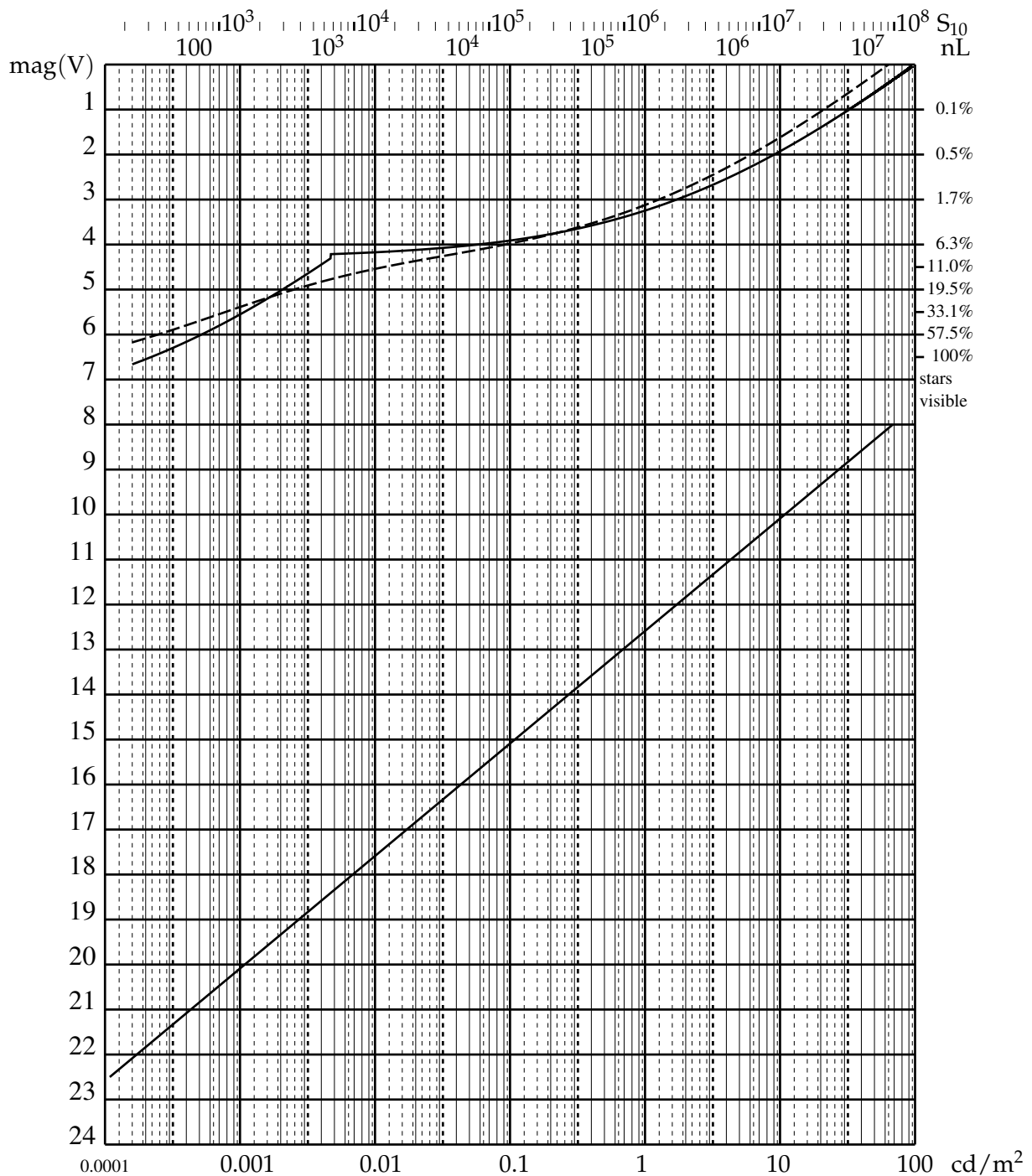


Figure 6.7: Limiting stellar magnitude *vs.* sky luminance. The horizontal axis is sky luminance b [cd/m^2] (also called nits, lower scale) and also in two other frequently used units: Nano-Lamberts (nL, upper scale, dotted vertical lines), and the S_{10} scale which represents the number of stars of 10^{th} magnitude per square degree that give equal luminance (tick marks near numbers). The vertical axis shows photometric (V) stellar magnitude mag_V . The lower straight line connects sky background in the $[\text{mag/arcsec}^2]$ scale with the other photometric units (6.1), and the upper curves shows the limiting stellar magnitudes visible with the unaided eye, depending on sky background luminance. The solid line follows GARSTANG [1986], the dotted line his later work [2000]. The bend at 0.005 cd/m^2 marks the transition from mesopic to scotopic (dark-adapted) vision.

Table 6.3: Visibility of the Milky Way depending on average Polluted Sky Luminance, after CINZANO [1997].

Sky Luminance [nL]		Description
1150	$3.7 \cdot 10^{-3}$	invisible
500	$1.6 \cdot 10^{-3}$	visible near zenith, rest immersed in grayish background
150	$5 \cdot 10^{-4}$	reduced contrast, details lost
80	$2.5 \cdot 10^{-4}$	brilliant if high, not visible on horizon
64	$2 \cdot 10^{-4}$	best conditions

Table 6.4: Zenith Sky Luminance values after CINZANO [1997]

Source	Zenith Values [$\cdot 10^{-6}$ cd/m ²]	
	Typical	Minimal
Zodiacal Light	91 (70–126)	56
Integrated starlight	77 (21–213)	21
Diffuse galactic light	6–14	5.6
Airglow (min)	35	35
Cosmic Background	<0.7	<0.7
Total	217	118

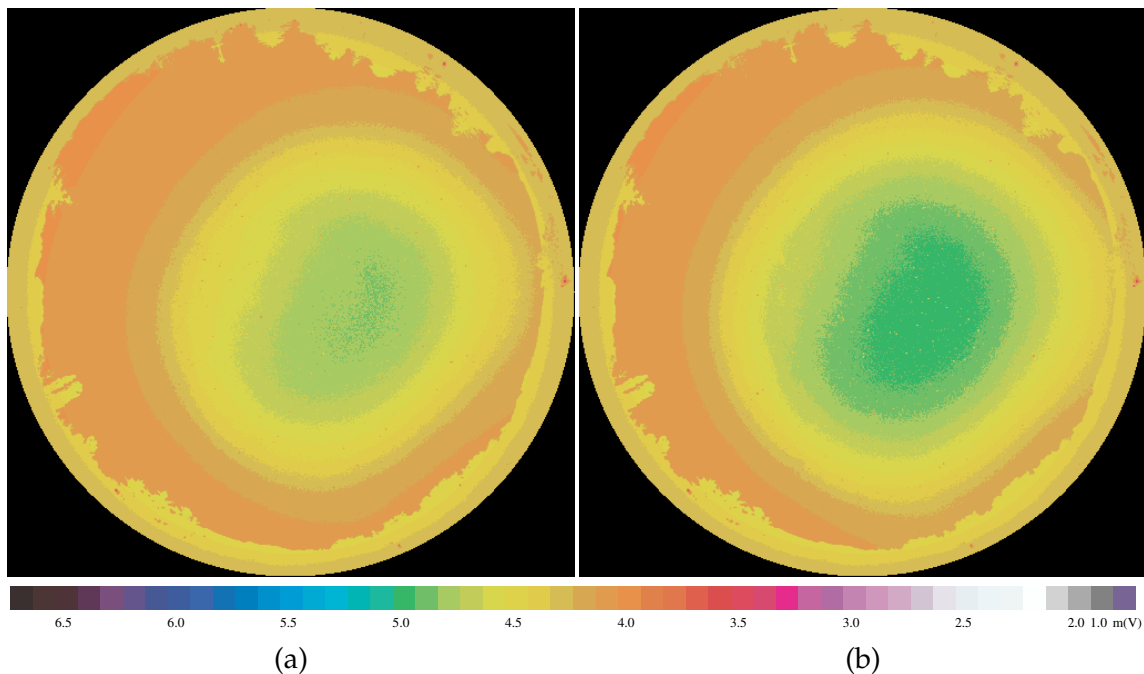


Figure 6.8: Sky quality given as plots of maximum visible magnitude: Effect of reduced public illumination. (a) Night sky in suburban Vienna, on 2006-07-05, 23:55CEDT (b) 15 minutes later, after reduction of public illumination, the sky gets notably darker.

A strongly light polluted sky is comparable to the sky luminance at Full Moon (1400 nL after SCHAEFER [1993]). Very slowly, also through activities of the International Dark-Sky Association [Darksky], public consciousness and legislative seems to be evolving towards the use of light fixtures that direct light towards the ground, where it is potentially useful, instead of into the sky, and generally towards the use of more energy-efficient lights, although there is still a long way to go. CINZANO [1997] studied light pollution and listed natural contributions of night sky luminance values, given in Table 6.4. From this data, the darkest skies to be expected should show zenith values around $1.2 \dots 2.2 \cdot 10^{-4} \text{ cd/m}^2$, values that also appear in the analysis of images taken under the pristine skies of the Libyan desert (Figure 6.3).

Recently, DURISCOE *et al.* [2007] presented an extensive high-precision study of sky luminance by light pollution in US national parks, using a science-grade CCD camera on a robotic telescope mount to acquire highly accurate light pollution data by scanning a multitude of directions in the sky over a period of about 35 minutes. From the point measurements, they produced fisheye-like plots of the sky, colour-coded in units of $[\text{mag/arcsec}^2]$ with a resolution of 0.1 mag.

The fisheye HDR images in this present work, after de-vignetting, can be evaluated and colour-coded in a similar way. As reference measurements, visual estimates by experienced observers and measurements with a Sky Quality Meter (SQM) [UNIHEDRON], a dedicated electronic low-light measuring device that provides direct sky background brightness on the $[\text{mag/arcsec}^2]$ scale, have been used. The latter two matched well with the connecting relations shown in Figure 6.7. It however turned out that the photographic estimates were slightly too optimistic (*i.e.*, the sky appeared too dark).

The reason for this discrepancy can be found in the fact that the Y luminance channel data provided by the PFSTools represents the photopic (daylight) sensitivity function of the human visual system, while visual limiting magnitudes obviously involve the scotopic (night) sensitivity function, which has its peak shifted towards shorter wavelengths. The spectral sensitivity of the SQM as described by CINZANO [2005] is much higher in the short wavelength range than that of the photopic sensitivity function, but also does not provide astronomically representative values, because it does not represent any astronomically standardized filter system. Also, its wide aperture angle poses a problem given that the horizon is considerably brighter in light polluted areas, so any comparison must take this wide angle into account.

A multiplicative correction factor as large as 1.4 (0.37 mag) has been found to be required for the sky luminance near Vienna by comparing the average of a large area in the image representing the area measured by the SQM – weighted by the SQM’s angular response given by CINZANO [2005] – to the single measurement value given by the SQM. This factor, which lies well within the range derived by CINZANO [2005], depends on the spectral emission characteristic of the street lamps involved, and Vienna’s high amount of mercury vapour lamps include a significant blue component where the SQM is sensitive.

To describe naked-eye visibility of the night sky around cities, we prefer to show limiting visual magnitude following the function given by GARSTANG [1986], instead of the more technical unit of $[\text{mag/arcsec}^2]$, and the plots in Figures 6.8–6.10 are colour-coded accordingly.

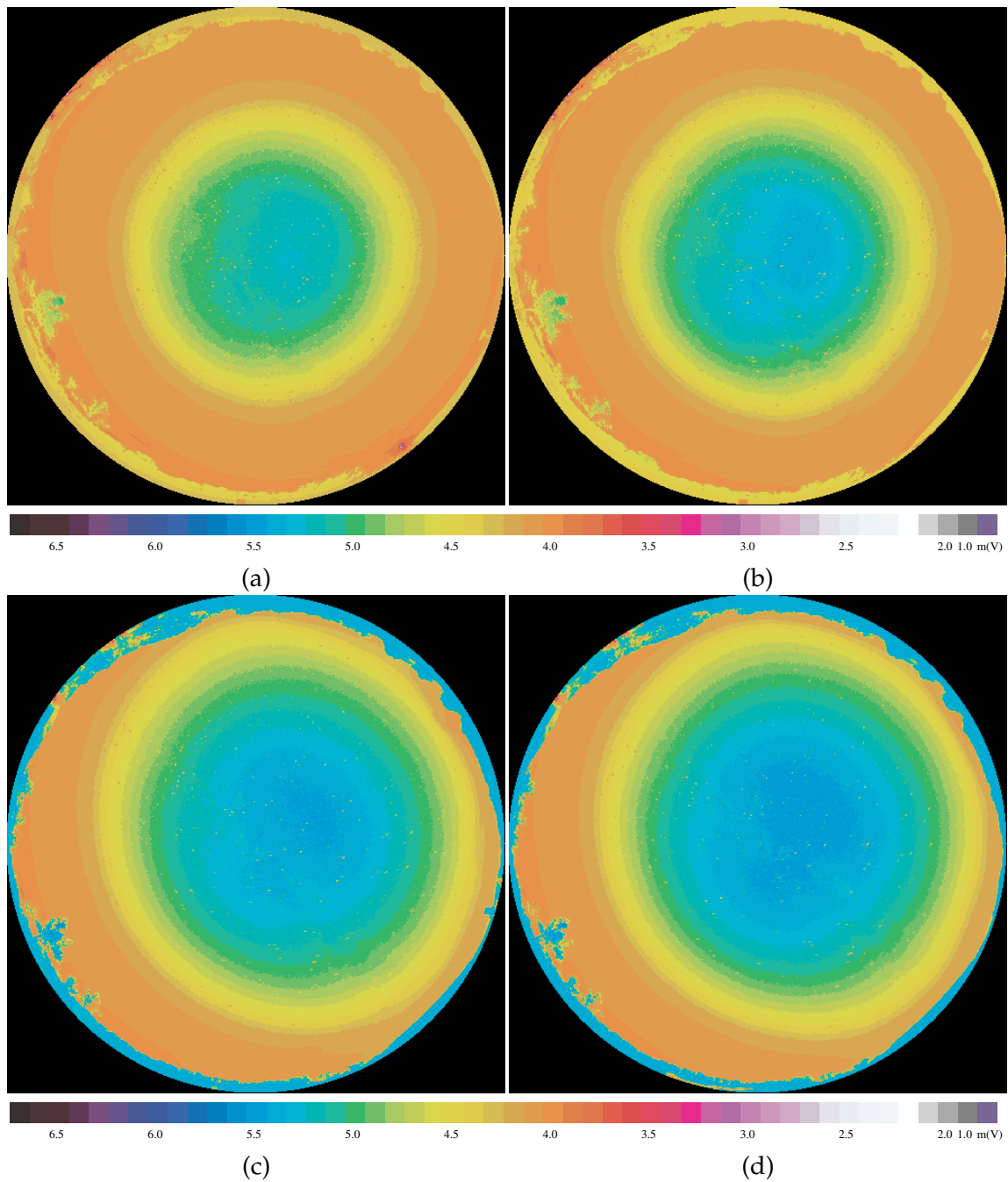


Figure 6.9: Sky quality given as plots of maximum visible magnitude: Effect of reduced public illumination on days of different turbidity on Sophienalpe close to Vienna. (a) Night sky on an average day (2007-08-22) (b) On the same location 30 minutes later. After reduction of public illumination, the sky got notably darker and better. (c) Night sky on a good day (2007-09-14) (d) On the same location 45 minutes later. After reduction of public illumination, the sky got notably darker.

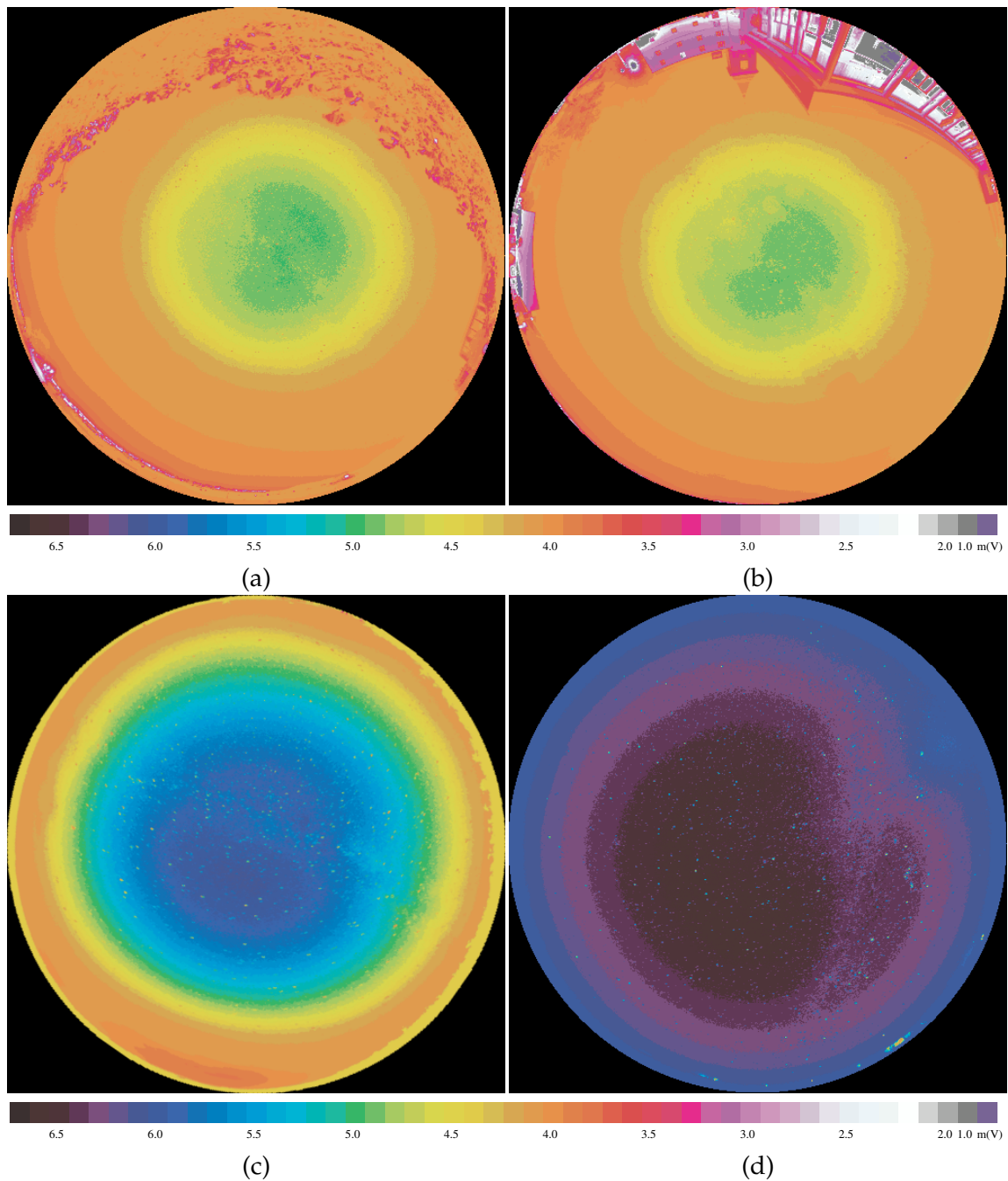


Figure 6.10: Sky quality given as plots of maximum visible magnitude: (a) Night sky at Cobenzl/Vienna, 2007-08-22, at midnight (b) Night sky at Kahlenberg/Vienna, 2007-08-22, after midnight (c) Night sky near Großmugl, Lower Austria, approx. 20km from Vienna, 2007-08-22. The glow of Vienna is on the southern (low) horizon. (d) Night Sky in the Libyan desert, 2006-03-28. Astronomers' dreamland!

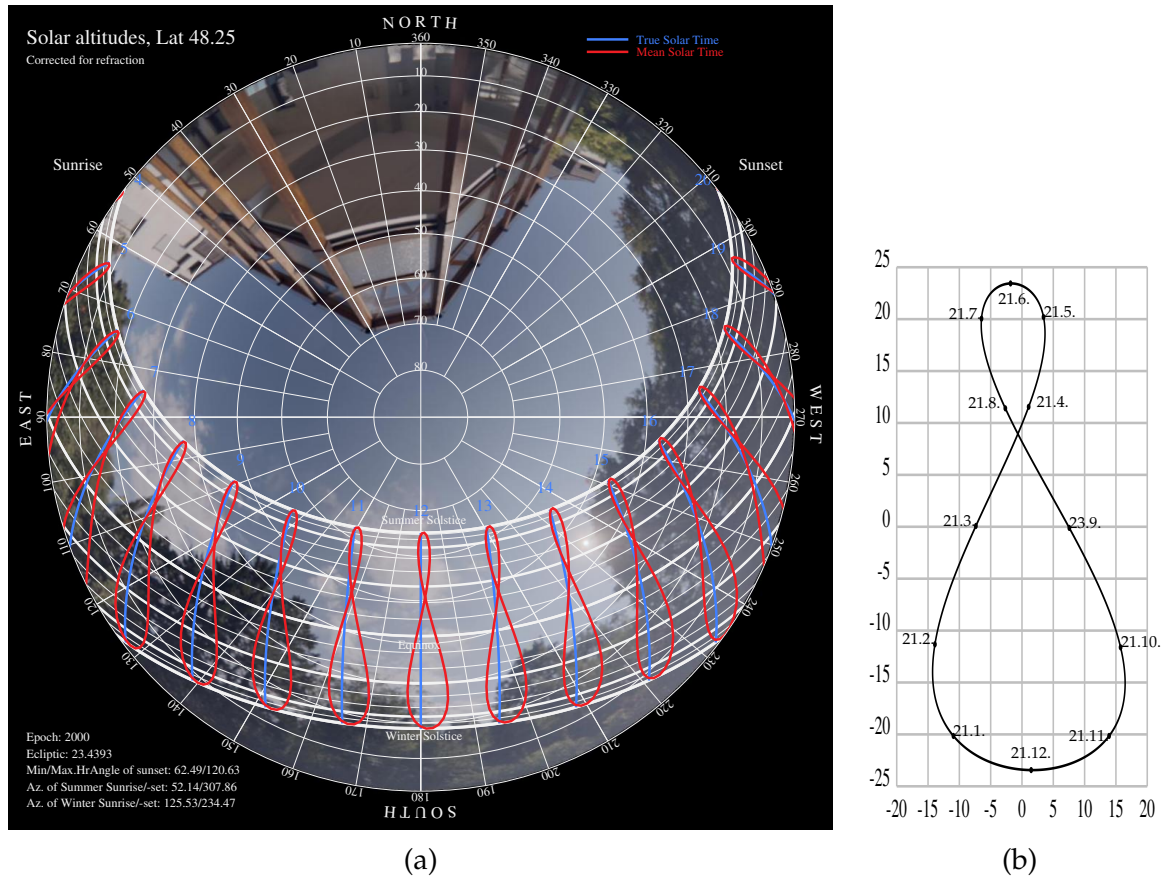


Figure 6.11: Estimation of Sunshine Hours: (a) Fisheye image with overlay of the Sun diagram similar to Fig. 1.4. The diagram includes diurnal paths of the Sun from 10 to 10 days. (b) Analemma with indications of solar positions during the year. It shows the offset between True and Mean Solar Time in minutes (lower scale).

6.4.3 Estimation of Sunshine Hours

In section 1.3.3, a mapping of diurnal arcs of celestial objects has been presented. As indicated later in that section, we can combine such a diagram with a fisheye sky capture to allow an estimate of sunshine duration throughout the year at a given location (Figure 6.11 (a)). The mapping of the diagram has to be adjusted to the geometrical distortion caused by the fisheye lens, which is described by KUMLER and BAUER [2000]. The diagram shows True Solar Hours (where noon is defined with the Sun's culmination) and Mean Solar Time represented by the *analemma* figures. This figure (known from many sundials, more detailed in Figure 6.11 (b)) results from the fact that civil (mean) time is strictly linked to the Earth's rotation, while the Sun can be up to 16 minutes off by the *equation of time* [MEEUS 1998, ch.28]. A further offset of the analemma is caused by the location's difference in geographical longitude to the central meridian of the respective time zone.

The HDR system has an advantage over similar systems based on conventional photography [e.g., Sunprognosis], in that the Sun's position is not hidden in a saturated image zone but remains visible in the HDR image and can be recovered with an adequate tone mapper. Tonemapping on the HDR image of Figure 6.11 (a) was performed with `pfstmo_reinhard05`,

which lets the Sun be visible without overexposure despite its enormous brightness, between the 14:00 and 15:00 analemmas.

This example shows that this particular location receives direct sunshine during the summer from 7:00 (8:00 daylight saving time) in the morning, but is blocked even in summer by the high trees past 14:45 (15:45 daylight saving time). Such results can be important for the planning of, *e.g.*, buildings, locations for outdoor-related activities, solar power plants, or film locations.

6.4.4 Application of HDR Imaging in Archaeo-Astronomy

HDR images can also be helpful in the study of the alleged alignment of buildings towards rising or setting points of the Sun on certain dates, to provide photographic proof of the solar disc right within the purported direction on the day in question – or not! Of course, long-time changes of these points as described in chapter 1 have to be taken into account.

6.5 Discussion

The HDR capture setup with a D-SLR camera described in this chapter was originally intended to provide high-quality daylight sky captures usable for image-based lighting in a high-quality rendering system and as ground truth against which a skylight simulation shall be compared.

Its application towards attempting high-precision measurements also of the night sky has been developed as side-effect, but seems to be well usable. Compared to incidence measurements like the SQM or a luxmeter, the method presented here provides high angular resolution, allowing the detection of emitters on the horizon. On the downside, the required processing capabilities are not negligible, but processing can be performed by a powerful notebook also in the field.

For applications in meteorology, irradiation devices like star pyranometers have been in use for decades [DIRMHIRN 1958]. They provide data on total hemispheric irradiance in a wide wavelength range of typically $0.3 \dots 3\mu\text{m}$, sometimes up to $30\mu\text{m}$, but lack sensitivity if the source is at low altitudes ($h \lesssim 15^\circ$). With such instruments, global radiation (sunlight and diffuse skylight) and sky radiation (with the Sun shaded) can be measured, and the relationship between these data allow an estimate of atmospheric conditions.

The HDR skylight capture system provides only data in the visible spectral range, but angular defects can be removed by flatfielding, and it seems quite likely that atmospheric conditions like cloud cover or turbidity can be extracted with (semi-)automatic image analysis methods, although this topic was out of the scope of this work.

To compute daylight spectral irradiance from the HDR image data, the correlated colour temperature approach described by JUDD *et al.* [1964] and used by TAKAGI *et al.* [1990] and PREETHAM *et al.* [1999] can be used. Care must be taken to select a lens that does not produce the annoying internal reflections in the lens near the Sun which could only be tediously “painted away”.

While glare artifacts are normally regarded as disturbing, they may on the other hand be expected to provide an interesting special effect when the images are used as sky backgrounds in renderings. The shape of the bright reflection artifacts in the first fisheye lens

was however more disturbing than effectful. For measurements, glare figures reduce the reliability of the evaluation, although in the light curves created by averaging the zenith area this was not apparent. For simple sky luminance and colour measurement *without* the Sun, it seems however advisable to follow the classical approach shown, *e.g.* by HERNÁNDEZ-ANDRÉS *et al.* [2003], who also used a fisheye lens, but covered the Sun with a shade. In this case, no filter and far fewer exposures would be required.

The *flat field* images for devignetting have been made by photographing the inside of a globular milk glass lamp-shade on a cloudy day with no direct solar illumination. Still better results would be expected from using an integrating sphere with images with and without filters to also identify a likely stronger filter effect near the horizon circle, where the light rays pass the filter at an oblique angle and thus would be filtered more strongly. Colour calibration would then have to be performed depending on radial distance from the image center.

The system was also used to capture twilight and night skies. The PFSTools allow an absolute calibration of the photographic exposure, so that day and night sky luminance on different sites can be captured with such a setup and be compared to other studies of night sky brightness [*e.g.*, DURISCOE *et al.* 2007]. This application has excited considerable interest in several astronomers and anti light pollution activists, who are mostly concerned about the adverse effects of urban illumination, and possibilities for collaboration are under investigation.

The absolute luminance levels were calibrated with a Minolta LS-110 luminance meter, which however has a minimum sensitivity of 0.01 cd/m^2 . By using longer exposure times, the fisheye sky capture system reaches considerably lower luminance levels. Calibration measurements with a Sky Quality Meter finally allowed the creation of maps of nocturnal sky brightness, although the absolute accuracy of the system cannot currently be determined and can only be estimated to be in the range of the SQM (10%). While the fully automated capture system is usable to capture night skies inside a city down to about 0.001 cd/m^2 , rural skies can only be measured using “bulb” exposure times of several minutes. Also, the spectral sensitivity of the camera would have to be determined to relate the “instrumental magnitudes” to astronomical magnitudes in standardized filter systems to further improve accuracy.

For more reliable results about the average quality of observing sites, many more systematic capture series would be required, which will also have to be correlated to systematic weather observations. Also, the influence of snow on urban and rural night sky luminance would be an interesting subject, which could however not be studied in the too mild, almost snowless winter of 2006/2007.

Chapter 7

Conclusions and Directions for Future Work

This work has shown several areas where sky observation meets computer graphics.

Prehistoric people have apparently cast their observations into cultic buildings which can be analysed by methods from the fields of scientific and information visualisation I have presented in this work, and reconstructed, explored and presented by virtual 3D models.

As example for the application of computer graphics in cultural heritage research, I have reconstructed the astrolabe, a medieval scientific instrument used for sky observations, using methods of *procedural modelling*, so that the *idea* of the instrument is transformed into parametrised functions, and the tedious plotting that requires mathematical precision is left to the printer. A wide variety of Western (European) and Eastern (Islamic) instruments can be created by modification of just a few parameters. Instruments usable for hands-on demonstrations can be built from the same programs by driving a laser engraver/plotter. The same approach can be exploited for the recreation of a variety of other mathematical and early astronomical instruments, like quadrants or sundials.

The extensive survey of papers from the domains of computer graphics and atmosphere physics tried to show the intersection of these domains and can certainly be used as collection of ideas for future research. Some atmosphere physics papers have used certain computational methods decades before they have been introduced in the computer graphics literature. On the other hand, researchers in computer graphics working with natural phenomena should not be afraid of leaving their desks and should compare their results not only visually, but also with measurements taken from nature, as demonstrated in this work (Chapter 5), so that the published models gain more reliability. Many research disciplines could certainly learn from each other when mutual blinkers would be dropped.

The use of digital cameras and novel image formats for measurements is a rapidly evolving field, and standard tools and formats begin to emerge and be used by the industry. Some work still has to be done in this respect, and instruments have to be understood better in order to develop accurate calibration methods and simple to use tools, and also to be able to compare results achieved with consumer-grade cameras against results from traditional measuring equipment.

The results presented in chapters 1 and 2 received considerable interest among archaeologists and amateur and professional astronomers interested in the history of astronomy and historical observations. Clearly, the developed diagram helped in the analysis of probable

doorway orientations. However, the results must still be classified as preliminary. The possible influence of the terrain in the immediate vicinity and possible close horizon features on the orientations have not been investigated yet, so the results should be complemented and verified by accurate *in-situ* surveys of the local terrain and the horizon line..

Stellar visibility in twilight has been extensively researched during the 20th century by SCHÖCH [1927], TOUSEY and KOOMEN [1953] and later by MEEUS [1997, p.289–296] and SCHAEFER [1985, 1987]. The twilight-enabled skylight model by HABER *et al.* [2005] (p. 68) seems to be a good starting point for a model usable for archaeo-astronomical simulations, and it should be completed with the appearance of stars in different stages of twilight, and also with consideration of mesopic (twilight) and scotopic (dark-adapted) vision. The recent developments of affordable graphics hardware that nowadays allow general purpose computations of the SIMD (single instruction, multiple data) kind should be exploited to speed up the simulation of radiative transfer, which still takes several hours on a current CPU. In this respect, for general acceptance of these new hardware devices by scientists of other fields, it seems to be a requirement that floating point numbers and operators as used on the GPU must be identical or even better, and not only “very close”, to the IEEE-754 standard, so the results would be identical to simulations on standard CPUs, and that the graphics hardware is capable of processing double precision floating point data. The fulfillment of both of these requirements seems to be only just below the horizon.

A simulation system optimal for research and demonstration of the alignments studied in archaeo-astronomy would include

- a digital elevation model with possibly several alternatives of the reconstructed archaeological structures and erosion profiles,
- an astronomically and physically correct skydome model, and
- the possibility to virtually walk through the terrain.

For public demonstrations, the whole system should be capable of all-sky projection, so this optimal system would be a planetarium with an all-sky digital projection system and software capable of driving the abovementioned live VR terrain walkthrough, and a sub-horizontal extension of the dome screen to provide the foreground context. This extension can be as simple as a cylindrical stripe below the dome, but must not interfere with the visitors in the auditorium.

Further research in collaboration between archaeologists, surveyors, astronomers, experts in psycho-physics and human vision and, for proper presentation, experts in computer graphics, virtual reconstructions, virtual reality installations and planetaria would be desirable.

The calibrated HDR skydome capturing system presented in this work can be used to capture, and afterwards measure, all-sky luminance and colour snapshots of the skydome, including the Sun, also during the rapidly changing phase of twilight or during a total eclipse of the Sun, when more accurate systems would require far too much time for all-sky measurements. Colorimetric evaluation is readily available from the image data, and accurate daytime skylight spectra for each point on the skydome could be reconstructed from the RGB image data and reference daylight spectra following methods of HERNÁNDEZ-ANDRÉS *et al.* [2004]. This kind of all-sky image capture system could provide an alternative method of recording water vapour and aerosol content (from the sky colour), or cloud cover data (from image analysis) in the atmosphere.

A full 180° skydome image can on the other hand also be evaluated to reconstruct the local horizon of an archaeological site, as long as it has only positive elevation, again providing data for archaeo-astronomical research. The geometric distortion properties of the fisheye lens can be reconstructed by analysis of star positions on a night sky photograph, so that the azimuthal camera orientation can be reconstructed from the position of the Sun in a daylight photograph. Using HDR images is of great utility for the photography of purported alignments towards rising or setting positions of the Sun, because both foreground and the Sun can be shown in a single image, and meaningful conventional (low dynamic range) images without the typical saturated perisolar area can be created from the HDR images by appropriate tone mapping.

The application of the skydome image acquisition system towards quantitatively capturing and monitoring the effects of urban light pollution causing nocturnal sky glow has also received considerable interest with astronomers, and should be extended by careful analysis of the spectral response of the camera system in order to provide results that can be accurately compared to results provided by other measurement methods. The advantage of the fisheye images over integral illuminance measurements is obviously the availability of spatial information, so that the direction of origin of the light pollution can be identified and hopefully at least reduced.

The night sky should be available for everybody, not only on remote sites, but just “in front of the door”. Despite all graphical simulation efforts, nothing can compare to the beauty and peaceful majesty of the *natural* night sky.

Appendix A

Skydome Capture System Based on PFStools

This chapter describes our setup for High Dynamic Range (HDR) skydome image acquisition using advanced consumer-grade digital cameras and extensions to free software which has been used for the results presented in chapter 6.

A.1 Skydome Capture System

Our camera is a Canon EOS 5D, which is equipped with a full-size CMOS sensor (full-size means identical in size to conventional 35mm film, *i.e.*, 24×36 mm). Our lens was originally a Sigma 8mm f/4 like the one used by STUMPFEL *et al.* [2004], but a newer model which has been improved especially for digital cameras. One reported improvement was a smaller divergence of the light beam which decreased vignetting, because vertical incidence is more important for electronic sensors than for film. However, internal reflections of the solar image created disturbing artifacts. The lens was later replaced by the further improved Sigma 8mm f/3.5, which does not show these artifacts. To avoid excessive heat buildup that could lead to more noise, the camera can be wrapped in a first-aid safety blanket (aluminized mylar, also known as “space blanket”), although exactly for the short exposures in daylight we did not experience a significant improvement with this professional-grade camera.

Canon provides a programming toolkit which we used to create a program that can take a sequence of exposures with different exposure times. The program is available for download at our institute’s website [DAUBNER 2007]. The images are downloaded to the controlling notebook, and a function based on `dcraw` (see section A.2) is used to analyze the raw image for over- and underexposure in the circular sky area. The first exposure time has to be preset, and additional exposures are done typically 2 f-stops apart (4 times longer or shorter), until the whole sky zone has been imaged with no under- and overexposed areas. Most images are taken at f/4, but capturing the sun requires f/16 to prevent overexposure. Like STUMPFEL *et al.* [2004] we also found the necessity for a Kodak Wratten #96 ND3.0 neutral density filter to reduce the intensity of direct sunlight during daytime, which however causes a colour shift that has to be corrected later in the processing pipeline. The filter must be removed after sunset for captures of twilight and the night sky.

A.2 Decoding RAW Images from Consumer Cameras

Camera vendors use different RAW formats for their cameras, which are usually closely dependent on the respective sensors and fulfill the purpose of providing the full sensor resolution, which is more than the 8 bits of common JPEG images. It seems impossible for the user to really get access to the original ADC values from the sensor, because at least the error map processing (averaging out single bad pixels) is done immediately by the onboard camera software. A great help in converting all the different raw formats to a single file format is `dcraw` [COFFIN 2007], which is provided in source code, supports over 250 camera models and can write 16-bit `.ppm` and `.tiff` files that are either totally unprocessed (so they show the Bayer filter pattern and raw, unscaled colours), or just interpolated and white-balanced images that are as close to linear as possible. It also includes functionality to process bad pixels which develop as process of detector aging via an external error map file that includes pixel coordinates and their failure dates, so that also images taken before the failure date can be processed again without “correcting away” the pixel that still worked nominally at that date. Also the subtraction of a dark frame is possible, and, with a compile switch, even whitepoint calibration from a Macbeth Color Checker chart can be performed.

A.3 Creation of HDR Sky Images with PFSTools

To create the HDR images, we use the PFSTools [MANTIUK *et al.* 2007; PFSTools 2006], a suite of (mostly) command-line programs intended as research and production toolbox of small programs that can be chained via UNIX pipes to create, modify, store and display HDR images in several formats. A programming extension towards GNU Octave allows analysis or simple modifications like devignetting or application of specialized filters to HDR images in shell scripts or even from the command line.

The program `pfshdr_calibrate`, which is part of the PFSTools, not only finds the sensor response curve for digital cameras required to properly create HDR images from a series of exposures with different exposure times, but even finds out approximate absolute luminance values in $[\text{cd}/\text{m}^2]$ from the exposure and image data. For JPEG images, the PFSTools authors estimate the accuracy of this evaluation to be near 8%, which is usually good enough for most applications in computer graphics, even for the application of luminance-dependent tone-mapping algorithms. True calibration by absolute measurements with a luminance meter is possible with `pfsabsolute`.

A.3.1 Finding Sensor Response

Combining truly linear images into HDR images would be trivial. Unfortunately, consumer-grade cameras usually deliver images which have been processed from the original linear sensor response to simulate classical film behaviour. Frequently, high luminance levels in the original 12-bit sensor data are stronger compressed in the final 8-bit images in order to enhance the low and midtones, and “image styles” can further influence the response mapping. But also the “raw” images can show nonlinearity by anti-blooming gates that practically reduce sensitivity near the saturation level. Creating HDR images from such nonlinear images requires the reconstruction of the response mapping from scene luminance to image

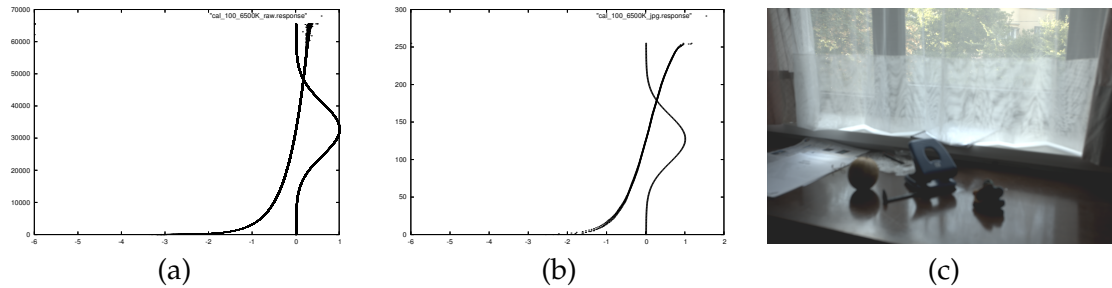


Figure A.1: Camera response curves for Canon 5D, Serial #1831204000, at ISO 100, colour temperature 6500 K, (a) for raw 12-bit format (b) for JPEG format. The Gaussian curves show the most reliable range of pixels. (c) The scene, tonemapped with `pfstmo_durand02`

value. Several methods have been proposed [e.g., DEBEVEC and MALIK 1997; ROBERTSON *et al.* 1999]. The PFSTools by default use the method of ROBERTSON *et al.* [2003].

In order to create a response curve, the only requirement is a series of photographs of a static scene which should not even show very high dynamic range, with identical settings except for exposure time. The authors recommend to slightly defocus the image, so that sharp contrast edges pose no problem in case of even minimal camera shake between exposures.¹ As further recommendation we shall note that glare around saturated areas in these images likewise leads to unusable results and *must* be avoided. So, the best image sequence includes frames that barely show anything and frames that contain only slightly saturated areas. Of course, a regular rectilinear lens has to be used with images completely filling the sensor area, or, rectangular image areas can be cut with `pfscut`, if only fisheye images (with black corners) are available.

`pfshdr_calibrate` originally supported only JPEG files, so the author of this work contributed a small program to read exposure parameters from RAW images (Fig. A.2).

First, exposure data for all image files are read from the image files and written into a parameter file (`hdrgen` script), then `pfshdr_calibrate` analyzes and matches the response of corresponding pixels, and writes a response file for the respective camera. Example:

```
$ dcraw2hdrgen *.cr2 > img.hdrgen
$ pfsinhdrgen img.hdrgen |
  pfshdr_calibrate -v -b 16 -s camera.response
```

The `-b 16` is applicable for RAW files only, for JPEG files, `jpeg2hdrgen` and `-b 8` should obviously be used.

The authors then recommend to analyze the resulting response curve visually with:

```
$ gnuplot
gnuplot> plot "camera.response" with dots
```

The result for our camera in `.cr2` and `.jpg` formats and the (irrelevant by motive) calibration image is shown in figure A.1. The curves for the RAW files overlap and are smooth and practically identical, while the curves for JPEG files show the typical S-profile of processed images.

The response curve can now be used for HDR generation of this and other image sequences taken with the same camera and the same white balance and sensitivity settings.

¹ Several HDR creation toolkits include programs to align the images before combination to the HDR image. For the PFSTools, a program `pfalign` has been presented [TOMASZEWSKA and MANTIUK 2007], but has not been integrated so far, and preliminary substitutes are recommended on the PFSTools website.

```
#!/bin/bash
#
# This file is a part of PFS CALIBRATION package.
#
# Copyright (C) 2004 Grzegorz Krawczyk, <gkrawczyk@users.sourceforge.net>
#
# This program is free software; you can redistribute it and/or modify
# it under the terms of the GNU General Public License as published by
# the Free Software Foundation; either version 2 of the License, or
# (at your option) any later version.
#
# This program is distributed in the hope that it will be useful,
# but WITHOUT ANY WARRANTY; without even the implied warranty of
# MERCHANTABILITY or FITNESS FOR A PARTICULAR PURPOSE. See the
# GNU General Public License for more details.
#
# You should have received a copy of the GNU General Public License
# along with this program; if not, write to the Free Software
# Foundation, Inc., 59 Temple Place, Suite 330, Boston, MA 02111-1307 USA
#
#-----
# This program by Georg Zotti <gzotti@cg.tuwien.ac.at>, derived from jpeg2hdrngen
#
# $Id: dcraw2hdrngen,v 1.2 2006/08/22 18:34:04 gkrawczyk Exp $

LC_NUMERIC=POSIX          # ensure dot is used as the decimal separator
export LC_NUMERIC

LC_ALL=POSIX              # apparently this is necessary on Gentoo
export LC_ALL

DCRAW="dcraw -i -v"        # program for extracting exposure info from "raw" images

TEST_DCRAW='which dcraw';
if [ "$TEST_DCRAW" = "" ]; then
    echo "Program 'dcraw' is required to run this script."
    echo "Install appropriate software, for example from:"
    echo "http://www.cybercom.net/~dcoffin/dcraw/"
    exit 1;
fi

#Note: Double backslash MUST be put in front of each $ sign
AWK_PROGRAM='cat <<EOF
BEGIN {
    exposure="";
    aperture="";
}

END {
    if( aperture=="")
        aperture=1;

    if( iso_speed=="")
        iso_speed=100;

    if( exposure=="")
        printf("unrecognized raw format!\n");
    else
        print exposure " " aperture " " iso_speed " 0";
}

/^Shutter: (1/)?([0-9]*\.[0-9]*) sec/ {
    if (substr($2, 1, 2)=="1/")
        exposure = substr($2, 3);
    else
        exposure = 1/$2;
}

/^Aperture: f\./([0-9]*\.[0-9]*)/ {
    aperture = substr($2,3);
}

/^ISO speed: ([0-9]*\.[0-9]*)/ {
    iso_speed = $3;
}

EOF'

while [ "$1" != "" ]; do
    EXPOSURE_INFO='$DCRAW $1 | awk "$AWK_PROGRAM"'
    echo $1 $EXPOSURE_INFO

    shift
done
```

Figure A.2: dcraw2hdrngen, a script contributed to the PFSTools to read exposure data from RAW images supported by dcraw

A.3.2 Creating Ordinary HDR Images

A series of raw images in .cr2 format is first again processed with `dcraw2hdrngen` to extract exposure data into a configuration file. From this file and the response data file, a regular HDR image is generated with the sequence

```
$ dcraw2hdrngen *.cr2 > img.hdrngen
$ pfsinhdrngen img.hdrngen |
  pfshdrcalibrate -v -b 16 -f camera.response |
  pfsouttrgbe img.hdr
```

where in this case an HDR image in Radiance RGBE format [LARSON and SHAKESPEARE 1998] is created. Note that the OpenEXR format [INDUSTRIAL LIGHT AND MAGIC 2003] is not capable of storing the full range of daylight luminance values including the solar disk, and `pfsoutexr` would emit a warning message for such images. For our evaluation, we use the native PFS format, which uses IEEE 754 32 bits floating point numbers per pixel and channel, and stores CIE XYZ values. The images require lots of disk space (94MB for an image in full resolution of the EOS-5D, cropped to the square including the circular fisheye image area), but could be converted to other formats or scaled with `pfssize` if required.

A.3.3 Correction of Lens Effects

Both Sigma 8mm fisheye lenses show slight *chromatic aberration*, which can be corrected in `dcraw` with the switch `-C 0.999 1.0001`.

The geometric radial imaging characteristic of fisheye lenses can be adequately described by a function $r = \alpha \sin(\beta\theta)$ with angle from image center θ and parameters α and β unique to a given lens [KUMLER and BAUER 2000]. These values can be derived, *e.g.*, from measuring stellar images and comparing the positions with catalog data. For the Sigma f/4.0 lens, $\alpha = 14.7$, $\beta = 0.54$ have been derived by KUMLER and BAUER [2000]. More accurate general formulations have been presented, *e.g.*, by VAN DEN HEUVEL *et al.* [2006] or SCHWALBE [2005].

The radial brightness falloff (*vignetting*) depends on the respective lens and field stop value. Ideally, to fix vignetting (and several other defects) in CCD images made with optical systems providing rectilinear images, a homogeneous white surface is imaged as *flat* calibration image, and the scene image of interest (*science frame*) is then divided pixel-wise by the normalized flat [BERRY and BURNELL 2000]. A method to correct vignetting in photographs from consumer cameras has recently been proposed by D'ANGELO [2007], who uses it for stitching HDR panoramic images.

A *flatfield image* for a fisheye image would have to be made inside a homogeneously lit white sphere known as *integrating sphere*. A fisheye image of this sphere ideally would be a homogeneously lit circle, but would typically rather show the vignetting pattern instead. As approximative solution, a globular lamp shade made from milk glass can be put over the fisheye lens in a location with unblocked horizon under a cloud-covered sky without direct sunshine, and series of exposures are then taken with all aperture settings used for the production images.

The images are processed into regular PFS files, but then normalized with the added program `pfsnormalize` (Fig. A.3).

With such an image, the sky images can be flat-fielded using `pfsflatfield` (Fig. A.4).

```
#!/bin/bash

# script calling pfsocetavelum with a fixed octave script.
# This script scales the Y channel so that its maximum is 1.
# Images can then be used to Flat-Field other images.

# Works with pfstools, the HDR suite by MPI.
# G. Zotti, 2007-08-07

pfsocetavelum 'Ymax=max(max(Y)) ;
               fprintf(stderr, "pfsnormalize: Ymax=%11.9f, scaling image\n", Ymax);
               Y /= Ymax ; '
```

Figure A.3: pfsnormalize: Setting maximum luminance to 1.

```
#!/usr/bin/octave -q
#
# This file is an addon to the PFSTOOLS package.
# author Georg Zotti, <gzotti@cg.tuwien.ac.at>
#
# Example usage: pfsin scene.pfs | pfsflatfield Flat.pfs | pfsout scene-flattened.pfs

if( length( argv ) != 1 )
    error( "pfsflatfield: Expecting exactly one parameter, the flatfield PFS image" );
endif

flat = pfsopen( argv{1} );
flat = pfsget (flat);

pin = pfsopen( "stdin" );
pin = pfsget( pin );

if ((pin.rows != flat.rows) || (pin.columns != flat.columns))
    error("pfsflatfield: Flat and Image Frame Size Mismatch!");
endif

pout = pfsopen( "stdout", pin.rows, pin.columns );

## Copy channels and tags from the source to destination stream
pout.channels = pin.channels;
pout.tags = pin.tags;
pout.channelTags = pin.channelTags;

[Yflat _xflat _yflat] = pfstransform_colorspace( "XYZ", flat.channels.X, \
        flat.channels.Y, flat.channels.Z, "Yxy" );

[Y _x _y] = pfstransform_colorspace( "XYZ", pout.channels.X, \
        pout.channels.Y, pout.channels.Z, "Yxy" );

Y = Y ./ Yflat ; # Octave allows element-wise division without looping!

[pout.channels.X pout.channels.Y pout.channels.Z] = \
    pfstransform_colorspace( "Yxy", Y, _x, _y, "XYZ" );

pfsput( pout );
pfsfclose( pin );
if( exist( "pout" ) != 0 )
    pfsfclose( pout );
endif

pfsfclose ( flat );
```

Figure A.4: pfsflatfield: Pixel-wise division of image data.

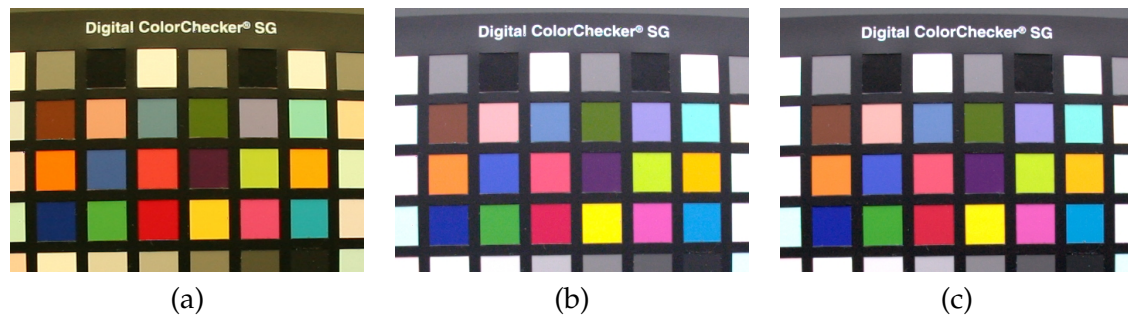


Figure A.5: Removing colour shift caused by Kodak Wratten #96 ND3.0 “neutral density” filter: (a) filtered image, exposed 180 seconds, without calibration. (b) filtered image after calibration. (c) unfiltered image (exposed 1/8s), after calibration.

A.3.4 Camera Colour Calibration

The Kodak Wratten #96 ND3.0 neutral density filter is not so neutral, but causes a colour shift that requires a white balancing step. The program `dcraw` is also capable of such colour correction: A Macbeth Digital ColorChecker® SG card was photographed in the institute’s lightbox under D65 illumination through the fisheye lens, with and without filter. The coordinates of the classical 24 Macbeth Color Checker patches were entered in the `dcraw` source and the program recompiled with the `-DCOLORCHECK` switch. The command

```
$ dcraw -v <filename>.CR2
```

then provides the required values for achieving white balanced images. The colour shift of filtered images can now be removed with a regularly built `dcraw` with the correct scaling values via the sequence

```
$ dcraw -r <values> <filename>.CR2
```

Figure A.5 shows the exposures through the filter before and after white balance correction and an unfiltered image for comparison. The result is not absolutely identical, but very close to an image taken without filter and likewise processed with the self-calibrating colour check. By default, `pfsindcraw` of the PFSTools calls `dcraw` with the “camera white balance” option. A patched version of this script is shown in figure A.6.

To better evaluate the filter characteristic, a transmission spectrum should be recorded with a calibrated spectroradiometer.

A.3.5 Absolute Calibration

While `pfsHDRcalibrate` finds approximate scene luminance values from the EXIF exposure data in JPEG images, luminance for both filtered and unfiltered RAW images must be adjusted with `pfsabsolute`. Correct absolute values are also required for a smooth transition of filtered and unfiltered images during twilight and are also important in some tone mapping algorithms.

The simplest way to achieve absolute calibration is to load the HDR image into `pfsview` and read the Y value of a spot close to the image center (where vignetting is still negligible, if the image has not been flat-fielded) that has also been measured in the real scene with a luminance meter. The command to add in the chain is then

```
#!/bin/bash
#####
# Wrapper for dcraw.
# Convert digital camera RAW files to 16bit PPMs.
#
# this is a stub with basic functionality
# PATCH BY GZOTTI: ADDED $PFSINDCRAW_DCRAWPAR
#####

if test -z $1 || test "$1" = "--help" || test "$1" = "-h"; then
cat <<EOF

Read an image in a camera RAW file format supported by
DCRAW and write pfs stream to the standard output as
if read from 16bit ppm file (no gamma correction,
white balance from camera if available).

Usage: pfsindcraw <file> [<file>...]

See the man page for more information.

If \PFSINDCRAW_DCRAWPAR is set, it is used as parameters to dcraw,
and it must include white balance commands.

EOF
    exit 1
fi

# This avoids problems if not calling via mkSky, and keeps original behaviour.
if [ -z "$PFSINDCRAW_DCRAWPAR" ] ; then
    echo >&2 "Using Camera White Point "
    PFSINDCRAW_DCRAWPAR="-w"
fi

if ! which dcraw 2>/dev/null 1>/dev/null; then
    echo >&2 "pfsindcraw: dcraw program not found. Check if it is installed and can be found in the PATH."
    exit 1;
fi

if ! which pfsinppm 2>/dev/null 1>/dev/null; then
    echo >&2 "pfsindcraw: pfsinppm program not found. Check if pfstools are compiled with netpbm support."
    exit 1;
fi

#Arguments used for all images passed to pfsindcraw
global_arguments=""
if test -n "$1"; then
    while test "${1:0:1}" = "-"; do
        case $1 in
            *)
                echo >&2 "No option is implemented at the moment."
                exit 1;
            esac
            global_arguments="$global_arguments $1"
            shift
        done
    fi

    while test "$1"; do
        file_pattern=$1

        dcraw -c -m -4 $PFSINDCRAW_DCRAWPAR $file_pattern | pfsinppm - 2> /dev/null | \
            pfstag --set "FILE_NAME=${file_pattern}" --set "LUMINANCE=RELATIVE"

        shift
    done
done
```

Figure A.6: Patched version of pfsindcraw to feed arguments to dcraw via environment variables.

```
$ pfsabsolute <measured_value> <current_image_value>
```

Typically, the values should be in the same order of magnitude for unfiltered JPEG exposures, because via `pfshdrcalibrate` approximately correct luminance values have been derived from ISO range, exposure time and aperture value. Comparative measurements with a Minolta LS-110 luminance meter showed however the necessity of a scale factor of 3.1 ± 0.3 to scale the luminance values in the PFS files resulting from RAW images combination. The presence of filters of course must be corrected in this way.

The real filter factor for the ND3 filter was reconstructed from the luminance difference between filtered and unfiltered exposures made in the lightbox. It is more correctly an ND3.18 filter with transparency of about 1/1700. The zenith brightness values now reconstructed from filtered and unfiltered exposures after calibration closely match those values given by SCHAEFER [1993, p.321], with an error estimate of typically less than 10%.

After this step, the HDR file now contains corrected luminance values in $[\text{cd}/\text{m}^2]$ and can be used as sky radiance map in a global illumination renderer or evaluated for other purposes.

A.3.6 HDR Skylight Script

The capture program creates file names in the format `SKY_YYYYMMDD_HHMMSS_seq.CR2`, with date and time of the first image in a sequence taken from the controlling notebook's clock, and `seq` a sequence number: 00 for the first image, and numbers `+nn` and `-nn` for longer and shorter exposures, respectively. The script `mkSky` (Fig. A.7) is used to process these series of `.cr2` images into a `.pfs` HDR file, where `pfscut` is used to trim the unused image area and create a square image. The flatfield command should be added in the command sequence as soon as a flatfield image has been created.

The combination of several Canon 5D RAW images takes several minutes and significant amounts of memory. On an Athlon™ 64 3500+ processor, the observed memory footprint was about 1.7GB.

To process a whole directory of captures, *e.g.*, a full day, we can use the obvious shell command sequence:

```
$ for f in SKY_20070807_*_00.CR2
do
    echo $f
    mkSky `basename $f _00.CR2`
done
```

A.3.7 Masking Empty Pixels

Ideal fisheye images consist of an image circle inside a black rectangle, which we have trimmed already into a square during the HDR image generation above. Bias, dark current or stray light from a low sun cause some unwanted illumination in the corner zones, which can be trimmed away easily with a tiny add-on script, `pfscircle`, that calls the general GNU Octave interface `pfsocetavelum` and can be added anywhere in the command sequence (Fig. A.8).

```
#!/bin/bash
# script to create one sky HDR image

# Let this variable point to your calibration file
CALIB_FILE=/data/Sky/Cal20070729/cal_100_6500K_raw.response
# chromatic aberration fix for Sigma 8mm f/4 Fisheye images for dcraw
CHROMATIC_ABERR="-C 0.999 1.0001 "

if [ "$1" == "" ]
then
    echo "Usage : $0 [-n] [-f] <SKY_DDMYYYY_HHMMSS> "
    echo "Option: -f apply colour match for filtered image "
    exit 0
fi

# define chromatic aberration fix, colour and absolute multipliers
# for sRGB with or without filters
# Comparative measurements with Minolta LS-110 indicate a factor 3.1 for RAW images.

if [ "$1" == "-f" ]
then
    echo "Creating sRGB Sky HDR image made with ND3 filter"
    export PFSINDCRAW_DCRAWPAR="$CHROMATIC_ABERR -v -r 1.846705 1.0 2.213889 1.0 "
    export PFSABSOLUTE_FACTOR="334800 63.7"

    shift
else
    echo "Creating sRGB Sky HDR image made without ND3 filter"
    export PFSINDCRAW_DCRAWPAR="$CHROMATIC_ABERR -v -r 2.381668 1.0 1.469678 1.0 "
    export PFSABSOLUTE_FACTOR="3.1 1"
fi

if [ -f $1.hdrngen ]
then
    echo "Using existing $1.hdrngen"
else dcraw2hdrngen $1_*.CR2 > $1.hdrngen
fi

pfsinhdrngen $1.hdrngen \
| pfscut --left 800 --top 50 --width 2800 --height 2800 \
| pfshdrcalibrate -v -b 16 -f $CALIB_FILE \
| pfsabsolute $PFSABSOLUTE_FACTOR \
| pfsout $1.pfs
```

Figure A.7: mkSky: Capture series to HDR conversion Script

```
#!/bin/bash
# script calling pfsoctavelum with a certain octave script. The image MUST be
# quadratic, or at least wider than high, and a circle of the height of the
# image will be left in the center, the borders will be blackened.
# Works with pfstools, the HDR suite by MPI.
# G. Zotti, 2007-08-07
pfsoctavelum 'Xcent=pin.columns/2 ; Ycent=pin.rows/2; radius = pin.rows/2; \
for y = 1 : pin.rows ; \
    angle=asin((Ycent-y)/radius); \
    xOff= ceil(cos(angle) * radius); \
    for x=1 : Xcent-xOff ; Y(y, x)=0 ; endfor ; \
    for x=ceil(Xcent)+xOff : pin.columns ; Y(y, x)=0 ; endfor ; \
endfor ; '
```

Figure A.8: pfscircle: Masking Image Corners

A.3.8 Tone Mapping

The HDR image can be used for purposes like image-based lighting, where the HDR data obviously provide far superior results over conventional photographs [REINHARD *et al.* 2006]. HDR monitors have been presented already, but are extremely expensive. For presentation of the HDR images on conventional screens and also in print, the dynamic range of daylight scenes, which can well be 6 orders of magnitude for images including the Sun, has to be compressed again by *tone mapping*, which ideally is used like an auto-exposure feature on a camera that produces conventional images, so that twilight and night scenes are visible even if luminance levels are about 6 orders of magnitude lower than average daylight scenes. The dynamic range of scenes without the Sun is obviously by far smaller.

The PFSTools include several implementations of tone mapping algorithms [PFStmo 2007]. Tone mappers are not aware of the black image circle but could be confused by stray light in the outer circle, and may on the other hand change this outer area, so `pfscircle` should be used before and after the tone mapper. Example use:

```
$ for f in *.pfs ; do
    pfsin $f | pfscircle | pfstmo_fattal02 | pfscircle |
    pfsout 'basename $f .pfs'_fattal02.jpg
done
```

A.3.9 Zenith Brightness Evaluation

The GNU Octave interface `pfsoctavelum` can be used for a variety of extensions to the PFSTools, of which we give a final example.

To record zenith brightness values for a full day capture sequence, a central box in the image (in the case below, the images had been scaled down with `pfssize`, so a 7×7 box was adequate) can be sampled with the following command sequence. Note that the script evaluated by `pfsoctavelum` must obviously not write to `stdout`, where the `pfs` stream is written.

```
$ for f in *.pfs ;
do
    echo -e -n "'basename $f .pfs' \t" ;
    pfsin $f |
    pfsoctavelum \
        'Yavg=0.0; cnt=0 ;
        for y=pin.rows/2 - 3 : pin.rows/2 + 3 ;
            for x=pin.columns/2 - 3 : pin.columns/2 + 3 ;
                Yavg+=Y(y, x) ;
                cnt++ ;
            endfor ;
        endfor ;
        Yavg/=cnt ;
        fprintf(stderr, "%11.9f\n", Yavg); ' > /dev/null ;
done
```

Similar, but longer scripts have been used to create the false-colour plots of the night sky for Figures 6.8–6.10.

Bibliography

- CHARLES N. ADAMS, GILBERT N. PLASS, and GEORGE W. KATTAWAR [1974]: The Influence of Ozone and Aerosols on the Brightness and Color of the Twilight Sky. In: *Journal of the Atmospheric Sciences* vol. 31, pp. 1662–1674
- ADOBE SYSTEMS, INCORPORATED [1990]: *PostScript Language Reference Manual*. Addison-Wesley, 2nd edn.. (“Red Book”)
- SAMEER AGARWAL, RAVI RAMAMOORTHY, SERGE BELONGIE, and HENRIK WANN JENSEN [2003]: Structured importance sampling of environment maps. In: *ACM Transactions on Graphics* vol. 22(3), pp. 605–612. ISSN 0730-0301. doi:<http://doi.acm.org/10.1145/882262.882314>
- MONZUR AHMED [1996/1997]: The Determination of Salat Times. (accessed July 6, 2005)
URL <http://www.ummah.net/astronomy/saltime/>
- DAVID ARNOLD and GUNTRAM GESER [2007]: D 2.11: Research Agenda. Tech. Rep., EPOCH: European Research Network on Excellence in Processing Open Cultural Heritage
URL http://private-repository.epoch-net.org/deliverables/epoch_d211_ra_v10_200107.pdf
- LAWRENCE H. AUER and E. MYLES STANDISH [2000]: Astronomical Refraction: Computational Method for All Zenith Angles. In: *The Astronomical Journal* vol. 119, pp. 2472–2474
- GLADIMIR V. G. BARANOSKI, JUSTIN WAN, JON G. ROKNE, and IAN BELL [2005]: Simulating the Dynamics of Auroral Phenomena. In: *ACM Transactions on Graphics* vol. 24(1), pp. 37–59
- HELMUT BECKER [1996]: Kultplätze, Sonnentempel und Kalenderbauten aus dem 5. Jahrtausend vor Chr. – Die mittelneolithischen Kreisanlagen in Niederbayern. In: HELMUT BECKER (Editor), *Archäologische Prospektion, Luftbildarchäologie und Geophysik*, pp. 101–122. No. 59 in Arbeitshefte, Bayerisches Landesamt für Denkmalpflege, München
- MARC BERGER, NANCY LEVIT, and TERRY TROUT [1990]: Rendering Mirages and Other Atmospheric Phenomena. In: C. E. VANDONI and D. A. DUCE (Editors), *Proc. EUROGRAPHICS’90*, pp. 459–468. Eurographics, Elsevier Science Publishers B.V. (North-Holland)
- RENE BERNDT, DIETER W. FELLNER, and SVEN HAVEMANN [2005]: Generative 3D Models: A Key to More Information within Less Bandwidth at Higher Quality. In: *Web3D ’05: Proc. 10th intl. conf. on 3D Web technology*, pp. 111–121. ACM Press, New York, NY, USA. ISBN 1-59593-012-4. doi:<http://doi.acm.org/10.1145/1050491.1050508>

- RICHARD BERRY and JAMES BURNELL [2000]: *The Handbook of Astronomical Image Processing*. Willmann-Bell, Inc., Richmond, Virginia, USA. ISBN 0-943396-67-0
- P. J. BIRCH, S. P. BROWNE, V. J. JENNINGS, A. M. DAY, and D. B. ARNOLD [2001]: Rapid Procedural-Modelling of Architectural Structures. In: *VAST '01: Proceedings of the 2001 conference on Virtual reality, archeology, and cultural heritage*, pp. 187–196. ACM Press, New York, NY, USA. ISBN 1-58113-447-9. doi:<http://doi.acm.org/10.1145/584993.585023>
- WOLFRAM G. BLÄTTNER, HENRY G. HORAK, DAVE G. COLLINS, and MICHAEL B. WELLS [1974]: Monte Carlo Studies of the Sky Radiation at Twilight. In: *Applied Optics* vol. 13(3), pp. 534–547
- J.F. BLINN [1982]: Light reflection techniques for simulation of clouds and dusty surfaces. In: *Computer Graphics* vol. 3(16), pp. 21–29. ISSN 0097-8930
- MARTIN BRUNOLD [2001]: *Der Messing-Himmel—Eine Anleitung zum Astrolabium*. Institut l’homme et le temps, La Chaux-de-Fonds. ISBN 2-940088-11-X
- DAN BRUTON [1996]: *Optical Determination of Atmospheric Temperature Profiles*. Ph.D. thesis, Texas A&M University. Major Subject: Physics
- ANTHONY BUCHOLTZ [1995]: Rayleigh-scattering calculations for the terrestrial atmosphere. In: *Applied Optics* vol. 34(15), pp. 2765–2773
- S. CHANDRASEKHAR [1960]: *Radiative Transfer*. Dover Publications, Inc., New York. ISBN 0-486-60590-6
- GEOFFREY CHAUCER [ca. 1391]: A Treatise on the Astrolabe. Medieval Source Book website URL <http://www.fordham.edu/halsall/sbook.html>
- PHILIP E. CIDDOR [1996]: Refractive index of air: new equations for the visible and near infrared. In: *Applied Optics* vol. 35(9), pp. 1566–1573
- CIE [1973]: *Standardization of Luminance Distribution on Clear Skies*. Paris
- CIE [1994]: *CIE-110-1994: Spatial distribution of daylight - luminance distributions of various reference skies*
- CIE [2004]: *ISO 15469:2004(E) / CIE S 011/E:2003 Spatial distribution of daylight - CIE standard general sky*. International Commission on Illumination (CIE), 2nd edn.
- PIERANTONIO CINZANO [1997]: *Inquinamento Luminoso e Protezione del Cielo Notturmo*, *Memoirie Classe di Scienze Fisiche, Matematiche e Naturali*, vol. XXXVIII. Istituto Veneto di Scienze, Lettere ed Arti, Venezia. ISBN 88-86166-48-6
- PIERANTONIO CINZANO [2005]: Night Sky Photometry with Sky Quality Meter. Tech. Rep. 9, ISTIL - Istituto di Scienza e Tecnologia dell’Inquinamento Luminoso (Light Pollution Science and Technology Institute), Thiene, Italy
URL <http://www.lightpollution.it/download/sqmreport.pdf>
- DAVE COFFIN [2007]: Decoding raw digital photos in Linux. online. (accessed July 27, 2007)
URL <http://cybercom.net/~dcoffin/dcrawl/>

- DAVE G. COLLINS, WOLFRAM G. BLÄTTNER, MICHAEL B. WELLS, and HENRY G. HORAK [1972]: Backwards Monte Carlo Calculations of the Polarization Characteristics of the Radiation Emerging from Spherical-Shell Atmospheres. In: *Applied Optics* vol. 11(11), pp. 2684–2696
- WILLIAM M. CORNETTE and JOSEPH G. SHANKS [1992]: Physical reasonable analytic expression for the single-scattering phase function. In: *Applied Optics* vol. 31(16), pp. 3152–3160
- FRANKLIN CROW [1977]: Shadow Algorithms for Computer Graphics. In: *Proc. SIGGRAPH '77*, pp. 242–248. ACM
- FALKO DAIM and WOLFGANG NEUBAUER (Editors) [2005]: *Zeitreise Heldenberg: Geheimnisvolle Kreisgräben — Niederösterreichische Landesausstellung 2005*. No. 459 in Katalog des NÖ Landesmuseums, Neue Folge, Verlag Berger, Horn, Wien. ISBN 3-85460-226-X
- PABLO D'ANGELO [2007]: Radiometric alignment and vignetting calibration. In: *Camera Calibration Methods for Computer Vision Systems (Proc. CCMVS 2007)*
URL <http://biecoll.ub.uni-bielefeld.de/volltexte/2007/101>
- Darksy : International Darksy Association website
URL <http://www.darksy.org>
- STANISLAV DARULA and RICHARD KITTLER [2002]: CIE General Sky Standard Defining Luminance Distributions. In: *Proceedings eSim*
URL <http://www.esim.ca/2002/documents/Proceedings/other2.pdf>
- FRANZ DAUBNER [2007]: HDR Capture GUI. Software
URL <http://www.cg.tuwien.ac.at/research/publications/2007/daubner-2007-HDR/>
- WAYNE P. S. DAVIDSON and SIEBREN Y. VAN DER WERF [2005]: The Toboggan Sun. In: *Applied Optics* vol. 44(27), pp. 5644–5651
- PAUL DEBEVEC, CHRIS TCHOU, ANDREW GARDNER, TIM HAWKINS, CHARIS POULLIS, JESSI STUMPFEL, ANDREW JONES, NATHANIEL YUN, PER EINARSSON, THERESE LUNDGREN, MARCOS FAJARDO, and PHILIPPE MARTINEZ [2004]: Estimating Surface Reflectance Properties of a Complex Scene under Captured Natural Illumination. Tech. Rep. USC ICT-TR-06.2004, University of Southern California Institute for Creative Technologies Graphics Laboratory
- PAUL E. DEBEVEC and JITENDRA MALIK [1997]: Recovering High Dynamic Range Radiance Maps from Photographs. In: *SIGGRAPH '97: Proceedings of the 24th Annual Conference on Computer Graphics and Interactive Techniques*, pp. 369–378. ACM Press/Addison-Wesley Publishing Co., New York, NY, USA. ISBN 0-89791-896-7. doi:<http://doi.acm.org/10.1145/258734.258884>
- INGE DIRMHORN [1958]: Untersuchungen an Sternpyranometern. In: *Theoretical and Applied Climatology* vol. 9(2), pp. 124–148. ISSN 0177-798X. doi:[10.1007/BF02242905](https://doi.org/10.1007/BF02242905)

- YOSHINORI DOBASHI, KAZUFUMI KANEDA, TAKANOBU NAKASHIMA, and HIDEO YAMASHITA [1994a]: Skylight for Interior Lighting Design. In: M. DAEHLEN and L. KJELLDAHL (Editors), *Proc. Eurographics '94, Computer Graphics Forum*, vol. 13(3), pp. C-85-C-96. Eurographics Assoc., Blackwell
- YOSHINORI DOBASHI, TOMOYUKI NISHITA, KAZUFUMI KANEDA, and HIDEO YAMASHITA [1994b]: Fast Display Method of Sky Color Using Basis Functions. In: *Proc. Pacific Graphics '94*, pp. 194-208. Also published as DOBASHI *et al.* [1997]
- YOSHINORI DOBASHI, KAZUFUMI KANEDA, HIDEO YAMASHITA, and TOMOYUKI NISHITA [1996]: Method for Calculation of Sky Light Luminance Aiming at an Interactive Architectural Design. In: J. ROSSIGNAC and F. SILLION (Editors), *Proc. EUROGRAPHICS '96, Computer Graphics Forum*, vol. 15(3), pp. C-109-C-119. Eurographics Assoc., Blackwell
- YOSHINORI DOBASHI, TOMOYUKI NISHITA, KAZUFUMI KANEDA, and HIDEO YAMASHITA [1997]: A Fast Display Method of Sky Colour Using Basis Functions. In: *The Journal of Visualization and Computer Graphics* vol. 8(2), pp. 115-127
URL <http://citeseer.ist.psu.edu/dobashi97fast.html>
- YOSHINORI DOBASHI, TSUYOSHI YAMAMOTO, and TOMOYUKI NISHITA [2002]: Interactive rendering of atmospheric scattering effects using graphics hardware. In: *HWWS '02: Proceedings of the ACM SIGGRAPH/EUROGRAPHICS conference on Graphics hardware*, pp. 99-107. Eurographics Association, Aire-la-Ville, Switzerland, Switzerland. ISBN 1-58113-580-7
- DAN M. DURISCOE, CHRISTIAN B. LUGINBUHL, and CHADWICK A. MOORE [2007]: Measuring Night-Sky Brightness with a Wide-Field CCD Camera. In: *Publications of the Astronomical Society of the Pacific* vol. 119, pp. 192-213
- ALOIS EDER-HINTERLEITNER, WOLFGANG NEUBAUER, and PETER MELICHAR [1999]: Magnetic modelling for the 3D reconstruction of the neolithic circular ditch system of Steinbrunn/Austria. In: J. FASSBINDER and W. IRLINGER (Editors), *Archaeological Prospection*, pp. 32-33. No. 108 in Arbeitshefte, Bayerisches Landesamt für Denkmalpflege
- BENGT EDLÉN [1953]: The Dispersion of Standard Air. In: *Journal of the Optical Society of America* vol. 43(5), pp. 339-344
- ESA Digital Universe [2004]: The Digital Universe. (accessed August 2, 2006)
URL <http://sci.esa.int/science-e/www/object/index.cfm?fobjectid=35171>
- ESA Hipparcos : Hipparcos Website. (accessed August 2, 2006)
URL <http://sci.esa.int/science-e/www/area/index.cfm?fareaid=20>
- EVANS&SUTHERLAND [2006]: Digistar 3 Laser. (accessed August 7, 2006)
URL http://www.es.com/products/digital_theater/digistar3-laser.asp
- MARIA G. FIRNEIS [1984]: Untersuchung zur astronomischen Orientierung des Domes zu St. Stephan/Wien. In: *Mitt. d. Mathematisch-Naturwissenschaftlichen Klasse, Österreichische Akademie der Wissenschaften* vol. 193(8-10)
- ALISTAIR B. FRASER [1977]: Solutions of the refraction and extinction integrals for use in inversions and image formation. In: *Applied Optics* vol. 16(1), pp. 160-165

- EDWARD R. FRENIERE, G. GROOT GREGORY, and RICHARD A. HASSLER [1999]: Polarization models for Monte Carlo ray tracing. In: R. C. JUERGENS (Editor), *Optical Design and Analysis Software, Proc. SPIE*, vol. 3780, pp. 148–150. Presented at the Society of Photo-Optical Instrumentation Engineers (SPIE) Conference
URL <http://adsabs.harvard.edu/abs/1999SPIE.3780..148F>
- BERNHARD FRISCHER [2003]: Mission and Recent Projects of the UCLA Cultural Virtual Reality Laboratory. In: R. VERGNIEUX and C. DELEVOIE (Editors), *Proceedings of the Conference Virtual Retrospect*, pp. 65–76. Biarritz, France. (accessed November 7, 2005)
URL <http://www.cvrlab.org/research/images/FrischerVirtRetro2003.pdf>
- C. FRÖHLICH and GLENN E. SHAW [1980]: New determination of Rayleigh scattering in the terrestrial atmosphere. In: *Applied Optics* vol. 19(11), pp. 1773–1775
- ROY H. GARSTANG [1986]: Model for Artificial Night-Sky Illumination. In: *Publications of the Astronomical Society of the Pacific* vol. 98, pp. 364–375
- ROY H. GARSTANG [2000]: Limiting Visual Magnitude and Night Sky Brightness. In: *Memorie della Società Astronomica Italiana (Journal of the Italian Astronomical Society)* vol. 71(1), pp. 83–92
URL <http://www.lightpollution.it/cinzano/memorie/garstang1.pdf>
- M. G. GIBBONS [1958]: Radiation Received by Uncollimated Receiver from a 4π Source. In: *Journal of the Optical Society of America* vol. 48(8), pp. 550–555
- S. GONZI, D. BAUMGARTNER, and E. PUTZ [2002]: Aerosol Climatology and Optical Properties of Key Aerosol Types Observed in Europe. Tech. Rep. for EU No. 1/2002, IGAM/University of Graz, Austria
- YVES GUÉNA and MOKHTAR TALEB-BENDIAB (Editors) [2005]: *L'Âge d'or des sciences arabes: Exposition présentée à l'Institut du monde arabe, Paris, 25 octobre 2005–19 mars 2006*. Actes Sud/Institut du monde arabe, Paris. ISBN 2-7427-5672-8
- ROBERT T. GUNTHER [1932]: *Astrolabes of the World*. The Holland Press Ltd., London. (reprint 1976)
- DIEGO GUTIERREZ, A. MUÑOZ, F. SERON, and E. JIMENEZ [2003]: Global Illumination in Inhomogeneous Media based on Curved Photon Mapping. In: M. H. HAMZA (Editor), *Proc. Visualization, Imaging, and Image Processing (VIIP2003)*, vol. II. ACTA Press
- DIEGO GUTIERREZ, F. SERON, O. ANSON, and A. MUNOZ [2004]: Chasing the Green Flash: a Global Illumination Solution for Inhomogeneous Media. In: *Proc. Spring Conference on Computer Graphics (SCCG 2004)*, pp. 95–103. Budmerice, Slovakia. ISBN 80-223-1918-X
- DIEGO GUTIERREZ, ADOLFO MUÑOZ, OSCAR ANSON, and FRANCISCO J. SERON [2005a]: Non-Linear Volume Photon Mapping. In: KAVITA BALA and PHILIP DUTRÉ (Editors), *Proc. EG Symposium on Rendering (EGSR2005)*. Eurographics
- DIEGO GUTIERREZ, FRANCISCO J. SERON, ADOLFO MUÑOZ, and OSCAR ANSON [2005b]: Rendering Ghost Ships and Other Phenomena in Arctic Atmospheres. In: *WSCG'2005 SHORT papers proceedings*. UNION Agency – Science Press, Plzen. ISBN 80-903100-9-5

- JÖRG HABER, MARCUS MAGNOR, and HANS-PETER SEIDEL [2005]: Physically based Simulation of Twilight Phenomena. In: *ACM Transactions on Graphics* vol. 24(4), pp. 1353–1373
- SVEN HAVEMANN and DIETER W. FELLNER [2004]: Generative Parametric Design of Gothic Window Tracery. In: K. CAIN, Y. CHRYSANTHOU, F. NICCOLUCCI, and N. SILBERMAN (Editors), *Proceedings of the 5th International Symposium on Virtual Reality, Archaeology and Cultural Heritage (VAST 2004)*, pp. 193–201. Eurographics
- GERALD S. HAWKINS [1973]: *Stonehenge Decoded*. Fontana/Collins, London and Glasgow, 4th edn.
- Hayden Planetarium : Website. (accessed August 7, 2006)
URL <http://haydenplanetarium.org/>
- L. HENYEY and J. GREENSTEIN [1941]: Diffuse radiation in the galaxy. In: *Astrophysical Journal* vol. 93, pp. 70–83
- JAVIER HERNÁNDEZ-ANDRÉS, RAYMOND L. LEE, JR., and JAVIER ROMERO [2003]: Color and luminance asymmetries in the clear sky. In: *Applied Optics* vol. 42(3), pp. 458–464
- JAVIER HERNÁNDEZ-ANDRÉS, JUAN L. NIEVES, E. M. VALERO, and JAVIER ROMERO [2004]: Spectral-daylight recovery by use of only a few sensors. In: *Journal of the Optical Society of America A* vol. 21(1), pp. 13–23. Improved by LÓPEZ-ÁLVAREZ *et al.* [2005]
- M. HESS, P. KOEPKE, and I. SCHULT [1998a]: Optical Properties of Aerosols and Clouds: The Software package OPAC. In: *Bulletin of the American Meteorological Society* vol. 79(5), pp. 831–844. Software available
URL <http://www.lrz-muenchen.de/~uh234an/www/radaer/opac-des.html>
- M. HESS *et al.* [1998b]: GADS – Global Aerosol Data Set
URL http://www.lrz-muenchen.de/~uh234an/www/radaer/gads_des.html
- FRANK A. VAN DEN HEUVEL, RUUD VERWAAL, and BART BEERS [2006]: Calibration of Fish-eye Camera Systems and the Reduction of Chromatic Aberration. In: H.-G. MAAS and D. SCHNEIDER (Editors), *Proceedings of the ISPRS Commission V Symposium 'Image Engineering and Vision Metrology'*, vol. XXXVI-5. ISSN 1682-1750
URL http://www.isprs.org/commission5/proceedings06/paper/1267_Dresden06.pdf
- GÖTZ HOEPPE [1999]: *Blau – Die Farbe des Himmels*. Spektrum Akademischer Verlag, Heidelberg, Berlin. ISBN 3-827-0485-1
- NATY HOFFMAN and ARCOT J. PREETHAM [2002]: Rendering Outdoor Light Scattering in Real Time. In: *Game Developers Conference*
URL <http://ati.de/developer/dx9/ATI-LightScattering.pdf>
- C. Y. HOHENKERK, B. D. YALLOP, C. A. SMITH, and A. T. SINCLAIR [1992]: *Celestial Reference Systems*, chap. 3. In: SEIDELMANN [1992]
- INDUSTRIAL LIGHT AND MAGIC [2003]: OpenEXR website
URL <http://www.openexr.com>

- M. F. INGHAM [1971]: The light of the night sky and the interplanetary medium. In: *Rep. Prog. Phys.* vol. 34, pp. 876–912
- JOHN IRWIN [1996]: Full-Spectra Rendering of the Earth's Atmosphere using a Physical Model of Rayleigh Scattering. In: *Proc. 1996 EG UK Conference*, pp. 103–115. Eurographics, London
URL <http://info.mcc.ac.uk/CGU/staff/irwin/atmos/>
- D. JACKÈL and B. WALTER [1997]: Modeling and Rendering of the Atmosphere Using Mie-Scattering. In: *Computer Graphics Forum* vol. 16(4), pp. 201–210
- HENRIK WANN JENSEN [1996]: Global Illumination using Photon Maps. In: X. PUEYO and P. SCHRÖDER (Editors), *Rendering Techniques '96 (Proc. EG Rendering Workshop)*, pp. 21–30. Eurographics, Springer-Verlag Wien New York. ISBN 3-211-82883-4. ISSN 0946-2767
- HENRIK WANN JENSEN, SIMON PREMOŽE, PETER SHIRLEY, WILLIAM B. THOMPSON, JAMES A. FERWERDA, and MICHAEL M. STARK [2000]: Night Rendering. Tech. Rep. TR UUCS-00-016, University of Utah
- HENRIK WANN JENSEN, MICHAEL M. STARK, SIMON PREMOŽE, PETER SHIRLEY, F. DURAND, and J. DORSEY [2001]: A Physically-Based Night Sky Model. In: *Proceedings of SIGGRAPH 2001*. ACM
- D. B. JUDD, D. L. MACADAM, and G. WYSZECKI [1964]: Spectral Distribution of Typical Daylight as a Function of Correlated Color Temperature. In: *Journal of the Optical Society of America* vol. 54(8), pp. 1031–1040
- KAZUFUMI KANEDA, TAKASHI OKAMOTO, EIHACHIRO NAKAMAE, and TOMOYUKI NISHITA [1991]: Photorealistic image synthesis for outdoor scenery under various atmospheric conditions. In: *The Visual Computer* vol. 7(5&6), pp. 247–258
- KAROLIN KASTOWSKI, KLAUS LÖCKER, WOLFGANG NEUBAUER, and GEORG ZOTTI [2005]: Drehscheibe des Sternenhimmels? Die Kreisgrabenanlage Immendorf. In: DAIM and NEUBAUER [2005], pp. 80–82
- SAAD MASOOD KHAN and SUMANTA N. PATTANAIK [2004]: Modelling blue shift in moonlit scenes using rod cone interaction. In: *Journal of Vision* vol. 4(8), pp. 316–316. ISSN 1534-7362
URL <http://journalofvision.org/4/8/316/>
- DAVID KING *et al.* [2002]: A Catalogue of Medieval Astronomical Instruments to ca. 1500. online
URL <http://web.uni-frankfurt.de/fb13/ign/instrument-catalogue.html>
- RICHARD KITTLER and STANISLAV DARULA [2006]: The method of aperture meridians: a simple calculation tool for applying the ISO/CIE Standard General Sky. In: *Lighting Res. Technol.* vol. 38(2), pp. 109–122
- R. VICTOR KLASSEN [1987]: Modeling the Effect of the Atmosphere on Light. In: *ACM Transactions on Graphics* vol. 6(3), pp. 215–237. doi:<http://doi.acm.org/10.1145/35068.35071>

- E. C. KRUPP [1994]: *Echoes of the Ancient Skies – The Astronomy of Lost Civilizations*. Oxford University Press, New York, Oxford
- JAMES KUMLER and MARTIN BAUER [2000]: Fish-Eye Lens Designs and Their Relative Performance. In: *Proceedings of the Lens and Optical System Design and Engineering Conference of the SPIE Annual Meeting*, vol. 4093, pp. 360–369. SPIE
- PAUL KUNITZSCH [1966]: *Typen von Sternverzeichnissen in astronomischen Handschriften des zehnten bis vierzehnten Jahrhunderts*. Otto Harrassowitz, Wiesbaden
- ROBERT L. KURUCZ [2005]: Solar Flux Atlas website
URL <http://kurucz.harvard.edu/sun/fluxatlas/>
- ROBERT L. KURUCZ, I. FURENLID, J. BRAULT, and L. TESTERMAN [1984]: *Solar Flux Atlas from 296 to 1300nm*. National Solar Observatory, Sunspot, New Mexico. 240pp
- TIROLER LANDESUMWELTANWALT and WIENER UMWELTANWALTSCHAFT (Editors) [2003]: *Die Helle Not: Künstliche Lichtquellen – ein unterschätztes Naturschutzproblem*. Innsbruck, Wien, 2nd edn.
- GREG WARD LARSON and ROB SHAKESPEARE [1998]: *Rendering with Radiance — The Art and Science of Lighting Visualization*. Morgan Kaufmann Publishers, San Francisco, CA. ISBN 1-55860-499-5
- RAYMOND L. LEE, JR. [1994a]: Horizon brightness revisited: measurements and a model of clear-sky radiances. In: *Applied Optics* vol. 33(21), pp. 4620–4628
- RAYMOND L. LEE, JR. [1994b]: Twilight and daytime colors of the clear sky. In: *Applied Optics* vol. 33(21), pp. 4629–4638
- RAYMOND L. LEE, JR. [1998a]: Digital imaging of clear-sky polarization. In: *Applied Optics* vol. 37(9), pp. 1465–1476
- RAYMOND L. LEE, JR. [1998b]: Mie theory, Airy theory, and the natural rainbow. In: *Applied Optics* vol. 37(9), pp. 1506–1519
- RAYMOND L. LEE, JR. and JAVIER HERNÁNDEZ-ANDRÉS [2003]: Measuring and modelling twilight’s purple light. In: *Applied Optics* vol. 42(3), pp. 445–457
- W. H. LEHN and M. B. EL-ARINI [1978]: Computer-graphics analysis of atmospheric refraction. In: *Applied Optics* vol. 17(19), pp. 3146–3151
- WALDEMAR H. LEHN [1979]: The Novaya Zenlya effect: An arctic mirage. In: *Journal of the Optical Society of America A* vol. 69(5), pp. 776–781
- ANDREI LINȚU, JÖRG HABER, and MARCUS MAGNOR [2005]: Realistic Solar Disc Rendering. In: VÁCLAV SKALA (Editor), *Proc. WSCG’2005*. University of West Bohemia, UNION Agency, Plzen. ISBN 80-903100-7-9
- K. N. LIOU [2002]: *An Introduction to Atmospheric Radiation, International Geophysics*, vol. 84. Academic Press, 2nd edn.

- P.J. LITTLEFAIR [1994]: A comparison of sky luminance models with measure data from Garston, United Kingdom. In: *Solar Energy* vol. 53(4), pp. 315–322
- QUANHUA LIU and FUZHONG WENG [2006]: Combined Henyey-Greenstein and Rayleigh phase function. In: *Applied Optics* vol. 45(28), pp. 7475–7479
- MIGUEL A. LÓPEZ-ÁLVAREZ, JAVIER HERNÁNDEZ-ANDRÉS, JAVIER ROMERO, and RAYMOND L. LEE, JR. [2005]: Designing a practical system for spectral imaging of skylight. In: *Applied Optics* vol. 44(27), pp. 5688–5695. Based on HERNÁNDEZ-ANDRÉS *et al.* [2004]
- RICHARD LORCH (Editor) [2005]: *Al-Farghānī: On the Astrolabe (ca. 856–857)*. Franz Steiner Verlag, Wiesbaden. ISBN 3-515-08713-3. Oldest surviving Islam text on the astrolabe, ca. 856–857
- DAVID K. LYNCH and WILLIAM LIVINGSTON [1995]: *Color and Light in Nature*. Cambridge University Press
- A. I. MAHAN [1962]: Astronomical Refraction—Some History and Theories. In: *Applied Optics* vol. 1(4), pp. 497–511
- RAFAŁ MANTIUK, GRZEGORZ KRAWCZYK, RADOSŁAW MANTIUK, and HANS-PETER SEIDEL [2007]: High Dynamic Range Imaging Pipeline: Perception-motivated Representation of Visual Content. In: BERNICE E. ROGOWITZ, THRASYVOULOS N. PAPPAS, and SCOTT J. DALY (Editors), *Human Vision and Electronic Imaging XII*. No. 649212 in Proceedings of SPIE, SPIE, San Jose, USA
- NELSON L. MAX [1986]: Atmospheric illumination and shadows. In: *Computer Graphics (Proc. SIGGRAPH '86)*, vol. 20, pp. 117–124. ACM
- JEAN MEEUS [1997]: *Mathematical Astronomy Morsels*. Willmann-Bell, Inc., Richmond, Virginia
- JEAN MEEUS [1998]: *Astronomical Algorithms*. Willmann-Bell, Inc., Richmond, Virginia, 2nd edn.
- LUDWIG MEIER [1992]: *Der Himmel auf Erden – Die Welt der Planetarien*. Johann Ambrosius Barth, Leipzig, Heidelberg
- HENRI MICHEL [1947]: *Traité de L'Astrolabe*. Gauthier-Villars, Paris
- MARCEL MINNAERT [1993]: *Light and Color in the Outdoors*. Springer, New York Berlin Heidelberg. ISBN 0-387-97935-2
- ANDREJ MOHAR (Editor) [2007]: *7th European Symposium for the Protection of the Night Sky*. Bled, Slovenia
URL <http://www.darksky2007.si>
- P. MOON and D.E. SPENCER [1942]: Illumination from a non-uniform sky. In: *Illuminating Engineering* vol. 37, pp. 707–726
- JAMES E. MORRISON [2005]: Astrolabes Website. (accessed April 2007)
URL <http://www.astrolabes.org>

- HERMANN MUCKE [1993]: Sichtbarkeitsverhältnisse und Sonnenlauf. In: HERMANN MUCKE (Editor), *Moderne Astronomische Phänomenologie*. No. 20 in Sternfreundeseminar, Planetarium der Stadt Wien, Österreichischer Astronomischer Verein, Wien. After SCHOCH [1927]
- PASCAL MÜLLER, PETER WONKA, SIMON HAEGLER, ANDREAS ULMER, and LUC VAN GOOL [2006]: Procedural Modeling of Buildings. In: *SIGGRAPH '06: ACM SIGGRAPH 2006 Papers*, pp. 614–623. ACM Press, New York, NY, USA. ISBN 1-59593-364-6. doi: <http://doi.acm.org/10.1145/1179352.1141931>
- ROLF MÜLLER [1970]: *Der Himmel über dem Menschen der Steinzeit, Verständliche Wissenschaft*, vol. 106. Springer-Verlag, Berlin–Heidelberg–New York
- STEFAN MÜLLER, WOLFRAM KRESSE, N. GATENBY, and FRANK SCHÖFFEL [1995]: A radiosity approach for the simulation of daylight. In: P. M. HANRAHAN and W. PURGATHOFER (Editors), *Rendering Techniques 1995 (Proc. EG Rendering Workshop 1995)*, pp. 137–146. Eurographics, Springer, Wien, New York, St. Etienne, France. ISBN 3-211-82733-1. ISSN 0946-2767
- M. R. NAGEL, W. KWETA, H. QUENZEL, and R. WENDLING [1978]: *Daylight Illumination – Color-Contrast Tables*. Academic Press, New York–San Francisco–London
- BRETT D. NENER, NEVILLE FOWKES, and LAURENT BORREDON [2003]: Analytic models of optical refraction in the troposphere. In: *Journal of the Optical Society of America A* vol. 20(5), pp. 867–875
- OTTO NEUGEBAUER [1975]: *A History of Ancient Mathematical Astronomy, Studies in the History of Mathematics and Physical Sciences*, vol. 1. Springer-Verlag, New York, Heidelberg, Berlin
- TOMOYUKI NISHITA [1998]: Light Scattering Models for the Realistic Rendering of Natural Scenes. In: GEORGE DRETTAKIS and NELSON MAX (Editors), *Rendering Techniques '98 (Proc. 9th EG Rendering Workshop)*, pp. 1–10. Eurographics, Springer Wien New York
- TOMOYUKI NISHITA and EIHASHIRO NAKAMAE [1986]: Continuous Tone Representation of Three-Dimensional Objects Illuminated by Sky Light. In: *Proc. SIGGRAPH '86, Computer Graphics*, vol. 20(4), pp. 125–132. ACM Press, Dallas, TX, USA
- TOMOYUKI NISHITA, YASUHIRO MIYAWAKI, and EIHASHIRO NAKAMAE [1987]: A shading model for atmospheric scattering considering luminous intensity distribution of light sources. In: *SIGGRAPH Computer Graphics* vol. 21(4), pp. 303–310. ISSN 0097-8930. doi: <http://doi.acm.org/10.1145/37402.37437>
- TOMOYUKI NISHITA, TAKAO SIRAI, KATSUMI TADAMURA, and EIHASHIRO NAKAMAE [1993]: Display of the Earth Taking into Account Atmospheric Scattering. In: *SIGGRAPH '93: Proceedings of the 20th annual conference on Computer graphics and interactive techniques, Computer Graphics*, vol. 27, pp. 175–182. ACM Press, New York, NY, USA. ISBN 0-89791-601-8. doi: <http://doi.acm.org/10.1145/166117.166140>
URL <http://citeseer.ist.psu.edu/tomoyuki93display.html>

- TOMOYUKI NISHITA, YOSHINORI DOBASHI, KAZUFUMI KANEDA, and HIDEO YAMASHITA [1996a]: Display Method of the Sky Color Taking into Account Multiple Scattering. In: *Pacific Graphics '96*, pp. 117–132
- TOMOYUKI NISHITA, YOSHINORI DOBASHI, and EIHASHIRO NAKAMAE [1996b]: Display of clouds taking into account multiple anisotropic scattering and sky light. In: *SIGGRAPH '96: Proceedings of the 23rd annual conference on Computer graphics and interactive techniques*, pp. 379–386. ACM Press, New York, NY, USA. ISBN 0-89791-746-4. doi:<http://doi.acm.org/10.1145/237170.237277>
- J. A. NORTH and M. J. DUGGIN [1997]: Stokes vector imaging of the polarized sky-dome. In: *Applied Optics* vol. 36(3), pp. 723–730
- WILLIAM TYLER OLCOTT [2004]: *Star Lore: Myths, Legends, and Facts*. Dover Publications, Inc., Mineola, New York. ISBN 0-486-43581-4. Reprint of 1911 edition
- STEPHEN JAMES O'MEARA [2005a]: Haidinger's Brush – Part I. In: *Sky&Telescope* vol. 110(1), pp. 72–73
- STEPHEN JAMES O'MEARA [2005b]: Haidinger's Brush – Part II. In: *Sky&Telescope* vol. 110(2), pp. 74–75
- SEAN O'NEIL [2004]: Real-Time Atmospheric Scattering. online. (accessed July 2007)
URL <http://www.gamedev.net/reference/articles/article2093.asp>
- JAMES C. OWENS [1967]: Optical Refractive Index of Air: Dependence on Pressure, Temperature and Composition. In: *Applied Optics* vol. 6(1), pp. 51–59
- OXFORD MUSEUM OF THE HISTORY OF SCIENCE [2006]: The Astrolabe: an Online Resource
URL <http://www.mhs.ox.ac.uk/astrolabe/>
- NORBERT PACHNER [1994]: Zur Erfassung der Sichtbarkeitsperioden ekliptikferner Gestirne. In: HERMANN MUCKE (Editor), *Astronomische Phänomenologie– Tatsachen, Probleme, Hilfsmittel*. No. 21 in Sternfreundeseminar, Planetarium der Stadt Wien, Österreichischer Astronomischer Verein, Wien. After SCHOCH [1927]
- PEKKA PARVIAINEN : Polar Image. online
URL <http://www.polarimage.fi/>
- JURAJ PAVÚK and VLADIMÍR KARLOVSKÝ [2004]: Orientácia Rondelov Lengyelskej Kultúry na Smery Vysokého a Nízkeho Mesiaca. In: *Slovenská Archeológia* vol. LII(2), pp. 211–280
- RUDOLF PENNDORF [1957]: Tables of the Refractive Index for Standard Air and the Rayleigh Scattering Coefficient for the Spectral Region between 0.2 and 20.0 μ and Their Application to Atmospheric Optics. In: *Journal of the Optical Society of America* vol. 47(2), pp. 176–182
- R. PEREZ, J.R. SEALS, and P. INEICHEN [1993]: An allweather model for sky luminance distribution. In: *Solar Energy*
- PFStmo [2007]: PFStmo::tone mapping operators. website
URL <http://www.mpi-inf.mpg.de/resources/tmo/>

- PFSTools [2006]: PFSTools website
URL <http://www.mpi-inf.mpg.de/resources/pfstools/>
- KEITH POWELL : Java Astrolabe. (accessed April 2007)
URL <http://www.autodidacts.f2s.com/astro/index.html>
- ARCOT J. PREETHAM [2003]: Modeling Skylight and Aerial Perspective. In: *ACM SIGGRAPH 2003 Course Notes*. ATI Research
- ARCOT J. PREETHAM, PETER SHIRLEY, and BRIAN SMITS [1999]: A Practical Analytic Model for Daylight. In: *SIGGRAPH '99: Proceedings of the 26th Annual Conference on Computer Graphics and Interactive Techniques*, pp. 91–100. ACM Press/Addison-Wesley Publishing Co., New York, NY, USA. ISBN 0-201-48560-5. doi:<http://doi.acm.org/10.1145/311535.311545>
- DAVID PYE [2001]: *Polarised Light in Science and Nature*. Institute of Physics Publishing, Bristol, Philadelphia
- R. C. RAMSEY [1962]: Spectral Irradiance from Stars and Planets, above the Atmosphere, from 0.1 to 100.0 Microns. In: *Applied Optics* vol. 1(4), pp. 465–471
- LORD RAYLEIGH [1871]: On the Scattering of Light by Small Particles. In: *Philosophical Magazine* vol. 41, pp. 447–454
- LORD RAYLEIGH [1899]: On the Transmission of Light through an Atmosphere containing Small Particles in Suspension, and on the Origin of the Blue Sky. In: *Philosophical Magazine* vol. 47, pp. 375–384
- ERIK REINHARD, GREG WARD, SUMANTA PATTANAIAK, and PAUL DEBEVEC [2006]: *High Dynamic Range Imaging – Acquisition, Display, and Image-Based Rendering*. Morgan-Kaufmann Publisher/Elsevier. ISBN 978-0-12-585263-0
- KIRK RILEY, DAVID S. EBERT, MARTIN KRAUS, JERRY TESSENDORF, and CHARLES HANSEN [2004]: Efficient Rendering of Atmospheric Phenomena. In: H. W. JENSEN and A. KELLER (Editors), *Proc. Eurographics Symposium on Rendering 2004*. Eurographics
- MARK A. ROBERTSON, SEAN BORMAN, and ROBERT L. STEVENSON [1999]: Dynamic Range Improvement through Multiple Exposures. In: *Proc. International Conference on Image Processing, ICIP 1999*, vol. 3, pp. 159–163. IEEE. ISBN 0-7803-5467-2
- MARK A. ROBERTSON, SEAN BORMAN, , and ROBERT L. STEVENSON [2003]: Estimation-Theoretic Approach to Dynamic Range Improvement Using Multiple Exposures. In: *Journal of Electronic Imaging* vol. 12(2)
- RUSSELL D. SAMPSON, EDWARD P. LOZOWSKI, and ARTHUR E. PETERSON [2003]: Comparison of modeled and observed astronomical refraction of the setting Sun. In: *Applied Optics* vol. 42(3), pp. 342–353
- HAROLD N. SAUNDERS [1984]: *All The Astrolabes*. Senecio Publishing Company Ltd., Oxford, England. ISBN 0-906831-04-0

BRADLEY E. SCHAEFER [1985]: Predicting Heliacal Risings and Settings. In: *Sky&Telescope* vol. 70, pp. 261–263

BRADLEY E. SCHAEFER [1987]: Heliacal Rise Phenomena. In: *Archaeoastronomy* vol. 11(JHA xviii), pp. S19–S33

BRADLEY E. SCHAEFER [1993]: Astronomy and the Limits of Vision. In: *Vistas in Astronomy* vol. 36, pp. 311–361

WOLFHARD SCHLOSSER and JAN CIERNY [1996]: *Sterne und Steine – Eine praktische Astronomie der Vorzeit*. Wissenschaftliche Buchgemeinschaft, Darmstadt

K. SCHOCH [1927]: *Planeten-Tafeln für Jedermann*. Linser-Verlag, Berlin-Pankow. With amendments in *Astr. Abh.* 8, 2 B17 (1930)

ELLEN SCHWALBE [2005]: Geometric Modelling and Calibration of Fisheye Lens Camera Systems. In: R. REULKE and U. KNAUER (Editors), *Proceedings of the ISPRS working group V/5 'Panoramic Photogrammetry Workshop'*, vol. XXXVI-5/W8. Berlin. ISSN 1682-1750
URL http://www2.informatik.hu-berlin.de/sv/pr/PanoramicPhotogrammetryWorkshop2005/Paper/PanoWS_Berlin

P. KENNETH SEIDELMANN (Editor) [1992]: *Explanatory Supplement to the Astronomical Almanac*. University Science Books, Sausalito, California

FRANCISCO SERON, DIEGO GUTIERREZ, GUILLERMO GUTIERREZ, and E. CEREZO [2004]: Visualizing Sunsets through Inhomogeneous Atmospheres. In: *Proc. Computer Graphics International (CGI 2004)*, pp. 349–356. IEEE Computer Society Press. ISSN 1530-1052

SkySkan [2003]: SkySkan Website. (accessed August 7, 2006)
URL <http://www.skyskan.com/>

JAROSLAV SLOUP [2002]: A Survey of the Modelling and Rendering of the Earth's Atmosphere. In: *Proceedings of SCCG2002*

JAROSLAV SLOUP [2003]: Visual Simulation of Refraction Phenomena in the Earth's Atmosphere. In: *Proc. of the Seventh International Conference on Information Visualization (IV'03)*. IEEE Computer Society

BOJANA SPASOJEVIĆ and ARDESHIR MAHDAVI [2005]: Sky Luminance Mapping for Computational Daylight Modeling. In: *Proc. 9th International IBPSA Conference, Building Simulation 2005*, pp. 1163–1169. Montréal

ROBERT SPENCE [2001]: *Information Visualization*. Addison-Wesley. ISBN 0-201-59626-1

PETER STADLER [1995]: Ein Beitrag zur Absolutchronologie des Neolithikums in Ostösterreich aufgrund der 14C-Daten. In: EVA LENNEIS *et al.* (Editors), *Jungsteinzeit im Osten Österreichs*, pp. 102–105. Wissenschaftliche Schriftenreihe Niederösterreich

JOS STAM and ERIC LANGUÉNOU [1996]: Ray Tracing in Non-Constant Media. In: *Rendering Techniques '96*, pp. 225–234. Eurographics, Springer

StarryNight : Starry Night website. (accessed August 7, 2006)
URL <http://www.starrynight.com/>

- JOHANN STÖFFLER [1513]: *Elucidatio fabricae ususque astrolabii*. Oppenheim
- JESSI STUMPFEL [2004]: *HDR Lighting Capture of the Sky and Sun*. Master's thesis, California Institute of Technology
- JESSI STUMPFEL, CHRIS TCHOU, ANDREW JONES, TIM HAWKINS, ANDREAS WENGER, and PAUL DEBEVEC [2004]: Direct HDR Capture of the Sun and Sky. In: *AFRIGRAPH '04: Proceedings of the 3rd international conference on Computer graphics, virtual reality, visualisation and interaction in Africa*, pp. 145–149. ACM Press, New York, NY, USA. ISBN 1-58113-863-6. doi:<http://doi.acm.org/10.1145/1029949.1029977>
- VERONICA SUNDSTEDT, ALAN CHALMERS, and PHILIPPE MARTINEZ [2004]: High Fidelity Reconstruction of the Ancient Egyptian Temple of Kalabsha. In: *Proceedings of AFRIGRAPH*. ACM SIGGRAPH
- Sunprognosis : Sunprognosis website. (accessed November 9, 2005)
URL <http://www.sunprognosis.com>
- KATSUMI TADAMURA, EIHACHIRO NAKAMAE, KAZUFUMI KANEDA, MASASHI BABA, HIDEO YAMASHITA, and TOMOYUKI NISHITA [1993]: Modeling of Skylight and Rendering of Outdoor Scenes. In: R. J. HUBBOLD and R. JUAN (Editors), *Proc. EUROGRAPHICS '93, Computer Graphics Forum*, vol. 12(3), pp. C-189–C-200. Eurographics, Blackwell
- ATSUSHI TAKAGI, HITOSHI TAKAOKA, TETSUYA OSHIMA, and YOSHINORI OGATA [1990]: Accurate Rendering Technique Based on Colorimetric Conception. In: *SIGGRAPH '90: Proceedings of the 17th annual conference on Computer graphics and interactive techniques*, pp. 263–272. ACM Press, New York, NY, USA. ISBN 0-201-50933-4. doi:<http://doi.acm.org/10.1145/97879.97908>
- ALEXANDER THOM [1967]: *Megalithic Sites in Britain*. Clarendon Press, Oxford
- ALEXANDER THOM and ALEXANDER S. THOM [1978]: *Megalithic Remains in Britain and Brittany*. Clarendon Press, Oxford
- CLAUDIO TOMASI, VITO VITALE, BOYAN PETKOV, ANGELO LUPI, and ALESSANDRA CACCIARI [2005]: Improved algorithm for calculations of Rayleigh-scattering optical depth in standard atmospheres. In: *Applied Optics* vol. 44(16), pp. 3320–3341
- ANNA TOMASZEWSKA and RADOSLAW MANTIUK [2007]: Image Registration for Multi-exposure High Dynamic Range Image Acquisition. In: *Proc. WSCG'2007*. University of West Bohemia, UNION Agency. ISBN 978-80-86943-98-5
- R. TOUSEY and M. J. KOOMEN [1953]: The Visibility of Stars and Planets During Twilight. In: *Journal of the Optical Society of America* vol. 43(3), pp. 177–183
- UCLA : UCLA Cultural Virtual Reality Laboratory. (accessed November 7, 2005)
URL <http://www.cvrilab.org/>
- UNIHDRON : *Sky Quality Meter (SQM)*. Grimsby, Canada
URL <http://www.unihedron.com>

- BERTRAM WALTER [1996]: *Erweiterung und Verbesserung eines strahlenphysikalischen Ansatzes zur Simulierung der Globalstrahlung und ihre Anwendung bei der Visualisierung windbewegter Wasseroberflächen*. Master's thesis, Universität Rostock
- H. F. WEAVER [1947]: In: *Publications of the Astronomical Society of the Pacific* vol. 59, p. 232
- RODERICK WEBSTER and MARJORIE WEBSTER [1998]: *Western Astrolabes*. Adler Planetarium & Astronomy Museum, Chicago. ISBN 1-891220-01-2
- SIEBREN Y. VAN DER WERF [2003]: Ray tracing and refraction in the modified US1976 atmosphere. In: *Applied Optics* vol. 42(3), pp. 354–366
- SIEBREN Y. VAN DER WERF, GÜNTHER P. KÖNNEN, and WALDEMAR H. LEHN [2003a]: Novaya Zenlya effect and sunsets. In: *Applied Optics* vol. 42(3), pp. 367–378
- SIEBREN Y. VAN DER WERF, GÜNTHER P. KÖNNEN, WALDEMAR H. LEHN, FRITS STEENHUISEN, and WAYNE P. S. DAVIDSON [2003b]: Gerrit de Veer's true and perfect description of the Novaya Zenlya effect, 24–27 January 1597. In: *Applied Optics* vol. 42(3), pp. 379–389
- ALEXANDER WILKIE, ROBERT F. TOBLER, CHRISTIANE ULBRICHT, GEORG ZOTTI, and WERNER PURGATHOFER [2004]: An Analytical Model for Skylight Polarisation. In: ALEXANDER KELLER and HENRIK WANN JENSEN (Editors), *Proceedings of the Eurographics Symposium on Rendering*, pp. 387–399. Eurographics. ISBN 3-905673-12-6
URL <http://www.cg.tuwien.ac.at/research/publications/2004/Wilkie-2004-AMS/>
- P. J. WILLIS [1987]: Visual Simulation of Atmospheric Haze. In: *Computer Graphics Forum* vol. 6, pp. 35–42
- LAWRENCE B. WOLFF and DAVID J. KURLANDER [1990]: Ray Tracing with Polarization Parameters. In: *IEEE Computer Graphics & Applications* vol. 10(6), pp. 44–55. ISSN 0272-1716
- PETER WONKA, MICHAEL WIMMER, FRANÇOIS SILLION, and WILLIAM RIBARSKY [2003]: Instant Architecture. In: *SIGGRAPH '03: ACM SIGGRAPH 2003 Papers*, pp. 669–677. ACM Press, New York, NY, USA. ISBN 1-58113-709-5. doi:<http://doi.acm.org/10.1145/1201775.882324>
- ANDREW T. YOUNG [2000]: Sunset science. III. Visual adaptation and green flashes. In: *Journal of the Optical Society of America A* vol. 17(12), pp. 2129–2139
- ANDREW T. YOUNG [2004]: Sunset science. IV. Low-altitude Refraction. In: *The Astronomical Journal* vol. 127, pp. 3622–3637
- ANDREW T. YOUNG and GEORGE W. KATTAWAR [1998]: Sunset science. II. A useful diagram. In: *Applied Optics* vol. 37(18), pp. 3785–3792
- ANDREW T. YOUNG, GEORGE W. KATTAWAR, and PEKKA PARVIAINEN [1997]: Sunset science. I. The mock mirage. In: *Applied Optics* vol. 36(12), pp. 2689–2700
- JAQUES ZANINETTI, PIERRE BOY, and BERNARD PEROCHE [1999]: An Adaptive Method for Area Light Sources and Daylight in Ray Tracing. In: P. BRUNET and R. SCOPIGNO (Editors), *Proc. EUROGRAPHICS '99, Computer Graphics Forum*, vol. 18(3). Eurographics

- ERNST ZINNER [1967]: *Deutsche und Niederländische Astronomische Instrumente des 11. bis 18. Jahrhunderts*. C. H. Beck'sche Verlagsbuchhandlung, München, 2nd edn.
- GEORG ZOTTI [2005a]: Die Untersuchung keltisch-römischer Umgangstempel auf astronomische Orientierung. In: STEFAN GROH and HELGA SEDLMAYER (Editors), *Der norisch-römische Kultplatz am Frauenberg*, pp. 156–168. No. 9 in *Protohistoire Européenne*, Édition Monique Mergoil, Montagnac. ISBN 2907303945
- GEORG ZOTTI [2005b]: Kalenderbauten? – Zur astronomischen Ausrichtung der Kreisgrabenanlagen in Niederösterreich. In: DAIM and NEUBAUER [2005], pp. 75–79
- GEORG ZOTTI [2006]: A Sky Dome Visualisation for Identification of Astronomical Orientations. In: *Information Visualization* vol. 2006(5), pp. 152–166. ISSN 1473-8716
URL <http://www.cg.tuwien.ac.at/research/publications/2006/zotti-2006-dgm/>
- GEORG ZOTTI [2007a]: Tangible Heritage: Production of Astrolabes on a Laser Engraver. In: DAVID B. ARNOLD and ANDREJ FERKO (Editors), *Eurographics 2007 Cultural Heritage Papers*, pp. 41–48. Eurographics, Praha. ISSN 1017-4656
- GEORG ZOTTI [2007b]: Measuring Light Pollution with a Calibrated High Dynamic Range All-Sky Image Acquisition System. In: MOHAR [2007]
URL <http://www.darksky2007.si>
- GEORG ZOTTI [2008]: Zur astronomischen Interpretation ausgezeichneter Richtungen der Kreisgrabenanlagen Niederösterreichs. In: *Acta Praehistorica et Archaeologica* vol. 40
- GEORG ZOTTI [to appear]: Versuch einer astronomischen Interpretation ausgezeichneter Richtungen der Kreisgrabenanlagen Niederösterreichs. In: FRANÇOIS BERTEMES, PETER F. BIEHL, and HARALD MELLER (Editors), *Neolithische Kreisgrabenanlagen in Europa. Tagungsband zur Internationalen Arbeitstagung in Goseck (Sachsen-Anhalt), 7.–9. Mai 2004*. Landesamt für Denkmalpflege und Archäologie Sachsen-Anhalt, Halle. (submitted 10/2004)
- GEORG ZOTTI and MEISTER EDUARD GRÖLLER [2005]: A Sky Dome Visualisation for Identification of Astronomical Orientations. In: JOHN STASKO and MATT WARD (Editors), *Proceedings IEEE Symposium on Information Visualization*, pp. 9–16. IEEE. ISBN 0-7803-9464-X
URL <http://www.cg.tuwien.ac.at/research/publications/2005/Zotti-2005-vis/>
- GEORG ZOTTI, ALEXANDER WILKIE, and WERNER PURGATHOFER [2006]: Using Virtual Reconstructions in a Planetarium for Demonstrations in Archaeo-Astronomy. In: CECILIA SIK LANYI (Editor), *Third Central European Multimedia and Virtual Reality Conference (Proc. CEMVRC2006)*, pp. 43–51. Pannonian University Press. ISBN 963-9495-89-1
URL <http://www.cg.tuwien.ac.at/research/publications/2006/zotti-2006-pla/>
- GEORG ZOTTI, ALEXANDER WILKIE, and WERNER PURGATHOFER [2007]: A Critical Review of the Preetham Skylight Model. In: VACLAV SKALA (Editor), *WSCG '2007 Short Communications Proceedings I*, pp. 23–30. University of West Bohemia. ISBN 978-80-86943-02-2
URL <http://www.cg.tuwien.ac.at/research/publications/2007/zotti-2007-wscg/>